Accelerated Magnetic Resonance Imaging Applications in Drug Discovery

Zur Erlangung des akademischen Grades einer

DOKTORIN DER INGENIEURWISSENSCHAFTEN (Dr.-Ing.)

von der KIT-Fakultät für Maschinenbau
des Karlsruher Instituts für Technologie (KIT)

angenommene

DISSERTATION

von

M.Sc. Dilara Faderl

Tag der mündlichen Prüfung:	01 April 2026
Erstgutachter:	Prof. Dr. Jan Gerrit Korvink
Zweitgutachter:	Prof. Dr. Pavel Levkin

Ich versichere wahrheitsgemäß, die Arbeit selbstständig angefertigt, alle benutzten Hilfsmittel vollständig und genau angegeben und alles kenntlich gemacht zu haben, was aus Arbeiten anderer unverändert oder mit Änderungen entnommen wurde.

Karlsruhe, 11.12.2025

. . . . . .

(Dilara Faderl)

Abstract

Magnetic Resonance Imaging (MRI) offers a unique, non-invasive window into molecular processes, allowing the visualization and quantification of biomolecular interactions under physiologically relevant, aqueous conditions without chemical modification or immobilization of the binding partners. Because protein binding pockets remain freely accessible and no steric perturbations are introduced, MR-based approaches enable the direct observation of binding dynamics that are essential for understanding and optimizing drug–target interactions.

In contrast to many optical or surface-based analytical platforms, magnetic resonance (MR) techniques do not require fluorescent or affinity labels, nor do they depend on coupling proteins or ligands to solid supports, both of which can alter native binding behavior. A key advantage is the ability to detect very small molecular fragments, which typically bind only weakly but represent highly valuable starting points in fragment-based drug discovery (FBDD). Under purely aqueous, near-physiological conditions, MR therefore provides chemically unperturbed readouts of ligand binding, selectivity, and competition.

Despite these strengths, conventional MR assays are limited to the sequential acquisition of individual samples. Each sample requires an independent spectral measurement, the duration of which is strongly influenced by the relaxation and diffusion properties of the ligand under investigation. This inherently low throughput restricts the number of candidates that can be evaluated per day. Early-stage drug discovery, in contrast, demands the efficient screening (high-throughput screening, HTS) of large and chemically diverse ligand libraries to identify promising lead candidates.

To address biochemical questions reliably, such as detecting binding, assessing selectivity, comparing competitors, or ranking their affinities, analytical methods must combine speed with comprehensive readouts across many candidates in parallel. High-throughput assay formats are therefore indispensable for the rapid interrogation of thousands of potential small-molecule binders. The intrinsically low throughput of conventional MR workflows poses a fundamental bottleneck: scaling such assays to the million-compound libraries common in industrial pipelines would require years to decades of continuous measurement.

Addressing this limitation, the first part of this thesis harnesses MRI's inherent spatial encoding to interrogate many independent reaction volumes in parallel. Using custom miniaturized sample holders that organize discrete microvolumes within the imaging field of view, MRI is transformed into a high-content screening modality in which each voxel represents an individual microreactor. This voxel-level parallelization enables the acquisition of hundreds of protein–ligand binding experiments within a single measurement. High-throughput MRI (HiT-MRI) thereby provides not only parallelized data acquisition but also access to multiple quantitative parameters supporting robust hit identification and validation.

In this work, we establish a ^{19}F-MRI platform for spatially parallelized quantification of protein–ligand interactions using spin-echo–based pulse sequences. Multi-slice multi-echo (MSME) and rapid acquisition with relaxation enhancement (RARE) experiments were implemented to obtain transverse relaxation(T_2)–weighted MR images, from which the apparent relaxation rate (R_2) was derived voxel-wise. The spin-echo principle inherently suppresses susceptibility-induced artifacts and isolates the pure T_2-decay component, providing reliable, quantitative contrast. It enables the extraction of molecular relaxation dynamics directly sensitive to ligand–protein binding equilibria.

For small fluorinated ligands such as 4-(trifluoromethyl)benzamidine (TFBA), exchange between free and bound states occurs in the fast-exchange regime on the MR timescale (ms–µs). Consequently, the observed R_2 reflects a population-weighted average of contributions from free ligand, and bound complex states. Therefore, changes in R_2 of the fluorinated reporter ligand report on equilibrium shifts induced by protein concentration or by competitive displacement. In such competitive binding experiments, non-fluorinated competitor ligands (drug candidates) displace the fluorinated reporters from the protein binding pockets, resulting in measurable recovery of their ^{19}F-signal. Apparent dissociation constants (K_C) can thus be extracted from each voxel from dose-dependent ^{19}F-T_2-weighted images. Based on this methodology on the TFBA–trypsin model system, we have demonstrated the ^{19}F-T_2-experiments in the second part of the thesis using a capillary-based microarray containing nine parallel samples. This proof of concept provided direct binding and affinity readouts for the benzamidine competitor ligand within a single MR scan. The platform was subsequently scaled to a 3D-printed honeycomb sample holder comprising 61 individually addressable cells, each forming a discrete micro-experiment. This configuration enabled the simultaneous screening of 55 compounds in a single measurement, extending the accessible affinity range toward weaker competitors (K_C in mM scale).

The platform was subsequently scaled to a 3D-printed honeycomb sample holder in the third part of the work, comprising 61 individually addressable cells, each forming a discrete micro-experiment. This configuration enabled the simultaneous screening of 55 compounds in a single measurement, extending the accessible affinity range toward weaker competitors (K_C in mM scale). , Here, we also examined spatial resolution constraints inherent to MRI. Accurate ^{19}F-T_2 quantification in the capillary and honeycomb formats requires sufficiently small voxels to localize individual microexperiments while preserving signal-to-noise ratio. Higher spatial resolutions, however, inevitably increase measurement time. To overcome this trade-off, we implemented a compressed sensing (CS) reconstruction scheme exploiting sparsity in *k*-space. By undersampling *k*-space while maintaining quantitative accuracy in K_C determination, total acquisition times were significantly reduced without loss of analytical precision. The transfer of the reproducibility of this ligand screening methodology from the well-studied trypsin protein to a complex protein target, phosphopantetheine adenylyltransferase (PPAT), was successfully implemented.

In the final chapter, gadolinium-based paramagnetic contrast agents (Magnevist and gadolinium chloride) were introduced to further accelerate relaxation-weighted imaging. Their presence shortens both T_1 and T_2-relaxation time, enabling faster scans. The combination of contrast agent Magnevist, advanced undersampling strategy of CS, and miniaturized sample geometries using the honeycomb cell array establishes a powerful route toward genuinely high-throughput MR-based screening.

In summary, this work demonstrates a scalable, quantitative, and spatially multiplexed ^{19}F-MRI framework for the direct visualization of protein–ligand binding and competition dynamics. By integrating spin-echo–based imaging, compressed sensing acceleration, and microstructured 3D-printed sample arrays, MRI is transformed from a purely diagnostic modality into a molecular screening tool. The approach bridges molecular-level sensitivity with imaging-based parallelization, opening a path toward rapid and reliable drug-candidate validation through simultaneous extraction of drug-related relaxation and binding affinity parameters within a single MR experiment.

Zusammenfassung

Die Magnetresonanztomographie (MRI) eröffnet ein einzigartiges, nicht-invasives Fenster in molekulare Prozesse und ermöglicht die Visualisierung von Biomolekülinteraktionen unter physiologisch relevanten, wässrigen Bedingungen, ohne dass chemische Modifikationen oder Immobilisierungsschritte erforderlich sind. Dadurch bleiben Proteinbindungstaschen frei zugänglich und sterische Störungen werden vermieden, was eine quantitative Erfassung der Bindungsdynamik erlaubt, die für die Arzneimittelentdeckung von zentraler Bedeutung ist.

Im Gegensatz zu vielen optischen oder oberflächenbasierten Methoden müssen die Bindungspartner bei magnetresonanzbasierten (MR) Techniken nicht an feste Oberflächen gekoppelt werden und benötigen keine fluoreszenten oder sonstigen Markierungen, die die natürlichen Bindungseigenschaften verändern könnten. Ein besonderer Vorteil liegt in der Fähigkeit der MR, auch sehr kleine Molekülfragmente detektieren zu können, die aufgrund ihrer geringen Größe oft nur schwach an Proteine binden – ein entscheidender Aspekt im fragmentbasierten Wirkstoffdesign (*fragment-based drug discovery*, FBDD). Unter vollständig wässrigen, nahezu physiologischen Bedingungen liefert MR damit ungestörte Informationen über Bindung, Selektivität und Konkurrenzverhalten kleiner Moleküle.

Trotz dieser Vorteile sind konventionelle MR-Assays durch die instrumentelle Umsetzung bislang auf die sequentielle Messung einzelner Proben beschränkt. Jede Probe erfordert eine separate spektrale Akquisition, deren Dauer stark von den Relaxations- und Diffusionseigenschaften des untersuchten Liganden abhängt. Diese inhärente Beschränkung führt zu einem niedrigen Probendurchsatz. In der frühen Phase der Wirkstoffforschung hingegen müssen analytische Methoden nicht nur zuverlässig Bindung nachweisen, Selektivität beurteilen, Konkurrenten vergleichen oder deren Affinitäten einordnen, sondern dies auch schnell und parallel für viele Kandidaten leisten.

Hochdurchsatz-Formate (*high throughput screening*, HTS) sind daher unerlässlich, um in kurzer Zeit tausende potenzielle niedermolekulare Binder untersuchen zu können. Die geringe Durchsatzrate herkömmlicher MR-basierter Assays stellt hierbei einen fundamentalen Engpass dar: Würde man mit klassischer NMR versuchen, die millionenfachen Substanzen industrieller Screening-Bibliotheken zu messen, würden hierfür aufgrund der sequentiellen Messweise Jahre bis Jahrzehnte kontinuierlicher Experimente benötigt.

Der erste Teil dieser Arbeit adressiert diese Herausforderungen, indem die inhärente räumliche Kodierung der MRI genutzt wird, um zahlreiche unabhängige Experimente simultan unter ein MR Scan auszulesen. Durch maßgeschneiderte, miniaturisierte Probenhalter, die diskrete Mikrovolumina innerhalb des Bildfeldes strukturieren, lässt sich die MRI zu einer hochparallelen Screening-Technologie weiterentwickeln. Jedes Voxel fungiert dabei als eigener „Mikroreaktor“. Diese voxelbasierte Parallelisierung ermöglicht die Durchführung dutzender Protein–Ligand-Bindungsexperimente innerhalb einer einzigen Messung. Das resultierende High-Throughput MRI (HiT-MRI)-Format erlaubt nicht

nur eine stark beschleunigte Datenerfassung, sondern liefert gleichzeitig quantitative Parameter, die eine robuste Hit-Identifikation und -Validierung unterstützen.

Im zweiten Teil der Arbeit wird eine ^{19}F-MRI-Plattform zur räumlich parallelisierten Quantifizierung von Protein–Ligand-Wechselwirkungen etabliert. Hierzu kommen Spin-Echo-basierte Pulssequenzen, Multi-Slice Multi-Echo (MSME) und Rapid Acquisition with Relaxation Enhancement (RARE) zum Einsatz. Diese ermöglichen die Aufnahme transversal relaxationsgewichteter (T_2) MR-Bilder, aus denen die apparente Relaxationsrate (R_2) voxelweise bestimmt wird. Das Spin-Echo-Prinzip kompensiert magnetfeldinhomogenitätsbedingte Dephasierungen und isoliert die reine T_2-Relaxation, wodurch ein stabiler und quantitativer Bildkontrast gewährleistet wird. Dies erlaubt die Erfassung molekularer Relaxationsdynamiken, die unmittelbar auf Änderungen des Bindungsgleichgewichts zwischen Proteine und Liganden reagieren.

Für kleine fluorierte Reporterliganden wie 4-(trifluormethyl)benzamidin (TFBA) erfolgt der Austausch zwischen freiem und gebundenem Zustand auf der MR-Zeitskala im schnellen Austauschregime (im Bereich ms–µs). Das beobachtete transversale Relaxationszeit R_2^{obs} stellt daher einen populationsgewichteten Mittelwert der Relaxationsraten des freien Liganden und des Protein–Ligand-Komplexes dar.

Änderungen von R_2 spiegeln Bindungsverschiebungen wider, die durch nicht-fluorierte kompetitive Inhibition des Reporterliganden ausgelöst werden. Die resultierende Signalerholung von dem Reporterligand im ^{19}F-MRI ermöglicht die Bestimmung scheinbarer Dissoziationskonstanten (K_C) aus dosisabhängigen ^{19}F-T_2-gewichteten Aufnahmen. Der methodische Transfer wurde zunächst in einem kapillarbasierten Mikroarray mit neun parallelen Proben validiert und lieferte direkte Bindungs- und Affinitätsinformationen innerhalb eines einzigen MR-Scans.

Im Anschluss für den dritten Teil der Doktorarbeit, wurde die Plattform auf einen 3D-gedruckten Wabenprobenhalter mit 61 individuell adressierbaren Zellen skaliert. Jede Zelle repräsentiert dabei ein unabhängiges Experiment. Diese Geometrie ermöglichte das simultane Screening von 55 kompetetiven Liganden als Leitstruktur von starken und schwachen Affinitätsskala (µM- bis mM-Bereich) in einer einzigen Messung.

Weiterhin, die räumlichen und messtechnischen Auflösungsgrenzen der MRI in den beschriebenen Mikrostrukturformaten wurden untersucht, um den Zusammenhang zwischen Auflösung, SNR und Messzeit zu optimieren. Eine präzise ^{19}F-T_2-Quantifizierung erfordert einerseits ausreichend kleine Voxel zur eindeutigen Zuordnung einzelner Mikroexperimente, andererseits jedoch ein ausreichendes Signal-Rausch-Verhältnis. Höhere räumliche Auflösung führt zwangsläufig zu längeren Messzeiten.

Zur Überwindung dieses Zielkonflikts (Hochdurchsatz-Screening) wurde ein Rekonstruktionsansatz Compressed Sensing (CS) implementiert, der die Sparsität der Bilddaten im k-Raum ausnutzt. Auf diese Weise ließen sich die Gesamtmesszeiten signifikant reduzieren, ohne die quantitative Genauigkeit der R_2- und K_C-Bestimmung zu beeinträchtigen. Die erfolgreiche Übertragung der Liganden-Screening-Methodik vom gut charakterisierten Modellprotein Trypsin auf das komplexe Zielprotein Phosphopantethein-Adenylyltransferase (PPAT) war ebefalls erfolgreich.

Im letzten Kapitel wurden gadolinium basierende paramagnetische Kontrastmitteln (Magnevist und gadolinium-chlorid) eingesetzt, um relaxationsgewichtete Bildgebungssequenzen weiter zu beschleunigen. Durch die Verkürzung sowohl der longitudinalen (T_1)

als auch der transversalen (T_2) Relaxationszeiten ermöglichen sie deutlich schnellere Messungen. Die Kombination aus dem Kontrastmittel Magnevist, CS-basierter Unterabtastung und miniaturisierten Probengeometrien etabliert damit eine leistungsfähige Plattform für ein echtes MR-basiertes Hochdurchsatz-Screening.

Zusammenfassend präsentiert diese Arbeit ein skalierbares, quantitatives und räumlich multiplexes ^{19}F-MRI-Framework zur direkten Abbildung von Protein–Ligand-Interaktionen und kompetitiven Inhibitionsprozessen. Durch die Integration von T_2-basierter Bildgebung, Compressed-Sensing-Beschleunigung und mikrostrukturierten 3D-gedruckten Probenarrays wird die MRI von einer primär diagnostischen Technik zu einem molekularen Screeningwerkzeug weiterentwickelt. Der Ansatz verbindet molekulare Sensitivität mit bildgebender Parallelisierung und eröffnet einen Weg zur schnellen, robusten Validierung von Wirkstoffkandidaten durch die simultane Bestimmung relaxations- und affinitätsbasierter Parameter in einem einzigen MR-Experiment.

Contents

Nomenclature

Abbreviations

Abbreviations	Meaning
3D	Three-dimensional
AQ	Acquisition Time
AI	Artificial Intelligence
ADME	Absorption, Distribution, Metabolism, and Excretion
CA	Contrast Agent
CEST	Chemical Exchange Saturation Transfer
CNR	Contrast-to-Noise Ratio
CPMG	Carr–Purcell–Meiboom–Gill
CS	Compressed Sensing
CSA	Chemical Shift Anisotropy
CSI	Chemical Shift Imaging
CT	Computed Tomography
DAC	Digital-to-Analog Converter
DD	Dipole–Dipole Coupling
DCE-MRI	Dynamic Contrast Enhanced MRI
DNP	Dynamic Nuclear Polarization
DSF	Differential Scanning Fluorimetry
EPI	Echo Planar Imaging
ETL	Echo Train Length
FAXS	Fluorine-Based Exchange Screening
FE	Frequency Encoding
FID	Free Induction Decay
FOV	Field of View
FSE	Fast Spin Echo
FWHM	Full Width at Half Maximum
FBDD	Fragment-Based Drug Discovery
FT	Fourier Transformation
GRASE	Gradient And Spin Echo
GRE	Gradient Echo
ITC	Isothermal Titration Calorimetry
HTS	High Throughput Screening
ML	Machine Learning
MRS	Magnetic Resonance Spectroscopy
MRI	Magnetic Resonance Imaging
MR	Magnetic Resonance
MSME	Multi-Slice Multi-Echo
MTX	Matrix Size

Abbreviations	Meaning
NEMA	National Electrical Manufacturers Association
NEX	Number of Experiments
NMR	Nuclear Magnetic Resonance
NOE	Nuclear Overhauser Effect
NOAH	NMR by Ordered Acquisition using ^{1}H-detection
PANSY	Parallel Acquisition NMR Spectroscopy
PD	Proton Density
PE	Phase Encoding
PET	Positron Emission Tomography
PPAT	Phosphopantetheine adenylyltransferase
PRE	Paramagnetic Relaxation Enhancement
RF	Radio Frequency
RARE	Rapid Acquisition with Relaxation Enhancement
ROI	Region of Interest
SI	Signal Intensity
SL	Slice Length (thickness)
SNR	Signal-to-Noise Ratio
SPR	Surface Plasmon Resonance
SS	Slice Selection
STD-NMR	Saturation Transfer Difference NMR
TA	Time of Acquisition
TFBA	4-(Trifluoromethyl)benzamidine
TI	Inversion Time
waterLOGSY	Water-Ligand Observed via Gradient SpectroscopY

Symbols

Symbol	Meaning
^{13}C	Carbon
^{15}N	Nitrogen
^{17}O	Oxygen
α_{FA}	Flip angle
B_0	Static magnetic field
B_1	Radiofrequency magnetic field
BW	Bandwidth
γ	Gyromagnetic ratio
h	Proton
Hz	Hertz
I	Nuclear spin number
IC_{50}	Half-Maximal Inhibitory Concentration
JPEG	Joint Photographic Experts Group
k_B	Boltzmann constant
K	Kelvin
K_C	Competitor binding affinity constant
mM	Millimolar
µM	Micromolar
m	Magnetic quantum number
$\vec{M}_0$	Bulk magnetization
$\vec{M}_{eq}$	Equilibrium magnetization
$\vec{M}_L$	Longitudinal magnetization
$\vec{M}_T$	Transversal magnetization
S	Spin quantum number
T	Tesla
T1W	T_1-weighted
T2W	T_2-weighted
τ	Pulse duration
$\hat{\mu}$	Magnetic moment
^{19}F	Fluorine
OD	Outer diameter
ω	Chemical shift
ω_0	Larmor frequency
ω_L	Larmor precession
	Longitudinal relaxation rate
R_2	Transversal relaxation rate
T_1	Longitudinal relaxation time
T_2	Transversal relaxation time

1. Introduction

1.1. Motivation

Early-stage drug discovery relies on the rapid and reliable screening of large libraries of candidate molecules for their interactions with protein targets. Among the available analytical techniques, magnetic resonance (MR) spectroscopy and imaging occupy a unique position: they probe matter at *sub-molecular* length scales, since it reports on individual nuclei within a molecule, simultaneously providing non-invasive, quantitative readouts.

While slice-selective and gradient-assisted nuclear magnetic resonance (NMR) methods can provide limited spatial differentiation of samples, magnetic resonance imaging (MRI) offers full 3D spatial encoding that enables many discrete protein–ligand experiments to be performed within a single measurement. Each sample compartment occupies a defined position within the imaging volume, and its corresponding voxels represent an isolated micro-assay that experiences identical global experimental conditions, including magnetic field strength, pulse sequence, and temperature. This intrinsic spatial encoding makes MRI particularly well suited for miniaturized high-throughput formats, with the achievable spatial resolution being the primary limiting factor.

Simultaneous data acquisition is achieved through frequency- and phase-encoding in MRI, allowing all micro-assays to be spatially resolved according to their positions within the 3D imaging volume, provided that the spatial resolution is sufficient to separate adjacent compartments. With an appropriate holder design dozens of protein–ligand reactions can be positioned within the field of view. This enables the parallel quantification of numerous ligand–protein interactions in a single experiment, substantially increasing screening throughput while preserving biochemical fidelity.

Using ^{19}F-MRI and competitive binding assays—where only the fluorinated reporter ligand is detected—the signal intensity of the reporter reflects its local molecular environment. Because ^{19}F nuclei are intrinsically highly sensitive to changes in their chemical surroundings, the transverse relaxation (T_2) of the reporter responds to alterations in molecular tumbling upon protein binding and subsequent displacement by a non-fluorinated competitor ligand. The resulting T_2-weighted ^{19}F-MRI readout is inherently free from background signals arising from proteins, buffers, or other assay components, making it particularly attractive as a high-throughput screening (HTS) modality.

Because MR image data are acquired in k-space, the intrinsic sparsity of MRI images enables compressed-sensing and other undersampling strategies for substantial acceleration of data acquisition. Furthermore, the use of paramagnetic contrast agents can shorten longitudinal (T_1) and transverse (T_2) relaxation times, thereby reducing the required repetition times (TR) and echo times (TE) for T_2-mapping and further accelerating the workflow.

Together, these strategies render fluorine-based MRI compatible with the demands of modern drug-discovery pipelines. To translate the molecular-level chemical sensitivity of MRI into a practical screening tool for pharmaceutical libraries, a substantial increase in measurement throughput is essential. The development of a high-throughput ^{19}F-MRI framework that maintains biochemical integrity while enabling parallelized, quantitative readouts has therefore been a central motivation of this thesis.

1.2. Objective

The work presented in this thesis unites biology, engineering, chemistry, and mathematical imaging science to address a central bottleneck in MR-based drug discovery:

- **High-density spatial parallelization**

  The first aim of this thesis was to develop **sample-parallelized hardware** capable of dramatically increasing throughput on existing MRI systems. We systematically engineered a series of miniaturized, 3D-printed sample holders—from bundled NMR tubes to capillary arrays and ultimately a 61-cell honeycomb array—each designed to maximize filling factor, voxel isolation, and sample accessibility. These platforms enable dozens of independent biochemical assays to be monitored simultaneously, transforming the MRI readout from a single-sample measurement into a multiplexed assay environment.

- **Competitive binding assays using fluorinated reporter ligands**

  Whether parallelized MRI measurements remain quantitatively reliable under low-volume, low-concentration ligand screening conditions was investigated to validate the binding affinity of the non-fluorinated unknown competitors, where proteins and novel candidates are often available only in limited quantities in early-stage drug discovery. To address this, a ^{19}F-MRI–based competitive displacement assay was implemented to encode displacement events directly through changes in transverse relaxation time T_2 of the reporter ligand to accurate extraction of binding constants K_C for both strong and weak competitors, facilitating quantitative multi-sample screening even under low-SNR conditions.

- **Compressed sensing for undersampled MRI reconstruction**.

  Even with increased spatial parallelization, acquiring full relaxation-based displacement curves can be time-intensive if conventional fully sampled k-space strategies are used. Therefore, we integrated compressed sensing (CS) as an acceleration method. CS exploits sparsity in MR images to reconstruct high-fidelity datasets from undersampled measurements. By sampling only the essential contrast information required for T_2 quantification, compressed sensing enables substantially shorter acquisition times while preserving quantitative accuracy. Parallelization increases the number of samples per scan, while CS reduces the number of measurements required per sample, providing orthogonal acceleration axes.

- **Paramagnetic Relaxation Enhancement using Gadolinium-based contrast agents**

  The gadolinium-based contrast agents Magnevist and gadolinium chloride $GdCl_3$ were introduced to shorten both T_1 and T_2, thereby enabling reductions in TR and TE and further decreasing the total acquisition time. Magnevist, a clinically approved contrast agent known for its chemical inertness and biological safety, proved particularly effective: it produced substantial relaxation acceleration while leaving the protein–ligand binding equilibrium unchanged. In parallel, the inorganic salt $GdCl_3$ was investigated as an *in vitro* reference.

1.3. Outline

This thesis is structured into ten chapters, preceded by an introduction and theory section, and followed by a concluding outlook. The chapters are organized as follows:

Introductory Chapters

- **Chapter 1** introduces the motivation, objectives, and overall scientific background that motivates the development of high-throughput ^{19}F-MRI for quantitative drug discovery applications.
- **Chapter 2** provides the theoretical foundations relevant to this thesis, including MR signal principles, instrumentation, spatial encoding, k-space, fast imaging sequences, contrast mechanisms, compressed sensing, and ligand-based ^{19}F-MR competition experiments.

Part I: Sample Parallelization and Image Optimization

- **Chapter 3** describes the development of sample-parallelized imaging hardware, including bundled NMR tubes, capillary arrays, and the 61-well honeycomb array. It covers array design, filling-factor considerations, ROI analysis, and workflow integration into MRI.

Part II: Accelerated Drug Discovery Using ^{19}F-MRI

- **Chapter 4** presents the imaging setup and experimental workflow, including spin echo-pulse sequence selection, image-quality optimization, and rapid-imaging considerations for multi-sample assays. It introduces the drug-screening concept in competition mode, details the ^{19}F-MRI experimental setup, and characterizes the reporter ligand TFBA. It offers a demonstration of protein–ligand interaction imaging as proof of concept, including direct protein binding detection, competitive screening, affinity determination of the non-fluorinated unknown competitor ligands, and the calculation of sensitivity and acceleration factors using a 9-capillary setup.

Part III: Highly Parallelized Enzyme Inhibition Imaging with Compressed Sensing

- **Chapter 5** reviews the state of the art in high-throughput ^{19}F-MRI, providing context for the integration of sparsity-driven imaging into parallelized MRI assays. It details the design, implementation, and characterization of the miniaturized cell array for compressed sensing, including its application in screening of strong and weak trypsin competitors as well as PPAT/CoaD inhibitors.

Part IV: Gd-based Contrast Tuning for Rapid Ligand Screening

- **Chapter 6** evaluates paramagnetic relaxation enhancement for rapid ^{19}F-MRI, comparing Magnevist and $GdCl_3$ as contrast agents for accelerating T_1- and T_2-weighted measurements while maintaining biochemical integrity.

Conclusion and Outlook

- **Chapter 7** concludes the thesis, summarizes the main results, and provides an outlook on future developments in high-throughput MR-based drug discovery.

1.4. Publications

This research has created four main publications with contributions as the first author (one published, one submitted, and one in preparation) and one other publication as coauthor (one published).

Published

- **Accelerated screening of protein–ligand interactions via parallel T_2-weighted ^{19}F-MRI**

  Published in: *ACS Analytical Chemistry* [DF1]

  Authorship status: Lead author

  Content: This paper introduced a parallelized ^{19}F-MRI methodology for quantifying protein–ligand interactions using T_2-weighted displacement imaging. A 9-capillary sample holder and a fluorinated reporter ligand enabled multiplexed binding assays, allowing simultaneous acquisition of dose–response curves. The study demonstrated reliable extraction of apparent binding constants and a substantial reduction in measurement time relative to conventional NMR-based approaches.

  Contribution: Conceived the experimental design. Performed all MRI experiments on the fabricated capillary sample holder, analyzed binding affinity data, and validated quantitative accuracy. Led the manuscript writing and prepared all figures.

- **A digital twin for parallel liquid-state nuclear magnetic resonance spectroscopy**

  Published in: *Nature Communications Engineering* [DF2]

  Authorship status: Coauthor

  Content: This work presented a digital-twin framework for simulating multi-sample NMR spectroscopy, encompassing electromagnetic field distributions, signal encoding, and reconstruction under parallelized conditions. The digital twin enabled prediction and optimization of coil performance, sensitivity profiles, and workflow design for multi-sample NMR systems.

  Contribution: Prepared the chemical solutions used for experimental validation, assisted in conducting the NMR measurements, contributed to benchmarking experimental data, and helped draft and revise the manuscript.

Submitted manuscript

- **Parallelized 61-sample inhibition screening accelerated by ^{19}F-MRI compressed sensing**

  Manuscript status: Submitted to Wiley Chemistry – *Angewandte Chemie*

  Authorship status: Lead author

  Content: This manuscript reports a highly parallelized ^{19}F-MRI screening platform employing a 61-well honeycomb array and compressed-sensing reconstruction. The method enables simultaneous quantification of enzyme inhibition across dozens of samples, achieving more than an order-of-magnitude acceleration by combining spatial parallelization and sparsity-driven imaging. The approach is demonstrated for strong and weak binders, clinically relevant proteins, and antimicrobial inhibition assays.

  Contribution: Conceived and led the study. Designed and optimized MRI acquisition protocols for the 3D-fabricated 61-well sample holder, including compressed-sensing undersampling strategies, performed all imaging experiments, analyzed binding affinity data, and developed the complete screening workflow. Led the manuscript writing and prepared the figures and supplementary material.

Manuscript in preparation

Gadolinium-Enhanced ^{19}F-MRI as a High-Throughput Platform for Protein–Ligand Screening

Manuscript status: In preparation

Authorship status: Lead author

Content: This work presents a paramagnetic contrast–enhanced ^{19}F-MRI methodology that exploits T_2-relaxation modulation by gadolinium-based contrast agent,

Magnevist, to accelerate the ligand-screening workflow. The approach integrates molecular contrast, spatial parallelization, and *k*-space undersampling to achieve substantial reductions in measurement time.

Contribution: Designed the experimental concept and established the PRE-enhanced ^{19}F-MRI workflow. Performed all imaging experiments with Magnevist, quantified relaxation enhancement, and evaluated the impact of both agents on protein–ligand binding equilibria. Developed the imaging and reconstruction protocols integrating parallelization and undersampling. Led manuscript writing and prepared all figures and supporting analyses.

Reproduction and Adaptation of Published Material

- The text and figures in Chapter 3-4 were reproduced and adapted from my publication [DF1] in *ACS Analytical Chemistry*, with permission from the American Chemical Society (Copyright © 2023, ACS).
- The text and figures in Chapters 5 were reproduced and adapted from the manuscript with the title "Parallelized 61-sample inhibition screening accelerated by ^{19}F-MRI compressed sensing", submitted to *Angewandte Chemie* (Wiley-VCH). Permission for reproduction is granted under the thesis reproduction policy.
- The text and figures in Chapters 6 were reproduced and adapted from the manuscript with the title "Gadolinium-Enhanced ^{19}F-MRI as a High-Throughput Platform for Protein–Ligand Screening", will be submitted. Permission for reproduction is granted under the thesis reproduction policy.

2. Theory

This chapter provides an overview of how to acquire a magnetic resonance signal arising from molecules at the atomic level and encode it into k-space for molecular imaging purposes. Investigating the trade-off of generating an image by optimizing MRI parameters, access acceleration mechanisms are accessed through pulse sequences, which control the speed, sampling pattern, and number of steps using a gradient system. Designing a sample holder that offers dense localization within a given space in a coil, each voxel can correspond to an individual experiment, delivering various biophysical properties of the monitored molecule, while multiple signals come from the shared signal environment.

Later in this chapter, general biophysical principles of protein-drug interactions are introduced to demonstrate how MRI is useful in gaining quantitative insights while accelerating the drug discovery process. The theoretical background information presented in this chapter has been primarily compiled and integrated from the following authoritative MRI textbook sources (cited papers are listed in the Reference section):

- Spin Dynamics by Malcolm Levitt
- Magnetic Resonance Imaging: Physical Principles and Sequence Design by E. Mark Haacke et al.
- The Physics and Mathematics of MRI by Richard Ansorge and Martin Graves
- Fundamentals of NMR and MRI by Fatemeh Khashami
- Magnetic Resonance in Medicine by Peter A. Rinck
- Compressed Sensing Magnetic Resonance Image Reconstruction Algorithms by Bhabesh Deka and Sumit Datta
- Biochemie by Werner Müller Esterl

2.1. Fundamental MR principles

Nuclear spin

Nuclear Magnetic Resonance (NMR) is fundamentally based on the principles of quantum mechanics, as it depends on the inherent characteristic of the particle. Every atomic nucleus has a significant physical characteristic: *spin*.

A rotating particle exhibits an angular momentum, and although spin is a particular manifestation of a kind of angular momentum, it is only an intrinsic property, such as

a particle's mass and electrical charge. It does not arise from any rotational motion of the particle itself. Every elementary particle possesses a specific spin quantum number,*I*, which is quantized. *Bosons* have integer values of I 0, 1, 2, etc.; meanwhile, for *fermions*, it has a half-integer 1/2, 3/2, 5/2, etc.

Protons and neutrons are defined as *fermions*, each possessing a spin quantum number of $\frac{1}{2}$ and therefore obeying the Pauli exclusion principle. Within a nucleus, the individual spins and orbital angular momenta of these nucleons couple to form a total nuclear spin, denoted by the spin quantum number I. In NMR, this total spin determines whether a nucleus exhibits a magnetic moment: only nuclei with $I \neq 0$ possess an intrinsic magnetic dipole moment. Such nuclei can interact with an external magnetic field and undergo transitions between discrete energy states upon absorption of radiofrequency radiation. Consequently, the magnitude of I governs the resonance frequency, signal intensity, and relaxation behavior characteristic of each nucleus.

For example, fluorine-19 (^{19}F) has nine protons and ten neutrons. Despite its even number of neutrons, the unpaired proton results in a net nuclear spin of $I = 1/2$. Consequently, ^{19}F qualifies as an NMR-active nucleus, alongside the most-known nuclei summarized in Table 2.1.

$$\boxed{|\mathbf{I}| = \hbar\sqrt{I(I+1)}} \tag{2.1}$$

On the other hand, ^{12}C and ^{16}O are NMR-silent nuclei because they have an even number of protons and neutrons; thus, the nucleus has no spin ($I = 0$).

The microscopic magnetic field produced by spin is characterized by a magnetic moment vector, denoted as $\vec{\mu}$. The ratio of the magnetic moment to the spin angular momentum is referred to as the gyromagnetic ratio, γ, which is an inherent property of the nucleus (Figure 2.1). Magnetic moment and spin angular momentum of a nucleus are linearly related:

$$\boxed{\vec{\mu} = \gamma \cdot \vec{I}} \tag{2.2}$$

Table 2.1.: Inherent spin properties of most common nuclei

Isotope	Nuclear spin (I)	Natural Abundance [%]	NMR Frequency at 11.7 T [MHz]
^{1}H	$\frac{1}{2}$	≈ 100	- 500
^{2}H	1	0.015	- 76.753
^{13}C	$\frac{1}{2}$	1.1	- 125.725
^{14}N	1	99.6	- 36.132
^{15}N	$\frac{1}{2}$	0.37	50.684
^{19}F	$\frac{1}{2}$	≈ 100	- 470.470
^{31}P	$\frac{1}{2}$	≈ 100	- 202.606

Each nucleus has a specific γ that can be positive or negative depending on the orientation of the magnetic moment and the angular momentum vectors being in the same

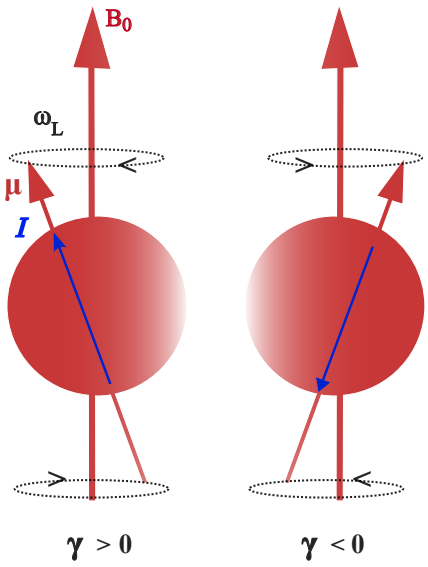

Figure 2.1.: Direction of nuclear spin and magnetic moment for positive and negative oriented gyromagnetic ratios. Collinearity and proportionality between the nuclear spin angular momentum (I) and the magnetic moment ($\vec{\mu}$) in an external magnetic field (B_0). The Larmor precession direction (ω_L) and the alignment of $\vec{\mu}$ relative to I are shown.

direction or opposite directions, respectively. It has units of MHz T^{-1}. Most commonly used nuclei in chemistry and biology are listed in Table 2.1 with the nuclear spin values, natural abundance of the isotopes, and gyromagnetic ratios.

Polarization and precession

The phenomenon of NMR arises from the orientation of the atomic magnetic moment ($\boldsymbol{\mu}$). Before a nucleus with a non-zero spin quantum number ($I \neq 0$) is placed in a static magnetic field, the orientations of its magnetic moments are random, and the corresponding energy levels are degenerate. When exposed to an external magnetic field B_0, nuclei with a non-zero magnetic moment interact with the field, leading to an energy level separation known as Zeeman splitting.

The energy levels split according to the magnetic quantum number m_I, which can take values from I to $+I$ in integer steps. For a spin -1/2 nucleus (e.g. ^1H or ^{19}F), there are two energy states (Figure 2.2): $m_I = +\frac{1}{2}$ ($\uparrow$, lower energy) and $m_I = -\frac{1}{2}$ ($\downarrow$, higher energy). The parallel orientation with the external magnetic field (which is typically in the z-direction) is the energetically favorable state, referred to as α-state (parallel to the external magnetic field). The antiparallel orientation of spins to the external magnetic field is called the β-state, where the energy is higher than the α-state. The energy difference between these two states is given by:

$$\boxed{\Delta E = -\vec{\mu} \cdot \vec{B_0}} \tag{2.3}$$

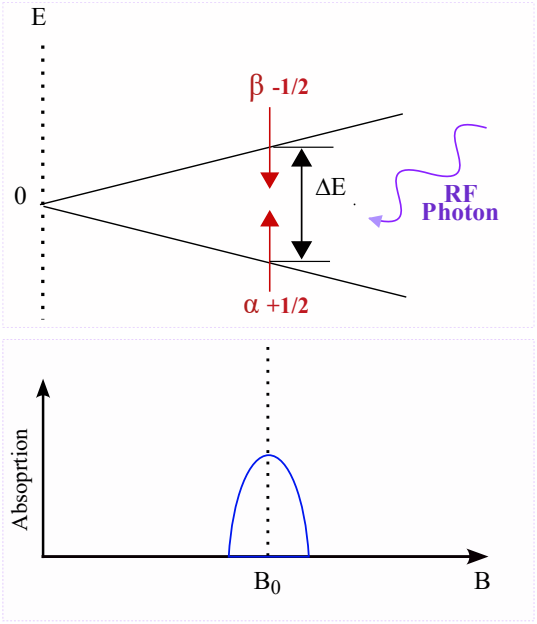

Figure 2.2.: Zeeman splitting and NMR absorption between α and β spin states. The energy separation ΔE determines the resonance frequency for NMR absorption, which occurs during transitions, when the nucleus absorbs an RF photon.

This energy gap corresponds to a specific frequency of electromagnetic radiation, known as the Larmor frequency, ω_0. It is directly proportional to the strength of the external magnetic field, B_0:

$$\boxed{\omega_0 = \frac{\gamma \cdot B_0}{2\pi}} \tag{2.4}$$

Thus, Zeeman splitting creates the fundamental condition for nuclear magnetic resonance: when a nucleus with spin $I \neq 0$ is placed in an external magnetic field B_0, its energy levels separate by $\Delta E = \gamma \hbar B_0$. Resonance absorption occurs when the frequency of the applied radiofrequency (RF) field matches the Larmor frequency, $\omega_0 = \gamma B_0$, allowing transitions between the split energy levels, as illustrated in Figure 2.2.

The population difference between these energy states follows the Boltzmann distribution, leading to a small excess of nuclei in the lower-energy α-states, expressed as:

$$\boxed{\frac{N_i}{N} = \frac{\exp\left(-\frac{E_i}{k_B T}\right)}{\sum_i \exp\left(-\frac{E_i}{k_B T}\right)}} \tag{2.5}$$

This slight imbalance gives rise to a net magnetization along the direction of the external field, which forms the detectable basis of the NMR signal. Here, $N = \sum_{i=1} Ni$, where N_i is the number of particles occupying the specific energy level E_i. The sum of the exponential terms in the denominator is known as the partition function, which normalizes

the distribution. k_B = 1.380510^{23} J/K is the Boltzmann constant, and T represents the absolute temperature in Kelvin (K). At room temperature 298 K, the orientations of the magnetic dipole moments fluctuate rapidly, since the thermal energy (k_BT) exceeds the Zeeman energy splitting between spin states. For example, spin population numbers in the two Zeeman states at 1 T:

- Population in the low energy (α) state ≈ 500,002
- Population in the high energy (β) state ≈ 499,998
- Net magnetization (population difference) ≈ 3.22 spins per million

Hyperpolarization [1, 2] and higher magnetic field strengths provide an advantage in increasing detection sensitivity.

Relaxation

At thermal equilibrium, the bulk magnetization $\vec{M}_0$ of a macroscopic sample is aligned predominantly parallel to the external magnetic field and is proportional to the population difference between the parallel and anti-parallel spin states. This alignment produces a net longitudinal magnetization along the z-axis.

To generate a detectable signal, a time-varying radiofrequency magnetic field (B_1) is applied for a short duration (RF pulse, Figure 2.3, green box in the pulse sequence) to rotate the magnetization away from the z-axis. The B_1 field can be viewed as a constant magnetic field applied perpendicular to the B_0 field. This transverse field exerts a torque on the net magnetization vector, causing it to precess away from the equilibrium direction. The angle of rotation, called the **flip angle** α_{FA}, depends on the RF field strength, the gyromagnetic ratio, and the pulse duration (τ):

$$\boxed{\alpha_{FA} = \gamma \cdot B_1 \cdot \tau} \tag{2.6}$$

For example, if the RF pulse is applied with the appropriate amplitude and duration such that $\alpha_{\mathrm{FA}} = 90°$, the net magnetization is rotated entirely into the transverse (xy) plane, for instance, along the -y-axis. By varying the pulse duration and power, the excitation bandwidth (BW) can be controlled: short, high-power (*hard*) pulses produce a broad excitation bandwidth, whereas long, low-power (*soft*) pulses generate a narrow, frequency-selective excitation.

Once the magnetization has been tilted away from equilibrium, it gradually relaxes back toward the z-axis. The recovery of the longitudinal magnetization follows an exponential time course described by the Bloch equation:

$$\boxed{M_L(t) = M_{\mathrm{eq}} \left(1 - e^{-\frac{t}{T_1}}\right)} \tag{2.7}$$

This exponential time constant T_1 is called the **longitudinal relaxation time**. It characterizes how quickly the net spin magnetization returns to its thermal equilibrium

value along the field direction after being disturbed. This re-establishment of M_{eq} is a key parameter for NMR measurements and is characteristic for each nuclear isotope.

In contrast, the transverse component of the magnetization is directly detectable. In the transverse plane, the spins precess at the Larmor frequency ω_0 and decay due to dephasing. This decay is described by the **transverse relaxation time** T_2:

$$\boxed{M_T(t) = M_T(0)\, e^{-\frac{t}{T_2}}} \tag{2.8}$$

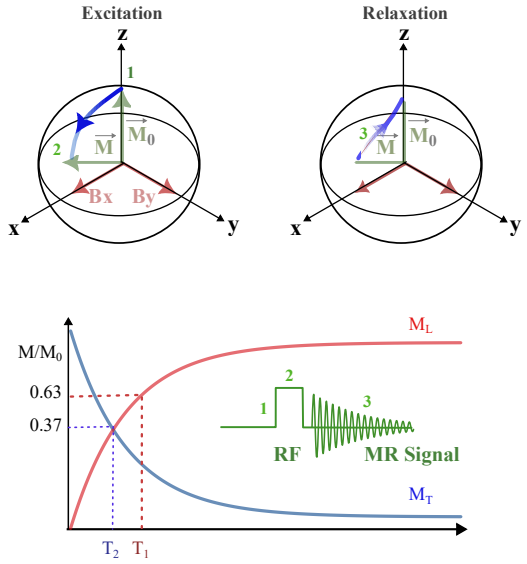

Figure 2.3.: Magnetization dynamics in MR signal generation: (Top) Bloch sphere illustration of excitation (1–2) and relaxation (3) processes. (Bottom) Corresponding longitudinal (M_L, red) and transverse (M_T, blue) relaxation curves. Pulse diagram (green) with RF excitation pulse (1–2), and resulting MR signal (3) with T_1 and T_2 time constants.

In liquid-state NMR of small molecules, the transverse relaxation time constant T_2 is generally comparable in magnitude to the longitudinal relaxation time T_1, often extending over several seconds. This prolonged coherence permits nuclear spins to perform tens of millions of Larmor precession cycles without significant dephasing. However, in systems involving macromolecules in solution or solid-state environments, the T_2 values are markedly shorter, frequently on the order of milliseconds, due to enhanced dipolar interactions and restricted molecular mobility. These relaxation properties, particularly in the context of proteins and drug-like molecules, are discussed further in Chapter 2.7.

Signal detection

The detection of MR signals within a modern spectrometer relies on a coordinated interaction between static magnetic fields, time-dependent RF excitation, and digitally controlled signal processing. Before starting with the nuclear spin excitation and collecting a spectrum, the first crucial step for the signal readout is to ensure a homogeneous magnetic field that is expanded over the entire volume of the sample equally and is stable over time.

Once the RF pulse has rotated the magnetization into the transverse plane, the precessing transverse component induces a voltage in the detection coil according to Faraday's law of electromagnetic induction. This time-dependent oscillating signal, observed at the nuclear Larmor frequency, is called the free induction decay (FID) (Figure 2.3, green). The FID contains the full spectral information of the nuclear spins and forms the raw data from which NMR spectra and MR images are reconstructed.

To implement this excitation and detection process in practice, the sample is carefully positioned within a dedicated NMR setup that enables precise manipulation and measurement of nuclear spin behavior. The primary component of this setup is the RF coil, which serves dual functions: applying the excitation pulse from the transmitter and capturing the induced signal for the receiver (Figure 2.4).

The sample is aligned along the z-axis and positioned within a homogeneous static magnetic field B_0 next to an RF coil, ensuring optimal interaction between the nuclear spins and the applied RF field. The RF coil, integrated into a resonant circuit (RF oscillator) tuned to a specific transmission frequency ω_0 which operates under precise computer control, is connected to an RF transmitter (TX) for signal excitation or to a receiver (RX) for signal acquisition (detailed in Chapter 2.2.

For the nuclear spin excitation, a calibrated 90° RF pulse at frequency ω_0 is applied, rotating the macroscopic magnetization vector $\vec{M}$ from its equilibrium orientation along B_0 into the transverse plane. Detection of the oscillating field is accomplished using an RF coil whose winding axis is oriented perpendicular to the main magnetic field B_0. This configuration is critical, as it allows the coil to sense the oscillating magnetic field generated by the precessing transverse component of the net magnetization.

To fully capture the signal, quadrature detection is employed. The received voltage is mixed with two reference waveforms at frequency ω_{ref}, shifted by 90° relative to each other. This yields two channels — the in-phase (I) and quadrature (Q) components (Figure 2.5)— which together form a complex representation of the detected signal at the difference frequency:

$$\boxed{\Omega_0 = \omega_0 - \omega_{\text{ref}}}$$

The resulting free induction decay (FID), $s(t)$, is therefore expressed as a complex time-domain signal containing both cosine (real) and sine (imaginary) contributions of the transverse magnetization:

$$\boxed{s(t) = M_x(t) + iM_y(t) = A\, e^{-t/T_2} e^{i\Omega_0 t}} \tag{2.9}$$

where T_2 is the effective transverse relaxation time, and A is the initial amplitude. To

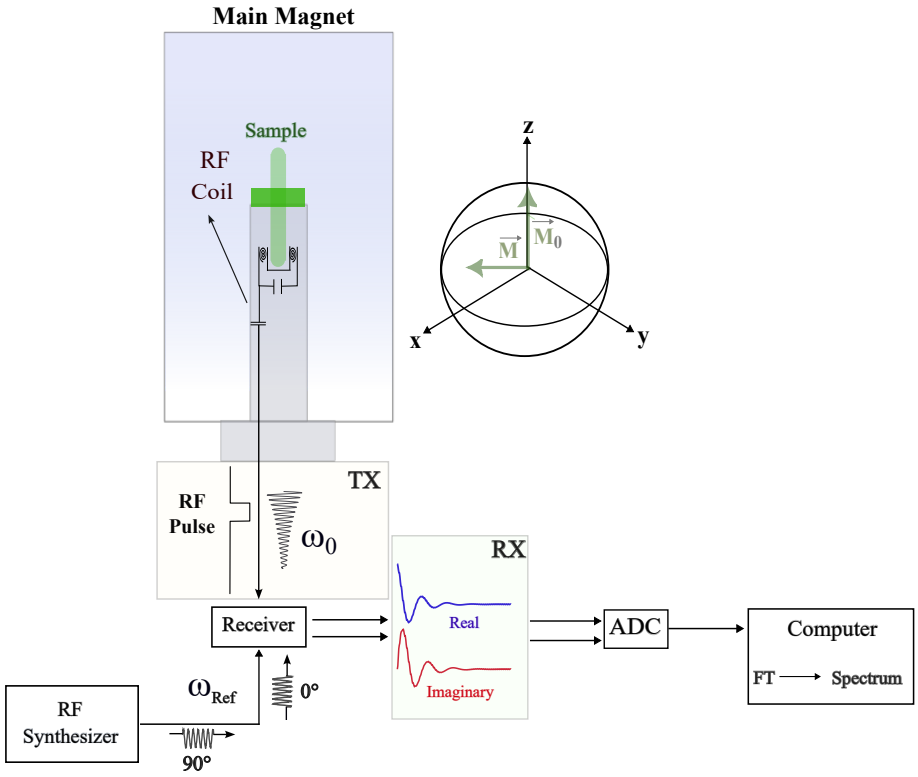

Figure 2.4.: MR signal acquisition chain. The RF coil detects the signal at the Larmor frequency, which is mixed using a reference frequency from an RF synthesizer (quadrature detection). The resulting complex signal, composed of real and imaginary components, is digitized by an ADC and processed by a computer to generate a spectrum.

transform the time-domain FID into a frequency-domain spectrum, a Fourier Transformation (FT) is applied:

$$S(\Omega) = \int_0^\infty s(t) e^{-i\Omega t}\, dt \tag{2.10}$$

This yields the MR spectrum, $S(\Omega)$, where each peak corresponds to a resonant frequency component of the sample, providing chemical shift and coupling information. Quadrature detection ensures that these spectra are single-sided, phase-sensitive, and free of ambiguities, thereby enabling accurate resolution of chemical environments and dynamic processes in MR experiments.

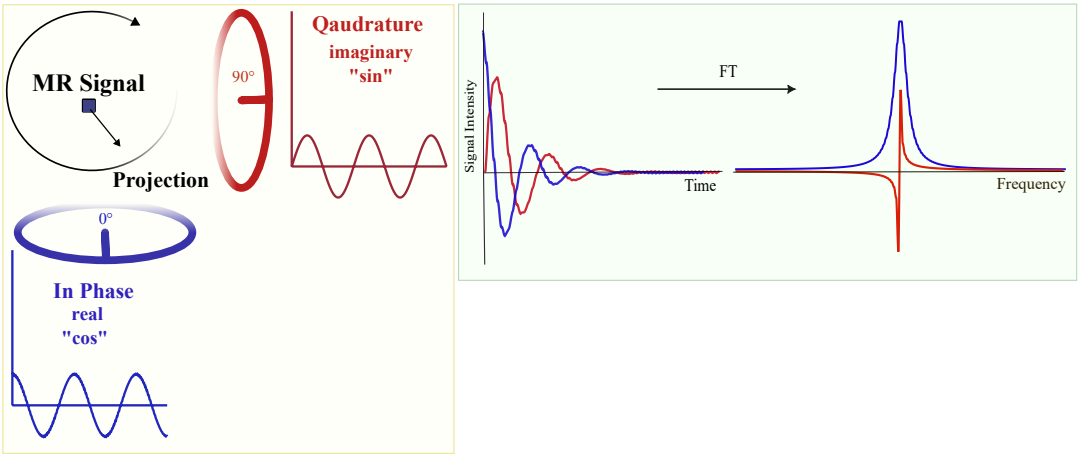

Figure 2.5.: Quadrature detection for MR signal acquisition. The real (in-phase, blue) and imaginary (quadrature, red) components of the detected signal are shifted by 90°. Fourier transformation converts the real and imaginary time-domain signals into their frequency-domain components, preserving amplitude and phase information.

2.2. Instrumentation

The functionality of MRI hardware is intrinsically linked to the software interface, with both elements operating cohesively to ensure accurate signal generation and acquisition (Figure 2.6). The main hardware units of a typical MR scanner include:

- A static magnetic field (B_0) system for establishing nuclear magnetization.
- Shimming coils for generating low-order magnetic field corrections to enhance spatial homogeneity.
- Radiofrequency (RF) coils for transmitting the electromagnetic B_1 field to excite the spins and for receiving the induced NMR signal during acquisition.
- Gradient coils for spatial encoding along the three orthogonal axes.
- RF electronics for signal generation, amplification, and detection, comprising RF synthesizers, power amplifiers, preamplifiers, and analog-to-digital converters that enable precise excitation and sensitive signal readout.

MR scanner and shimming coils

A typical MRI scanner has a horizontal bore magnet composed of a special superconducting wire, often coiled into a solenoidal configuration and housed within a stainless steel cryostat filled with liquid helium. This cryogenic environment is essential for maintaining the superconducting temperature for the wiring, so that the system carries persistent currents without resistance.

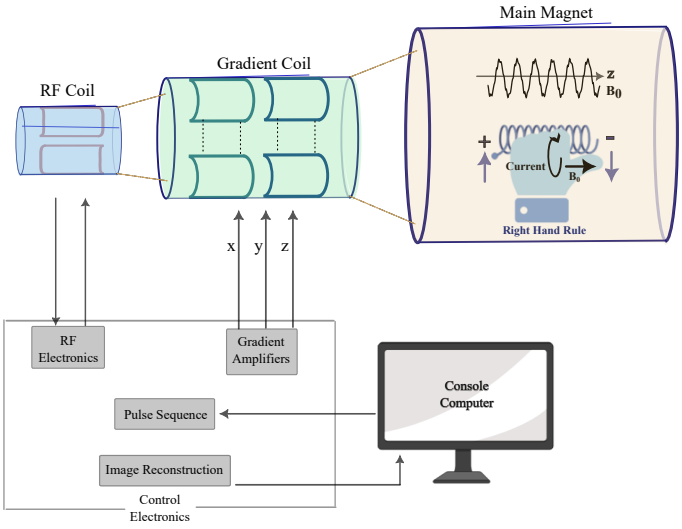

Figure 2.6.: MRI system with the signal pathway from the magnet to the computer. The system is controlled by electronics. RF electronics manage transmission and reception, enabling the excitation pulses generated by the RF coil, while gradient amplifiers deliver current to the gradient coils to produce spatially varying fields in the x, y, and z directions under the static field of the main magnet. Pulse sequence instructions from the console computer orchestrate these components, defining the precise timing of RF pulses, gradient switching, and signal acquisition. The acquired data are subsequently reconstructed into images and displayed on the console.

The geometry of the winding is critical for the generation of a stable and uniform magnetic field, where the field orientation is dictated by the direction of the current flow, which follows the right-hand rule (Figure 2.6). The number of coil windings and the magnitude of the applied current determine the strength of this magnetic field.

Clinical scanners for hospitals have a standard MRI scanner with 1.5 T – 3 T, whereas for preclinical research purposes, stronger fields in a range of 11.7 T – 21.1 T are in use. A strong magnetic field is necessary to enhance signal detection sensitivity to monitor minor changes of the molecule of interest at atomic resolution. Ultra-field-magnets possesses a smaller bore size with a diameter 20 mm – 40 mm that is not suitable for human imaging. To maintain the uniformity of any cryogenic integrity over the available space in the bore volume, smaller bore sizes are favored.

A highly homogeneous magnetic field is a fundamental requirement in magnet and coil design. The spatial variation in B_0 is typically measured using imaging-based field mapping and can be iteratively corrected by generating spherical harmonic magnetic fields. Shimming coils are employed to restore and optimize the uniformity of the magnetic field, ensuring the stability and accuracy required for both imaging and spectroscopic applications.

RF coil

The radiofrequency (RF) coil is precisely tuned to the Larmor frequency corresponding to the target nucleus. It is operating in two different modes: transmit or receive mode (Figure 2.4). In the transmit mode, the duration of the RF pulse is controlled to generate a certain flip angle of the net magnetization vector to excite nuclear spins. Depending on the application need, this flip angle can be adjusted. In the receive mode, the released energy during spin relaxation is captured in the form of electromotive force (EMF) within the coil. Therefore, the coil must be positioned in proximity to the sample as a receiver.

Gradient coils

Gradient coils are responsible for the spatial encoding of the MR signal. There are three independent gradient coils, each oriented along one of the orthogonal spatial axes (X, Y, and Z). Their geometry enables the generation of linear, space-dependent magnetic field variations that make the resonance frequency of nuclear spins position-dependent (see equation 2.11).

Two important parameters characterize the performance of gradient coils: the *amplitude*, which defines the achievable field strength variation across the imaging volume, and the *slew rate*, which quantifies how rapidly the gradient can be switched on or off. The gradient system is driven by dedicated electronic subsystems consisting of current amplifiers (Figure 2.6), gradient pulse programmers, and digital-to-analog converters (DACs).

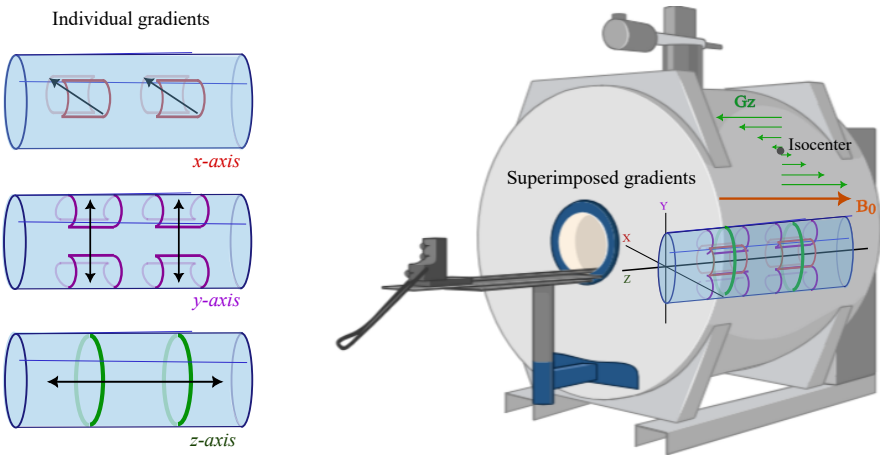

Figure 2.7.: MRI gradients for spatial encoding. Direction of three individual gradient coils along the X-, Y-, and Z-axes (left). Each coil produces a linear magnetic field gradient in its respective direction, as indicated by the coil geometry and associated arrows. The superimposed gradients are shown within the bore of the MRI scanner (right) to the main static magnetic field B_0 (orange), the gradient in the Z-direction (G_z, green), and the scanner isocenter.

In MRI, the static magnetic field B_0 is always present to align the nuclear spins. Gradient fields, by contrast, are applied transiently and in a programmed manner during a pulse se-

quence. At the magnet's central point, referred to as the *isocenter*, the resonance frequency is defined solely by B_0, and all three gradient fields vanish. As one moves away from the isocenter, the local resonance frequency increases or decreases linearly depending on the applied gradient's polarity and direction. Thus, gradients introduce a spatial dependence into the precession frequency of the spins, enabling the localization of their positions within the sample (Figure 2.7).

Assuming the direction of the external magnetic field is aligned with the z-axis, the magnetic field at an arbitrary spatial position $\mathbf{r} = (x, y, z)$ can be expressed as

$$\boxed{\mathbf{B}(\mathbf{r}) = \Big(B_0 + G_x x + G_y y + G_z z\Big)\,\hat{\mathbf{z}}} \tag{2.11}$$

where G_x, G_y, and G_z denote the applied gradient strengths along the respective axes. In the absence of gradients, the expression reduces to $\mathbf{B}(\mathbf{r}) = B_0\,\hat{\mathbf{z}}$.

2.3. Spatial encoding and *k*-space

NMR vs MRI

Magnetic Resonance Imaging (MRI) has emerged as one of the most powerful and versatile diagnostic tools in modern medicine and biomedical research. As a non-invasive technique, magnetic resonance imaging (MRI) enables the visualization of internal anatomical structures and physiological processes with high spatial and temporal resolution.

Apart from other imaging modalities such as computed tomography (CT), ultrasound, and positron emission tomography (PET), MRI enables diagnostic imaging, particularly in neurology, musculoskeletal studies, cardiovascular assessment, and oncology. The successful implementation of MRI represents a convergence of fundamental physics, advanced hardware, and computational techniques, exemplifying the translation of a quantum mechanical principle into a critical biomedical application.

Based on non-ionizing radiofrequency (RF) waves and strong static magnetic fields, MR imaging does not expose the patient to ionizing radiation, making it inherently safer compared to CT [3]. Compared to ultrasound [4], MRI offers deeper tissue penetration and higher spatial resolution, particularly in areas obscured by bone or air, making it a more effective imaging modality. In contrast to PET [5], MRI does not require radioactive tracers; high-resolution imaging is achieved without introducing radiopharmaceuticals, although it can be complemented with contrast agents when necessary.

This technique is fundamentally based on the physical principles of nuclear magnetic resonance (NMR), a phenomenon described in detail in Chapter 2.1. Although both NMR and MRI share the same underlying quantum mechanical technique, the behavior of nuclear spins in external magnetic fields, the objectives of the signal output, and the implementations are significantly different (Table 2.2). As shown in Figure 2.8, conventional NMR yields a spectrum that represents an averaged signal from all mobile water molecules in the sample, without distinguishing between water populations in different tissues. In contrast, MRI employs spatially varying magnetic field gradients and Fourier transformation of the acquired k-space data to reconstruct images composed of individual

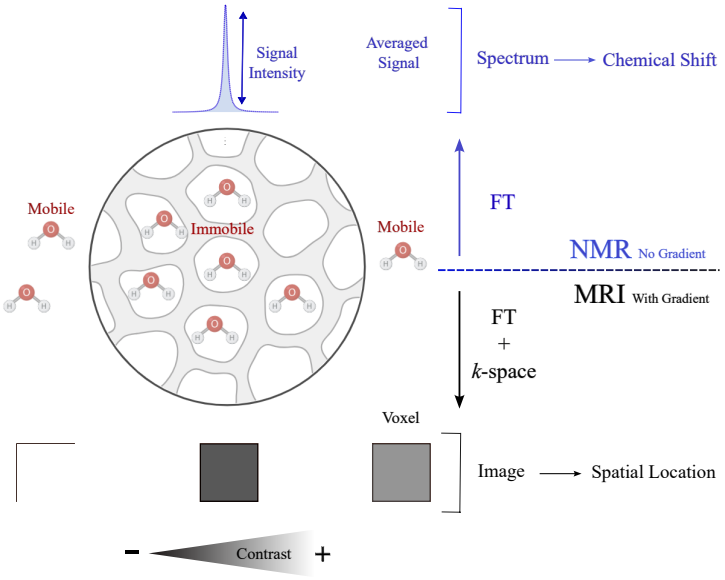

Figure 2.8.: Simplified illustration of nuclear magnetic resonance (NMR) spectroscopy and magnetic resonance imaging (MRI) using water signals. Without spatial encoding gradients, NMR detects an averaged signal from the sample, producing a frequency spectrum (chemical shift) that reflects molecular environments, predominantly from mobile water. In MRI, spatially varying magnetic field gradients encode position, and Fourier transformation (FT) of *k*-space data reconstructs an image composed of voxels. Image contrast arises from differences in water properties, which determine the grayscale intensity of each voxel.

voxels. Each voxel contains signals from mobile water molecules within a defined spatial environment, thereby enabling localization and tissue-specific contrast.

The key technological innovation that transforms NMR into MRI, the spectrometer is additionally equipped with gradient coils capable of systematically altering the Larmor frequency of nuclear spins as a function of spatial position. This spatial dependence enables slice selection, frequency and phase encoding, and image reconstruction via the Fourier Transformation.

For this purpose, a pulse sequence running on the computer (details explained in Chapter 2.4) specifies the timing, amplitude, and waveform shape of the gradients. The digitally generated signals are converted into analog waveforms by the DACs and subsequently amplified by high-power current amplifiers to deliver precise and temporally accurate currents to the gradient coils. In practice, the formation of an MR image involves four main steps (Figure 2.10):

1. Localization of the spins of interest,
2. Excitation of selected spins,
3. Encoding of their signal,

4. Signal detection and reconstruction.

Table 2.2.: Signal characteristics in NMR spectroscopy and MR imaging.

Property	**NMR Spectroscopy**	**MR Imaging**
Signal output	Frequency-domain spectrum	Spatial image (2D or 3D)
Contrast source	Chemical shift, J-coupling, T_1, T_2 relaxation times	T_1, T_2 relaxation times, proton density, flow
Chemical shift	Yes	No (except MRS or CSI)
Signal interpretation	Concentration, chemical environment, density	Spatial location and relaxation properties
Encoding method	Spectral (frequency) encoding	Spatial encoding
Dimensionality	1D, 2D, or 3D spectra	2D or 3D images (voxels)
Spectral resolution	Very high (sub-Hz)	Low for imaging 10–100 Hz (unless spectroscopic sequences used)
Spatial resolution	Not applicable (except 1D z-profiling [6])	High (down to sub-mm or μm resolution)

Slice Selection

A typical MR experiment starts with a slice selection (SS) (steps 1 and 2, Figure 2.10) done by applying a linear gradient in the z-direction with a proper RF excitation profile. The RF pulse is carefully designed to have a "sinc"-shaped waveform in the time domain, which translates into a rectangular profile in the frequency domain (Figure 2.9). This ensures uniform excitation of spins within a defined frequency range. The effective excitation bandwidth of the RF pulse is denoted by Δf_{exc}. The slice thickness ΔZ is directly influenced by two primary parameters: the RF pulse's excitation bandwidth and the strength of the applied gradient field $G_z z$. The relationship is expressed by:

$$\boxed{\mathbf{B_z}(\mathbf{r}, \mathbf{t}) = B_0\,\hat{\mathbf{z}} + G_z\,(t)\,\hat{\mathbf{z}}}$$

$$\boxed{\Delta Z = \frac{\Delta f_{exc}}{\gamma G_z}} \tag{2.12}$$

This equation shows that slice thickness is inversely proportional to the gradient strength and directly proportional to the RF bandwidth. Therefore, to achieve thinner slices (which improves spatial resolution), two parameters can be optimized (Figure 2.9):

- Increase the gradient strength G_z
- Decrease the RF excitation bandwidth f_{exc}

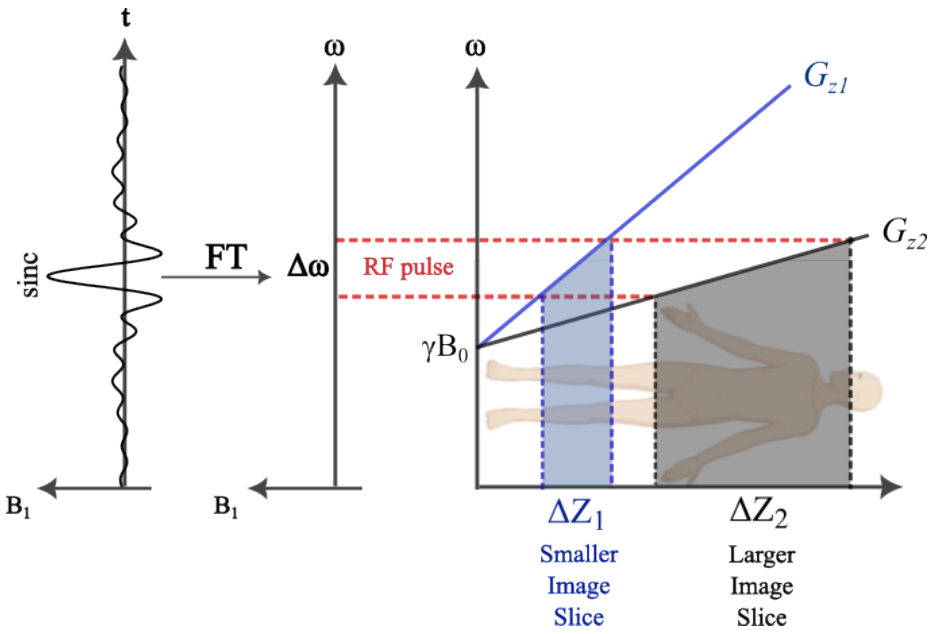

Figure 2.9.: Slice thickness dependence on the gradient strength. The applied RF excitation pulse $B_1(t)$ in the time domain is Fourier transformed (FT) into its frequency domain. A finite RF bandwidth determines the range of Larmor frequencies excited. A step gradient G_{z1} results in a thinner slice (Δ_{Z1}), whereas a shallower gradient G_{z2} yields a thinner slice (Δ_{Z2}).

To be noted, reducing f_{exc} can lead to longer pulse durations due to the time-bandwidth trade-off inherent in Fourier-based signal design. This could affect imaging effectiveness and be prone to off-resonance effects. Conversely, increasing G_z requires stronger hardware capability and may introduce higher demands on gradient linearity and system performance.

The interplay between the RF pulse profile and the gradient steepness defines the selective excitation region (or voxel depth) within the imaging volume. The time dependency present in equation (2.3) allows for the possibility of switching the gradient on and off. Depending on the slope of the applied gradient, the separation degree of spin systems is different. The steeper the gradient slope, the greater the separation (2.9).

Fourier Encoding

To create an MR image of localized spins in an excited slice, 2-dimensional Fourier encoding is necessary: phase (PE) and frequency encoding (FE) in y-, and x-axes, respectively. Superimposed, time-varying gradient fields induce spatially dependent changes in frequency and phase within the region of interest (ROI).

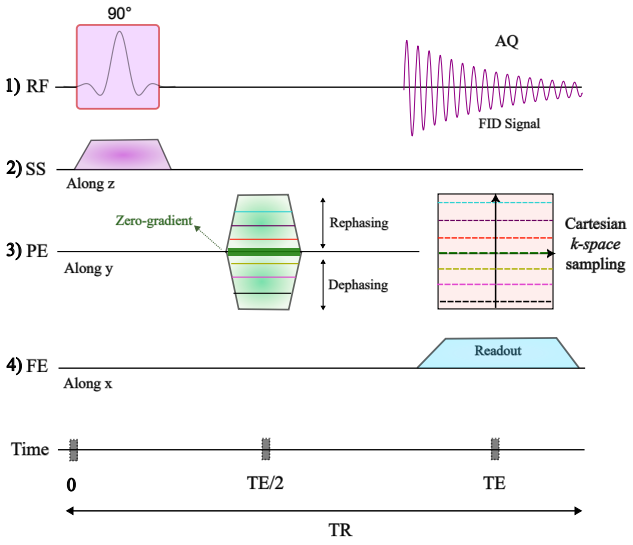

Figure 2.10.: Gradient-echo pulse sequence and Cartesian k-space sampling.(1) A radio frequency (RF) excitation pulse combined with a slice-selection (SS) gradient along the z-axis defines the imaging slice. (2) A phase-encoding (PE) gradient along the y-axis introduces controlled phase shifts; with each repetition time (TR), a different PE amplitude is applied, thereby encoding lines of k-space. (3) A frequency-encoding (FE) gradient along the x-axis is applied during acquisition time (AQ), allowing continuous sampling of spatial frequencies. The lower timeline illustrates measurement time representing the excitation, encoding, signal readout at echo time (TE), and repetition across TR.

The **PE** gradient is applied briefly after the RF excitation pulse and before signal acquisition. This gradient induces a position-dependent phase shift in the transverse magnetization, which remains even after the gradient is turned off. The accumulated phase shift (ϕ) is given by:

$$\boxed{\phi(y) = \gamma \cdot y \cdot \int_{t_0}^{t_1} G_y(t)\, dt} \tag{2.13}$$

The phase shift is linearly proportional to position y, which is the basis of phase encoding. The effective moment via the time integral of the frequency offset determines the gradient shape (square, trapezoid, sinusoidal), where the area under the gradient controls the amount of phase shift.

A time-dependent gradient field along the x-axis is applied for the **FE** step during the readout process, which causes spins across the object to experience slightly different magnetic field strengths. At a given time t, the Larmor frequency ω (x, t) varies linearly with position x, which can be exploited by considering 1D imaging given ω_0:

$$\boxed{\omega(x,t) = \omega_0 + \omega_G(x,t) = \omega_0 + 2\pi x G_x(t)}$$

$$S = \int \psi(x)\, e^{iG(x,t)}\, dx = \int \psi(x)\, e^{-i\int_0^t \omega_G(x,t_0)\, dt_0}\, dx = \int \psi(x)\, e^{-i2\pi x \int_0^t G_x(t_0)\, dt_0}\, dx \tag{2.14}$$

The time-dependent representation of the gradient component G changes in the x is shown as $G_x(t)$. The measured signal S is converted by the Fourier transform of the spatial distribution ($\psi(x)$) and encoded through phase modulation induced by the applied magnetic field gradients. As a result, spins precess at different frequencies, allowing spatial encoding along the x-direction.

The resulting signal, known as the echo, is typically centered at the echo time (TE) (see timeline in the pulse sequence in Figure 2.10), which is the midpoint of the FE period. TE is the time between the excitation pulse and the center of the echo with the strongest signal. Depending on the gradient duration and the size of the acquired matrix, the field of view (FOV) along the x-axis is set by the amplitude of the FE gradient.

k-space

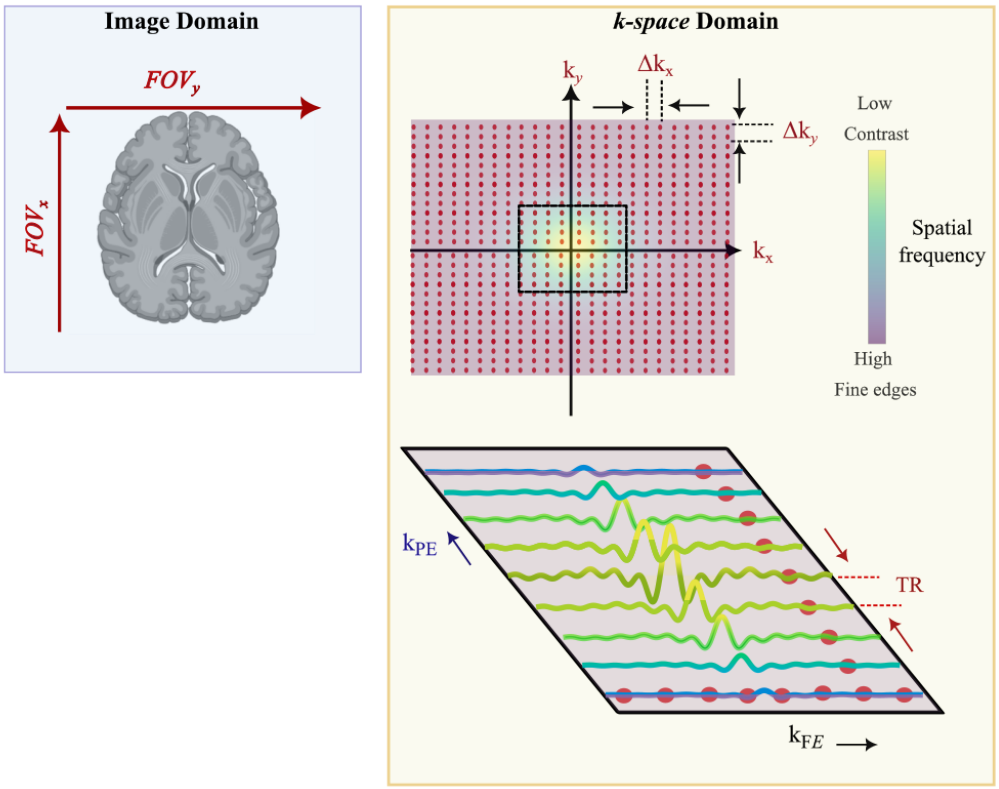

Figure 2.11.: Spatial frequency encoding and sampling in Cartesian k-space. The image domain (left) demonstrates the reconstructed anatomy within the defined field of view (FOV) along the PE and FE. The k-space domain (right) represents the Fourier-encoded spatial frequency plane. k-space is filled line by line with Δk_x increments across repetition times (TR).

All spatially encoded signals obtained during the scan are methodically arranged into a data matrix called *k*-space to reconstruct an image from raw MRI data. Once all lines of *k*-space have been acquired, a two-dimensional inverse Fourier transform is applied to the fully sampled data. The *k*-space matrix represents spatial frequency components while decomposing these components into a frequency domain representation (Figure 2.11).

In a typical 2-dimensional MRI acquisition, the encoding gradient is incrementally stepped through N_y or N_x distinct values to sample *k*-space with the spacing between adjacent steps defined as Δk_y or Δk_x:

$$\begin{aligned} k_{(x,y)\max} &= \gamma \int_0^{\tau} G_{(x,y)\max}\, dt = \tfrac{1}{2}(N_{(x,y)} - 1)\Delta k_{(x,y)} \\ \mathrm{FOV}_{(x,y)} &= \frac{1}{\Delta k_{(x,y)}} \\ A_{(x,y)\max} &= \frac{(N_{(x,y)} - 1)}{\gamma\, \mathrm{FOV}_{(x,y)}} \end{aligned} \tag{2.15}$$

where FOV_x and FOV_y are the field of view in the frequency- and phase-encoding directions, respectively (Figure 2.11). Consequently, the total extent of sampled *k*-space in that direction is (Δk_y-1), and each PE gradient amplitude corresponds to a specific line in *k*-space.

The central *k*-space consists of the low spatial frequency components of the image. These components contain high signal intensity that contributes to overall brightness, contrast resolution,and is critical for signal-to-noise ratio (SNR). Conversely, the data points located near the periphery (edges of *k*-space) have low signal intensity with high spatial frequency information (Figure 2.11).

The fully sampled *k*-space yields an image with preserved contrast and structural detail (Figure 2.12). When only low spatial frequencies are retained (low-pass filter), overall image contrast is preserved with the trade-off of blurred fine anatomical details. In contrast, retaining only high spatial frequencies (high-pass filter) enhances edges and fine structures, while the main contrast and smooth intensity variations are lost. Therefore, these components are essential for finer spatial resolution and distinguishing small features with sharpness.

Sampling trajectories

Among the various *k*-space sampling strategies, Cartesian acquisition is one of the most commonly used in clinical and research MRI. **Cartesian sampling** acquires *k*-space line-by-line, which starts from one edge of *k*-space and stops at the opposite edge. Each PE step is periodically varied in amplitude across repetitions (TRs), which fills a single position along the k_y-axis, defining the vertical location of a line in *k*-space (Figure 2.13A). After the application of each PE gradient lobe, an FE gradient is applied during the signal readout section while acquiring the data along the k_x-axis (Figure 2.11). This process samples horizontal lines of *k*-space sequentially, with the PE steps progressing line-by-line through k_y, typically in a linear or centric ordering scheme.

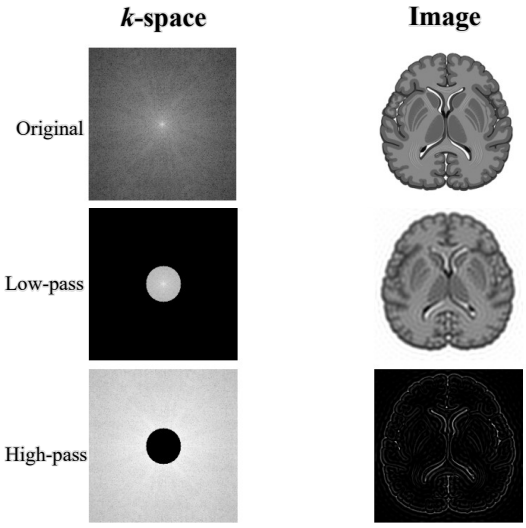

Figure 2.12.: Influence of *k*-space frequency components on image quality. The left column illustrates *k*-space representations with different frequency filters, and the right column the corresponding reconstructions.

This structured approach allows for systematic and efficient *k*-space coverage, which produces high-resolution images without artifacts due to field non-uniformities. However, this sampling technique has the disadvantage of low temporal resolution due to sequential coverage of *k*-space per unit time, which makes it sensitive to motional artifacts.

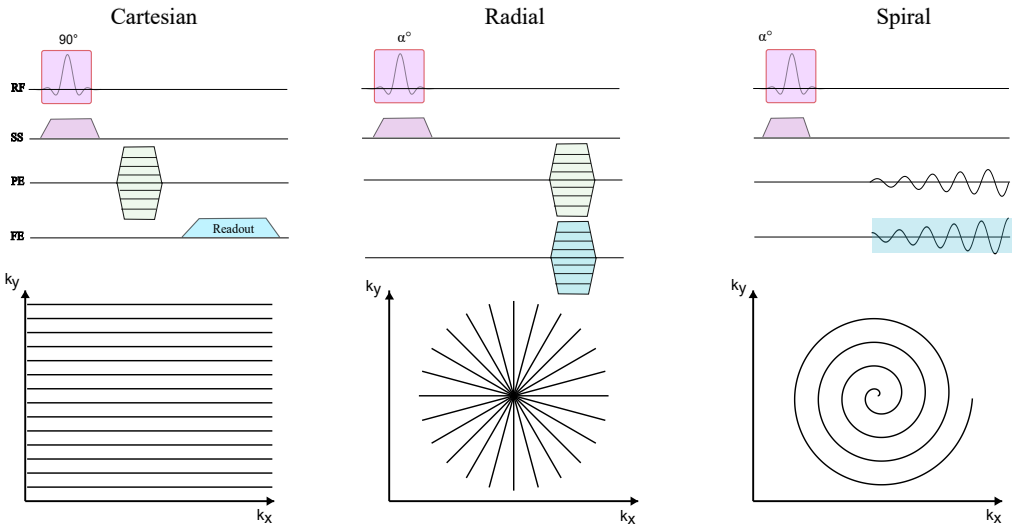

Figure 2.13.: Trajectories for Cartesian, radial, and spiral acquisitions and corresponding MRI pulse sequences.

Non-Cartesian trajectories offer different sampling designs with various features: **spiral** and **radial**. The frequency and phase gradient oscillation and amplitude changes yield spiral or radial patterns from the central *k*-space to the edges. The sampling spokes

through the center (like a wheel) for the radial sampling, which makes it robust to motion inhomogeneities since each spoke densely oversamples the central *k*-space where the low frequency is stored (Figure 2.13 B). Motion artifacts blur edges with high-frequency content.

In the spiral scheme, time-varying sinusoidal gradients along FE and GE produce a continuous spiral trajectory, enabling efficient central sampling and reduced acquisition time. In addition to this sampling similarity, the spiral sampling adds one more advantage of using continuous gradient flow, thereby minimizing the gradient switching and collecting many *k*-space points in a single readout (Figure 2.13 C). Therefore, it is more usable for fast imaging techniques.

Image quality and resolution

The smallest measurable feature for a given object defines the spatial resolution, which represents the system's ability to distinguish between two closely localized structures in the same signal environment. Image quality is influenced by a combination of acquisition and system parameters, including:

- Signal-to-Noise Ratio (SNR): Voxel size, magnetic field strength, receiver bandwidth, and the number of signal averages.
- Contrast-to-Noise Ratio (CNR): Pulse sequence parameters such as repetition time (TR), echo time (TE), and inversion time (TI), as well as the use of contrast agents.
- Spatial Resolution: Trade-offs between voxel size and scan time.
- Field of View (FOV): Extent of the imaged region.
- Receiver Bandwidth (rBW): Width of bandwidths correlated with susceptibility to off-resonance effects.
- Gradient Performance: Strength and skew-rate of gradients.
- Acquisition Time: Trade-offs between acquisition time, SNR, and resolution.

Spatial resolution is determined by the extent of *k*-space sampling and the imaging matrix size (MTX). As described in non-Cartesian sampling, the pattern of the trajectory and density of the sample *k*-space region defines the spatial resolution and FOV. The highest achievable spatial resolution is restricted by the maximum *k*-space extent, gradient timing, and receiver bandwidth as follows:

$$\boxed{rBW = \frac{1}{\Delta t} = \frac{N_x}{t_s} G_x = \frac{\mathrm{rBW}}{\gamma\, FOV_x}} \tag{2.16}$$

where Δt is the time interval, N_x is the number of data points, t_s is the sampling time, γ is the gyromagnetic ratio, and FOV_x is the field of view in the x-direction.

How much detail is preserved in an MR image defined by the size of pixels in 2D acquisitions or voxels in 3D datasets in a given FOV with a defined matrix size (MTX) and

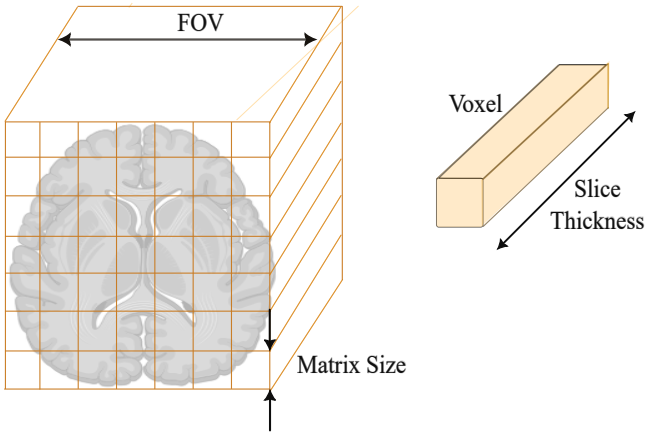

Figure 2.14.: Image resolution and voxel. The field of view (FOV) is discretized into a reconstruction matrix, which determines the physical area (in millimeters or centimeters) that is represented in the image.

slice thickness (SL). Each pixel or voxel represents the localized signal intensity arising from a defined volume element within the object. The voxel (in mm^3) dimensions are defined by the ratio of the FOV to the matrix size:

$$\boxed{\text{Voxel size} = \left(\frac{\text{FOV}}{\text{MTX}}\right) \times \text{SL}} \tag{2.17}$$

The spatial resolution is inversely correlated with the size of the pixel or voxel. A decrease in the dimension of a voxel increases the in-plane resolution at the cost of increased scan time. With the large size of voxels, the image gets blurred with a low contrast between two objects located densely. On the other hand, an inadequate sampling in the frequency direction can cause a known artifact, wrap-around “aliasing.” Therefore, one of the important criteria must be fulfilled to avoid "aliasing" and find a trade-off between in-plane resolution, sampling, and voxel size: The Nyquist-Shannon sampling criterion.

The digital sampling rate of the MR signal must be at least twice the highest frequency contained within that signal. The minimum sampling rate in k-space is given by:

$$\boxed{\Delta k \leq \frac{1}{\text{FOV}}}$$

Overall, the MTX must be large enough to capture all spatial frequencies to fulfill this criterion. This correlation plays a role in compressed sensing, which is described in detail in Chapter 2.6.

2.4. Fast imaging pulse sequences

In the previous section, it was explained how, through a pulse sequence, the electronic components of the MRI system operate to enable data acquisition. In this chapter, another important outcome of the pulse sequence is addressed: *the measurement time*.

The total acquisition time is determined by key pulse sequence parameters: the number of phase-encoding (N_{PE}) steps, the repetition time (TR), the number of signal averages (N_{avg}), the number of slices (N_{slice}), and the number of signal averages (N_{avg}) acquired. By combining these parameters, the overall scan duration can be described as:

$$\boxed{T_{acq} = N_{avg} \cdot N_{PE} \cdot TR \cdot N_{slice}} \tag{2.18}$$

Higher spatial resolution requires sampling more k-space data, which typically results in longer acquisition times. In practice, a long measurement can increase patient discomfort, motion artifacts, and limit throughput. Fast imaging techniques with dedicated pulse sequences aim to accelerate data acquisition without degrading image quality. First, the traditional MRI protocols of Gradient (GRE) and Spin Echo (SE) are covered by the fast imaging pulse sequences of turbo/fast spin-echo (TSE/FSE) and echo-planar imaging (EPI).

Gradient- vs Spin Echo

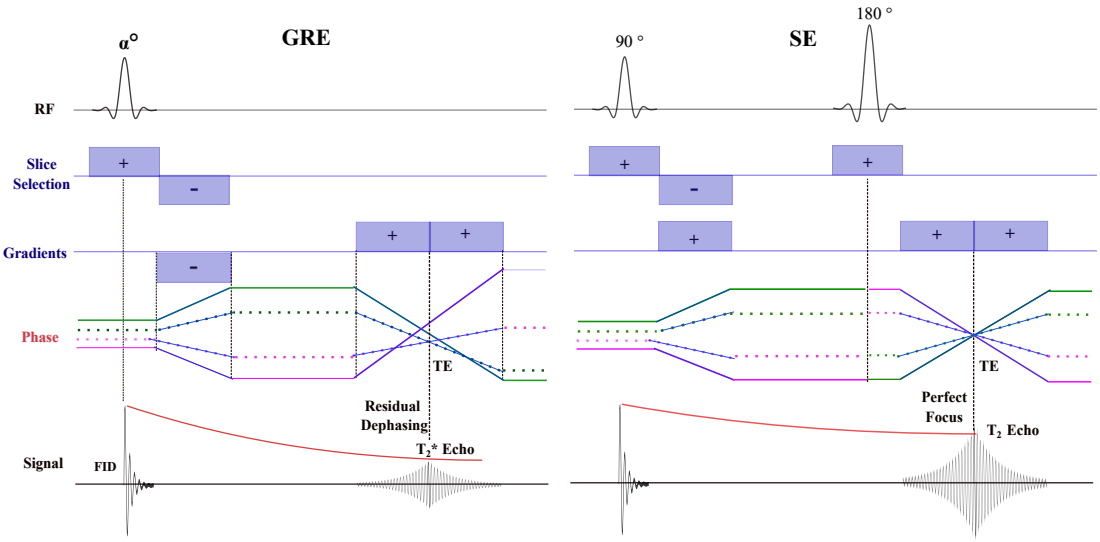

Figure 2.15.: Gradient Echo (GRE) versus Spin Echo (SE) pulse sequences. The diagrams illustrate the differences in frequency- and phase-encoding steps. GRE forms the echo by reversing the readout gradient, whereas SE employs a 180° RF refocusing pulse to rephase spins. The phase evolution of four representative spins is shown in relation to the applied gradients, and the resulting MR signal with its echo formation and decay dependence is depicted above.

The typical **GRE** sequence excites spins in the selected slice with a 90° excitation pulse, aligning the transverse magnetization in phase. Afterward, a defined phase-encoding (PE)

gradient is applied along the y-axis to impart a spatially dependent phase shift (not shown in Figure 2.15, which illustrates only four representative spins). A negative frequency-encoding (FE) gradient lobe is then applied to dephase the spins along the x-direction. The subsequent positive FE gradient rephases the spins, producing a gradient-recalled signal derived from the free induction decay (FID). During this rephasing period, when the FID is sampled, the acquired data fill successive lines of k-space. Each repetition time (TR) fills one line of k-space corresponding to the applied phase-encoding gradient, and the complete image is reconstructed after all encoding steps have been acquired.

The **SE** pulse sequence is structurally similar to GRE. After the PE step, a *slice-selective* 180° refocusing pulse (applied with the same slice-select gradient as the excitation) inverts the dephasing that occurred after the 90° pulse and produces a *true spin echo* at $TE = 2\tau$ (Figure 2.15, SE). In contrast, in GRE, the flip angle for spin excitation is typically smaller than 90° ($\alpha \approx 5°–60°$), and the echo is formed *without* a 180° pulse by first applying a readout dephasing lobe ($-G_x$) and then a rephasing lobe ($+G_x$). Slice selection (with a rephaser) and phase encoding proceed as usual. Because a 180° pulse is not used, static field inhomogeneities and susceptibility-induced phase errors are not refocused, causing the signal to decay with T_2^* rather than the true T_2. With short TR and small α, the GRE pulse sequence is time-efficient, enabling rapid 2D/3D imaging and dynamic studies. GRE is generally more sensitive to flow and motion unless compensated (e.g., using flow-compensation gradients).

In a basic SE acquisition, only one k-space line is collected per TR (one echo per TR), thus, the scan time is relatively long. A strong T_2 weighting requires a long TE, and TR is typically made long to minimize T_1 weighting; together, these choices lengthen the total acquisition. Each repetition (TR) contributes exactly one phase-encode (N_{PE}) line to k-space, so the scan time scales as

$$\mathrm{Time}_{\mathrm{CSE}} \approx TR \times N_{\mathrm{PE}} \times NEX \times N_{\mathrm{slices}}\,,$$

which can be long, especially for strong T_2-weighting (long TE and typically long TR).

Additionally, achieving full longitudinal recovery of magnetization limits another constraint on TR, as it must allow adequate time for T_1 relaxation. To fully recover T_1 magnetization, TR should ideally be at least $5 \times T_1$. For example, the required TR for complete recovery of tissue water magnetization typically ranges from approximately 1 s – 4 s, depending on the magnetic field strength.

FSE

To improve efficiency, fast spin-echo (FSE) strategies collect an echo train after a single excitation using successive refocusing pulses. Two widely used approaches are:

- **RARE (Rapid Acquisition with Relaxation Enhancement)**: within each TR, each echo in the train is assigned a different phase-encode value, so multiple k-space lines of the same image are filled per TR. The echo-train length (ETL, "RARE factor") therefore divides the number of required k-space lines:

$$\mathrm{Time}_{\mathrm{RARE}} \approx TR \times \frac{N_{\mathrm{PE}}}{ETL} \times NEX \times N_{\mathrm{slices}}\,,$$

i.e., for fixed TR, N_{PE}, NEX, and N_{slices}, the total time shrinks approximately in proportion to $1/ETL$. The center of k-space is acquired at a chosen echo, defining an *effective* TE. Large ETL and/or long echo spacing increase T_2-related blurring (primarily along the PE direction) and RF power.

- **MSME (Multi-Spin Multi-Echo)**: within each TR' (extended TR, must be longer than the total echo train), an echo train of length E is recorded, where E denotes the number of echoes (and thus the number of different echo times, TEs). All echoes in one train share the same phase-encode value: echo #1 contributes to the image at TE_1, echo #2 to the image at TE_2, and so forth. After N_{PE} repetitions a stack of E images is obtained at different TEs. However, compared with running E separate CSE scans to obtain E TEs, MSME acquires all E TE images in roughly the time of one scan:

  $$\mathrm{Time}_{\mathrm{MSME}} \approx TR' \times N_{\mathrm{PE}} \times NEX \times N_{\mathrm{slices}} \quad \text{vs.} \quad \mathrm{Time}_{\mathrm{CSE}} = E \times TR \times N_{\mathrm{PE}} \times NEX \times N_{\mathrm{slices}},$$

  giving a dataset-level speed-up $\approx E \times (TR/TR')$. Because each TE image is built from lines acquired at the same TE, MSME avoids TE-mixing (no T_2 blurring across k-space) and is well-suited to T_2 mapping. Later-TE images, however, have lower SNR due to T_2 decay.

With TR = 3 s and N_{PE} = 128:

- CSE for E = 4 TEs (sequential): 4 × 3 × 128 = 1536 s (25.6 min).
- MSME with E = 4 echoes per TR: 3 × 128 = 384 s (6.4 min).

RARE accelerates a single image by filling ETL phase-encode lines per TR (time $\propto 1/ETL$), at the cost of T_2 blurring. MSME accelerates multi-TE acquisition by echo-multiplexing across TE (time $\approx$ one SE scan for E TEs), preserving clean TE-specific contrast for T_2 mapping but not shortening the per-image acquisition time. Thus, MSME is $\approx 4\times$ faster for the full multi-TE dataset, whereas RARE is faster per image by a factor $\approx ETL$.

In CSE, one echo is acquired per TR, and TE_{eff} is defined by the single $k_y = 0$ acquisition. In FSE, a train of refocusing (180°) pulses produces multiple echoes, each filling a different k_y line; the effective TE corresponds to the echo at which the central k-space line ($k_y = 0$) is sampled (Figure 2.16).

EPI

In a standard spin-echo sequence (as described above), each excitation is used to acquire a single line of k-space. In contrast, Echo Planar Imaging (EPI) utilizes the concept of rapid gradient switching to fill the entire 2D k-space in a single, continuous trajectory.

In Figure 2.16, a schematic EPI sequence is shown with a series of gradient echoes formed by rapidly oscillating the readout gradient along the FE direction, while applying a series of small gradient "blips" along the PE direction between successive readouts. This creates a zigzag trajectory pattern to enable fast traversal of Cartesian k-space in a single

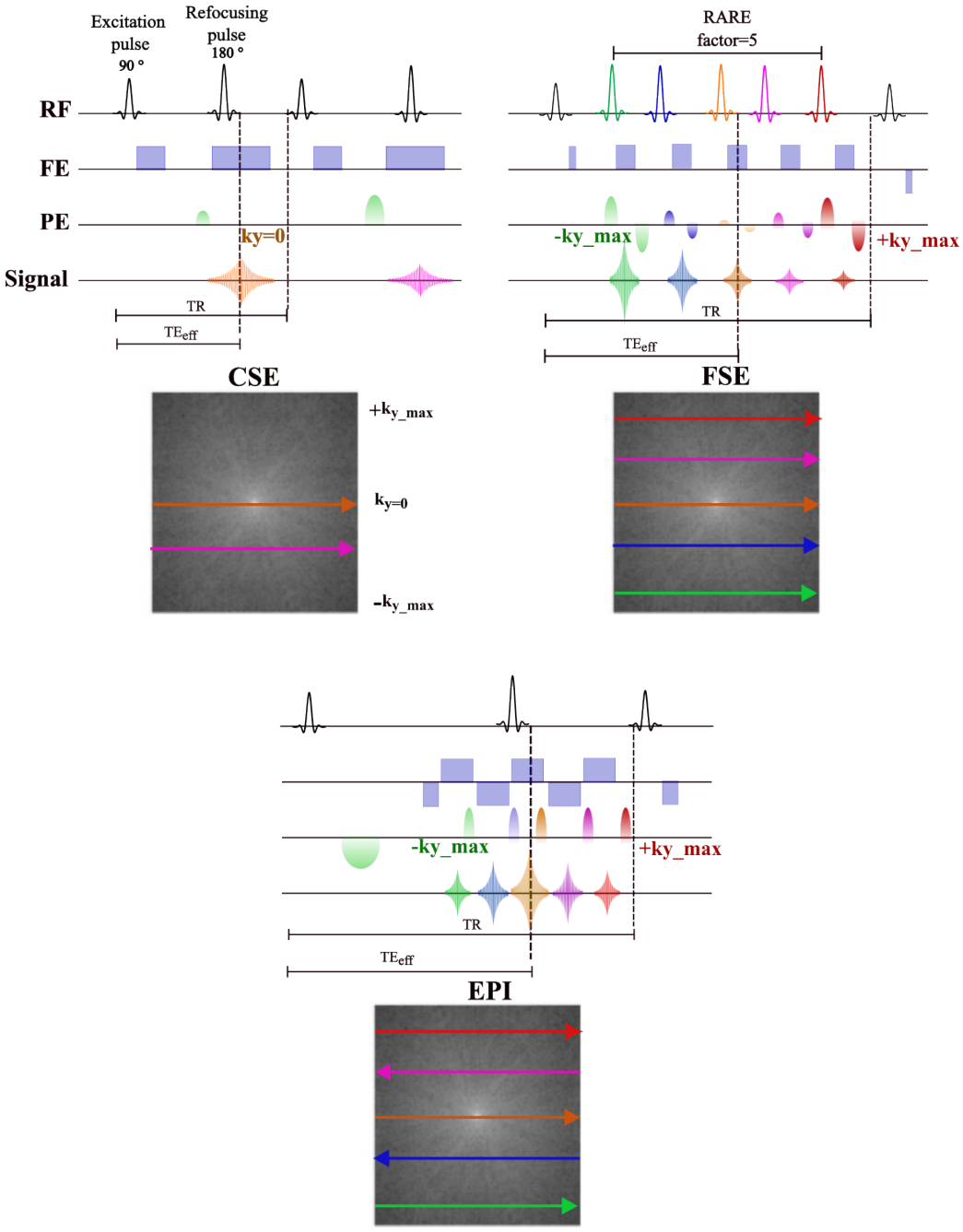

Figure 2.16.: Spin-echo–based acquisition schemes and corresponding *k*-space trajectories. Pulse sequence diagrams for Conventional Spin Echo (CSE), Fast Spin Echo (FSE/RARE, factor = 5), and Echo Planar Imaging (EPI). *k*-space schematics (bottom row) illustrate the different filling patterns: single-line Cartesian filling (CSE), multi-echo segmented filling (FSE), and continuous zig-zag readout (EPI).

excitation. In EPI, an initial PE prephaser places the trajectory at -$k_{y_{max}}$ = 0, and successive PE blips increment line-by-line during alternating FE readouts; the effective TE is again

determined by the echo coinciding with $k_y = 0$.

The true snapshot capability enables the acquisition of a complete image within a fraction of a second.Its high sensitivity to magnetic field inhomogeneities is a key limitation of this trajectory. The inhomogeneities cause such artifacts as geometric distortions, T_2^* signal loss, and phase errors.

2.5. Contrast Imaging

The versatility of MRI lies in its ability to exploit various contrast mechanisms, such as T_1- and T_2-weighted imaging, to highlight specific molecular characteristics or physiological phenomena. CNR is one of the major parameters influencing image quality, especially the ability to distinguish and characterize certain properties of a molecule (binding interaction, tissue density, etc.) reflected in the signal intensity variations of the voxels on the image.

Contrast is governed by numerous parameters divided into intrinsic and extrinsic factors (shown in Table 2.3) that influence the net magnetization behavior during image acquisition. In this chapter, only T_2 relaxation and paramagnetic contrast agents will be discussed.

Table 2.3.: Intrinsic (sample) and extrinsic (acquisition) parameters governing MR image contrast.

Intrinsic Parameters	Extrinsic Parameters
Proton density	Static and gradient field strength
T_1 relaxation	Magnetic field homogeneity
$T_1\rho$ relaxation	Type of coil
T_2 relaxation	Number of slices, slice thickness, and gaps
Temperature	Number of averages
Chemical shift	Pulse shape/bandwidth
Diffusion	MTX and FOV
	RF pulse sequences and TR-TE parameters
	Contrast-enhancing agents

T_2 weighted images

To emphasize the T_2 contrast in an MR image, imaging parameters must be adjusted, due to the fact that no MR image is governed by only one of the relaxation mechanisms. That is the reason the MR images are called T_1 or T_2 "weighted" (sensitive) (T1W, T2W).

Depending on the relaxation times of the molecule of interest, the signal intensity varies, allowing its sensitivity to be modulated by the pulse sequence parameters TE and TR (Figure 2.18), which is reflected in the contrast of monitored molecular properties.

TR mainly controls the T1W, and it must be set long enough to minimize the T_1 effect to acquire only T_2 relaxation-dominated images. A short TR enforces T_1-weighting by emphasizing sample-specific differences in T_1 relaxation, whereas a long TR allows full recovery of longitudinal magnetization, reducing T_1 influence and permitting proton density (PD) or T_2 weighting (Figure 2.18, bottom).

The extent of T_2 decay before **TE** controls signal acquisition. In a spin-echo sequence, T_2 relaxation time contributes to the final signal intensity S as:

$$\boxed{S \propto \left(1 - e^{-\frac{TR}{T_1}}\right) \cdot e^{-\frac{TE}{T_2}}} \tag{2.19}$$

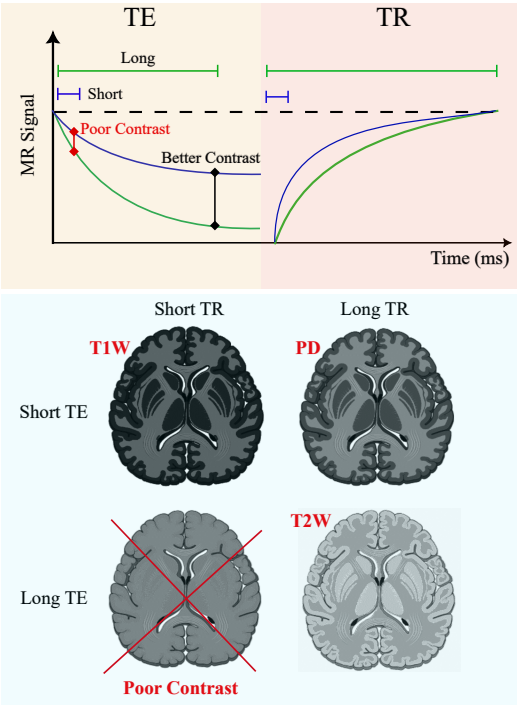

Figure 2.17.: Contrast mechanisms as a function of repetition time (TR) and echo time (TE). (Above) The length of the TE influences the sensitivity to T_2 relaxation differences, thereby affecting the image contrast. (Bottom) Depending on the TR and TE choices, the resulting contrasts in brain imaging are shown: short TR with short TE produces T_1-weighted images (T1W), long TR with short TE yields PD weighting, and long TR with long TE provides T_2-weighted (T2W) contrast.

The longer the chosen **TE**, the greater the differentiation,T_2 which is essential for the T_2-weightening (Figure 2.18 bottom). Choosing a short TE can cause sufficient T_2 decay, suppressing the image contrast, whereas excessively long TE values reduce overall signal intensity due to decay from all samples with different T_2 values. A combination of short TR and long TE results in poor image contrast due to simultaneous T_1 saturation and T_2 decay.

One of the main contributions to the T_2 relaxation time is molecular tumbling, characterized by the *rotational correlation time* τ_c. The rotational correlation time τ_c cannot be measured directly, as molecular tumbling occurs on the picosecond to nanosecond timescale. Instead, τ_c is inferred indirectly from relaxation measurements—most commonly through the analysis of T_1, T_2, and nuclear Overhauser effect (NOE) data by fitting to theoretical models such as the Bloembergen–Purcell–Pound (BPP) framework. According to the BPP theory, the efficiency of relaxation depends on the relationship between the molecular motion and the Larmor frequency ω_0. Local magnetic field fluctuations that occur near ω_0 are most effective in inducing relaxation and therefore shorten T_2.

Image contrast in T_2-weighted (T2W) imaging is directly influenced by this molecular-

scale behavior. In general, small, rapidly tumbling molecules (e.g., free water in low-viscosity environments) exhibit relatively long T_2 values, since their rapid motions average out local magnetic field variations. In contrast, larger or more slowly tumbling molecules (e.g., macromolecules, bound water, or protein-bound contrast agents) often show shorter T_2 values when their tumbling rates approach the Larmor frequency. However, this relationship is field-dependent — at very high magnetic fields, where ω_0 is large, even moderately mobile molecules can experience increased relaxation.

Consequently, the observed T_2-weighted contrast depends on both molecular motion and magnetic field strength. The image contrast can be adjusted experimentally via the echo time (TE) and repetition time (TR): long TE (with an appropriately long TR) enhances sensitivity to T_2 differences, improving T_2-weighted contrast, whereas short TE reduces it.

PRE Contrast agents

An alternative strategy for enhancing image contrast involves the use of paramagnetic contrast agents, which accelerate relaxation processes and thereby reduce the required measurement time. These agents perturb the local magnetic environment of nearby nuclei through indirect, non-covalent interactions (Figure 2.18).

In particular, gadolinium (Gd)-based compounds are widely used as T_1 contrast agents in molecular and clinical imaging [7–9]. Their unpaired electrons create fluctuating local magnetic fields that enhance the longitudinal relaxation rate, leading to signal enhancement (brightening) in T_1-weighted images. At very high concentrations, secondary effects on T_2 relaxation can occur due to increased local susceptibility, but under typical imaging conditions, the dominant mechanism is T_1 shortening.

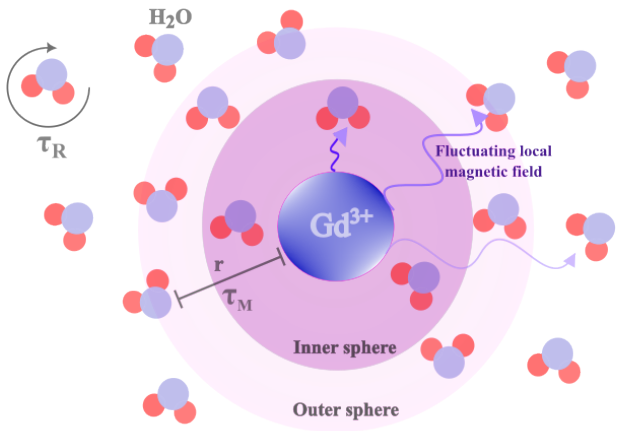

Figure 2.18.: Paramagnetic relaxation effects on water molecules by a contrast agent Gd^{3+} ion in solution. Water molecules in the inner sphere are directly coordinated to the paramagnetic center, with their residence lifetime (τ_M), while water molecules in the outer sphere interact through diffusion and hydrogen bonding. The electron spin and nearby protons are coupled by the internuclear distance r spatially, while water molecules tumble with a rotational correlation time (τ_R).

Gadolinium (Gd^{3+}) has seven localized unpaired electrons. Among other contrast agents (manganese, dysprosium, and iron), it generates significant magnetic dipole fluctuations through perturbations of the local magnetic field. The effect on the relaxation properties resulting from the dipole-dipole interaction between the unpaired electrons of the paramagnetic agent and nearby nuclei is known as the paramagnetic relaxation enhancement (PRE).

The contrast is distance-dependent (r) relaxation enhancement based on the Solomon—Bloembergen theory. This is expressed as,

$$\boxed{J_{\mathrm{SB}}(\omega) = r^{-6}\frac{\tau_C}{1 + (\omega\tau_C)^2}} \tag{2.20}$$

which explains the correlation between the molecular motion (τ_C), the spectral density function ($J_{\mathrm{SB}}(\omega)$), and the importance of matching the frequency to the Larmor frequency (ω) of the observed nuclei. The PRE efficiency increases with the PRE-agent concentration [CA] and influences the relaxation rate of the observed nuclei ($1/T_1$ or $1/T_2$) that is quantified as relaxivity (r_1 or r_1) with the knowledge of the inherent relaxation rate of the molecule in the absence of the agent in equation 2.21.

$$\boxed{\frac{1}{T_{1,2}} = r_i \cdot [\mathrm{CA}] + \frac{1}{T_{1,2}^{noPRE}}} \tag{2.21}$$

A reduction in the longitudinal relaxation time (T_1) enables the application of shorter repetition times (TR) while maintaining equivalent signal intensity, as described by Eq. 2.19. To achieve optimal image contrast in MRI, both the selection of pulse sequence parameters such as repetition time (TR) and the incorporation of biophysical effects introduced by PRE-agents play an essential role.

2.6. Compressed Sensing

Another acceleration mechanism for imaging time is Compressed Sensing (CS) that utilizes the *k*-space reconstruction technique. CS in MRI exploits the sparsity feature of an image in a transform domain (e.g., wavelets, total variation), so undersampling can be applied in the *k*-space (acquisition domain), such as taking fewer phase-encoding lines. Therefore, it introduces image artifacts (e.g., ghosting). During reconstruction, an iterative optimization algorithm requires three essential aspects:

- Signal sparsity: A sparse representation of the acquired signal must be present in a known and mathematically fixed domain (*k*-space or transform domain).
- Incoherence sampling pattern: Random *k*-space sampling in the acquisition domain ensures optimal suppression of image artifacts.
- Nonlinear reconstruction: Algorithm necessary for the image recovery from undersampled data.

Sparsity

The most important criterion for undersampling is the sparsity, which should exist either in the acquisition (*k*-space) or transform domain in the reconstructed image. An image exhibits low sparsity in the acquisition (Fourier) domain but can be represented sparsely in transformed image domains (e.g., wavelets) (Figure 2.19). The sparsity is prior knowledge for assumptions about the amount of acquired data that can be reduced while preserving the accurate reconstruction ability.

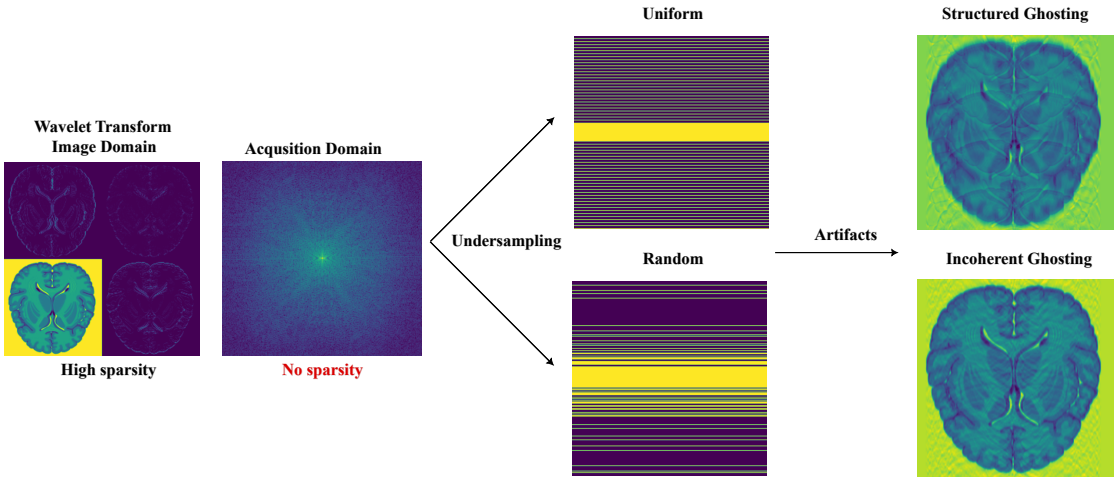

Figure 2.19.: Sparsity and undersampling patterns with resulting artifacts. Undersampling in *k*-space leads to aliasing artifacts: uniform undersampling produces structured ghosting, whereas random undersampling produces incoherent artifacts.

Most MR images are compressible. The sparsity in the transform domain is due to large regions of similar signal intensity with sharp edges in the image. Sharp edges are represented with just a few wavelet or finite coefficients with nonzero values, with many zeros (noise or background signals). Compressing only the largest coefficients, the measurement time is reduced with less or no information lost. One of the common usages of the wavelet transformation for compression is image coders like JPEG-2000 [10].

Incoherence sampling

Sampling is incoherent when the MR signal is sparse in the transform domain, whereas it does not have a sparse representation in the acquisition domain (*k*-space). Random undersampling of phase encoding in the acquisition domain produces incoherent artifacts due to the violation of the Nyquist criteria. Encoding fewer PE-lines by skipping the lines randomly spreads the missing data irregularly. This results in noise-like artifacts rather than a structured ghost when skipping the PE-lines periodically. The ghost artifact is structured by applying a uniform undersampling pattern and is incoherent in the case of random undersampling.

Randomized noise can be distinguished from the true sparse signal during CS reconstruction, like wavelets/TV minimization, because the caused ghosting artifact is not replicated and shifted periodically across the field of view overlapped with the real image.

2.7. MR in drug discovery

Drug-related MR parameters

The MR signal inherently captures the full molecular fingerprint of the protein–ligand binding event, which takes advantage of chemical exchange with the bound and unbound states. Physical consequences of the binding event, including thermodynamic, kinetic, and dynamical alterations, are reflected in line width and signal intensity of the NMR signal due to longitudinal (T_1) and transverse (T_2) relaxation effects (Figure 2.20).

Observing different components of the protein-ligand complex allows access to different aspects of the binding mechanism: chemical environmental changes, binding kinetics, competition, conformational dynamics, and binding sites on the protein surface. Protein observed MR experiments face the challenges of the need for large amounts of labeled protein, measurement limitation on the protein size (larger and more protein amount, longer measurement times), and complex protein spectra for further assignment.

Ligand-observed MR experiments bring several advantages over protein-observed such as the usage of small amounts of protein, typically at low micromolar concentrations, since the only relevant signal changes come from the monitored ligand upon protein binding. As there is no need for ^{15}N- or ^{13}C-labeled protein, ligand-observed experiments are low in cost and complexity.

Another important advantage is their suitability for high-throughput screening. Ligand-detected methods such as Water-Ligand Observed via Gradient SpectroscopY (Water-LOGSY), saturation transfer difference(STD)-NMR, and arr–Purcell–Meiboom–Gill(CPMG) relaxation dispersion experiments can be rapidly applied and are easy to automate. These advantages make ligand-detected experiments well-suited to screening large compound libraries. Another important advantage is straightforward analysis of the ligand signal, which is typically sharp and well-resolved, even in cases of low-affinity fragments (affinity will be discussed later).

Upon ligand binding, the most pronounced changes in MR parameters are typically observed in the relaxation behavior of the ligand, specifically in the T_1 and T_2 relaxation times, as well as in the chemical shift. These changes arise due to alterations in electron cloud polarization (σ_{iso}, isotropic part of the shielding tensor), such as displacement of surface water molecules upon ligand binding or conformational adjustments of the protein.

Relaxation parameters provide insight into changes in molecular tumbling rates, the mobility of the observed molecule, and fluctuations in the local magnetic field. In the case of T_1 relaxation, the effective molecular weight of the ligand increases upon association with a protein, leading to slower rotational motion and enhanced dipole-dipole interactions. The orientation of the molecule relative to the external magnetic field is influenced by the symmetry and distribution of the surrounding electron clouds, which contribute to the local magnetic environment.

Variations in molecular motion also affect T_2 relaxation, which is reflected in the width and intensity of the MR signal. The full width at half maximum (FWHM) of the signal, in hertz, is directly proportional to the transverse relaxation rate constant R_2 (see Figure 2.20). In linear frequency units, this relationship is expressed as:

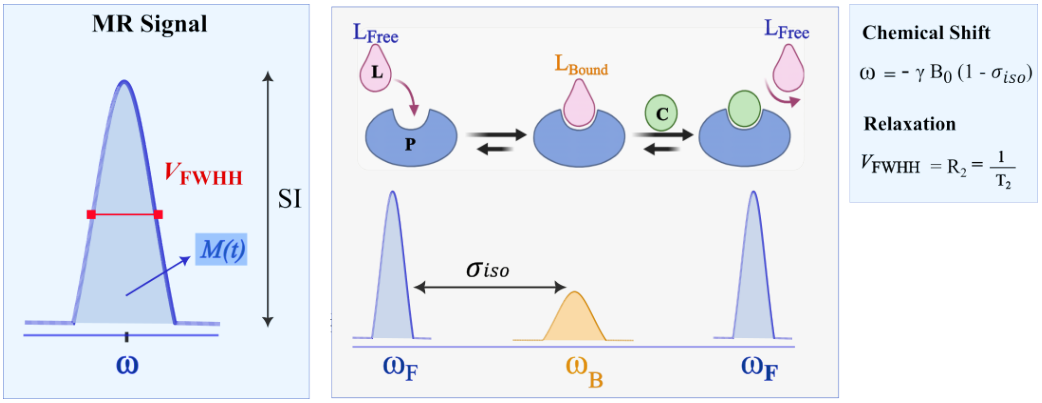

Figure 2.20.: Drug-related NMR parameters of ligand binding. The resonance frequency (ω) reflects the chemical environment of the ligand (L), enabling discrimination between free or (L_{free}) displaced by competitor (C) and protein (P) bound (L_{bound}) states via chemical shift (ω). The signal intensity (SI) is proportional to the population of each state, while the linewidth (V_{FWHM}) reports on relaxation processes and molecular dynamics.

$$\text{FWHM (Hz)} = \frac{R_2}{\pi}$$

Alternatively, in angular frequency units (rad/s), the relationship becomes:

$$\text{FWHM (rad/s)} = 2R_2$$

The shape and local electron density distribution of a molecule's electron clouds are critical to its chemical environment. Electrons shield nuclei from the external magnetic field through diamagnetic and paramagnetic induced currents, leading to changes in the chemical shift. This shift appears as the position of the signal along the spectral axis and reflects the precession frequency of the nucleus. In MR experiments conducted with an excess of ligand, changes in chemical shift can provide quantitative information about ligand binding.

Together, T_1 and T_2 relaxation times, along with chemical shift perturbations, serve as sensitive indicators for detecting and characterizing ligand–protein interactions. Their quantitative and mechanistic interpretation enables insights into binding kinetics, affinity, and dynamic exchange processes.

Enzyme as drug target

The search for biologically active substances capable of relieving pain, treating illness, or prolonging life has been a central pursuit of drug discovery projects since the earliest days of civilization. Obtaining insights into these substances, drugs, is important to understand biology and find ways to manipulate physiological processes.

A ligand is a small molecule that forms a complex upon reversible binding to a target biomolecule, most commonly a protein, non-covalently (Figure 2.21, trypsin with a ligand

BZD). Proteins are polymers composed of amino acids, which serve as the fundamental building blocks of their structure and function. The spatial structure of the binding site determines the ability of the binding of a ligand with a protein. The interaction occurs by non-covalent forces such as hydrogen bonding, van der Waals interactions, electrostatic forces, and hydrophobic effects.

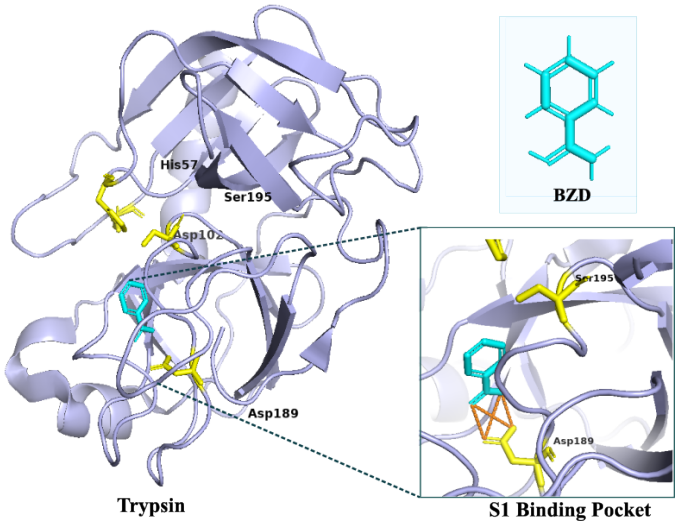

Figure 2.21.: Interaction of benzamidine (BZD) with trypsin. The overall trypsin (protein) is shown as a cartoon (light blue) with the catalytic triad residues (His57, Asp102, Ser195) and the specificity-determining Asp189 highlighted in yellow sticks. The positively charged amidinium group of benzamidine (cyan) forms a salt bridge (red dotted line) with Asp189 inside the S1 pocket.

Upon binding, conformational changes in the protein are induced, which modulate its activity, stability, or interaction with other biomolecules. The activity of many biological processes can be promoted, including enzymatic catalysis, signal transduction, transport, and gene regulation. Ligands with a function of activating the receptor are classified as agonists and antagonists if they inhibit its function.

One important mode of enzymatic regulation is reversible inhibition, in which small molecules compete with natural substrates for access to the active site (Figure 2.21). Benzamidine (BZD) binding to trypsin is a well-characterized model system of this mechanism. BZD is a low-molecular-weight ligand to the serine protease trypsin; it specifically occupies the S1 binding pocket. Its amidine group mimics the positively charged side chain of arginine, enabling electrostatic interaction with the negatively charged Asp189 and stabilizing the binding.

Binding affinity

Molecular recognition and biofunctional feedback of a binding event is determined by the specificity and affinity of ligand binding. Insight into protein-ligand interactions provides information on many molecular mechanisms underlying cellular function and regulation.

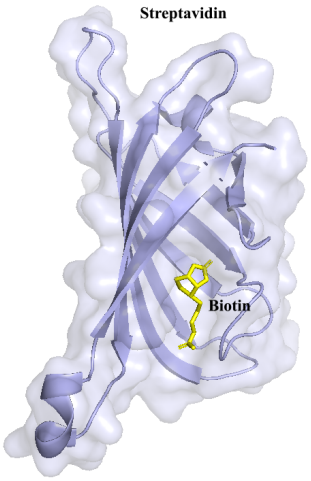

Figure 2.22.: Streptavidin–biotin complex (PDB ID: 1STP). Streptavidin is shown as a cartoon (light purple) with its molecular surface rendered semi-transparent. Biotin is displayed in stick representation and highlighted in yellow.

The strength of the association between a ligand [L] and protein [P] is referred to as binding affinity and reflects how tight the binding of the protein-ligand [PL] complex is. The affinity is characterized by using equilibrium dissociation constants of K_D and is quantified using the equation 2.22. Considering thermodynamics of the interaction, K_D represents the thermodynamic equilibrium between the bound and unbound (dissociated) states of a protein–ligand complex (Figure 2.20). The lower K_D value, the stronger the binding between two molecules.

$$\boxed{K_D = \frac{[P][L]}{[PL]}} \tag{2.22}$$

Typical therapeutic compounds exhibit in the range of high (sub-nanomolar) to moderate (low-nanomolar) affinities. The most well-known example of a strong binding affinity occurs between biotin and streptavidin (Figure 2.22) with a $K_D \approx 10^{-15}$ M [11].

2.8. Ligand-based ^{19}F-MR

Approximately 20–25% of Food and Drug Administration (FDA)-approved drugs on the market contain at least one fluorine atom [12], including well-known examples such as *Fluoxetine* (Prozac), *Ciprofloxacin*, *Atorvastatin* (Lipitor), and *Fluticasone* (2.23). The introduction of fluorinated functional groups in pharmaceuticals enhances drug properties, making them highly favorable in the pharmaceutical industry.

Due to the strong carbon–fluorine (C–F) bond, which arises from fluorine's high electronegativity, fluorinated drugs often exhibit greater metabolic stability, increased membrane permeability, and tunable acidity (pK_a). Furthermore, because fluorine is the smallest halogen, it can fit into receptor binding sites with minimal steric hindrance, allowing other parts of the molecule to interact effectively with biological targets [13].

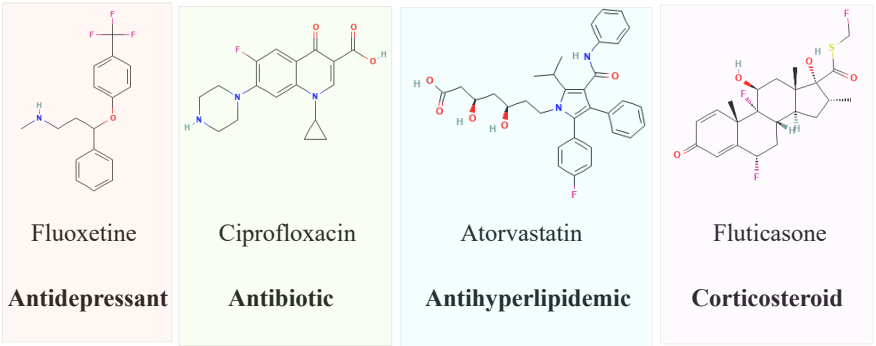

Figure 2.23.: Representative-Fluorinated blockbusters

High sensitivity of ^{19}F

The amount of fluoride ions (F^-) in the human body is small (e.g., in bones and teeth after fluoride exposure) and undetectable due to the negligible presence of the molecular environment and the low mobility required for molecular imaging. This enables background-free detection for investigations based on protein-ligand interactions, unlike conventional proton MRI, which has a background signal originating from water and fat protons in biological tissue. This results in high specificity and contrast for fluorine-containing compounds.

^{19}F is an NMR-active nucleus with a spin of $\frac{1}{2}$, a gyromagnetic ratio (83% of the sensitivity compared to ^{1}H) with 100% natural abundance that leads to great signal response to changes in the magnetic field, which translates into high MR sensitivity.

Relaxation contributions of ^{19}F

The combination of no background signal arising from the observed medium, such as buffer or protein, and the high sensitivity of the observed ^{19}F-MR signal, makes ^{19}F molecular imaging a valuable tool in detecting ligand-target interactions for early drug discovery.

Ligand-based (LB) ^{19}F-molecular imaging can exploit these unique properties of the fluorine nucleus to monitor signal alteration upon binding.

Depending on the interactions between the spins and their surrounding molecular environment, MR signals relax back to their equilibrium state differently, which translates to different T_2relaxation times linked to molecular tumbling and plays a critical role in determining spectral resolution and sensitivity. The transverse relaxation rate (R_2) of ^{19}F nuclei is a powerful parameter in MR studies because it demonstrates underlying mechanisms involving time-dependent magnetic field fluctuations: variations in the local magnetic field, measured by dipole–dipole coupling (DD), and in chemical shift, known as chemical shift anisotropy (CSA).

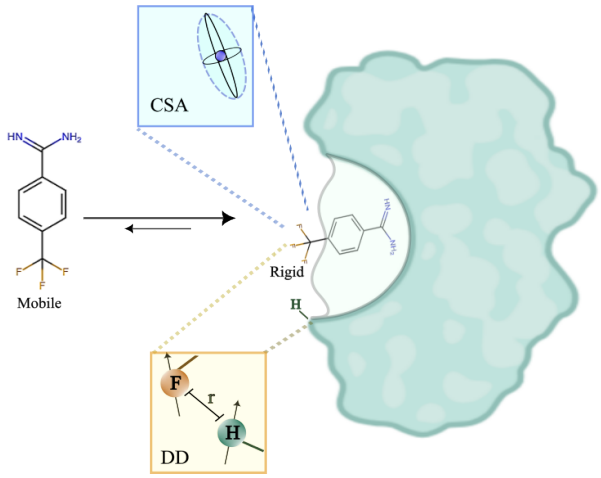

Figure 2.24.: ^{19}F NMR relaxation mechanisms for the high sensitivity for ligand–protein binding detection. A fluorinated ligand (left) undergoes from a mobile, free state to a rigid, protein-bound state (right). Upon binding, the ligand's motion slows down, enhancing contributions from the ^{19}Fchemical shift anisotropy (CSA). In addition, ^{19}F nuclei experience strong dipole–dipole (DD) interactions with nearby protein protons depending on the internuclear distance (r).

Nuclear spin state transitions can be induced by the magnetic field fluctuations in case of matching the energy gap between spin states and the right frequency content. Transition efficiency depends on the frequency components of those fluctuations, which are described by the spectral density function, $J(\omega)$. $J(\omega)$ quantifies the amplitude of magnetic fluctuations at a specific frequency ω, and the relevant frequency is typically the Larmor frequency (ω_0) for T_1- and a mix of zero frequency and ω_0 for T_2 relaxation mechanisms.

The ^{19}F nucleus exhibits a large chemical shift anisotropy (CSA) spanning several hundred parts per million, as it experiences an anisotropic electronic environment due to its high electronegativity and sensitivity to local chemical surroundings. The efficiency of CSA-mediated relaxation depends on the product of the Larmor frequency and the rotational correlation time ($\omega_0\tau_c$). When molecular motion slows, τ_c increases, and if $\omega_0\tau_c \approx 1$, the spectral density at ω_0 reaches its maximum, resulting in the strongest CSA contribution to transverse relaxation and thus broader NMR linewidths. Higher magnetic

fields have a bigger effect on ^{19}F-CSA because its contribution is proportional to the square of the magnetic field strength (ω_F) [14]:

$$\boxed{\frac{1}{T_2} = \frac{2}{15}(\sigma_{\parallel} - \sigma_{\perp})^2 \omega_F^2 \tau_c \left(\frac{2}{3} + \frac{1/2}{1 + \omega_F^2 \tau_c^2} \right)} \tag{2.23}$$

In the bound state of a fluorinated ligand attached to a large macromolecule, the overall tumbling of the complex slows down, reducing the motional averaging of the CSA interaction [15]. The shielding anisotropy of the ^{19}F nucleus ($\sigma_{\parallel} - \sigma_{\perp}$) remains large, and CSA-driven relaxation becomes more efficient. Consequently, the T_2 relaxation rate increases, leading to line broadening in NMR spectra or signal darkening in T_2-weighted ^{19}F MRI.

2.9. ^{19}F MR competition experiments

In recent years, substantial progress has been achieved with ligand-based NMR methods such as STD and CPMG experiments, which enable the direct quantitation of binding affinities within the fragment range (low M to low mM) [14, 16]. Despite these advances, direct binding affinity measurement approaches remain inherently constrained in both throughput and information content, as each new ligand typically requires dedicated optimization of experimental conditions and parameter settings. Indirect, competitive binding experiments overcome these limitations by relying on a relatively small set of well-characterized reporter molecules, for which the optimization of MR parameters and detailed characterization of the binding site need only be carried out once. This strategy not only streamlines the experimental workflow but also increases the efficiency of ligand screening campaigns.

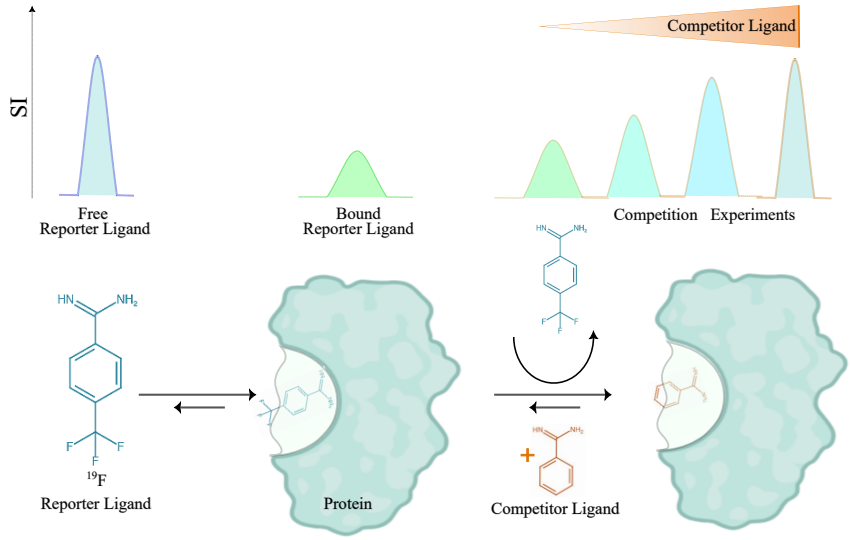

Figure 2.25.: Fluorine-based affinity competition screening (FAXS). The reporter ligand containing a fluorine group yields distinct ^{19}F MR signals (signal intensity, SI) in the free (blue) and protein-bound (green) states. In titration experiments with increasing concentrations of a competitor ligand (orange), the reporter ligand is displaced from the binding pocket, resulting in a progressive recovery of the free reporter signal.

^{19}F MRI offers high sensitivity to molecular interactions due to its strong CSA, improving its utility for detecting binding events. Building on this, methods such as ^{19}F-based exchange screening (FAXS) exploit both CSA effects and chemical exchange to detect weak and transient ligand binding, thus enabling rapid screening of fragment libraries or lead candidates with high sensitivity and throughput.

This methodology was first introduced by Dalvit et al. as a competitive binding assay that uses a fluorinated weak-affinity ligand as a reporter ligand, which can be displaced by stronger competitors upon protein binding [17–19]. To monitor this displacement event, a

CPMG pulse sequence is applied with a ligand-specific T_2-filter. The underlying principle is that the reporter ligand shows a markedly reduced T_2 relaxation time when it is bound to the protein, whereas its T_2 is long in the free state. Consequently, the displacement of the bound reporter ligand by a stronger competitor leads to a recovery of the T_2-weighted signal.

Protein–ligand binding kinetics are governed by the on- and off-rates of complex formation and dissociation, which are reflected in NMR by the exchange rate k_{ex} between bound and free states. The dissociation constant, $K_D = \frac{[P][L]}{[PL]} = \frac{k_{\mathrm{off}}}{k_{\mathrm{on}}}$, quantifies the equilibrium between free protein, free ligand, and the protein–ligand complex.

The exchange rate modulates NMR observables such as chemical shifts and relaxation rates and can lead to different apparent values. This dependence is commonly rationalized by distinguishing three limiting exchange regimes (slow, intermediate, and fast), defined by the relative magnitude of k_{ex} with respect to the frequency and relaxation-rate differences between free and bound states. In the fast-exchange limit, the conditions:

$$|\omega_{\mathrm{F}} - \omega_{\mathrm{B}}| \ll k_{\mathrm{ex}} \quad \text{and} \quad |R_{2,\mathrm{F}} - R_{2,\mathrm{B}}| \ll k_{\mathrm{ex}}$$

must be fulfilled [15]. Under these fast-exchange conditions, NMR detects a single resonance whose position and transverse relaxation rate are given by population-weighted averages of the free and bound states and can be described by relatively simple expressions. In contrast, in the slow-exchange limit:

$$|\omega_{\mathrm{F}} - \omega_{\mathrm{B}}| \gg k_{\mathrm{ex}} \quad \text{and} \quad |R_{2,\mathrm{F}} - R_{2,\mathrm{B}}| \gg k_{\mathrm{ex}},$$

separate signals for free and bound species are observed at their respective chemical shifts, with signal intensities proportional to their populations and apparent relaxation rates that are modulated by the lifetimes of the two states:

$$k_{\mathrm{ex}}^{L} = k_{\mathrm{off}} + k_{\mathrm{on}}[P] \qquad k_{\mathrm{ex}}^{P} = k_{\mathrm{off}} + k_{\mathrm{on}}[L]$$

$$R_{2,\mathrm{fast}} = p_F R_{2,F} + p_B R_{2,B} + \frac{(\omega_F - \omega_B)^2 p_F p_B}{k_{\mathrm{ex}}}$$

$$\omega_{\mathrm{fast}} = p_F \omega_F + p_B \omega_B$$

Definitions of the parameters:

- $k_{\mathrm{ex}}^{L,P}$: exchange rate of the ligand or protein, describing the transition of the ligand from the protein-bound state to the free state.
- k_{on}: bimolecular association rate constant and k_{off} dissociation rate constant of the protein–ligand complex.
- $[P, L]$: concentration of free (unbound) protein or ligand.
- $p_{F,B}$: fractional population of the free or bound ligand
- $R_{2,F}$: intrinsic transverse relaxation rate of the free ligand.

- $R_{2,B}$: intrinsic transverse relaxation rate of the protein-bound ligand.
- $R_{2,\text{fast}}$: observed transverse relaxation rate under fast-exchange conditions (population-weighted).
- $\omega_{F,B}$: resonance frequency (chemical shift) of the free or bound ligand.
- ω_{fast}: population-weighted averaged resonance frequency under fast exchange.

The competitive ^{19}F-NMR assay operates in the fast-exchange regime. Here, the reduction in T_2 upon binding is manifested as line broadening in the MR spectrum (Figure 2.25). The broadening arises because the bound ligand experiences restricted molecular tumbling, increased local magnetic field fluctuations, and a substantially shorter transverse relaxation time. In a two-state fast-exchange system, the observed linewidth reflects the effective transverse relaxation rate $R_{2,\text{obs}}$, which is a population-weighted average of the free and bound contributions. Since the bound state exhibits a very short T_2 (large R_2), even a modest bound population leads to notable broadening of the observed resonance. Displacement of the reporter ligand by a stronger competitor shifts the equilibrium toward the free state, decreases $R_{2,\text{obs}}$, and thereby produces the characteristic T_2-weighted signal recovery that is used to quantify binding in this assay.

For the assay to be sensitive to displacement, there are several requirements to be fulfilled. First, the reporter ligand must exhibit a suitable affinity to the protein (detailed later in this section). At the same time, the bound state must induce strong T_2-shortening, ensuring a large relaxation contrast between the free and bound forms. Thus, the optimal reporter ligand combines low affinity with a pronounced difference in transverse relaxation properties, maximizing the dynamic range of the competitive assay.

Next, the competitor ligands and the reporter ligand must compete for the same binding pocket on the protein. Once the conditions are optimized, the signal alteration in the reporter ligand delivers two important points for competition experiments:

- The displaced fractions (F in %) of the bound reporter ligand using R_2 values of three experiments consisting free reporter ligand $R_{2,c}$, bound reporter ligand under non-competitive conditions $R_{2,nc}$ and displaced reporter ligand $R_{2,c}$ upon competition:

$$\boxed{F = 100 * \left(1 - \frac{R_{2,c} - R_{2,f}}{R_{2,nc} - R_{2,f}}\right)} \tag{2.24}$$

- Quantitative determination of the inhibition constant (K_C), under the knowledge of the reporter ligand's dissociation constant (K_D), competitor [C] & reporter ligand $[L_T]$ concentrations:

$$\boxed{K_C = \frac{(100 - F)[C]K_D}{F([L_T] + K_D)}} \tag{2.25}$$

A suitable reporter ligand for ^{19}F ligand-observed assays should fulfill several physicochemical and spectroscopic criteria to enable quantitative competition measurements [15, 20]:

- **Moderate affinity** toward the target protein (K_D in the low micromolar range) to ensure partial binding equilibrium and allow measurable displacement by competing ligands [14, 16].
- **Fast exchange regime** on the NMR timescale, leading to averaged signal properties (chemical shift or relaxation rates) that respond sensitively to binding and displacement [21].
- **Single, well-resolved ^{19}F resonance** far from other fluorinated species, enabling unambiguous signal integration and minimal spectral overlap [22].
- **High aqueous solubility and chemical stability**, preventing aggregation or precipitation at micromolar concentrations [23].
- **Adequate relaxation properties** (T_1, T_2) providing sufficient signal-to-noise ratio (SNR) for detection within short experimental times, especially relevant for parallelized or imaging-based assays [24].

These properties ensure that a partial binding equilibrium can be established, allowing quantitative monitoring of competition while maintaining measurable signal differences between the free and bound states.

To experimentally demonstrate these principles in a controlled and well-understood system, we selected the *trypsin–benzamidine* pair as a model for ^{19}F reporter development and validation. **Trypsin** is a serine protease that catalyzes the hydrolysis of peptide bonds on the carboxyl side of basic amino acids such as lysine and arginine. Its active site contains a catalytic triad (His57, Asp102, Ser195) and a negatively charged S1 pocket that provides specificity for positively charged substrates and inhibitors (Figure 2.21). Due to its well-characterized structure and predictable binding behavior, trypsin serves as an ideal model enzyme for investigating protein–ligand interactions.

Benzamidine is a classical competitive inhibitor of trypsin that mimics the guanidinium group of arginine and binds strongly within the S1 pocket through electrostatic and hydrogen-bond interactions. This well-understood interaction has been extensively employed as a reference system for benchmarking protease inhibition and validating novel analytical approaches for binding studies.

Building upon this established model, we employed 4-trifluoromethylbenzamidine (**TFBA**) as a ^{19}F reporter molecule for MRI-based ligand screening. TFBA fulfills the criteria of an ideal reporter ligand, as summarized below:

(i) TFBA is structurally related to benzamidine, a well-established trypsin inhibitor, and therefore binds reliably to the catalytic site of trypsin.

(ii) The trifluoromethyl group provides a single, sharp ^{19}F resonance, facilitating quantitative detection without spectral overlap.

(iii) Upon binding to trypsin, molecular tumbling of TFBA is restricted, which enhances chemical shift anisotropy (CSA)–mediated relaxation and leads to pronounced T_2 shortening of the fluorine signal, thereby producing strong relaxation-driven contrast in MRI.

(iv) TFBA can be competitively displaced by non-fluorinated ligands such as benzamidine, enabling indirect detection of clinically relevant, non-fluorinated drug candidates.

Taken together, the trypsin–TFBA system provides an ideal and well-characterized platform to validate *parallelized* ^{19}F-MRI-based ligand screening as a rapid and quantitative approach for enzyme–inhibitor interaction studies.

3. Sample Parallelization and Image Optimization

This chapter is based on work conducted in collaboration with Francisco Ayuso Penna, Dr. Mazin Jouda, and Ajmal Jamal. FAP designed the sample holder for NMR tubes. The ^{19}F-RF coil hardware was manufactured and optimized for ^{19}F-MRI experiments. The capillary sample holder was designed and fabricated by AJ. The content of this chapter focuses on image quality assessment and parameter optimization for parallelized sample acquisition utilizing different sample holder designs, where multiple samples were imaged simultaneously along one frequency-encoding dimension.

3.1. Introduction

Magnetic resonance imaging (MRI) combines the principles of nuclear magnetic resonance (NMR) with spatial encoding to create image contrast. MRI can encode a variety of contrast mechanisms into the image, including spin density, nuclear relaxation properties (transversal and longitudinal relaxation), and transport processes such as diffusion and flow [25–29]. These versatile contrast mechanisms make MRI particularly attractive for spatially resolved detection of molecular interactions across diverse physical and chemical environments. However, the ability to encode such rich information is inherently linked to long acquisition times (see Chapter 2.4), since each form of contrast requires repeated signal averaging or additional phase-encoding steps. As a result, MR techniques are often constrained by limited measurement throughput (Figure 3.1). The main limiting factors include:

- Individual sample loading, which constrains parallelization, increases total acquisition time, and requires repeated system stabilization (e.g., shimming).
- Low (sub-micromolar) analyte concentrations, which reduce SNR and necessitate extensive averaging.
- Sequential sampling schemes (e.g., conventional phase-encoded acquisitions), which extend total acquisition time.
- Long T_1 relaxation times of observed molecules, which set a lower bound on repetition rates between scans.

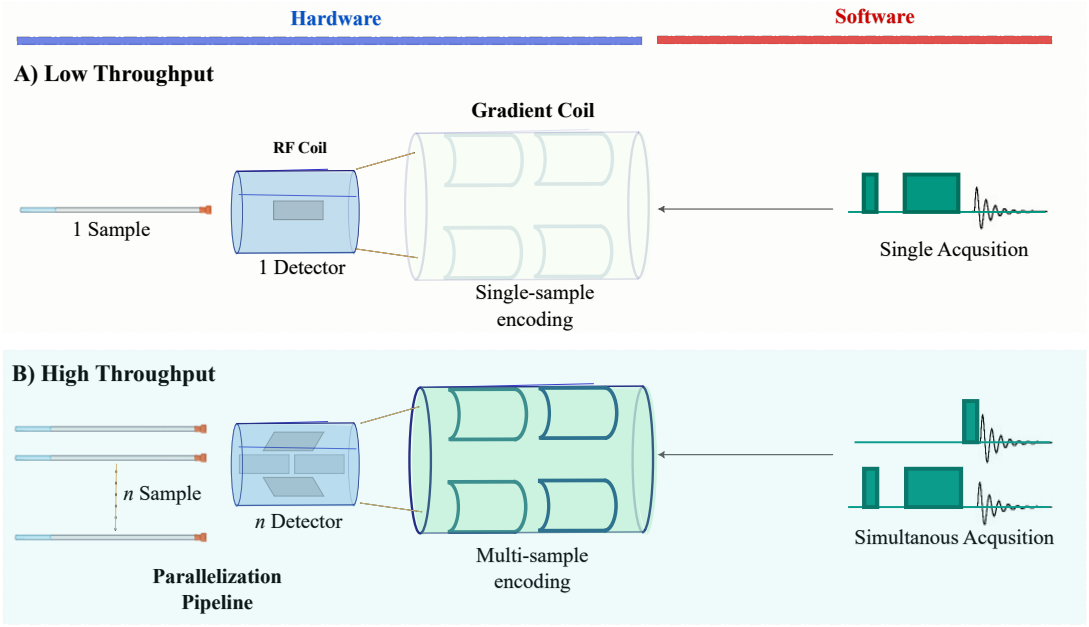

Figure 3.1.: MR instrument hardware and software modification possibilities for higher throughput. (A) Conventional single-sample setup with one RF coil and sequential acquisition. (B) Parallelized setup with multiple samples localized through spatial encoding and/or multi-coil arrays for simultaneous signal reception.

- Diffusion and molecular motion in solution, which broaden lines and reduce coherence during imaging gradients.

Parallelization and miniaturization are therefore critical to improving efficiency in both data acquisition and sample handling. Several methodologies have been developed to accelerate MR data collection. Strategies include flow-through systems, microfluidic devices, and positioning bundles of samples within the sensitive volume of a single RF coil. These approaches are rooted in hardware design, as they directly determine how many distinct samples can be interrogated simultaneously within a given detection volume of the MR instrument.

In flow-through systems, parallelization is achieved temporal manner: multiple samples are transported sequentially through a single coil via continuous or segmented flow, enabling automated high-throughput measurements while minimizing dead time between acquisitions [30–32]. Microfluidic platforms extend this concept by spatially separating small sample compartments (e.g., droplets or microchannels) within a compact chip, which can be integrated into stripline or planar coils to allow many samples to be probed in parallel [33, 34]. In contrast, sample bundles address parallelization at the macroscopic scale, where multiple NMR tubes or capillaries are positioned within the same RF coil active volume [35]. This requires proposed coil design and spatial encoding strategies to distinguish signals originating from each compartment while maintaining homogeneous excitation. In all three cases, the common principle is to re-engineer the physical sample

environment such that either space (multiple compartments), time (flow sequences), or both are exploited to increase throughput beyond that of conventional single-sample measurements.

While these hardware strategies expand the number of samples that can be positioned within the detection region, there are also advanced signal acquisition schemes. In particular, multi-receiver architectures, when integrated with parallelized pulse sequences, enable simultaneous acquisition and maximize the information content of a single experiment. Examples include Parallel Acquisition NMR Spectroscopy (PANSY) [36–38] and concatenated multi-experiment schemes such as NMR by Ordered Acquisition using ^{1}H detection (NOAH) [39–41], which share recovery delays across modules to reduce total experimental time. Each module in such schemes can be considered an individual NMR experiment, illustrating how parallelization can be achieved even within a single pulse sequence.

By altering imaging gradients in resonance frequency and phase, **MRI** can spatially encode signals from multiple samples [42,43] (Figure 3.2). In this sense, MRI can be viewed as a massively parallel experiment, where the spatial dimension of the MR image provides a natural platform for parallelization. Every voxel can be regarded as an independent acquisition channel [44]. For an n-dimensional image with resolution d along each axis, the acquisition corresponds to d^n separate experiments. For example, a three-dimensional image with 256 pixels per axis implies $256^3 \approx 1.68 \times 10^7$ distinct NMR experiments embedded within a single dataset. Consequently, multiple samples placed within the sensitive volume of the RF coil can be simultaneously encoded and reconstructed. The central challenge is to design acquisition strategies such that each spatial dimension efficiently contributes to the overall data content. One approach to achieve this parallelized acquisition is to associate each voxel with an individual experiment by means of spatial encoding (Figure 3.2).

While **Chemical Shift Imaging (CSI)** bridges the gap between imaging and spectroscopy by retaining full spectral information, conventional MRI experiments lack chemical shift resolution. In MRI, signals from solvent, buffer components, ligands, and proteins overlap because they are distinguished only by their spatial position, rather than by their resonance frequency. To introduce chemical specificity into MRI-based measurements, several strategies have been developed. CSI achieves this by encoding both spatial and spectral dimensions, thereby enabling the reconstruction of a full spectrum for each voxel. However, its requirement for extensive phase encoding and echo acquisitions often leads to long measurement times and reduced spectral resolution. Furthermore, CSI is prone to spectral overlap and highly sensitive to magnetic field inhomogeneity, particularly in multi-voxel settings [45].

One widely used alternative approach is Chemical Exchange Saturation Transfer (CEST), where exchangeable protons are selectively saturated and transferred to water or targeted molecules, thereby amplifying contrast for otherwise invisible metabolites [46]. In addition, hyperpolarization techniques (e.g., dynamic nuclear polarization) greatly enhance the signal intensity of specific nuclei, enabling chemically resolved imaging even at low concentrations [47]. Finally, spectral–spatial pulse designs can suppress unwanted background signals, such as water or fat, thereby improving chemical specificity [48].

In this work, we took advantage of ^{19}F-MRI, which offers a unique advantage, as fluorine

nuclei provide intrinsic chemical selectivity and negligible biological background, allowing direct spatial mapping of fluorinated reporter ligands without the need for additional spectroscopic encoding [49](see more details in Chapter 2.8).

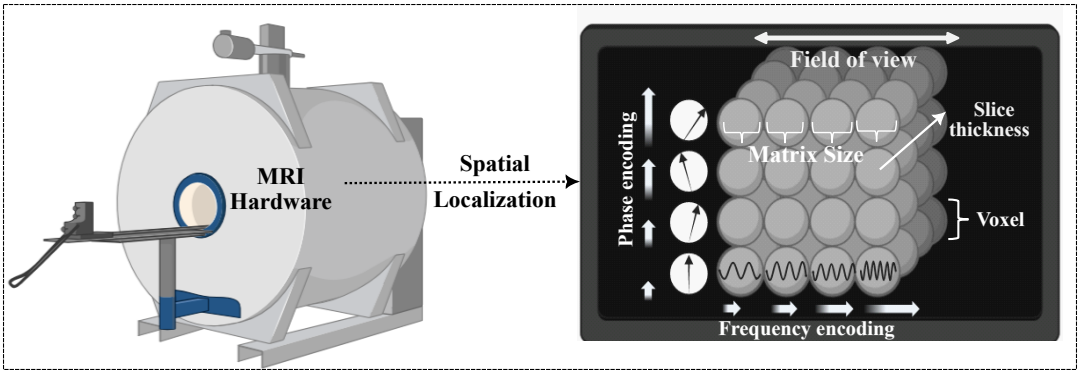

Figure 3.2.: Spatial localization of multiple voxels through gradient field altering. Each voxel can represent an individual experiment. Image parameters of the field of view, matrix sizes, and slice thickness have a direct influence on the image properties.

By introducing purpose-manufactured sample holders that accommodate several samples within the available detection space of the chosen RF coil, parallelization can be implemented directly at the hardware level. When carefully designed with respect to geometry, spacing, and filling factor, such holders ensure that each sample occupies a distinct spatial location corresponding to an individual voxel in the MR image. Spatial encoding thereby transforms the RF coil into a multi-sample detector array, enabling parallelized acquisition without the need for additional receiver channels. In the context of ^{19}F-MRI, the intrinsically background-free nature of fluorine detection allows the focus to be placed on imaging rather than localized spectroscopy, thereby enabling faster acquisition of chemically specific information across multiple samples.

The present chapter focuses on sample-parallelized imaging using optimized holders (NMR tubes and capillaries) and evaluates key parameters including magnetic field homogeneity, sample orientation and spacing, probe filling factor, and signal-to-noise ratio (SNR). These factors are essential for achieving reproducible image contrast and constitute the methodological basis for robust multi-sample MR imaging. Building on these fundamental evaluations with conventional NMR tubes and capillaries, the subsequent section introduces the honeycomb sample holder, which was specifically developed to maximize parallelization by integrating a large number of wells within a single RF coil.

3.2. Molecular imaging setup

Molecular imaging of protein–ligand interactions in parallelized sample arrangements requires an integrative approach. The molecular determinants of signal intensity alterations are dictated by biochemical properties, whereas mechanical and engineering considerations govern the simultaneous acquisition of multiple MR signals within a shared detection volume. For this purpose, multiple sample holders were designed to maximize filling factor, spatial resolution, and signal-to-noise ratio (SNR), enabling reproducible measurements across densely arranged samples.

Contrast agent

For the preparation of water stock solutions of the gadolinium-based contrast agent Magnevist (Diethylenetriaminepentaacetic acid gadolinium(III) dihydrogen salt hydrate; Sigma-Aldrich, 381667) was dissolved in deionized water and subsequently diluted to the desired final concentrations.

The solutions were filled into 5 mm NMR tubes and placed into the NMR sample holders (Figure 3.3).

Protein and ligands

Trypsin from bovine pancreas (Sigma-Aldrich, T9935), 4-(trifluoromethyl)benzamidine (TFBA) (Enamine, EN300-73109), and benzamidine (BZD) (Sigma-Aldrich, 434760) were used as protein, reporter, and competitor ligand, respectively. In the honeycomb setup, additional competitors were employed; however, since their functions are not relevant here, they are discussed separately in Chapter 5. All solutions were prepared in phosphate-buffered saline solution (PBS, 1×, pH 7.4, ThermoFisher, 10010-015) and subsequently diluted to their final concentrations.

For the capillary setup, the solutions were transferred into 2.4 mm OD glass capillaries (CM Scientific) using a microliter syringe (Hamilton Central Europe S.R.L.). The capillaries were then sealed with UV glue (Delo Photobond) to prevent evaporation and contamination.

For the honeycomb setup, the solutions were filled directly into the wells of the holder (Figure 3.5) using a microsyringe, without the need for glass capillaries.

In both cases, custom-built sample holders (capillary array: Figure 3.4 and honeycomb cell array (Figure 3.5) are inserted into the RF-coils prior to acquisition.

3.2.1. Sample holder designs

In order to accommodate the NMR tubes and glass capillary samples employed in this study, a modular sample holder was conceived, designed, and subsequently fabricated from polylactic acid (PLA) using an Ultimaker 2+ 3D printer at Karlsruhe Institute of Technology (KIT) in the Institute for Microtechnology (IMT). Particular emphasis was placed on achieving a geometry that would provide both mechanical stability and reproducible positioning of multiple individual tubes within a compact array, thereby preventing relative

motion or misalignment during the course of repeated experiments and ensuring that systematic parallelized screening could be performed under identical conditions. For the honeycomb cell array, the printing described in its own section.

The design was optimized with respect to the internal dimensions of the radiofrequency (RF) coil (see Figure 3.6) to maximize the filling factor and guarantee long-term reproducibility of the experimental setup. Once assembled, the entire sample holder together with tubes was carefully inserted into the resonator in a horizontal orientation to minimize susceptibility-induced field inhomogeneities along the tube axis, to reduce gravitational bending or displacement of the tubes, and to ensure that each sample experienced uniform B_1 excitation as well as homogeneous detection sensitivity across the array. This careful alignment and stabilization of the sample geometry constituted an essential prerequisite for a quantitatively reliable and reproducible workflow.

NMR tubes

The sample holder with 2.4 cm diameter was designed to accommodate standard 5 mm outer diameter NMR tubes with a usable length of up to 180 mm. The holder contained *five* slots in which the tubes could be inserted vertically and held in fixed positions.

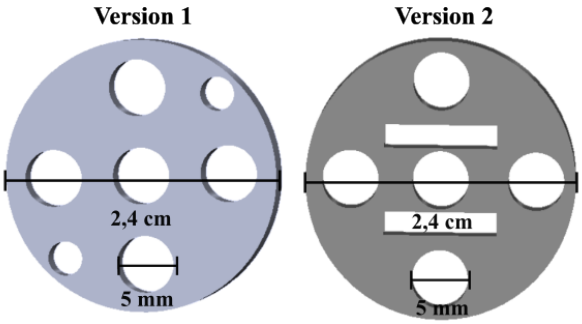

Figure 3.3.: NMR sample holder assemblies for five individual sample tubes in two different designs. NMR tubes were with an OD of 5 mm, and filled with 2.4 mL – 2.6 mL sample volume.

Two different designs (Figure 3.3) were manufactured to ensure both mechanical stability and compatibility with the Bruker 25 mm RF coil and custom-built ^{19}F-coil.

Capillaries

As illustrated in Figure 3.4, for experiments addressing smaller sample volumes than 2.45 mL, a separate capillary holder was designed. This holder accommodated *five* to *nine* thin-walled glass capillaries with an outer diameter of 2.4 mm and an inner diameter of 2 mm. Each cell inside the sample holder provided a tight fit such that the capillaries remained fixed during insertion into the ^{19}F probe. The overall diameter of the capillary sample holder was 14.8 mm.

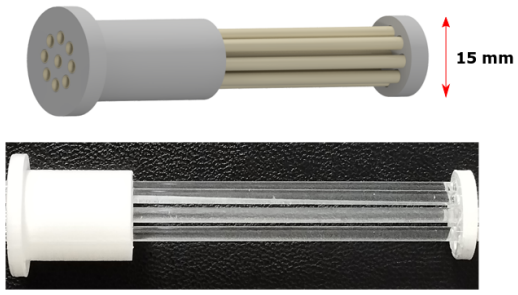

Figure 3.4.: Sample holder assembly for nine individual sample capillaries. Capillaries with an OD of 2.4 mm were filled with 150 µL – 200 µL sample volume.

Honeycomb cell array

The cell array sample holder consists of 61 hexagonally arranged cells, each with an internal diameter of 1.4 mm and a depth of 3.9 mm (calculated for the active signal volume inside of the ^{19}F-coil), separated by 150 µm thick walls. The overall active length of the holder is 14.8 mm, designed to fit within a 15 mm ^{19}F-MRI coil. The sample holder was fabricated by 3D-Druck-Service [50] (Zurich, Switzerland), on a 3D Systems VIPER Si2 printer using Somos Prototherm 12120HT resin.

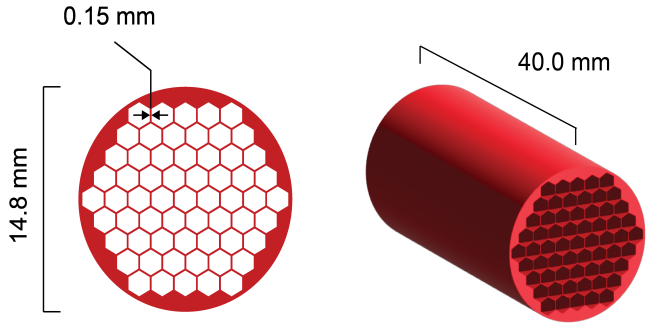

Figure 3.5.: Honeycomb-style cylindrical sample holder design with multiple hexagonal wells for 61 individual samples. Wells were filled with 50 µL – 60 µL sample volume.

3.2.2. ROI analysis

A region of interest (ROI) was drawn over MR images, and their ROIs were analyzed to determine relaxation times using the image analysis function of ParaVision 360 (version 360.3). The ROI calculations were made on magnitude-reconstructed images. The signal-noise-ratio (SNR) values were determined by the single image method according to the National Electrical Manufacturers Association (NEMA) standards [51] i.e., the mean signal intensities in the area of interest (signal ROI) and the background (noise ROI) were quantified and the SNR calculated by dividing the signal ROI by the noise ROI.

Statistical analysis was performed using OriginPro 2023 (Originlab Corporation, Wellesley Hills, USA).

3.2.3. ^{19}F-Hardware

The ^{19}F-MRI measurements were conducted using a custom-designed RF coil operating at a frequency of 612 MHz, which corresponds to the Larmor frequency of ^{19}F in a 15.2 T homogeneous magnetic field. This coil was engineered based on an Alderman-Grant topology due to its inherently low inductance and low electric field. As a result, it features a sufficiently high self-resonance frequency, providing a broad tunability range, making it particularly well-suited for isotopes with high gyromagnetic ratios, such as ^{1}H and ^{19}F.

Following the geometric optimization strategy outlined by Mispelter et al. [52], we fashioned a coil with specific dimensions: a diameter (d) of 15 mm and a length (l) of 21 mm, resulting in an l/d ratio of 1.4. This ratio was chosen to achieve optimized sensitivity, denoted as $B_1/(i\sqrt{r})$, where B_1 represents the field intensity, and r is the coil's resistance. The coil itself is constructed from a 35 µm-thick adhesive copper foil, meticulously wound around a 3D filament-based printed support, produced using a PLA printer (Ultimaker 2+). The constructed coil is shown in Figure 3.6a.

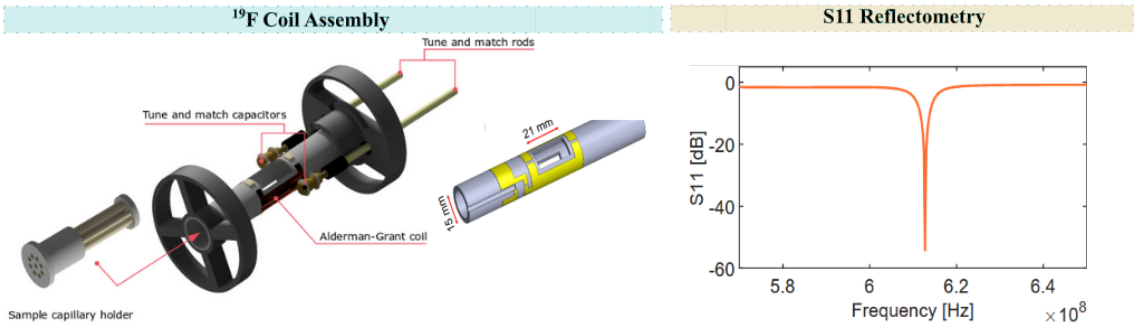

Figure 3.6.: Alderman-Grant coil designed to operate at 612 MHz corresponding to the ^{19}F NMR Larmor frequency at 15.2 T. A 3D-printed coil holder (black) and a sample holder are also shown. The schematic insert above shows the geometry of the coil tracks. The S_{11} reflection curve of the unloaded Alderman-Grant resonator.

To facilitate tuning and matching, the coil was capacitively coupled to a coaxial cable through two high-Q non-magnetic trimmer capacitors (V9000 Voltronics). Figure 3.6b illustrates the S_{11} reflection curve of the unloaded coil, tuned and matched at 612 MHz. In this configuration, the unloaded Q factor registered at 151, which was reduced to 136 when loaded with a 10 mm glass tube filled with distilled water.

3.3. MRI experiments

Initial experiments with ^{1}H-MRI on water paramagnetic phantoms with Magnevist were performed using a Bruker commercial probe to benchmark contrast generation and to validate transversal relaxation–driven imaging under well-defined conditions. Optimization focused on sequence parameters, including echo time (TE), repetition time (TR), and spatial encoding settings to achieve maximal signal contrast between samples with differing relaxation properties. These measurements on aqueous solutions with varying relaxation times provided a systematic framework for optimizing image sequence parameters, image fidelity, and reproducibility.

Subsequently, these optimization principles were transferred to ^{19}F-MRI using a custom-built RF coil. This ensured that the optimization strategies developed in the ^{1}H-MRI test system could be directly applied to the ^{19}F-MRI experiments employed for protein–ligand binding assays, in which reliable discrimination between free and bound ligand states critically depends on both high image quality and robust acquisition conditions.

All ^{1}H- and ^{19}F-MRI experiments were performed using a Bruker 650 MHz (15.2 T) BioSpec imaging system (Bruker BioSpin GmbH & Co. KG, Ettlingen).

^{1}H-MRI experiments of the water phantoms containing different Magnevist concentrations were performed using a commercial Bruker RF coil with a diameter of 25 mm. All ^{19}F-experiments were performed with a 15 mm diameter custom-built ^{19}F-coil. Rapid Acquisition with Relaxation Enhancement (RARE) experiments or Multi Slice Multi Echo (MSME) were conducted to generate transversal relaxation time (T_2) maps. The corresponding imaging parameters are provided in the figure captions.

3.4. Hardware considerations for multi-sample MRI: The role of sample holders

To enable the acquisition of MR images from multiple samples arranged within the sensitive volume of the RF coil, the necessity of employing a dedicated sample holder was systematically evaluated. Although individual NMR tubes or capillaries can, in principle, be densely packed and directly positioned inside the coil, this configuration was investigated specifically to assess whether a dedicated holder is required to achieve reproducible parallelized MRI and to ensure reliable validation of the samples of interest.

For this purpose, five NMR tubes containing paramagnetic relaxation-enhanced water phantoms with different Magnevist concentrations were imaged both in a bundled arrangement without a holder and with the version 1 holder (Figure 3.3). Rapid Acquisition with Relaxation Enhancement (RARE) was used to validate the sensitivity of the holder design by detecting variations in T_2 relaxation, while additional B_1-mapping protocols were applied to assess the homogeneity of signal distribution within the tubes, as shown in Figure 3.7.

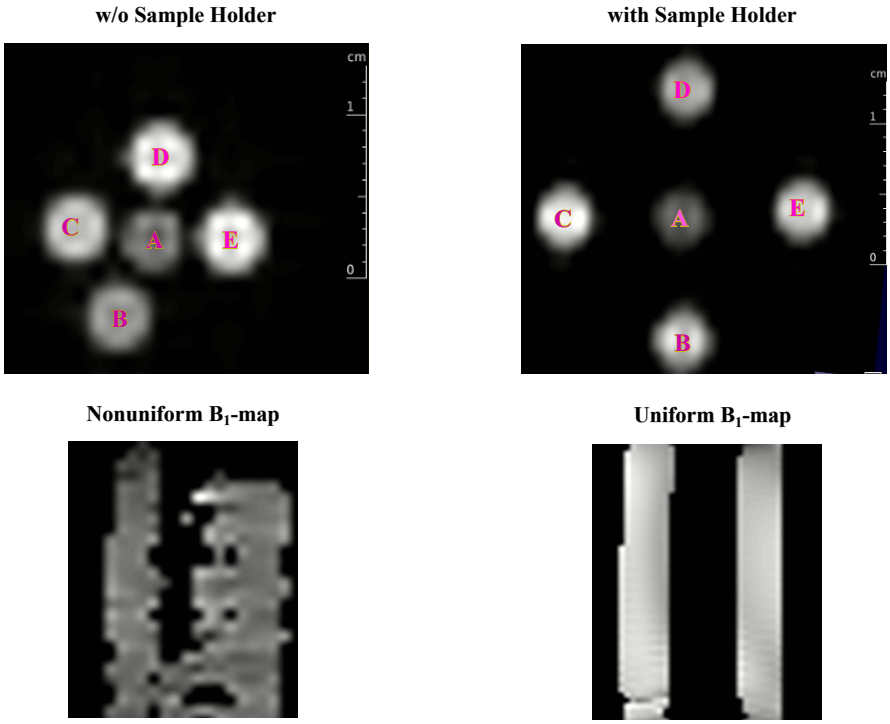

Figure 3.7.: Multiple sample ^{1}H-MR images of contrast-enhanced water phantoms shown for two configurations: bundled arrangement without a sample holder and positioning with the version 1 sample holder. Samples contained different Magnevist concentrations: only water (A), 125 µM (B), 250 µM (C), 500 µM (D), and 1 mM (E). The imaging parameters were FOV 30 mm×30 mm, MTX 64×64, SL 10 mm, TR/TE = 5000 / 100 ms, NEX 1.

The corresponding B_1-maps acquired with the sample holder confirmed homogeneous

excitation and reception conditions with equal distribution across the NMR tubes. In the absence of the holder, however, the B_1 field distribution was inhomogeneous. This effect likely originated from slight misalignment and tilting of the bundled tubes within the coil (before insertion into the RF coil), which altered the local filling factor along the 10 mm imaging slice. Such geometric instability caused spatial variations in the effective B_1 amplitude and, consequently, uneven signal intensity across the samples. This observation demonstrated the necessity of a dedicated sample holder to ensure reproducible field homogeneity.

Utilizing a designed sample holder enabled a reproducible and geometrically defined arrangement of multiple water samples (A–E). Each sample exhibited distinct ^{1}H-signal intensities at a TE of 100 ms, based on the paramagnetic-relaxation enhancement (PRE) effect causing different T_2-decay of the same water sample due to varying amounts of the Gd-based contrast agent Magnevist (for technical aspects, see Chapter 2.5). This configuration also enabled the simultaneous acquisition of multiple relaxation datasets (T_2 mapping) under consistent spatial encoding conditions, a critical prerequisite for high-throughput MRI measurements. Furthermore, it improved experimental efficiency by eliminating repeated manual shimming and reloading steps, while maintaining optimal coil sensitivity through an improved filling factor.

For applications in which the RF coil remains permanently mounted inside the magnet and cannot be removed, another version of the sample holder (Figure 3.3 version 2) was designed. The underlying concept was to insert the NMR tubes from the patient-entrance side of the magnet, provided that the detection volume of the RF coil is well defined. This approach enabled sample loading without disturbing the coil's position, maintaining consistent geometric alignment. Although minor shim adjustments remained necessary after sample exchange, the holder ensured reproducible magnetic field conditions and minimized the extent of re-shimming, while preserving optimal coil tuning and matching.

After testing NMR tubes arranged in a dedicated sample holder, we next explored the use of capillaries to image a larger number of samples simultaneously. For this purpose, another sample holder was developed (see Figure 3.4) for tubes with smaller dimensions than standard NMR tubes, carrying sample volumes of 150 µL – 200 µL. This design increased the throughput from *five* to *nine* samples.

Building on this approach, the final step involved implementing a honeycomb-shaped sample holder, which enabled the parallel imaging of up to 61 samples. With this design, the required sample volume per experiment was reduced to approximately 50 µL. However, the reduction in volume and the closer proximity of individual samples introduced new challenges, particularly with respect to SNR, spatial resolution, measurement time, and the limits of detectable concentration.

It was expected that the reduction in sample volume would lead to a decrease in SNR, which in turn required longer measurement times. Starting from five samples in standard NMR tubes (⊘5 mm, sample volume ≈ 2.45 mL), the transition to nine capillaries (⊘2.4 mm, sample volume ≈ 150 µL – 200 µL) already resulted in an approximately 3–4-fold reduction in SNR due to the smaller voxel filling factor. At this stage, imaging was still performed with a matrix size of 32 × 32 and a FOV of 20 mm × 20 mm to locate two adjacent cells at this spatial resolution.

With the honeycomb design (61 samples, ≈ 50 µL per cell, effective cell diameter ≈

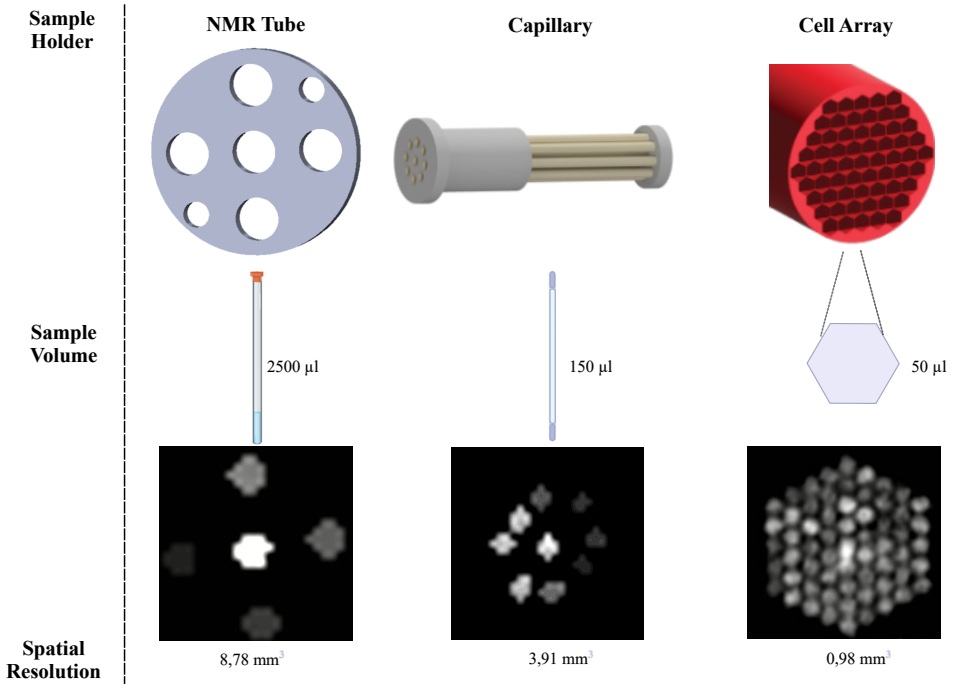

Figure 3.8.: Comparison of different sample holder designs used for multi-sample MR imaging. Illustrations depict holder geometries (top), typical sample volumes (middle), and corresponding MR images (bottom). (Left) Conventional NMR tubes with the MR image with a voxel volume of 8.78 mm^3, TR/TE = 7218 / 100 ms, NEX 20. (Middle) Capillary-based holders accommodate multiple thin-walled glass capillaries, yielding smaller voxel sizes of 3.91 mm^3. (Right) Honeycomb cell array integrating 61 hexagonal wells optimized for parallel acquisition with minimal sample volume, with a voxel volume of 0.98 mm^3. The acquisition parameters for all sample holders were TR/TE = 7218 / 100 ms with one of NEX for NMR tubes, 200 for capillaries, and 400 for honeycomb with different spatial parameters.

1.2 mm), the SNR was further reduced by an order of magnitude compared to the NMR tube configuration. To achieve sufficient spatial discrimination between neighboring cells, the matrix size was therefore increased to 64×64 while keeping the same FOV of 20 mm × 20 mm, corresponding to an in-plane resolution of 312 µm × 312 µm per voxel (compared to 625 µm × 625 µm at 32×32). This increase in resolution, combined with the lower voxel signal intensity, resulted in substantially longer acquisition times. To compensate for these limitations, we employed later undersampling strategies based on compressed sensing (CS), which are described in detail in Chapter 5.

3.5. Rapid imaging pulse sequence selection

To explore the performance limits of different pulse sequences for planned accelerated applications, we evaluated rapid imaging methods using the capillary sample holder for nine samples (Figure 3.4). For this purpose, multi-echo multi-slice (MSME) and turbo rapid acquisition with relaxation enhancement (TurboRARE, T-RARE) experiments (k-space filling comparison in Figure 3.9) were performed with identical numbers of averages (NEX) and matrix sizes (MTX) on paramagnetic relaxation-enhanced (PRE) water samples containing Magnevist.

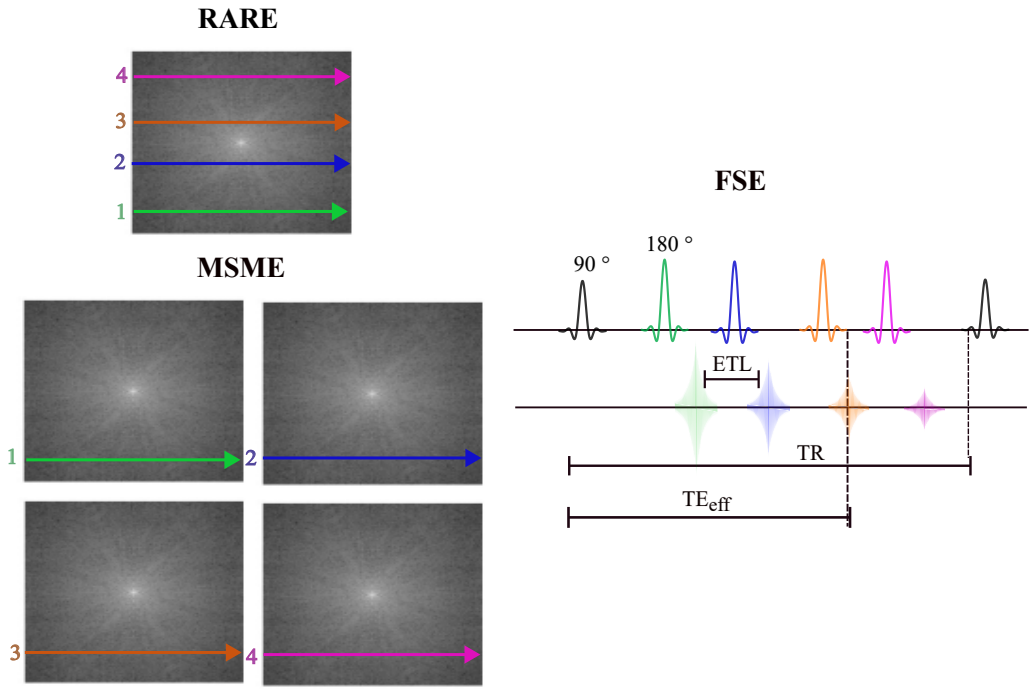

Figure 3.9.: k-space filling of two rapid imaging pulse sequences, Rapid Acquisition with Relaxation Enhancement (RARE) and Multi-Spin Multi-Echo (MSME), using a fast spin-echo (FSE) scheme with the indicated parameters. The echo train length (ETL) denotes the number of spin echoes collected (signals shown with different colors) per repetition time (TR), determining the acceleration factor of the FSE sequence. The effective echo time (T_{Eff}) corresponds to the echo that samples the center of k-space and thus defines the image contrast.

Each Fast Spin Echo (FSE) imaging protocol consisted of a series of images acquired at multiple echo times (TE) to monitor the signal decay of the water phantoms. The voxel-wise signal intensities were fitted to a mono-exponential decay function,

$$S(TE) = S_0\, e^{-TE/T_2},$$

to extract the transverse relaxation time (T_2) of each sample. The resulting T_2 maps served as a quantitative basis for comparing the MSME, RARE, and T-RARE sequences with respect to measurement time, precision, and reproducibility (Table 3.1).

In Table 3.1, the total acquisition time (TA), the maximum measurable echo time, and the relative standard deviation (Std. Dev.) of the three MRI protocols are compared after T_2 fitting of the data shown in Figure 3.7.

Table 3.1.: Comparison of rapid T_2-mapping protocols for identifying an optimal molecular imaging method.

Criteria	MSME	RARE	T-RARE
TA	53 min	6 min	15 s
Number of TEs	> 50	8	8
Overall std. Deviation (%)	1–2	1–6	0.1–6
T_2 of sample C (ms)	935	926	942

The T_2 relaxation times were determined from selected regions of interest (ROI analysis as described in Section 3.2.2). At this stage, the primary objective was to evaluate the effect of different pulse sequences on the accuracy and precision of T_2 estimation, with particular attention to the number of echo times (TEs) available for fitting. Therefore, only the T_2 relaxation results of sample C are reported here. Since the optimized protocol was intended for subsequent protein–ligand experiments, it was also essential to quantify the variability introduced by the choice of pulse sequence.

MSME provided the most stable fitting conditions, as it allowed for a large number of echo times (typically more than 50) distributed across a wide temporal range. This dense sampling stabilized the exponential decay fitting. It minimized sensitivity to noise and ROI selection, resulting in relative standard deviations of 1–2% and a measured T_2 of 935 ms for sample C. However, this higher accuracy came at the cost of long acquisition times (approximately 53 min).

By contrast, both RARE and T-RARE protocols were much faster (Table 3.1) but were inherently limited to about eight usable echo times due to the finite length of the echo train. In RARE, this restriction increased the sensitivity of the T_2 fitting to noise, leading to deviations of 1–6% and a relaxation time of 926 ms. T-RARE, which employs extended echo trains and, in many implementations, variable refocusing flip angles, provided slightly improved precision (0.1–6%) and a relaxation time close to MSME (942 ms), while still enabling rapid acquisition. Nonetheless, the reduced flexibility of TE sampling in both RARE-based protocols occasionally caused larger fluctuations in T_2 estimates, especially under suboptimal ROI placement or handling conditions.

Taken together, these results highlight the trade-off between speed and precision: while MSME ensured robust T_2 fitting, the faster RARE and T-RARE methods significantly reduced measurement time and thus increased throughput. In the following chapters, the choice of pulse sequence was adapted to the experimental objectives, ensuring that the most suitable protocol was applied for each application.

3.6. Spatial image quality optimization

While MSME had been identified in the preceding phantom study as the most robust pulse sequence for accurate T_2 estimation, its suitability for the following applications also depended on its ability to generate sufficient contrast. Good image contrast was one of the key requirements not only for the limit-of-detection (LOD) experiments, but also for resolving differences in signal intensity between multiple MR signals exhibiting similar T_2 relaxation times within the same simultaneously acquired MR image. Achieving such contrast is essential for distinguishing samples under different binding conditions and for ensuring that small variations in relaxation behavior can be reliably detected. The fundamental mechanisms of contrast formation and the influence of imaging parameters on relaxation weighting were already outlined in the theory section 2.5.

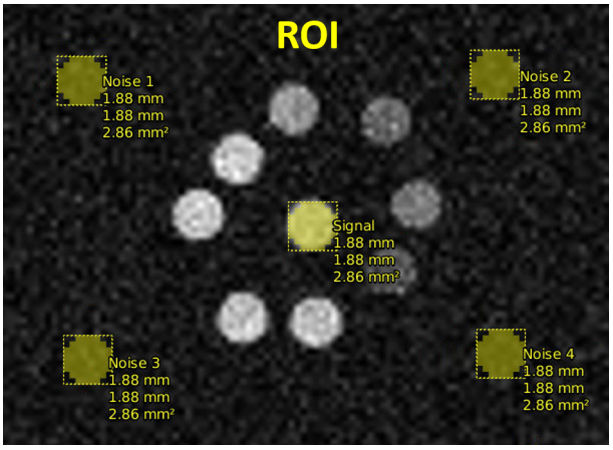

Figure 3.10.: Region of interest (ROI) selection on the MR-image for SNR quantification. Signals acquired in a single MSME experiment, including multiple samples, were chosen as a circular ROI to measure their mean signals separately. Random noise was measured as the average of the chosen four square ROIs located at the corners of the image. All chosen ROI areas were the same and 2.86 mm^2. The imaging parameters were FOV 30 mm × 30 mm, MTX 128 × 128, SL 10 mm, TR/TE = 7218 / 100 ms, NEX 20.

In ligand-binding experiments using fluorine (^{19}F) reporters, such as TFBA, the contrast between the free and bound reporter is especially critical. When a reporter molecule binds to a protein, its local environment changes, leading to restricted molecular motion and consequently modified relaxation properties (as discussed in Chapter 2.8). These relaxation alterations form the basis for detecting binding and displacement events through changes in signal intensity and T_2 reduction of the reporter ligand. These changes allow for the detection of binding and displacement by observing altered signal intensity and T_2 drops of the reporter ligand. So, in this section, in addition to exploring how TE selection, pulse sequence design, number of echoes, and ROI choice influence contrast, we also evaluated optimal imaging quality parameters field of view (FOV), matrix size (MTX), and number of experiments (NEX) with respect to signal-to-noise-ratio (SNR), while ensuring a short overall measurement time.

Prior to further analysis, it was necessary to illustrate the procedure used for SNR quantification based on ROI selection. Figure 3.6 shows representative MR images from nine TFBA binding experiments (content analysis done elsewhere) acquired with the MSME protocol. SNR values were determined as described in Section 3.2.2 following NEMA guidelines. The analysis confirmed that the chosen ROI strategy provided stable SNR values across replicates, with minimal influence of structured background noise.

For the quantification of free TFBA signals, a minimum SNR threshold of 11 was defined. This choice was based on previous quantitative MRI studies, which have shown that exponential fitting of relaxation times becomes unreliable at SNR values below approximately 10, leading to large uncertainties in the extracted parameters [53, 54]. Thus, maintaining SNR ≥ 11 ensured reproducibility and stable fitting of the T_2 values across different binding experiments.

Within this constraint, the following image quality parameters of the MSME protocol were optimized for the best spatial resolution: field of view (FOV), matrix size (MTX), and number of averages (NEX). The impact of these parameters on the total acquisition time (TA) and the resulting SNR was systematically investigated, while slice thickness (SL) and flip angle (FA) were kept constant at 10 mm and 30°, respectively. By repeating the MSME experiments across nine different TFBA binding conditions and monitoring only the ^{19}F signal alterations of TFBA, the optimal imaging parameters for reproducible experiments were identified.

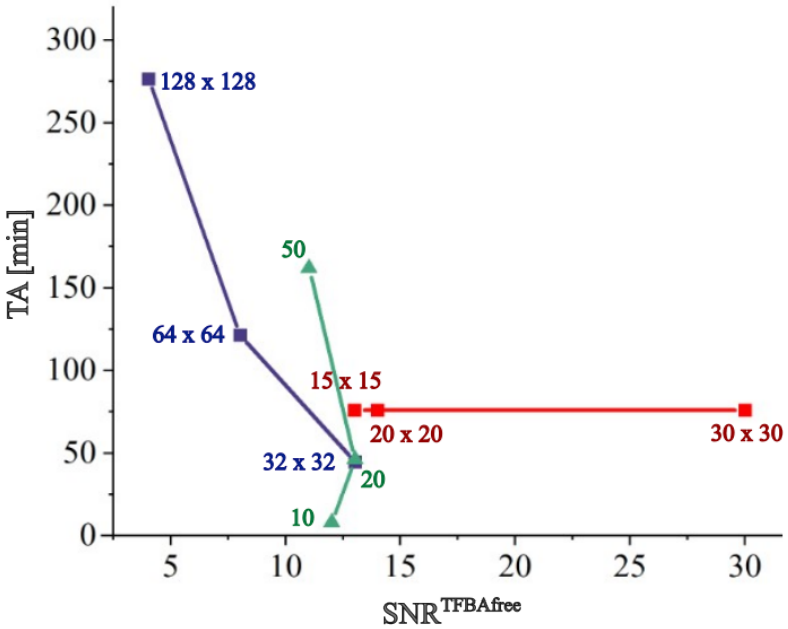

Figure 3.11.: Optimization strategy to balance acquisition efficiency (TA) with sufficient SNR for reliable ligand detection of the free TFBA reporter ligand (^{19}F-MRI). Different matrix sizes (blue) from 32 × 32 to 128 × 128, scan numbers (green) with 10 to 50 NEX, and field of view (red) selection of 15–30 interleaves.

When the MTX was kept constant at 32 × 32, reducing the field of view FOV to 15 mm × 15 mm resulted in smaller pixel dimensions and, consequently, less signal

detected per pixel. This reduction lowered the SNR to 12, which was defined as the minimum acceptable limit. Conversely, increasing the FOV enhanced the spatial resolution, but at the expense of reducing the effective voxel size and thereby constraining the size of the chosen ROI for subsequent analysis.

The voxel volume is defined as

$$V_{\text{voxel}} = \frac{FOV_x}{MTX_x} \cdot \frac{FOV_y}{MTX_y} \cdot SL,$$

where FOV_x and FOV_y denote the field of view in the phase- and frequency-encoding directions, MTX_x and MTX_y the corresponding matrix sizes, and SL the slice thickness. Since SNR scales with the voxel volume, reducing FOV or increasing MTX reduces V_{voxel} and thus decreases SNR.

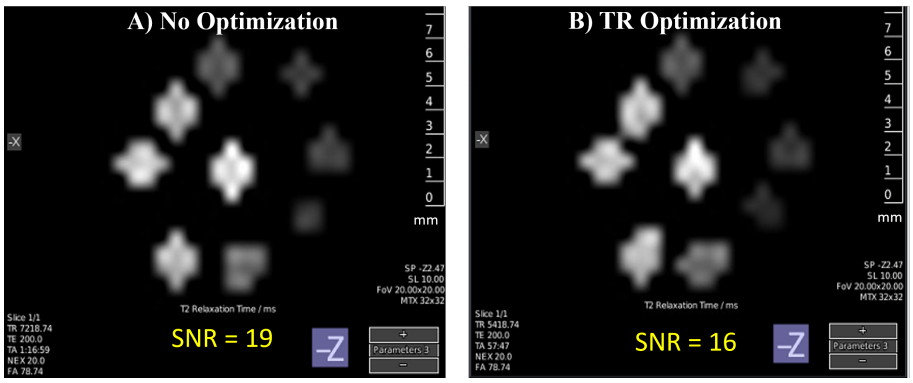

Figure 3.12.: Measurement time optimization by changing the imaging parameter of repetition time (TR). All experiments were collected via MSME protocol. A) Reference T_2-mapping using 9 capillaries reflected in T_2-contrast of different TFBA-trypsin-BA experimental conditions, which are described in chapter 5. B) Optimized imaging time with a TR time of 5 s with the same spatial imaging parameters as A.

Furthermore, increasing the NEX did not yield a substantial improvement in SNR, since the expected gain follows only the square-root dependence

$$\text{SNR} \propto \sqrt{\text{NEX}}.$$

The highest SNR values (above 8) were obtained with a matrix size of 32×32 and a fixed FOV of 20 mm $\times$ 20 mm. This improvement arises because larger voxel volumes contain more contributing spins while the noise level per voxel remains nearly constant, leading to a higher SNR. Conversely, increasing the matrix size reduces the voxel volume, enhancing spatial resolution at the expense of SNR.

Based on these considerations, the optimal imaging parameters to achieve good image quality with the targeted SNR were defined as: MTX = 32×32, NEX = 20, and FOV = 20 mm $\times$ 20 mm. With these settings, the acquisition of T_2-weighted images using 11 echo times required approximately 76 minutes for the capillary setup (Figure 3.8).

In addition to the spatial parameters, the repetition time (TR) was shortened from 7 s to 5 s to reduce the total acquisition time, while TR and flip angle α were kept constant within a dataset (Figure 3.12). For MSME imaging, the time scales approximately as

$$TA \approx TR \times N_{\mathrm{PE}} \times NEX \times N_{\mathrm{slices}},$$

so this adjustment yields a reduction of about $2/7 \approx 29\%$ in TA. Since T_2 was estimated from mono-exponential fits within each dataset,

$$S(TE) = S_0(TR, \alpha)\, e^{-TE/T_2},$$

the change in TR affects only the scale factor S_0 (via partial saturation) but not the decay constant T_2. Consequently, the shorter TR value decreased measurement time with a 1.9-fold acceleration without introducing systematic bias in T_2; any impact was limited to a modest SNR reduction. It was expected, since incomplete recovery of the longitudinal magnetization (M_z) reduces the available signal for each excitation.

In particular, when $TR < 5T_1$, the equilibrium magnetization is not fully restored, leading to partial saturation effects that lower $S_0(TR, \alpha)$. For the present experiments using small flip angles ($\alpha = 30°$), the recovery time required for steady-state magnetization is shorter than the conventional $5T_1$ rule that applies to 90° excitations. According to the Ernst equation,

$$M_{z,\mathrm{ss}} = M_0 \frac{1 - e^{-TR/T_1}}{1 - \cos\alpha\, e^{-TR/T_1}},$$

the longitudinal magnetization reaches more than 95 % of its equilibrium value at approximately $TR \approx 2.5\, T_1$ for a 30° flip angle. Nevertheless, incomplete recovery still reduces the available signal per excitation. The noise level, however, remains essentially unchanged, so the overall SNR decreases while the fitted T_2 values remain unbiased. Despite this signal reduction, the measured SNR remained above our threshold (SNR $\geq$ 11) under the chosen settings (see Figure 3.12).

3.7. Conclusion

Acquiring signals from multiple NMR tubes simultaneously is, in principle, straightforward, with the number of samples determined mainly by the physical dimensions of the RF coil. Yet, transforming this simple idea into a reliable experimental strategy is far from trivial. Without appropriate methods, the transmit/receive B_1 field is distributed unevenly across tubes, leading to inhomogeneous excitation, variable sensitivity, and ultimately a loss of quantitative accuracy [55–57]. Furthermore, conventional pulse sequences are not designed to disentangle superimposed signals and therefore lack the gradient preparation steps required for robust multi-sample acquisition [54, 58].

Introducing MRI principles to resolve signals from different tubes spatially provides a key advantage: signals can be assigned to distinct sample locations with high precision. This approach is not new in principle, since MRI routinely distinguishes tissues within the body. But here, the voxels of an MR image correspond to separate *in vitro* samples rather than biological tissues. What is novel is the application of such contrast mechanisms to ligand-binding studies: instead of probing tissue contrast, the measurement encodes molecular properties such as longitudinal (T_1) and transverse (T_2) relaxation times to screen ligand libraries.

To pursue this concept, our project began with sample-parallelization strategies for how to physically arrange different samples in proximity. Whereas tissues *in vivo* are naturally adjacent, *in vitro* measurements require deliberate design: was it sufficient to place all tubes in a simple bundle, or could a purpose-built sample holder increase throughput while maintaining sensitivity?

Insights from T_2 relaxation measurements on contrast-enhanced water phantoms (using paramagnetic Magnevist) guided the design of an optimized sample holder (Figure 3.3). In these tests, a B_1-map of five bundled NMR tubes revealed pronounced field inhomogeneity, which was attributed to slight misalignment and tilting of the tubes within the coil. Such geometric instability compromised reproducibility and prevented consistent sample positioning, highlighting the necessity of a mechanically defined holder to ensure uniform excitation and detection conditions.

By refining the design, an initial throughput of five samples was expanded from nine to 61 (Figure 3.5) using a honeycomb-shaped cell array that maximized the filling factor, even when used with home-built probes such as our ^{19}F-coil without compromising image quality. This established the first step toward accelerating MRI measurements by simultaneously acquiring signals from multiple samples. With 3D-printing and further miniaturization, the design was adapted to hold up to nine capillaries containing microliter volumes. This parallelization not only shortened measurement times but also reduced material costs and post-experiment waste.

The critical challenge arose when scaling to 61 samples in the honeycomb array. Here, densely packed samples increased the demands on spatial resolution, requiring careful balancing of voxel size, field of view, and SNR. Each sample-holder iteration addressed different requirements of drug-discovery workflows, from basic reproducibility to high-density screening.

Overall, these experiments established the sample holder as a key enabling technology for scalable, high-throughput MR screening workflows. They demonstrated the potential for rapid drug discovery through spatial parallelization on standard MRI systems. The specific acceleration factors achieved are presented in their respective sections later, each reflecting the type of sample holder employed and the underlying biochemical goal.

While the present work focused on hardware-level acceleration via sample parallelization, additional improvements in acquisition efficiency can be realized through data-domain approaches such as sparse or compressed sampling, which are discussed in the chapter 5.

4. Accelerated Drug Discovery

This chapter is based on work carried out in collaboration with Dr. Alvar G. Gossert and has been published [DF1]. The project combined Dr. Gossert's expertise in the design of competitive drug screening with our development of an optimized ligand screening workflow and the determination of compound binding affinities using T_2-relaxation measurements.

4.1. Introduction

The speed of drug discovery is limited by how fast a big library consisting of millions of drug candidates can be screened for activity against biological targets such as enzymes or proteins.

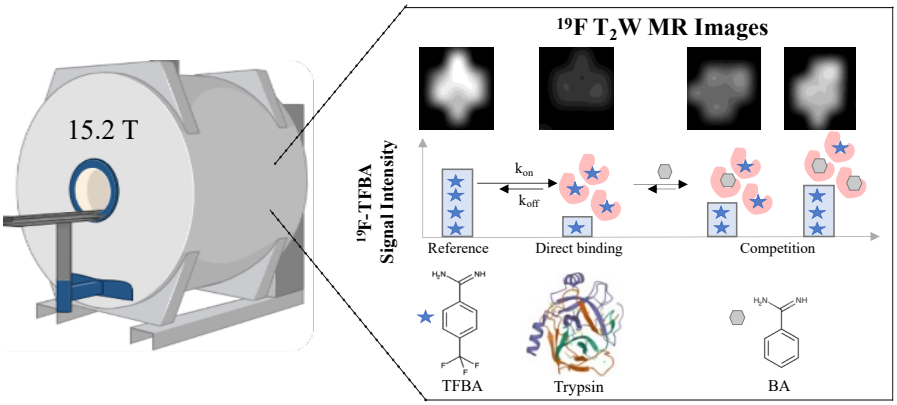

Figure 4.1.: Molecular imaging of protein-reporter and competitor ligand interaction by T_2-weighted spin-echo MR sequence. **Reference experiment)** The T_2-weighted image of observed ^{19}F-reporter ligand-TFBA (blue, star) results in high signal intensity proportional to its long T_2-relaxation time. **Direct binding experiment)** The ^{19}F signal of TFBA signal attenuates together with an increased trypsin (red) concentration due to restricted motion and a reduced T_2. **Competition experiments)** The non-fluorinated competitor ligand-Benzamidine (BA) (gray, hexagon) displaces the reporter ligand TFBA from trypsin, which again tumbles freely in solution and T_2 recovers yielding a bright image. Created with BioRender.com.

Modern drug discovery leverages screening methods such as high-throughput screening (HTS) and fragment-based drug discovery (FBDD) [59]. HTS enables rapid and systematic evaluation of compound libraries to identify hits, i.e., small molecules that interact with disease-relevant targets. These hits serve as chemical starting points for further optimization in lead discovery. FBDD, a complementary approach, relies on smaller libraries of low-molecular-weight compounds, known as *fragments* (typically < 300 Da) [60, 61].

Drugs, aka hits/fragments/ligands, exert their therapeutic function by modulating target proteins such as enzymes, receptors, ion channels, or transporters. Their effects depend on binding affinity, specificity, and mode of interaction, thereby influencing downstream biochemical pathways. Non-covalent interactions govern binding kinetics and pharmacodynamics, while pharmacokinetic properties (Absorption, Distribution, Metabolism, and Excretion-ADME) determine the effective concentration at the site of action [62, 63]. A deeper understanding of the underlying molecular interactions is therefore essential to prioritize promising candidates and to rationalize their mechanism of action. Thus, identified binders are characterized in terms of affinity, binding mode, and specificity.

Meeting these analytical demands requires experimental platforms that can deliver both molecular-level information and sufficient throughput. In this context, the speed, sensitivity, and information content of both HTS and FBDD increase with automation, chemical diversity, sensitive detection technologies, and sample parallelization.

Nuclear Magnetic Resonance (NMR) was among the first biophysical methods introduced into HTS and, in particular, established FBDD. Its ability to detect weak ligand–protein interactions in a label-free manner and to provide both affinity and structural information made NMR the initial workhorse for fragment screening approaches [64, 65].

Aside from its advantages as a ligand screening MR platform, the imaging ability of the MR signal via Magnetic Resonance Imaging (MRI) offers the additional benefit, namely the ability to localize signals from multiple samples within a single measurement spatially. Since each line in k-space of an MR image represents the entire field of view along one spatial dimension, it therefore contains information from all voxels along the orthogonal axis. This mechanism effectively transforms MRI into a massively parallel sampling system, where a single image may encompass approximately one million voxels.

In the context of drug discovery, this raises the intriguing possibility of treating each voxel in an MR image as an individual binding experiment, provided that an appropriate sample and imaging design are implemented. To experimentally realize this concept, suitable sample holder designs are required to accommodate multiple independent ligand–protein mixtures within a single imaging volume. In this way, the intrinsic voxel-parallelism of MRI can be translated into physically parallelized drug screening assays.

MRI is therefore a powerful method for hit detection and quantitative validation of lead compounds in terms of accelerated drug discovery. Unlike many conventional screening techniques, MR-based screening relies on direct, label-free observation of molecular interactions. It may provide a general workflow for evaluating a wide range of drug candidates with varying binding capabilities and modes.

A further strength of MR-based screening is its sensitivity to changes in nuclear relaxation parameters upon ligand binding [15]. A commonly exploited mechanism is the alteration of the ligand's molecular motion: upon binding to a protein, its rotational correlation time increases by up to two orders of magnitude. This change directly correlates

with T_2 relaxation, which can be conveniently monitored in T_2-weighted MR images. In high-throughput applications, such T_2-based contrast enables distinction between free ligands, protein-bound ligands, and displacement by competitor compounds. The reliable detection of these three states is a prerequisite for quantifying binding affinities of unknown drug candidates.

A remaining limitation of conventional proton-based MRI, however, is its insufficient chemical shift resolution, which prevents the differentiation of solvent, buffer components, ligands, and proteins in complex mixtures. This limitation can only be addressed by spectroscopic techniques that preserve chemical shift information, such as localized MR spectroscopy (MRS). In parallel, heteronuclear MRI and MRS extend the accessible nuclei beyond ^{1}H, enabling the investigation of specific biochemical processes in vivo and in vitro.

For example, ^{31}P-MRS allows non-invasive mapping of cellular energy metabolism and pH by detecting phosphate-containing metabolites such as adenosine triphosphate (ATP), phosphocreatine, and inorganic phosphate [66]. ^{17}O-MRI provides direct access to oxygen metabolism and water turnover through the detection of ^{17}O-enriched water molecules [67, 68]. Similarly, ^{15}N-MRS enables the visualization of nitrogen-containing compounds such as amino acids and metabolic intermediates, particularly when combined with dynamic nuclear polarization (DNP) for signal enhancement [69, 70].

Among these, ^{19}F-MRI has gained particular relevance for molecular imaging and drug discovery to track fluorinated reporter ligands with high specificity and quantitative accuracy [71] [DF1]. Several advantages make ^{19}F an ideal nucleus for ligand screening [17, 72]:

- nearly 100% natural abundance,
- most fluorinated ligands contain only one fluorine atom or one CF_3 group, yielding a single sharp resonance,
- negligible background signal in physiological buffers,
- high sensitivity of T_2 relaxation to the chemical environment due to chemical shift anisotropy and exchange broadening.

Together, these properties make ^{19}F T_2-weighted MRI an exceptionally suited approach for detecting protein–ligand interactions. In this work, we exploited these advantages by implementing a fluorine-based competitive binding assay. As a model system, the fluorinated ligand 4-(trifluoromethyl)benzamidine (TFBA, reporter) and the non-fluorinated competitor ligand benzamidine (BA) were studied with serine protease trypsin from *B. taurus* as the target protein. Binding of TFBA to trypsin was detected directly by attenuation of the ^{19}F signal. Subsequent displacement of TFBA by BA enabled quantitative determination of BA affinity in a dose-dependent competition experiment.

By exploiting voxel-based parallelization, a factor of nine in sample parallelization and a three-fold reduction in total measurement time were achieved. This proof-of-principle suggests that complete binding curves (dose-dependent screening) can be recorded in a single parallelized MRI experiment, bridging methodological developments in MR hardware with pharmacological applications in drug discovery.

4.2. ^{19}F-MRI experimental setup

Imaging measurements

Ligand-observed ^{19}F-MRI experiments were carried out with different concentrations of trypsin, 4-(trifluoromethyl)benzamidine (TFBA), and benzamidine (BA), which were prepared as described in Chapter 3.2. All samples were prepared fresh on the day of measurement and stored in a cool transport box. Afterward, nine samples were inserted into a custom-built capillary sample holder (Figure 3.4) prior to acquisition.

All ^{19}F-experiments were performed using a custom-fabricated RF coil with a 15 mm inner diameter, tuned to 612 MHz, corresponding to the Larmor frequency of ^{19}F at 15.2 T. The capillary sample holder, accommodating nine samples arranged on its surface, was used as illustrated in Figure 3.4.

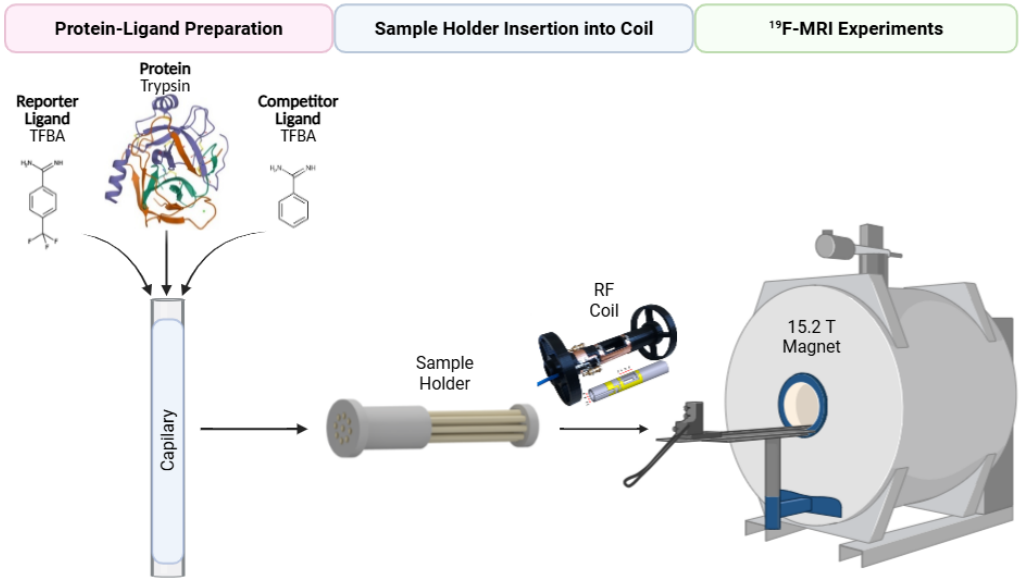

Figure 4.2.: Ligand screening pipeline via ^{19}F-MRI. Sample preparation starts from compounds of interest for protein-ligand experiments to sample holder insertion into the RF coil and MRI measurements acquired in the magnet.

A single FLASH MRI scan was first performed to locate the samples within the holder, followed by T_2-weighted imaging using a standard MSME (multi-slice, multi-echo) sequence used a field of view (FOV) of 20 mm × 20 mm and a slice thickness (SL) of 10 mm, a matrix size of (MTX) of 32 × 32, a repetition time (TR) of 7218 ms, and 20 averages unless otherwise indicated. The representative findings were confirmed in at least three independent experiments.

4.3. ^{19}F Probe characterization

In magnetic resonance signal detection, the signal-to-noise ratio (SNR) directly determines the sensitivity of the workflow and precision of measured relaxation parameters and thus the reliability of binding quantification. The detected signal amplitude scales linearly with the number of nuclear spins within the sensitive coil volume, i.e., with sample concentration, active volume, and coil sensitivity [57, 73]. Consequently, when operating in the millimolar concentration regime typical for ligand-observed assays, the achievable SNR becomes a key limiting factor.

Therefore, in the first step of this work, the ^{19}F-ligand-based workflow was evaluated using a custom-built fluorine coil (see Figure 3.2.3), specifically designed to maximize sensitivity for ^{19}F nuclei and enable reliable signal detection at low reporter concentrations.

In protein–ligand studies, the amount, volume, concentration, and binding affinity of the observed reporter ligand are critical [24]. The lower the required reporter concentration, the less expensive the experimental setup, the smaller the environmental impact. Conversely, if a high concentration of reporter ligand is required, a correspondingly larger amount of protein must be used, which is often the most costly reagent in the assay.

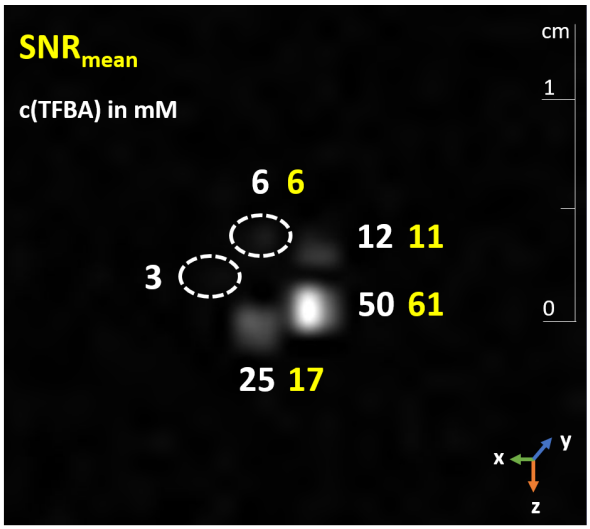

Figure 4.3.: ^{19}F limit of detection of TFBA in a capillary system. Five different TFBA concentrations (white) and their calculated SNR (yellow) values are shown from the FLASH experiment in one acquisition experiment. The imaging parameters were FOV 30 mm × 30 mm, MTX 32 × 32, SL 5 mm, TR/TE = 100 / 4 ms, NEX 200, TA 10 min 40 s. SNR was calculated as described in the Methods section, taking a slice ROI area covering 3.55 voxels, with a volume of 4.4 mm^3 per sample.

In selecting reporter–protein concentrations for competitive ^{19}F ligand-observed assays, the choice of an appropriate reporter is critical (see Chapter 2.8). Dalvit and co-workers systematically analyzed this regime and demonstrated that effective competition assays can be performed with reporter and protein concentrations as low as $[L_T] = [E_T] = 5$–$15\ \mu$M when the reporter affinity is moderate ($K_D \approx 5$–$20\ \mu$M), enabling the detection of

competitors with inhibition constants in the submicromolar range ($K_C \approx 100–500$ nM) [16]. These concentration regimes minimize material consumption while preserving quantitative accuracy and sensitivity.

At equilibrium, the reversible binding of a reporter ligand (L) to a target protein (E) is described by the reaction and dissociation constant:

$$E + L \rightleftharpoons EL$$

$$K_D = \frac{[E][L]}{[EL]}$$

$$E_T = [E] + [EL], \qquad L_T = [L] + [EL]$$

$$\theta_L = \frac{[EL]}{E_T} = \frac{L_T}{L_T + K_D} \quad (\text{for } E_T \ll L_T,\ L \approx L_T)$$

These relations define the equilibrium occupancy θ_L, which increases with ligand concentration for a given K_D. In competition (reporter L vs competitor C), the condition for a measurable displacement is that the observed free reporter fraction changes appreciably; a practical design rule is to choose E_T on the order of L_T (e.g., $E_T \sim 0.5–1 \times L_T$) and L_T comparable to or modestly above K_D of the reporter to maximize sensitivity to displacement [16].

To best exploit MRI parallelization, it was first necessary to identify the concentration regime that yielded sufficient SNR (SNR $\geq$ 11) for the reporter molecule TFBA. As we showed before in chapter 3, good image contrast was one of the key requirements not only for these limit of detection (LOD) experiments but also for resolving differences in signal intensity between multiple MR signals exhibiting similar T_2 relaxation times within the same simultaneously acquired MR image. Achieving such contrast is essential for distinguishing samples under different binding conditions and for ensuring that small variations in relaxation behavior can be reliably detected.

Establishing the LOD for the reporter molecule TFBA was therefore a crucial prerequisite for the subsequent binding experiments, as it defined the minimum detectable concentration that still provides sufficient contrast for quantitative analysis. Thus, a Fast Low Angle Shot (FLASH) protocol was employed to acquire images of five capillary samples containing TFBA at concentrations ranging from 3 mM – 50 mM.

Using the imaging parameters given in Figure 4.3, resulting in voxel volumes of approximately 4.4 µL, it was found that 3 mM TFBA was not sufficient to observe a signal. Conversely, 50 mM was more than sufficient; however, significantly more protein would be needed at this concentration for the binding assay. 25 mM TFBA represented a good compromise between sufficient SNR (17) such that the quantification threshold was achieved (SNR > 10), and reducing the required protein amount for the binding assays.

4.4. Proof of concept: Protein-ligand interaction imaging

In particular, transversal (T_2)-relaxation-driven contrast provides a direct readout of molecular environments, as changes in T_2 relaxation may manifest as grayscale intensity differences across multiple samples in a single MRI experiment. This enables binding states to be assessed simultaneously without additional labeling. By combining indirect, reporter-based competition with the scalability of T_2-weighted imaging (see Chapter 2.9), ligand screening can be performed in a highly parallel and quantitative manner, enhancing both throughput and information content relative to conventional direct detection strategies.

Since this project represents the first ^{19}F-MRI ligand screening protocol in competition mode, the system was designed as a proof-of-concept to evaluate the feasibility of screening non-fluorinated unknown competitor candidates using MRI. To implement this approach, the fluorine reporter TFBA (4-trifluoromethylbenzamidine) was selected for a competition assay in the well-studied trypsin–ligand system (for details Chapter 2.9). The setup also includes benzamidine (BA) as a competitor ligand.

In this case study, the MRI technique combined with sample parallelization via a sample holder was tested as a platform for ligand screening. To establish these principles experimentally, we carried out a quantitative spin-echo imaging protocol (multi-spin-multi-echo, MSME) to extract T_2 values of TFBA in all three regimes (Figure 4.4). The experimental regimes were examined as contrast resources in a single measurement [15, 74, 75]:

1. **Reference experiment** with free TFBA in solution in the absence of the protein-trypsin,
2. **Direct binding experiment** with TFBA in the presence of trypsin, and
3. **Competitive experiments** with the addition of a competitor ligand BA, a known trypsin binder that displaces TFBA.

As expected, the T_2 of TFBA decreased upon addition of trypsin due to binding-induced motional restriction. The measured T_2 decreased by approximately 75%, from 950 ms for free TFBA to 230 ms in the non-competition sample ($T_{2,\mathrm{nc}}$) (Figure 4.4A). In a free solution, TFBA exhibits a comparatively long T_2 because rapid isotropic molecular tumbling efficiently averages out dipole–dipole interactions, thereby minimizing transverse relaxation. Under these conditions, the molecular correlation time is short relative to the Larmor period, leading to reduced spectral density at the resonance frequency and thus slower dephasing of transverse magnetization.

Upon binding to trypsin, the TFBA T_2 decreased by 75% relative to the free reporter (167:1 TFBA:trypsin), yielding $T_{2,nc}$ = 231 ms (nc = non-competition) (Figure 4.4B), consistent with strong binding of TFBA and the expected restriction of molecular tumbling upon complex formation. The fast exchange regime was further confirmed by ^{19}F spectroscopy, which showed a single resonance for TFBA in the presence of trypsin [76].

The single-exponential fit indicated fast exchange between free and bound states, which is advantageous for T_2-weighted imaging assays as the observed relaxation reflects a population-weighted average. Consequently, T_2 values directly correlate with the effective bound fraction, enabling robust and quantitative contrast. Slow or intermediate exchange, by contrast, would result in multi-exponential decay, complicating interpretation.

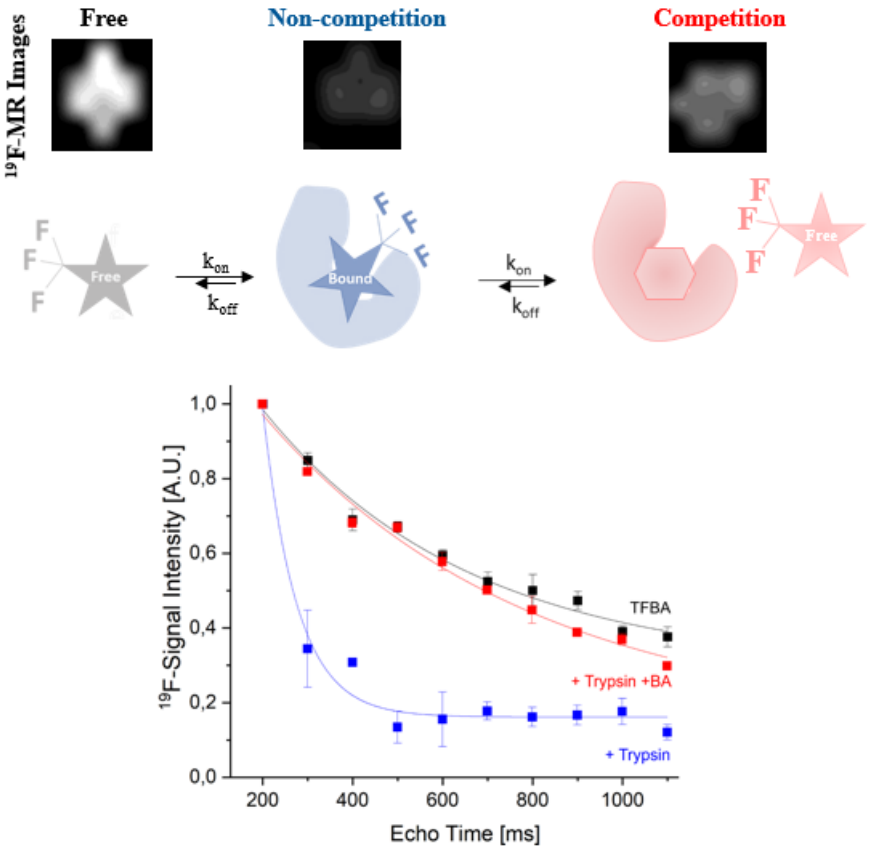

Figure 4.4.: Transverse relaxation time dependence on binding between trypsin and its reporter and competitor ligands, TFBA and BA. Spin-echo intensities extracted from the chosen ROI of the MR-image averaged 20 scans, of 25 mM TFBA obtained in the absence (black) and presence of 150 µM trypsin (blue), and in the presence of both 150 µM trypsin and 10 mM benzamidine (red). T_2 relaxation times were obtained by fitting the mean of three replicate measurements to a single exponential (error bars are ± standard deviation); $T_{2,f}$ = 952 ms, $T_{2,nc}$ = 231 ms and $T_{2,c}$ = 738 ms, (ParaVision) with a fit quality (R^2) of 0.98, 0.98, and 0.97 (originLab), respectively. The corresponding relaxation rates are $R_{2,f}$ = 1.05 s^{-1}, $R_{2,nc}$ = 4.33 s^{-1}, and $R_{2,c}$ = 1.36 s^{-1}.

Upon addition of BA (2.5:1 TFBA:BA), the TFBA T_2 increased to 70% of the free value ($T_{2,c}$ = 740 ms, c = competition), consistent with displacement of TFBA and preferential binding of BA (Figure 4.4C). The contrast arising from reporter displacement adds a further dimension: when BA competed with TFBA, the equilibrium shifted, and TFBA relaxation recovered toward its free-state value.

Together, these results demonstrate that fluorine-based MRI enables both direct detection of fluorinated ligand binding and indirect detection of non-fluorinated ligands via competitive displacement in a parallelized, imaging-compatible format. Detecting such changes in signal intensity and decay speed provides information not only on the presence of binding but also on the relative affinity and competition strength of the ligands.

This principle is particularly important for drug discovery, since most clinically relevant compounds are non-fluorinated (Figure 2.23). By using a fluorinated reporter, binding of non-fluorinated candidates can be inferred indirectly via competitive displacement, thus extending the applicability of ^{19}F-MRI beyond fluorinated ligands alone.

4.5. Direct binding detection

The concept of parallelized MRI-based drug screening is presented in Figure 4.5. For demonstration, two titration series were measured in a single imaging experiment: first, a series of samples with a fixed concentration of TFBA 25 mM and varying amounts of trypsin (Experiments B-E), and second, a series of samples with fixed concentrations of TFBA and trypsin and varying concentrations of the competitor BA (Experiments F-I).

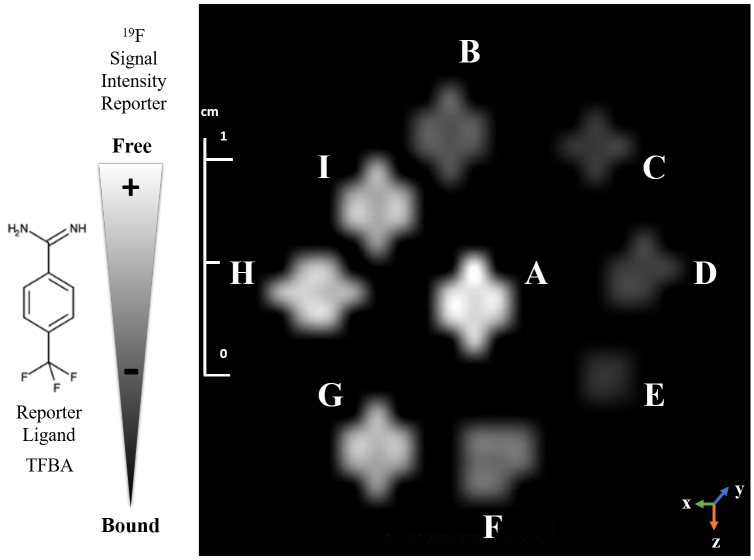

Figure 4.5.: ^{19}F T_2-map of TFBA obtained using MSME. Samples for non-competitive binding to trypsin and competitive binding in the presence of BA were measured in a single experiment. The MSME experiment was a collection of nine samples with 10 echo times, ranging from 200 ms – 1100 ms. Fixed amounts of TFBA (A, 25 mM) were added to trypsin in different concentrations (B-25 µM, C-50 µM, D-75 µM, E-150 µM) for non-competitive experiments. BA (F: 1 mM, G: 10 mM, H: 25 mM, I:50 mM) was then added to the fixed TFBA and trypsin at 150 µM for the competition format. The imaging parameters were FOV 20 mm × 20 mm, MTX 32 × 32, SL 10 mm, TR/TE = 5418 / 100 ms, NEX 20. The full set of 10 echo experiments required 76 minutes. The image displayed was obtained at 200 ms echo time.

The binding of TFBA to trypsin can easily be detected on the plain MR image. The sample of free TFBA was placed in the center of the sample holder (Figure 4.5A). In position B, 25 µM of trypsin was added to the 25 mM TFBA solution (corresponding to a ratio of 1 : 1000 of trypsin : TFBA). The decrease in intensity is clearly apparent on this single T_2 weighted image, thus enabling a quick screening of binders.

The T_2 contrast decreased progressively with rising trypsin concentrations, reflecting the increasing fraction of TFBA bound to the protein. Samples B–E constituted a titration series with trypsin concentrations ranging from 25 µM – 150 µM. Upon binding, the rotational mobility of TFBA became increasingly restricted, which in turn enhanced dipole–dipole relaxation and accelerated transverse relaxation. As a result, the measured T_2 values of

TFBA decreased with protein concentration, leading to reduced signal intensity in the MRI images. At the highest trypsin concentration, up to 60% attenuation of the ^{19}F signal was observed (Figure 4.6).

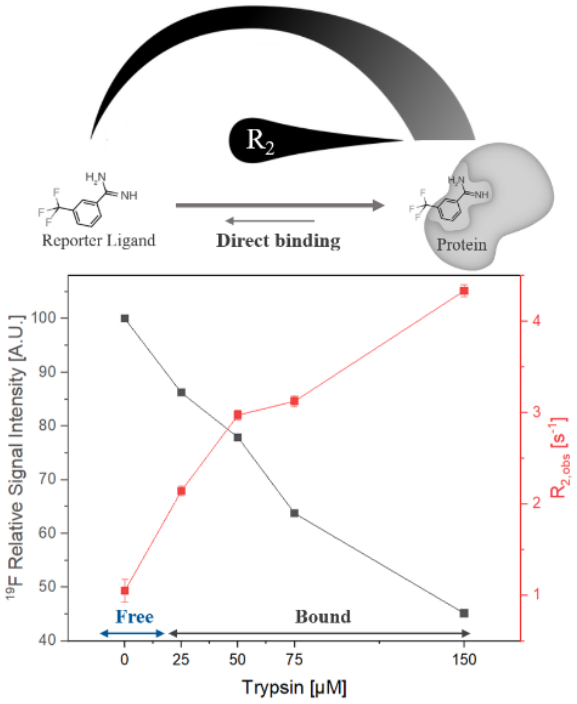

Figure 4.6.: Dependence of TFBA ^{19}F signal intensity (black) and R_2 rates (red) on titrating trypsin ([TFBA] = 25 mM). ^{19}F-signal intensities are normalized with the sample without trypsin.

To enable quantitative comparison across nine samples, the transversal relaxation rates R_2 (= $1/T_2$) were calculated, using sample A (free TFBA) as the reference for intensity normalization (Figure 4.6). Expressing the data in terms of R_2 is advantageous, as relaxation rates add linearly with increasing contributions from binding interactions, thereby providing a more robust measure of the underlying exchange processes.

The TFBA R_2 rates increased approximately 3-fold at the highest trypsin concentration (150 µM), confirming the progressive shift of the equilibrium toward the bound state across the titration series. This clear concentration-dependent relaxation effect demonstrates the sensitivity of the assay to incremental alterations in bound TFBA fraction and provides a quantitative basis for distinguishing between different binding regimes.

4.6. Competition screening

Using ^{19}F MRI in a competitive ligand binding assay has several advantages. Since the reporter ligand is the only source of ^{19}F, there is a direct measurement of its population distribution between bound and free states without background interference. As a reporter ligand has a relatively weak binding interaction (compared to a typical drug), the concentration can be increased so that there is sufficient SNR to obtain MR images in a reasonable measurement time.

The sensitivity to competitor binding becomes relatively high since observation of the competing ligand binding depends on the signal detection limit of a reporter ligand [14]. Consequently, the method requires only minimal quantities of the protein and the competing ligand, since the binding event is not observed directly but detected indirectly through the relaxation changes of the fluorinated reporter. The present study builds upon this concept to enable efficient and material-saving screening experiments.

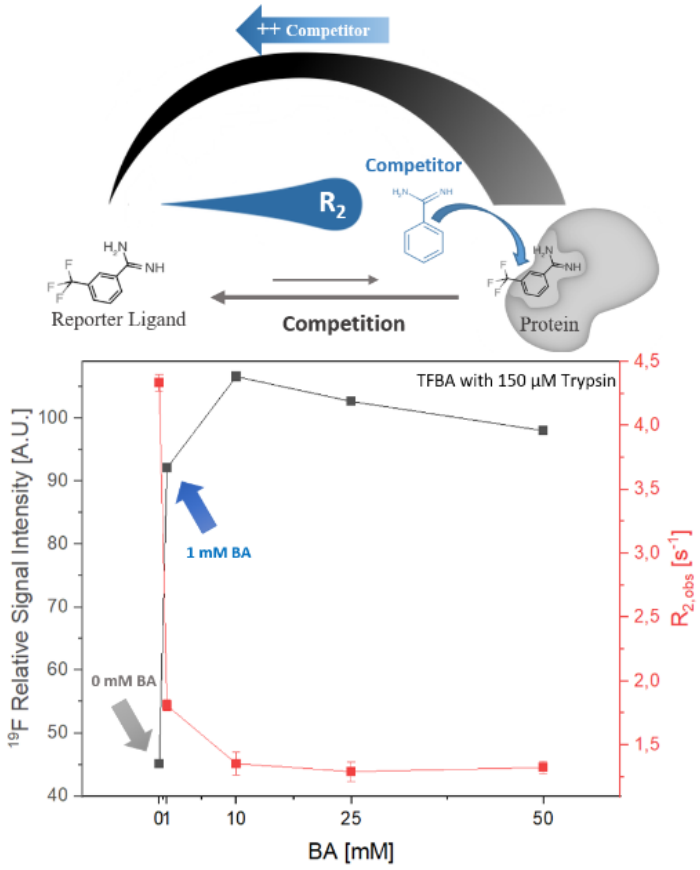

Figure 4.7.: TFBA ^{19}F signal intensity (black) and R_2 rates (red) in the competitive assay. BA was titrated with [TFBA] = 25 mM and [trypsin] = 150 µM. Lines connecting the data points are intended to guide the eye.

Building upon this concept, TFBA showed a pronounced difference in its R_2 between free and trypsin-bound states, providing a sensitive assay window for detecting competitive binding of non-fluorinated ligands such as BA. The highest protein concentration 150 µM

was selected, since it ensured a sufficiently large bound fraction of TFBA and thereby maximized the T_2 contrast between the displaced (therefore free) and bound states. A high occupancy of the binding pocket is essential for competition assays, as it provides both a strong relaxation-driven signal alteration upon displacement and a robust dynamic range for quantifying binding affinities of displacer ligands even in a range of weak displacement.

As seen in Figure 4.7, the ^{19}F-signal intensity of TFBA was recovered from 45% up to 100% when adding the non-fluorinated competitor BA to the solution, as demonstrated in samples F – I (Figure 4.7), where BA was titrated with concentrations ranging from 1 mM – 50 mM.

Even at 1 mM BA, nearly 90% of the ^{19}F signal intensity from TFBA could be recovered, showing that competitors can be screened at much lower concentrations, which would make less soluble compounds accessible to this assay. At higher BA (up to 10 mM concentrations, the apparent recovery of TFBA relaxation even exceeded 100% of the free reference. This effect can be attributed to experimental variability and to the high competitor excess, which may not only fully displace TFBA but also alter the local environment of the reporter, resulting in slightly longer effective T_2 values than observed in the reference measurement.

In agreement with the TFBA signal recovery, increasing concentrations of the competitor BA progressively displaced bound TFBA from the trypsin binding site, shifting the equilibrium toward the free reporter state. Under these competitive conditions, the observed R_2 values decreased from the bound-state value ($R_{2,b} = 4.3\ s^{-1}$) to an intermediate level ($R_{2,c} = 1.3\ s^{-1}$ to $R_{2,c} = 1.8\ s^{-1}$), approaching that of free TFBA ($R_{2,f} = 1.05\ s^{-1}$). This relaxation change was accompanied by a visible whitening of the MR images, as the ^{19}F-signal intensity of the increasingly free reporter increased.

These results confirm that the observed R_2 values in the competitive regime reflect a population-weighted average of the free and bound reporter fractions. Increasing the concentration of the competitor BA progressively displaced TFBA from the trypsin binding pocket, resulting in slower transverse relaxation and increased signal intensity. This continuous R_2 shift serves as a quantitative indicator of ligand displacement and competitive binding strength.

Moreover, the pronounced difference in T_2 relaxation rate and the strong correlation between R_2 and signal recovery-image brightness underline the robustness of the TFBA-based reporter system. Changes in the equilibrium composition lead to detectable variations in quantitative relaxation data, which confirms the suitability of this approach for high-throughput, relaxation-driven binding analysis.

4.7. Affinity determination

The dose-dependent behavior of signal alterations of the reporter ligand observed in the competition experiment and the quantitative outcome of the relaxation data obtained enable calculation of the dissociation constant of the competitor BA (termed K_I to distinguish it from the K_D of the reporter TFBA). The dissociation constant of the competitor BA (K_I) was determined from the fraction of displaced reporter ligand TFBA in the presence of trypsin and under competition with the trypsin competitor BA (F, Equation 4.1). The binding affinity of BA can be determined under the assumption that BA and TFBA compete for the same binding pocket on trypsin, which contains a single primary substrate-binding site. [77]

Displacement (F)-values (in %) were calculated based on the reporter relaxation rates measured in the free state ($R_{2,f}$), under non-competitive conditions with trypsin only ($R_{2,nc}$), and under competitive conditions in the presence of both trypsin and the competitor ligand BA ($R_{2,c}$) [17]:

$$\boxed{F = 100 \times \left(1 - \frac{R_{2,c} - R_{2,f}}{R_{2,nc} - R_{2,f}}\right)} \tag{4.1}$$

With knowledge of the known TFBA dissociation constant ($K_\mathrm{D} = 142\,\mu\mathrm{M}$), [76] the following equation was used to derive K_I for competitor ligand BA [17]:

$$\boxed{K_I = \frac{(100 - F)\,[C]\,K_D}{F\,([L_T] + K_D)}} \tag{4.2}$$

The dissociation constant of the competing ligand yielded $K_I = 5.8\,\mu\mathrm{M}$ at the total reporter ligand concentration (L_T) of 25 mM bound with 150 µM trypsin and in the presence of the competing ligand (C) of 10 mM. The R_2 values obtained from the experiments are given in Figures 4.6 and 4.7.

Importantly, the R_2 alteration upon displacement could be used to extract the dissociation constant of the competitor ligand. This was possible with knowledge of the dissociation constant (K_D) of the reporter ligand TFBA (142 µM), resulting in a calculated K_I of BA $\approx 6\,\mu\mathrm{M}$, which indicates that BA is a relatively strong binder to trypsin. Our value is in good agreement with literature values (13 µM – 16 µM) reported under different conditions using NMR as the analytical method [74, 78].

4.8. Sensitivity and acceleration factor

Using a single multi-slice multi-echo (MSME) experiment for T_2 mapping, 10–11 echo times could be acquired within 58 min (20 scans, $SNR_{overall} = 16$), corresponding to an effective R_2 measurement time of approximately 6 min per sample after TR optimization (see Chapter 3).

In comparison presented in Figure 5.1, a conventional ^{19}F-NMR T_2-relaxation CPMG experiment (10 scans, 11 echo delays, $SNR_{highest} = 23$) required about 18 min per sample at 25 mM TFBA concentration using standard 5 mm NMR tubes.

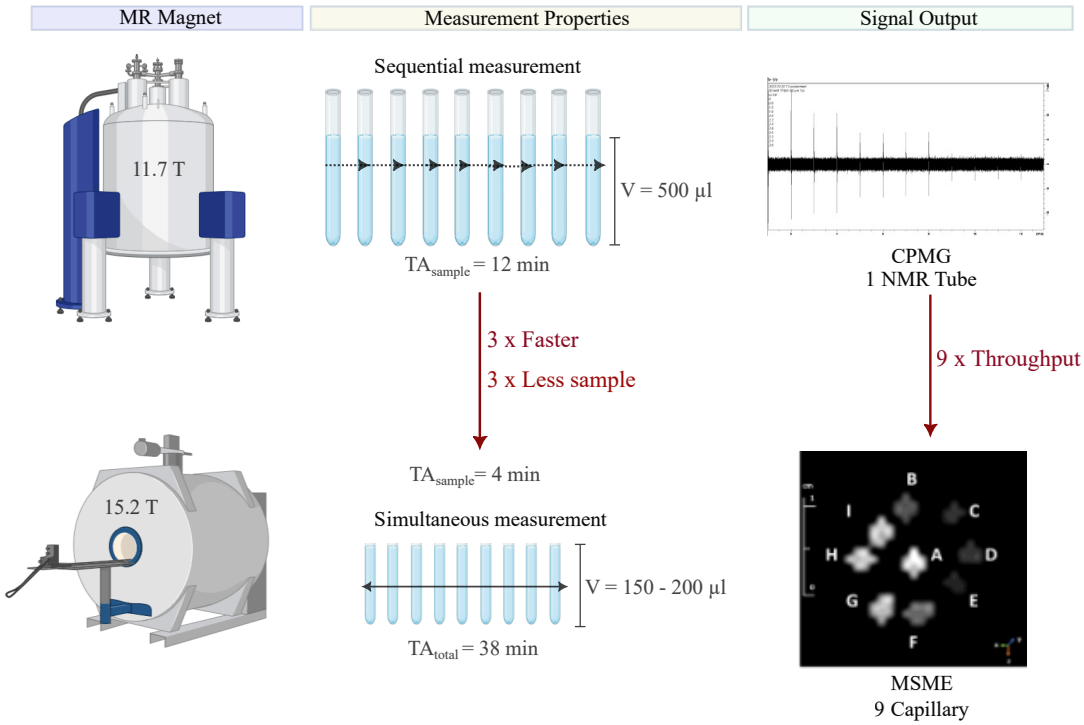

Figure 4.8.: Increased throughput and accelerated measurement via MRI sample parallelization. Imaging and spectral acquisition of samples using different magnets (15.2 T and 11.7 T) with sample preparation (capillary and NMR tube) and resulting MR signal outputs (MR images with nine samples, one spectrum per one sample).

In terms of sample efficiency, the capillary-based setup required only 150 µL – 200 µL of each sample, less than half of the volume typically needed for a 5 mm NMR tube (500 µL). The corresponding voxel volume in the imaging experiment was approximately 4 µL, containing around 300 nmol of ^{19}F nuclei at a TFBA concentration of 25 mM. Even with these small sample volumes, sufficient sensitivity was achieved to detect relaxation-driven signal changes, demonstrating the feasibility of MRI-based ligand screening at sub-micromole scales.

Thus, even without accounting for sample exchange and instrument adjustments, the MRI-based approach provided approximately a threefold reduction in total acquisition time. Moreover, by accommodating nine samples simultaneously, additional acceleration and higher experimental reproducibility were achieved, as all datasets were recorded under identical conditions, minimizing systematic variability.

In the present competitive assay, 1 mM of the competing ligand was already sufficient to recover 90% of the TFBA signal, corresponding to a total of approximately 4 nmol of ligand per voxel. In a high-throughput screening context, only a single concentration of the competing molecule is required to characterize relative binding affinities [16], highlighting the practical efficiency of this approach.

4.9. Conclusion

Previous studies have demonstrated that MRI can be applied to detect ligand binding through various contrast mechanisms. For instance, ^{1}H-MRI has been used to monitor relaxation changes of the surrounding water with fast spin echo (FSE) sequences, [42], and paramagnetic contrast agents have been employed to shorten T_1 by forming chelate complexes around target ligands [43]. Although these strategies provide valuable information on molecular interactions, they typically depend on indirect observation of bulk water or on the use of labeled or chemically modified ligands. Such modifications can alter molecular affinity, reduce water solubility, or limit transferability to other protein systems. Moreover, direct approaches require individual optimization for each new ligand, which restricts throughput and general applicability.

To overcome these constraints, this work established a fluorine-based MRI strategy that detects ligand binding events using a small fluorinated reporter molecule, without requiring any modification of the protein or competing ligands. The assay is fully solution-based and exploits the favorable magnetic properties and high sensitivity of the ^{19}F nucleus while maintaining chemical simplicity and aqueous compatibility. This approach provides an indirect readout of binding interactions through competitive displacement by BA of the bound reporter ligand TFBA to the protein-trypsin: the affinity of an unknown competitor ligand BA was derived from the reduction in reporter–protein binding fraction observed, resulting in measurable changes in the TFBA's transverse relaxation rate ($R_2 = 1/T_2$).

Beyond the demonstration of the displacement principle, the study systematically evaluated how experimental parameters, including echo time (TE), pulse sequence type, number of echoes, and region-of-interest (ROI) selection, affect image contrast and the precision of T_2 quantification. These analyses confirmed that the method achieves sufficient sensitivity to discriminate between free and bound reporter states, to detect ligand-induced displacement, and to quantify relaxation-driven signal differences under identical experimental conditions.

By combining this concept with the intrinsic spatial encoding capability of MRI, nine individual binding experiments could be performed simultaneously within a single measurement. The integration of tailored 3D-printed sample holders in a capillary array geometry with high-field MRI hardware enabled the implementation of these competitive assays in a parallelized format. This design directly exploited T_2-encoded contrast to achieve high sensitivity, enhanced throughput, and robust quantitation of binding events.

Overall, this work demonstrates the feasibility and advantages of spatially parallelized ^{19}F-MRI as a versatile platform for ligand screening. The simultaneous measurement of nine samples within a single scan resulted in at least a threefold reduction in total acquisition time compared to conventional single-sample experiments, highlighting its potential for high-throughput applications on existing MRI systems.

In the following chapter, this competitive ^{19}F-MRI framework is extended by incorporating sparse-sampling strategies to accelerate image acquisition and is applied to quantify the binding affinities of multiple trypsin/CoAD-targeting ligands, thereby demonstrating its suitability for systematic and quantitative drug discovery studies.

5. Highly Parallelized Enzyme Inhibition Imaging via Compressed Sensing

This chapter is based on work carried out in close collaboration with Dr. Alvar G. Gossert and represents a direct continuation of the ligand-screening strategy established in Chapter 4. The results presented here form the core of a manuscript currently submitted for peer review. The focus of this work is the implementation of a miniaturized honeycomb sample holder, enabling a high-density cell array that further increases the experimental throughput achieved previously. In addition to physical sample parallelization, the integration of compressed sensing provided substantial acceleration of the acquisition time, allowing quantitative ^{19}F MRI-based ligand screening to be performed with improved efficiency. Dr. Gossert contributed to the expansion of the ligand library to 55 compounds and coordinated the fabrication, organization of the honeycomb holder, and provided guidance in terms of binding affinity classification.

5.1. Introduction

Time is a critical factor in modern drug discovery, driven not only by the urgency to respond rapidly to global health threats such as pandemics but also by the ongoing need to develop effective treatments for chronic and rare diseases that continue to impact life expectancy and quality of life. The efficiency of drug development pipelines increasingly depends on the ability to generate, analyze, and interpret data with high reproducibility and clinical relevance. Inaccurate or poorly validated data can lead to false positives or negatives, causing significant delays, unnecessary costs, and potential safety concerns in downstream clinical testing.

In recent years, artificial intelligence (AI) and machine learning (ML) tools have transformed the early stages of drug discovery by enabling the rapid analysis of vast chemical and biological datasets. These algorithms can process millions of molecular structures and clinical data points within hours, identifying potential lead compounds and predicting their physicochemical, pharmacokinetic, and pharmacodynamic properties with remarkable speed [79, 80]. Through such computational approaches, AI-guided high-throughput screening (HTS) facilitates the prioritization of candidate molecules before costly experimental validation, significantly accelerating the identification of new therapeutic leads.

While later stages of drug development focus on accurately predicting drug–enzyme interactions in the bloodstream and assessing compound toxicity during preclinical and clinical testing, such evaluations remain challenging. Factors such as metabolic conversion,

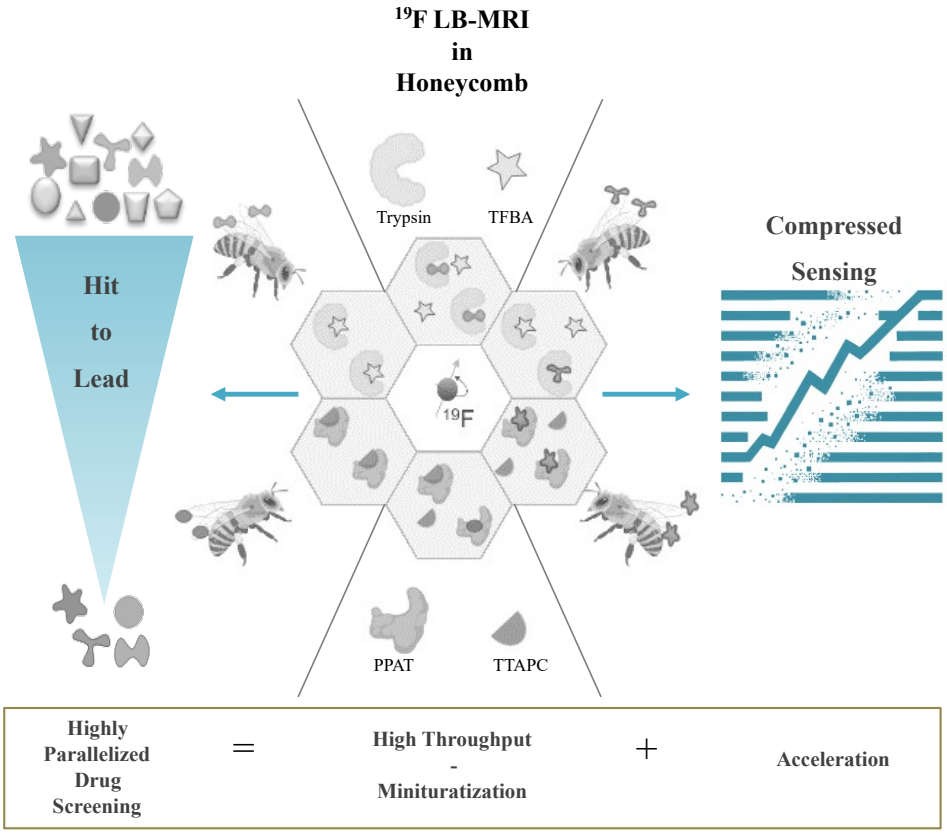

Figure 5.1.: Compressed sensing and miniaturized cell array for highly parallelized enzyme inhibitors screening. ^{19}F-MR imaging is a powerful approach for studying binding mechanisms of non-fluorinated drug candidates by exclusively monitoring the ^{19}F signal alterations of a reporter binder (ligand) in competition mode, interacting with the target protein in a physiological environment. By spatially parallelizing various competitor ligands (drug candidates) within one MR image covering 61 well-isolated cells in a honeycomb sample holder, the validation of potential hits from a library of non-fluorinated drug candidates is straightforward by observing physicochemical parameter motional changes of a ligand upon binding. By adjusting how many data points participate in the experiment, the advantage of the intrinsic redundancy of the MR images can be used to accelerate the drug screening process by utilizing a compressed sensing undersampling technique, without compromising image quality or diagnostic efficiency.

plasma protein binding, and off-target effects often limit the reliability of computational and in vitro predictions. Therefore, high-quality experimental datasets are indispensable for validating these models and supporting the rational design of safer, more effective therapeutics.

In contrast, the early stage of drug discovery is primarily driven by the systematic screening of large and chemically diverse compound libraries to identify initial hits with

specific interactions toward the biological target. Broad early screening maximizes the likelihood of discovering molecules with both high affinity and favorable physicochemical properties, while also capturing multiple binding chemotypes. This enables the derivation of structure–activity relationships (SAR) and provides a robust foundation for subsequent lead optimization.

The various strategies that accelerate the identification of high-quality hits include parallelization, miniaturization, and automation. Several biophysical methods have been established for this purpose, such as surface plasmon resonance (SPR), isothermal calorimetry (ITC), differential scanning fluorometry (DSF), or nuclear magnetic resonance (NMR), which can be used both for initial hit identification and for subsequent affinity determination. However, hardly any of these techniques satisfy all three criteria of high throughput through parallelization, reduced sample consumption through miniaturization, and compatibility with automation. Existing approaches typically suffer from a lack of sensitivity to weak binders (e.g., SPR or enzymatic assays), inherently low throughput (e.g., ITC), or uncertainties in affinity determination (e.g., DSF or X-ray methods) [81–89]. As a result, multiple orthogonal assays are often required to cross-validate results, yet these frequently yield conflicting outcomes because the experimental conditions differ across techniques.

NMR stands out in that it fulfills all requirements essentially: it has the highest sensitivity to weak binding events and is the preferred method for screening of fragment libraries with hits of very low affinity. Although the technique provides direct and label-free detection of molecular binding events, its sensitivity and dynamic range are governed by the kinetics and affinity of the interaction. Ligand-observed NMR methods such as Saturation Transfer Difference (STD) spectroscopy [90], Water–Ligand Observed via Gradient Spectroscopy (WaterLOGSY) [21], and Carr–Purcell–Meiboom–Gill (CPMG) relaxation-filtered experiments [22, 65] are particularly effective for detecting weak to moderate binders (K_D in the micromolar–millimolar range) [64, 91–95], where rapid exchange between the free and bound states produces measurable relaxation or chemical-shift changes. Together, these ligand-observed methods provide complementary sensitivity profiles across different binding regimes, enabling reliable detection of a wide range of affinities. In contrast, protein-observed techniques such as ^{1}H–^{15}N HSQC titrations are more suited for tighter complexes (K_D below 10 μM) but often suffer from line broadening or signal disappearance in the intermediate exchange regime [96].

Therefore, while NMR uniquely enables the identification and characterization of weak interactions that are frequently overlooked by HTS, practical limitations in sensitivity and exchange kinetics still constrain its ability to fully capture both extremes of the binding spectrum. Hardware improvements, isotope labeling, and complementary imaging-based methods such as ^{19}F-magnetic Resonance Imaging (MRI) can help extend this range by enhancing detection sensitivity and throughput.

As described in Chapter 4, MRI leverages spatially resolved MR signals from multiple voxels to encode key biophysical properties, including molecular dynamics, diffusion, and influences of the chemical environment [42, 97–99]. Such parallelized information enables the detection of intra- and intermolecular changes, thereby facilitating the monitoring of protein–ligand interactions. In this context, transverse relaxation–weighted MR imaging can distinguish signal magnitude differences correlated with the tumbling rates of free and bound molecular states, applicable to both ligands and proteins.

Building on this concept, fluorine-19 (^{19}F) ligand-based screening in an indirect competitive mode has emerged as a powerful approach for detecting and quantifying molecular binding events. Here, a fluorinated reporter molecule with low binding affinity is displaced by a non-fluorinated competitor, that is, the lead compound under investigation. Because the transverse relaxation rate of ^{19}F nuclei is highly sensitive to changes in the chemical environment, this method enables the quantification of K_D of unknown competitors through image contrast alterations resulting from reporter displacement [DF1].

Such MRI-based screening provides a direct link between molecular binding and spatially resolved signal readouts, making it particularly attractive for early-stage drug discovery. Validating strong ligands (K_D in the low nanomolar range) targeting specific biomolecular sites offers valuable insights into disease mechanisms and target engagement. Conversely, detecting weak binders with rapid dissociation rates ($k_{\text{off}} \approx 0.1\text{s}^{-1}$) and low binding affinity ($K_D > 100\,\mu\text{M}$) helps characterize transient interactions that may serve as starting points for lead optimization.

At the same time, the practical context of drug discovery is defined by the scale of modern screening efforts, both in terms of the number of molecules investigated and the throughput required to evaluate them efficiently. Typical compound libraries encompass millions of small molecules, a number that has grown with the adoption of combinatorial chemistry [100] in the pharmaceutical industry (e.g., Pfizer: 4 million [101]; BHC, 2.75 million [102]; Novartis, 1.7 million [103]).

Consequently, acceleration strategies rely on optimized pulse-sequence design and efficient manipulation of the *k*-space sampling scheme (see Chapter 2.4). However, to ensure high image fidelity, data acquisition must still comply with the Whittaker–Nyquist–Shannon sampling criterion, which dictates that the sampling frequency must be at least twice the highest spatial frequency contained in the image.

To remind ourselves, the spatial frequencies of the MR signals are sampled in a so-called *k*-space. Traditional MRI studies acquire multidimensional *k*-space data through 1-D free induction decay (FID) or echo signals, which is slow for high-resolution or dynamic imaging. Data sampling is still in sequential order in the frequency encoding (FE) direction, with repetitions at each phase encoding (PE) step, constrained by the T_1 time (e.g., for a living tissue, approx. 1 second). Thus, acquiring 256 PE lines can take approximately 4 minutes for ^{1}H-MRI. The more phase encoding steps are required, the slower the scanning speed. To expedite data collection, alternative methods have been explored.

Undersampling, a common *k*-space manipulation strategy, enables rapid imaging by acquiring fewer data points, particularly in regions of *k*-space that contribute substantially to the image contrast of interest. Because the central region of *k*-space encodes most of the signal intensity and contrast, while the outer regions primarily define spatial resolution, sampling can be concentrated in the center and reduced toward the edges. This structured sparsity allows us to retain the essential MR information required to detect binding-related contrast changes, while significantly shortening the acquisition time.

Radial sampling was an early approach for rapid *k*-space coverage using a non-Cartesian trajectory, densely collecting low-frequency lines in a star-shaped pattern. Such trajectories using time-varying gradient waveforms offer flexibility in sparsity patterns. Echo Planar Imaging (EPI) introduced simultaneous sampling of echo trains in one acquisition step. Subsequently, spiral undersampling techniques collected redundant data in spherical

patterns, aligning scan times with dynamic processes like speech [104].

In conventional MRI, full k-space sampling is typically employed to preserve signal integrity, suppress image artifacts, etc. However, in high-throughput MR screening applications focusing on ligand-binding assays, the objective is binary classification (hit, no hit) rather than high-resolution imaging; thus, exhaustive sampling may not be necessary. Accurate detection of binding events can be achieved using substantially undersampled data by exploiting signal sparsity in an appropriate transform domain (e.g., the wavelet domain). This leads to a more focused question: *what is the minimal extent of k-space sampling required to ensure robust quantification and classification in sparsity-driven MR assays?* In this chapter, this question is examined in the context of affinity screening.

Compressed sensing (CS) is a widely adopted sparsity-promoting method that facilitates undersampling by exploiting low k-t sampling rates (sub-Whittaker-Nyquist-Shannon). Using Cartesian k-space trajectories with random undersampling patterns requires full sampling in the FE direction, allowing redundancy along the PE direction. By acquiring only a fraction of the data (e.g. 32 out of 256 lines), imaging time can be accelerated fivefold. While fewer encoding steps may introduce image distortions due to unmet Whittaker-Nyquist-Shannon criterion [105, 106], reducing high-frequency noise has been shown to mitigate artifacts and improve signal-to-noise ratio (SNR) [107].

Assuming a dataset of N samples, the total number of data points required for reliable reconstruction depends on the frequency characteristics of the signal. If the relevant signal components exhibit an oscillatory behavior with a maximum frequency of m Hz, then, according to the Nyquist criterion, each sample requires at least $n = 2m$ data points in the time domain to be accurately captured. This yields a total requirement of $2m \times N$ data points across the dataset. In the context of k-space acquisition, let s denote the number of acquired k-space points, which corresponds to $2s$ real-valued data points (assuming complex-valued measurements). If the condition

$$2s \leq 2m \times N$$

is satisfied, then the compressed sensing strategy achieves a net reduction in acquisition burden without violating fundamental sampling constraints. This expression thus provides a practical lower bound on the number of measurements needed for successful reconstruction. Additional overhead related to sample handling or system delays can be incorporated into this model to refine acquisition time estimates further.

Predicting the extent of acceleration achievable without compromising image quality or diagnostic relevance depends on selecting appropriate k-space sampling patterns. CS techniques are effective when the necessary data points and their k-space locations are chosen to preserve the relevant image contrast. Given that medical images are highly interpretable in specific transform domains and can be represented sparsely, CS is frequently utilized in medical imaging applications (e.g. 3D abdominal MRI, free-breathing DCE-MRI, 4-D flow imaging) [108]. Hence, the question arises: *Why not take advantage of CS for imaging-based drug discovery as well?*

This chapter of the thesis presents a highly parallel and sparsely sampled hit-to-lead compound screening assay based on a ^{19}F-MRI methodology. The approach combines transverse relaxation measurements with compressed-sensing undersampling to accelerate imaging. By monitoring ^{19}F-signal alterations of the fluorinated reporter molecule 4-trifluoromethyl-benzylamine (TFBA),in competitive binding with 55 non-fluorinated drug candidates arranged in a densely packed honeycomb array, we successfully screened potential inhibitors within a single ^{19}F-MR image acquisition. From this, 13 primary hits capable of displacing bound TFBA trypsin were identified. We then quantified their binding affinities K_C by measuring changes in R_2 relaxation times in a dose-dependent manner, effectively filtering out false positives.

To validate and further characterize weak binders, we constructed a reference library of known TFBA competitors with different binding affinities (low to strong) and compared their binding regimes with weak primary hits. By leveraging undersampling k-space methods, and developing a highly spatially resolved assay using a custom honeycomb sample holder, we were able to significantly reduce imaging time from 18 min[DF1] to 2 min per sample while preserving diagnostic efficiency by monitoring variation in T_2-relaxation times (± 20 ms).

As a disease-relevant case study, we applied our screening workflow to the CoaD encoded enzyme phosphopantetheine adenylyltransferase (PPAT), which is a promising target in the development of a novel class of antibacterial agents [109, 110]. By analyzing the displacement of the fluorinated reporter molecule (1-[3-(trifluoromethyl)-[1,2,4]--triazolo[4,3-b]pyridazin-6-yl]piperidine–4-carboxylic acid (TTAPC), we identified three non-fluorinated inhibitors with differing binding strengths as competitive displacers. This demonstrates the successful extension of our ^{19}F-T_2 relaxation-based drug screening methodology from the well-characterized enzyme trypsin to the more complex, disease-relevant enzyme CoaD encoded PPAT.

5.2. Material and Method

Solution preparation

In this study, two different protein–reporter ligand systems were prepared: trypsin paired with TFBA (trifluoromethyl benzamidine), and PPAT (phosphopantetheine adenylyltransferase) paired with TTAPC (1-[3-(trifluoromethyl)-[1,2,4]triazolo[4,3-b]-pyridazin-6-yl]-piperidine-4-carboxylic acid). While trypsin served as a robust and highly reproducible reference system for method development, PPAT represented a structurally more complex enzyme with more binding sites. TFBA has been extensively validated as a reporter ligand for serine proteases such as trypsin, where it binds in the active site with a dissociation constant that positions the equilibrium in the optimal sensitivity window for competitive displacement. TTAPC was selected because it forms a stable complex with PPAT, maintains solubility under the assay conditions, and exhibits a relaxation profile suitable for quantitative ^{19}F-MRI readout. By applying the ^{19}F-MRI displacement assay to both protein systems, we evaluated the transferability and robustness of the screening approach across different binding environments.

Trypsin-TFBA

Trypsin from bovine pancreas was purchased as a lyophilized powder from Sigma-Aldrich (T9935), and TFBA was obtained from Enamine (EN300-73109). A ligand-protein stock solution of 50 mM of TFBA with 1.5 mM of trypsin was prepared in a PBS buffer (1x, pH 7.4, ThermoFisher, 10010-015), aliquoted, then frozen at −20 °C and stored until further use.

The hydrophilic competitors were prepared in PBS buffer (Table A.2); meanwhile, hydrophobic ones were prepared in different solvents (Table A.1). A 50 mM stock solution of those compounds was prepared for phase 1 and phase 2, aliquoted, frozen, and stored at −20 °C until further use.

PPAT-TTAPC

The *E. coli* protein **PPAT** was prepared as described by Lorz et al. [111]. A solution containing PPAT and TTAPC was prepared by combining a 20 mM TTAPC stock solution (dissolved in 7:8 v/v DMSO:PBS) with a 100 µM PPAT stock solution, and diluting with PBS to obtain the final protein and reporter concentrations. Competitor compounds were added from two categories of stock solutions: (i) PPAT hits 14, 15, and 16 with a final solvent composition of **1:1,5 (v/v) DMSO:PBS**, and (ii) trypsin hits 1, 5, 6, 7, and 12 with a final solvent composition of **1:2,6 (v/v) DMSO:PBS**. In all cases, the protein, reporter ligand, and competitor ligands were combined such that the final PPAT and TTAPC concentrations remained constant across all 61 samples.

Sample loading

The final compound solutions for both protein systems were then filled into two different sample holders: 2.4 mm OD glass capillary (CM Scientific) or the honeycomb sample

holder with a microliter syringe (Hamilton Central Europe S.R.L.). Both ends of the sample holders were sealed by UV glue (Delo Photoband). All samples were freshly prepared on the measurement day and kept in a cooled transport container. They were then placed into a custom-built ^{19}F-coil for data acquisition (probe details in [DF1]).

^{19}F-MRI T_2-relaxation experiments

All ^{19}F-T_2 relaxation experiments were performed on a Bruker 650 MHz (15.2 T) BioSpec imaging system (Bruker BioSpin, Ettlingen) with a 15 mm diameter home-built ^{19}F-coil. Magnetic resonance (MR) images were acquired with RARE (Rapid Acquisition with Relaxation Enhancement) protocol and T_2-mapping experiments were performed using a multi-echo spin-echo (CPMG-type) sequence as implemented in ParaVision 360 (V 3.3). Imaging parameters are provided in the respective figures unless stated otherwise.

Statistical analyses were conducted using OriginPro 2025b (OriginLab Corporation, Wellesley Hills, USA).

Compressed Sensing setup

The compressed Sensed (CS) images were reconstructed directly in ParaVision 360. In the reconstruction interface, the following parameters were used and kept the same for all CS experiments (Figure 5.2). Only the CS parameters of sampling and center area percentage were varied in the resolution card.

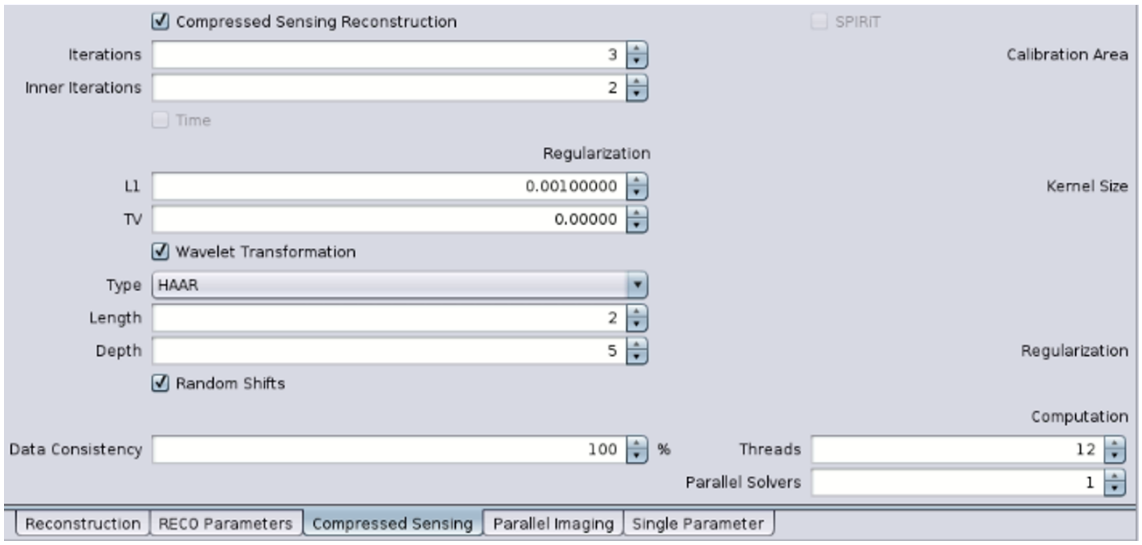

Figure 5.2.: Compressed Sensing reconstruction parameters on the ParaVision interface.

Python code for CS simulation

A custom Python script was employed to generate Cartesian undersampling masks for numerical simulations. These masks were used to systematically vary the center-area

(CA) and overall sampling (S) parameters, thereby illustrating their influence on the undersampling pattern and enabling direct comparison with the corresponding experimental datasets. In this convention, the total sampling fraction is *S%* of all *k*-space points, of which *CA%* are placed in a fully sampled central square and the remainder distributed uniformly at random. The code is attached as in Appendix A.3.

TFBA concentration optimization

In our previous setup in Chapter 4, the reporter ligand TFBA concentration was 25 mM while the trypsin concentration was much lower (150 µM). Under these conditions, the majority of TFBA molecules remained free in solution, and only a small fraction was bound to trypsin.

In the present study, we reduced the TFBA concentration to 5 mM to accommodate a large window of competitor ligands with weak binding affinity ranges by increasing the bound reporter fraction. To reliably detect displacement across a broad range of competitor affinities (K_C), the equilibrium between protein, reporter, and competitor must be tuned to yield partial reporter occupancy [17, 91]. In this regime, the observed ^{19}F relaxation rates represent a population-weighted average between free and bound reporter states, providing maximal sensitivity to changes in binding equilibrium.

If the reporter binds too weakly, only a small fraction will associate with the protein, resulting in low contrast and poor displacement sensitivity. Conversely, overly tight binding prevents measurable release upon competitor addition. Maintaining a moderate fraction of bound reporter (typically 30–70%) ensures that incremental addition of a competing ligand induces detectable relaxation shifts that can be quantitatively related to the competitor's affinity [14]. This adjustment theoretically increases the fraction of TFBA bound to trypsin and thereby enhances the detectable alterations upon competitor displacement of the bound TFBA:

$$\boxed{K_C = \frac{(100 - F)[C]K_D}{F([L_T] + K_D)}}$$

For demonstration, we fitted the estimated K_C values as a function of TFBA concentration while keeping the protein concentration constant (Figure 5.3). Based on these calculations shown in Figure 5.3, the detectable competitor affinity range K_C shifts from approximately 0.3 mM to 1.6 mM by lowering the reporter ligand concentration. Thus, the equation predicts that reducing TFBA expands sensitivity to weaker competitors. However, since the goal of this project is to maximize measurement acceleration, we did not further reduce TFBA concentration, as this would compromise signal-to-noise ratio. For consistency, the binding constants derived from displacement experiments are denoted as K_C, distinguishing them from the TFBA reporter's intrinsic K_D (142 µM).

In particular, this adjustment should improve sensitivity to weak competitors with higher K_C, which would otherwise fail to produce measurable displacement at excess reporter concentrations.

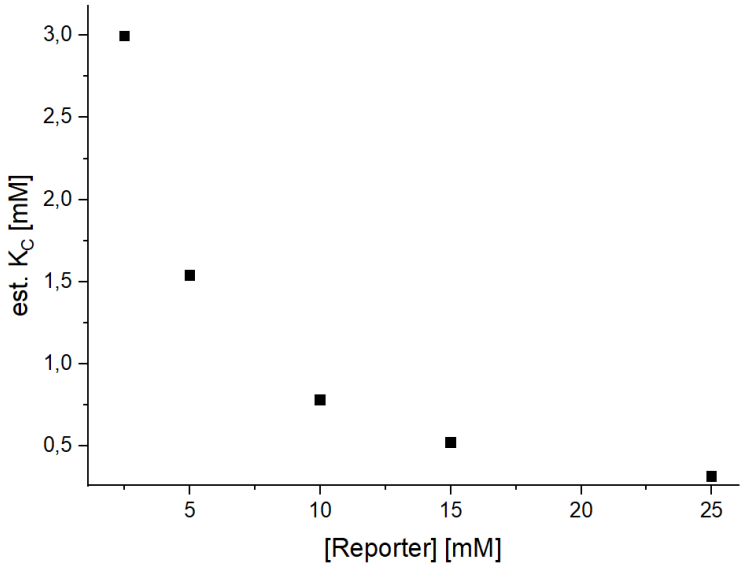

Figure 5.3.: Estimated K_C as a function of reporter ligand concentration

Binding affinity classification

To facilitate interpretation of the competitive displacement assays, competitors were categorized according to their experimentally observed fractional displacement values ($F\%$) using Equation 2.9, where the extracted R_2 values from the ^{19}F-MRI assay were used. Rather than directly comparing the competitor's apparent binding constant (K_C) to the reporter ligand TFBA ($K_D = 142\,\mu M$), the classification relied on the empirically established relationship between $F\%$ and the expected K_C range under the assay conditions ($[L_T] = 5\,mM$ TFBA, $[C] = 30\,mM$ competitor, $[P_T] = 150\,\mu M$ trypsin).

This displacement-based scheme provides a practical and robust criterion to classify competitors without requiring exact K_C extraction in the initial screening step. The numerical rule applied in this study is as follows:

- **Strong:** $F = 99{-}85\%$ corresponding to $K_C = 8{-}140\ \mu M$
- **Weak:** $F = 84{-}65\%$ corresponding to $K_C = 141{-}450\ \mu M$
- **Very-weak:** $F = 64{-}30\%$ corresponding to $K_C = 451{-}2000\ \mu M$

For example, a competitor producing $F = 92\%$ falls into the *strong-binding* regime, whereas one giving $F \approx 70\%$ is assigned to the *weak-binding* regime. Displacement values below 50% indicate *very-weak* or negligible binding. The mapping between F and the corresponding K_C ranges provides the quantitative justification for this classification.

5.3. Miniaturized cell array and sparse sampling

In previous chapters, we demonstrated a ^{19}F-MRI ligand-based assay using a simultaneous T_2 mapping methodology to screen 9 densely localized samples containing three different types of ligand-protein binding in competition mode using a well-studied trypsin (protein)-4-trifluoromethylbenzamidine (TFBA, reporter)-benzamidine (BZD, competitor) system [DF1].

In this work, sample parallelization was increased by employing a further miniaturized honeycomb cell array for ligand screening. The overall goal was to achieve the highest possible throughput and acceleration factor within the available spatial resolution of the custom-built ^{19}F RF coil (15 cm diameter, details in Figure 3.2.3) while maintaining an optimal signal-to-noise ratio (SNR). To this end, several interdisciplinary objectives concerning MRI technique—biochemistry of investigated molecules were pursued:

- **Sample parallelization and undersampling:** Development of a miniaturized honeycomb cell array accommodating up to 61 compounds within the active detection volume of the home-built coil, combined with the implementation of spatial undersampling strategies and compressed sensing reconstruction to increase acquisition throughput while preserving image quality.
- **Optimization of SNR, spatial resolution, and acceleration:** Adjustment of RARE imaging parameters and voxel geometry to achieve the highest feasible acceleration factor (AC), accounting for trade-offs between spatial resolution, reporter concentration, and overall SNR performance.
- **Expansion of the detectable binding-affinity range:** Broadening of the dynamic detection window within the competitive ^{19}F-MRI framework to allow quantitative analysis of both strong and weak competitors, extending into the millimolar (K_C) affinity regime.
- **Extension to complex enzyme systems:** Transition from the well-characterized trypsin–BZD–TFBA benchmark to the structurally and mechanistically more complex CoaD/PPAT enzyme, employing the TTAPC reporter ligand. Thereby, the methodology is validated beyond a model enzyme, demonstrating its potential applicability for broader drug discovery and pharmaceutical screening efforts.

Sample parallelization and voxel size

For the first step towards higher parallelization, the degree of sample parallelization was extended from 9 (in the original work) to 61 using a custom sample holder in a honeycomb shape designed to exploit the readily accessible physical space inside our home-built ^{19}F-coil [DF1].

To ensure optimal imaging resolution and spatial discrimination of individual compartments (cells) within the custom-built honeycomb sample holder (Figure 3.5), the image matrix was optimized without altering the field of view (FOV), as it was already matched to the active detection volume of the RF coil. From an imaging perspective, such spatial resolution is essential to prevent partial-volume effects between neighboring compartments

and to accurately map variations in ^{19}F signal intensity arising from different reporter displacements. Adequate voxel definition ensures that each cell contributes a distinct localized signal, allowing reliable quantification of signal heterogeneity across the array.

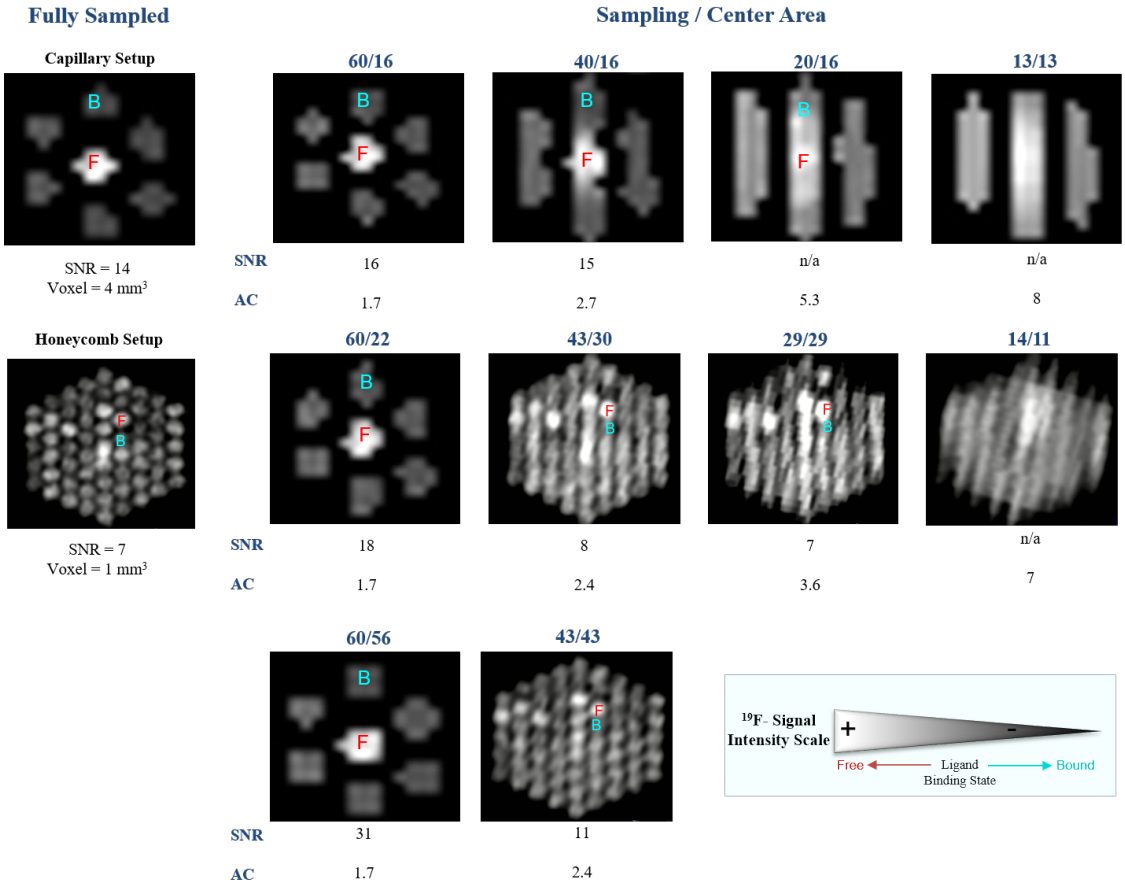

Figure 5.4.: CS parameter optimization on capillary and honeycomb sample holder system using spin echo pulse sequence. ^{19}F-T_2-maps of seven trypsin-TFBA-BZD experiments in capillaries and a 55 compound screen in a honeycomb sample holder are shown. Fully sampled (left column) and undersampled experiments with SNR values are given for comparison. *k*-space sampling percentages and center area amounts were varied and are given over each image, and acceleration factor values together with SNR are given beneath the images. Only two samples are labeled: = F (red) free TFBA and B (cyan) trypsin-bound TFBA. The imaging parameters for the capillary system reference image were FOV 20 mm × 20 mm, MTX 32 × 32, SL 10 mm, TR/TE = 2.5 s / 200 ms, NEX 20, TA 38 min and for the honeycomb sample holder FOV 20 mm × 20 mm, MTX 64 × 64, SL 10 mm, TR/TE = 6 s / 200 ms, NEX 500, TA 2 h. The color bar indicates the ^{19}F signal intensity scale used to visualize the reporter ligand in its free and bound states, allowing direct comparison of relative intensities.

Inadequate resolution would cause signal averaging between adjacent cells, blurring intensity boundaries, and compromising the sensitivity of subsequent analyses, such as competitive binding contrast evaluation [112–114]. As this ^{19}F-MRI ligand screening protocol is designed to operate under undersampled acquisition schemes, minimizing blurring and related artifacts was essential to maintain image fidelity and quantitative reliability.

As a starting point, the in-plane matrix size was set to 64×64 while maintaining a constant FOV of 20 mm, yielding an in-plane spatial resolution of approximately 312 µm. With a slice thickness of 10 mm, this corresponds to a nominal voxel volume of ~0.97 mm^3, which was sufficient to spatially resolve adjacent cells in the honeycomb array that are separated by 150 µm wall thickness (Figure A.1). The chosen resolution thus represents a practical compromise between spatial fidelity, SNR, and total acquisition time within the constraints of the parallelized ^{19}F-MRI setup.

The spatial resolution optimization was performed using a 5 mM TFBA reporter concentration instead of 25 mM, as used in the previous work [DF1]. The rationale for this adjustment was discussed in detail in the previous chapter (Materials and Methods). Since the reporter ligand concentration was reduced, the corresponding protein (trypsin) concentration was also re-evaluated to maintain a detectable binding equilibrium. This adjustment ensured sufficient ^{19}F signal contrast for the quantification of binding affinities of non-fluorinated competitors, where strong signal discrimination is required to assess displacement effects accurately.

Signal contrast optimization

The optimal protein concentration and echo delay time (TE) for the spin echo RARE protocol were determined by investigating the ^{19}F-signal contrast C_{SI} on the MR images using the honeycomb sample holder. By comparing the ^{19}F signal intensity (SI) of the TFBA reporter in the free (*f, free*) and trypsin-bound states (*b, bound*), we calculated the contrast (adapted [24]):

$$\boxed{C_{SI} = \frac{SI_f - SI_b}{SI_b} \times 100} \tag{5.1}$$

Using 5 mM TFBA, a ^{19}F-C_{SI} of 84% was achieved with a trypsin concentration 300 µM. A TE time 200 ms was chosen to ensure large assay windows for competition experiments where the contrast should be greater than 70% [24]. These values were used for single-echo displacement experiments (referred to as Phase 1, primary hit screening) in all experiments unless otherwise described.

Towards undersampling: CS

To accommodate the increased sample density in this work, experimental parameters were updated relative to the previous 9-capillary version[DF1]:

- Reporter ligand TFBA concentration and volume was reduced (25 mM to 5 mM, and 200 µL to 50 µL)
- Acquisition matrix size was increased from 32 × 32 to 64 × 64

These experimental conditions, particularly the 20-fold reduction in reporter concentration, necessitated longer measurement times to maintain sufficient SNR. In the previous chapter 4, the per-sample acquisition time for the ^{19}F-T_2 measurement was approximately 18 min using a conventional NMR setup (measurement per sample, not in a bundle). Implementing the 9-capillary array reduced this measurement time to about 6 min per sample, corresponding to a 3-fold acceleration. With the current honeycomb configuration (61 miniaturized individual experiments under one MR scan), the measurement time was further decreased to roughly 2 min per sample, yielding an overall 9-fold speed-up relative to the conventional single-sample experiment. This additional acceleration became possible through the integration of compressed-sensing (CS) undersampling, which compensated for the otherwise increased acquisition time.

Since the CS technique is achieved by skipping some *k*-space data that are normally acquired, two parameters in ParaVision (Bruker) were optimized for good diagnostic efficiency and image quality: sampling (*S*) and center area (*CA*). The degree of sampling (*S*) altered the total number of phase encoding steps collected relative to the whole *k*-space. By adjusting the parameter center area (*CA*), the distribution of collected *k*-space data points between the central and peripheral regions was optimized (*k*-space visualization of experimental results in Appendix A.2). We investigated the optimal *k*-space undersampling through CS parameter optimization, where image quality was kept as high as possible and extracted T_2-relaxation time deviations were minimized to maintain diagnostic efficiency compared to the fully encoded T_2-weighted images.

As a reference point, multi-echo T_2-relaxation experiments using compressed sensing were first carried out using the capillary system with a larger sample volume (200 µL) to investigate the correlation between the two CS parameters, spatial resolution factor, and the T_2-relaxation time of the observed protein-ligand experiments. To accomplish this, seven capillaries containing 5 mM free TFBA with 300 µM trypsin, and five different BZD experiments ranging over 100 µM – 500 µM were investigated by varying the acquired *k*-space data sampling percentage and center area. In our compressed-sensing T_2-weighted-^{19}F-MRI experiments, *k*-space was acquired with the RARE encoding scheme (order of acquisition), where the phase-encoding lines are distributed across successive echo trains rather than being sampled strictly linearly.

The fraction of *k*-space sampling was varied between 16% and 56% of the central area while keeping an overall sampling of 60%. The results were compared to the $TFBA_{free}$ sample from the fully sampled reference T_2-weighted ^{19}F-MR image carrying 7 capillaries (sample "F" in Figure A.1). The remaining noncentral *k*-space data points were selected randomly in the outer spatial frequencies of the 32 x 32 matrix.

SNR analysis based on the sample denoted "F" demonstrated that an increased number in the central *k*-space region by varying *CA* parameter only changed the SNR values proportionally without impacting the imaging time, since the low spatial frequencies located in this region encode image contrast and smooth structures. In the case of the honeycomb sample holder, less central *k*-space data point collection led to aliasing distortions and caused signal overlapping of the neighboring samples. These artifacts were also observed when fewer phase encoding steps (lower sampling points) were collected. Even though we lowered the *CA* values up to 16%, the blurring appeared only when the *S* was less than 50%, proving the inverse dependency for the Whittaker-Nyquist-Shannon criteria.

By varying *S* between 20% and 60% with a central *k*-space coverage of 16% to investigate the trade-off between *CA* and *S*, we aimed to identify the highest feasible acceleration factor. The T_2-weighted images of sample F exhibited blurring artifacts as *S* decreased to 40%, and the derived T_2 relaxation times showed increasing deviations from 4 ms for 56% *S* to 138 ms when *S* fell below 30%. Although blurring effects were also present at 40% sampling, each experiment's region of interest (ROI) was moderately isolated to allow independent T_2-time analysis, despite minor signal overlap between neighboring experiments. Thus, for both sample holder systems, we could reduce the *S* to 43 % – 40 % with an acceleration factor of 2.7 for the capillary system and 2.4 for the honeycomb system and still perform distinctive ROI analysis on the undersampled ^{19}F-images (Figure A.1). To eliminate signal overlap between neighboring cells for the honeycomb structure, the spatial resolution was enhanced by a factor of 4 compared to the capillary system.

The optimal balance between SNR and acceleration was achieved with 43% coverage of the central *k*-space and *S* of 43% for both sample holders. This configuration resulted in only a minor deviation (approximately 20 ms) in the measured T_2 relaxation time for experiment F while enabling drug candidate screening per sample within just 2 min. Therefore, these CS parameters were applied for the primary hit screening (phase 1) as well as for the binding affinity determination of the lead competitors (phase 2) described below.

5.4. Reference competitor system for weak binders

Low-affinity (K_C over 250 µM) competitors may be mistakenly classified as non-binders when their displacement of the reporter produces only subtle changes in the observed ^{19}F signal, particularly under limited contrast or SNR conditions. In the fast-exchange regime, the measured chemical shift and transversal relaxation rates (R_2) are population-weighted averages of the free and bound reporter states; consequently, the detectable contrast scales with the change in reporter occupancy upon competition adapted from [115]:

$$\boxed{\Delta\theta = \theta_0 - \theta_c = \frac{[P_T]}{K_D + [P_T]} - \frac{[P_T]}{K_D\left(1 + \frac{[C]}{K_C}\right) + [P_T]}}$$

where θ_0 and θ_c denote the reporter occupancy in the absence and presence of a competitor, respectively; $[P_T]$ is the total protein concentration, $[C]$ the competitor concentration, K_D the dissociation constant of the reporter ligand, and K_C the inhibition constant of the competitor ligand. A small $\Delta\theta$ implies that only minor population shifts occur, leading to minimal observable contrast. This situation arises when $K_C \gg [C]$, i.e., when the competitor binds much more weakly than the reporter, or when the reporter–protein complex is nearly saturated ($[P_T] \gg K_D$) [116].

For example, in a TFBA–trypsin system with $K_D = 150\,\mu\text{M}$ and $[P_T] = 300\,\mu\text{M}$, addition of a weak competitor with $K_C = 2\,\text{mM}$ at $[C] = 5\,\text{mM}$ yields:

$$\theta_0 = \frac{[P_T]}{K_D + [P_T]} = \frac{0.3}{0.45} = 0.667,$$

and

$$\theta_c = \frac{[P_T]}{K_D\left(1 + \frac{[C]}{K_C}\right) + [P_T]} = \frac{0.3}{0.825} = 0.364.$$

Thus, the fractional occupancy change is

$$\Delta\theta = \theta_0 - \theta_c = 0.667 - 0.364 = 0.303.$$

In this case, the calculated occupancy change of $\Delta\theta \approx 0.30$ indicates that roughly 30% of the bound TFBA population is displaced by a competitor with K_C = 2 mM at [C] = 5 mM. Although this displacement is biochemically significant, it corresponds to only a modest change in the observed ^{19}F signal. Under the imaging conditions employed here, where spatial undersampling, limited SNR, and relaxation weighting influence contrast, such subtle differences may fall below the visually detectable threshold. As a result, weak or high (micromolar to millimolar) affinity competitors can appear as non-binders in MR images despite measurable interaction at the molecular level.

In practice, even when competitor concentrations are increased, the achievable contrast gain often may remain limited by partial-volume averaging and undersampling-related artifacts inherent to the imaging process. This highlights the need for a calibrated reference library to correlate measured MR contrast with known binding affinities and thereby improve the reliability of affinity classification in parallelized ^{19}F-MRI screening.

To mitigate this challenge and strengthen the reliability of our ^{19}F-MRI hit screening, we further created a reference competitor system using the capillary system with known trypsin competitors for TFBA spanning a range of binding affinities: BZD (strong binder, K_C = 35 µM), BZA (weak binder, 300 µM), and MZA (very weak binder, K_C = 1.5 mM) [117–119]. The capillary sample holder accommodated a larger sample volume (200 µL) compared to a single honeycomb cell (50 µL), thereby improving SNR 4-fold. The strategy was to determine the binding affinities of weak TFBA competitors, estimate detection thresholds for these competitors, and monitor possible aggregation using an optimized capillary system.

Fully encoded, dose-dependent T_2-weighted ^{19}F-MRI experiments were conducted using the same TFBA (5 mM) and trypsin (300 µM) concentrations to establish the reference competitor library for trypsin inhibitors in different concentration ranges (Figure 5.5).

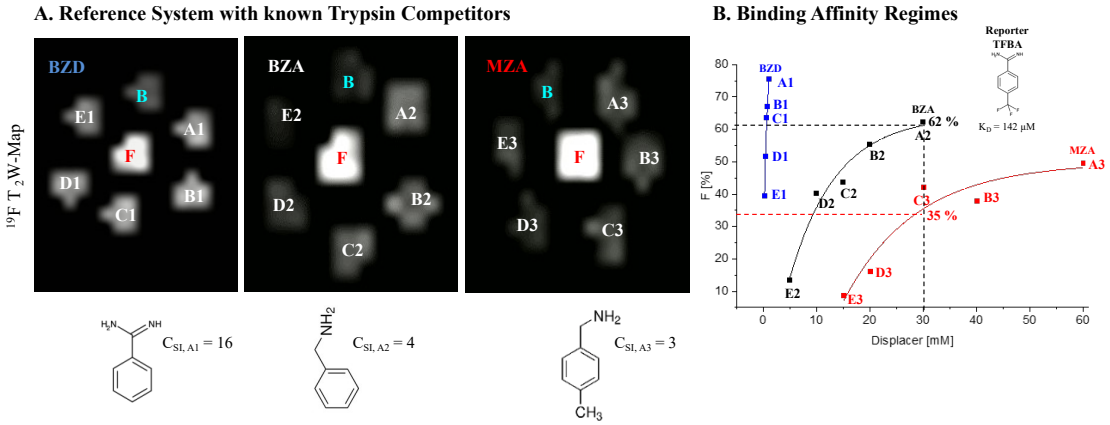

Figure 5.5.: Reference competitor system for TFBA displacement with BZD, BZA, MZA. **(A)** T_2W snapshots of TFBA using fully encoded MSME imaging protocol, competitors at different concentrations (A - F). The competitor molecular structures and calculated signal contrast (calculated between sample A and F for each competitor) are given under the snapshots. **(B)** Displacement percentages (F) of bound TFBA (green) to trypsin (300 µM) are shown as a function of competitor concentrations in a range of (5 mM - 60 mM (white)). The TFBA displacement experiments (A — F in the MR images) are in different concentrations: A indicates the highest competitor concentration and E the lowest. The numbers of experiments correspond to 1 for BZA and 2 for MZA, accordingly. The imaging parameters were FOV 20 mm × 20 mm, MTX 32 × 32, SL 10 mm, TE = 200 ms, NEX 500, TA 2 h – 4 h depending on the TR selection. Voxels correspond to a volume of approx.4 mm^3 per sample. The compressed sensing step was not applied.

^{19}F-signal-based displacement analysis demonstrated detection sensitivity sufficient to distinguish the weak binder BZA and the very weak binder MZA, with a calculated K_C of approximately 1 mM and 200 µM, respectively. In addition to the displacement behaviour, the SNR based on the contrast of the highest displacement (A samples for three competitors) was utilized as an indicator of the practical detectability of competitors with different binding strengths. The strongest competitor, BZD, achieved the highest displacement (75%) at 1 mM, whereas BZA and MZA induced maximum displacements of 60% at 30 mM and 50% at 60 mM, respectively. As the binding affinity decreased (A1 to A3), the fractional displacement became smaller (75% to 50%), which directly lowered the SNR of the displacement readout.

In the reference trypsin system (Figure 5.5), strong competitor BZD produced bright, high-SNR (over 10) free-ligand signals due to nearly complete displacement of TFBA. Compounds with weaker affinity (BZA or MZA) generated progressively lower SNR values because only partial displacement occurred, resulting in reduced contrast between the displaced and protein-bound reporter ligand pools.

This behaviour highlights the intrinsic sensitivity limits of the ^{19}F-MRI screening platform. When the difference between the displaced and the bound reporter fraction becomes too small, the image contrast and SNR fall below the threshold required for reliable quantification. Therefore, characterizing the SNR dependence across strong, weak, and very-weak competitors was essential for identifying the operational detection limits of the system and for defining the affinity regime in which the assay remains robust.

T_2-weighted ^{19}F-MR image contrast in the displacement experiments became distinguishable for all three binding-affinity regimes at a competitor concentration of 30 mM. This concentration was therefore defined as the threshold distinguishing weak and very weak competitors.

5.5. Phase 1 – Highly parallel hit screening

Phase 1 represents the initial step towards the ligand screening workflow and is conceptually analogous to the *hit identification* phase in pharmaceutical drug discovery pipelines. At this stage, a broad set of non-fluorinated potential competitors was evaluated for their ability to interact with the protein by displacing a fluorinated reporter ligand.

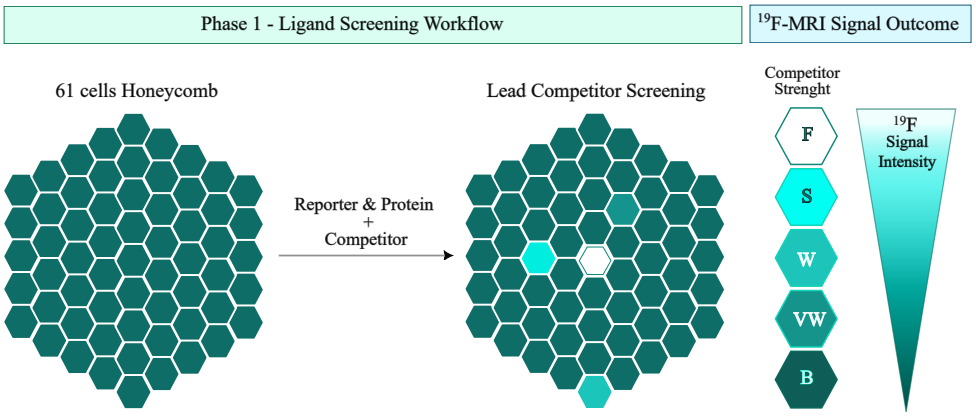

Figure 5.6.: Phase 1 – Hit identification workflow to ^{19}F-MRI read-out based on the reporter ligand's signal alteration. The highly parallelized ^{19}F-MRI assay enables simultaneous monitoring of ligand displacement reactions in a 61-cell honeycomb arrangement. An ^{19}F-MR image of the mixture of fluorinated reporter ligand, target protein via RARE protocol reflects the degree of reporter displacement, which is directly linked to the competitor's binding affinity. Strong competitors (*S*) fully displace the reporter, yielding high signal recovery, whereas weak (*W*) or very weak (*VW*) competitors produce intermediate contrast, and non-binders or control protein bound (*B*) remain dark. The highest signal intensity serves as a reference-free output, which indicates the free reporter ligand.

In the pharmaceutical industry, this corresponds to the *primary screening* step in the early stage of drug discovery, where large compound libraries are systematically tested to identify initial *hits* that exhibit measurable target engagement [120–122]. In this, a parallelized ^{19}F-MRI readout shall enable simultaneous monitoring of the displacement of non-fluorinated competitors against fluorinated reporter ligands within a structured honeycomb array. Each voxel represents one individual binding condition, allowing multiplexed detection of ligand competition events in a single imaging experiment.

The *primary hit screening* aims to narrow down these initial hits by quantifying their apparent binding strength relative to the bound reporter ligand's ^{19}F-signal intensity recovery from the bound state using transversal (T_2) relaxation approach. Compounds that induce near-complete recovery of the reporter belong to the *strong-binding* regime, whereas partial or negligible recovery identifies *weak* or *non-binding* competitors.

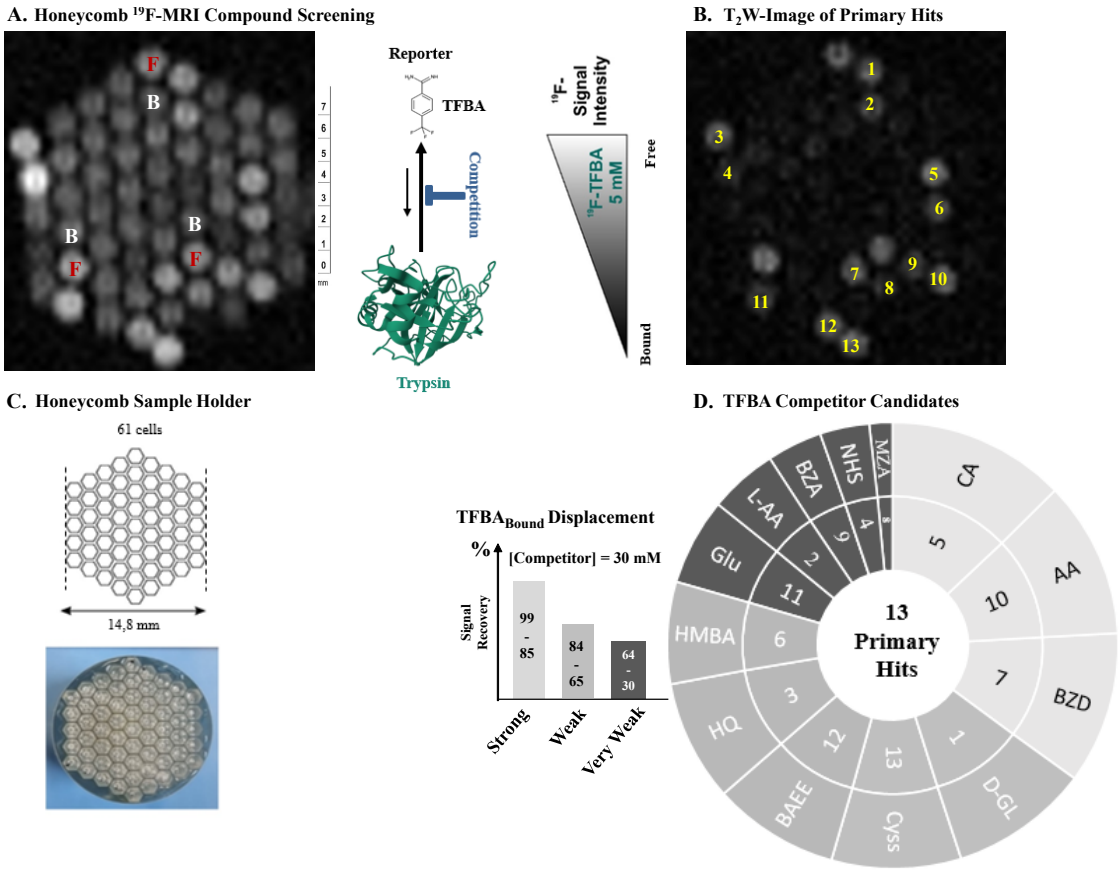

Figure 5.7.: Miniaturized T_2-weighted-^{19}F-MRI compound screening in a honeycomb-shaped sample holder accommodating 61 cells. **A)** Localization of individual experiments in isolated cells representing three binding experiments based on ^{19}F-signal alteration of the fluorinated reporter ligand-TFBA at TE = 20 ms: free TFBA-5 mM (F-red), trypsin-bound TFBA (300 µM trypsin) (white-B), displaced TFBA (not labeled). **B)** Detection of primary hits (30 mM (yellow)) upon displacement based on the ^{19}F-signal recovery of the trypsin-bound TFBA using a spin echo RARE protocol. **C)** Technical details of the honeycomb sample holder and a representative picture of one of the fabricated holders. **D)** Validation of primary hits as competitor candidates based on their displacement strength at TE = 200 ms. All listed chemicals with abbreviations are detailed in table 5.1 and 5.2. The imaging parameters were FOV 20 mm × 20 mm, MTX 64 × 64, SL 10 mm, TR = 2.5 s, NEX 500, TA 2 h 5 min. Voxels correspond to a volume of 0.97 mm^3 per sample. Compressed sensing parameters are 43% sampling / 43% center area. Structure visualization of trypsin (PDB ID: 1TGB).

Once experimental conditions with the amount of TFBA and trypsin (as described in the first section in this chapter) were optimized, a library of 55 compounds was screened to filter primary hits that may displace bound TFBA from trypsin binding pocket. We

included triplicate control samples of free TFBA and trypsin-bound TFBA for signal intensity normalization, bringing the total number of samples to 61. Compound screening was done at 30 mM of competitor concentration, ensuring a large excess was available for weak competitors to cover even a small fraction of a TFBA displacement.

The primary hit screening experiment was conducted using a ^{19}F-MRI *Rapid Acquisition with Relaxation Enhancement* (RARE) sequence, employing two echo times (TE) to visually represent two different states. At the short echo time (TE = 20 ms), the spatial arrangement of samples, positive control (free TFBA), negative control (TFBA bound to trypsin), and various competitor candidates, was visualized, showing the filling pattern of the honeycomb holder (Figure 5.7A). In the T_2-weighted image, the variation in TFBA signal intensities arises primarily from local B_1 field inhomogeneities, which are amplified in multi-echo spin-echo–based acquisitions. Small air bubbles introduced during the sample-loading may process distort the local magnetic susceptibility, producing microscopic field gradients that lead to accelerated dephasing and thereby artificially shortened apparent T_2 effect in affected voxels. Thus, free and bound TFBA samples were marked on the image.

Primary hits were identified using a single-point CPMG experiment (TE = 200 ms) where T_2 contrast alterations were assessed. By increasing the TE time to 200 ms, we have recorded also the signal recoveries of the bound TFBA done by the displacement of competing compounds as brighter images. 13 primary hits from 55 compounds were identified based on the fraction of reporter ^{19}F-signal recovered (Figure 5.7B, yellow). The fraction of signal recovered was calculated by taking the ratio of the displaced ^{19}F-signal to the free TFBA ^{19}F-signal, where the displaced TFBA was the difference between the ^{19}F-signals in the displaced and bound states.

Hits were grouped into three affinity categories (strong, weak, very weak) according to their signal recovery: **strong** binders (99-85%, **weak** binders (84-65%, and **very weak** binders (64-30%). This classification guided further quantitative affinity determination (numerical details in Material and Method section).

The strongest displacement of bound TFBA, corresponding to a signal recovery of 70–99%, was observed for compounds **1**, **5**, **10**, and **13**, all of which contain hydroxyl-bearing functional groups, as well as for the known trypsin inhibitor **7** (benzamidine). The pronounced restoration of the ^{19}F signal in these cases reflects near-complete release of the reporter ligand from the binding site, indicating with high-affinity competitive binding. Those hits have hydroxyl moieties which suggests a common interaction motif, likely involving hydrogen bonding with residues of the trypsin S1 binding pocket or the catalytic triad (His57, Asp102, Ser195) [123–125]. Such polar interactions have been widely reported to stabilize non-covalent complexes with serine proteases and contribute substantially to ligand affinity and specificity.

Hits **3**, **6**, and **12** yielded intermediate signal recovery above 50%, indicative of partial reporter displacement and hence classified as *weak binders*. In contrast, hit **8** showed only minimal recovery of 13%, comparable to hits **2**, **4**, **9**, and **11**, which were thus categorized as *very weak competitors* (Figure 5.7D). The remaining 42 compounds exhibited no detectable change in the ^{19}F signal relative to the negative control and were therefore assigned as *non-binders* under the present assay conditions.

5.6. Phase 2 – Affinity determination of trypsin lead competitors

A Phase 2 assay was established to differentiate true binders as lead competitor from the 13 primary hits identified in Phase 1 by employing a dose-dependent competition format. In this secondary screening stage, the reporter displacement was monitored across a range of competitor concentrations to extract quantitative binding information and validate hit binding affinity. This step is critical in early-stage drug discovery, as it enables the identification of *false positives* and *aggregation-based artifacts* that can compromise initial screening outcomes [15].

False-positive hits typically are detected as binders due to non-specific assay effects such as colloidal aggregation, compound precipitation, or indirect signal interference rather than accurate molecular recognition. Aggregation in particular can enclose the target protein and artificially induce apparent reporter displacement or inhibition, leading to steep, non-saturable dose–response curves [126, 127].

Within the MRI-based assay, these phenomena can be recognized by an atypical or non-monotonic signal–concentration relationship or irreproducible signal recovery across repeated measurements. By integrating the dose–response design, only ligands that display a consistent, concentration-dependent restoration of the free-state ^{19}F signal are advanced as *lead competitors*. This validation step ensures that the screening outcome reflects genuine competitive binding rather than non-specific or aggregation-driven effects.

TE time selection

For this purpose, T_2-relaxation time alterations of the trypsin-bound reporter TFBA ^{19}F-nuclei were monitored upon the addition of 13 hits in a titration series, using identical sample preparation and imaging parameters to phase 1 except for the TE time window. A broader TE series ranging from 20 ms to 1100 ms (7 echo points, RARE factor of 9) was used to sample the full signal decay curve, allowing a more accurate and noise-robust fit of the T_2 relaxation constant compared to the two-point estimation in screening.

Competitor concentration choice

The hit concentration series for Phase 2 measurements was defined based on the TFBA ^{19}F signal recovery profiles obtained in the phase 1 screening, which classified compounds into strong, weak, or very weak competitors. Benzamidine (BZD, hit **7**) served as a reference inhibitor representing the strong-binding regime, with a known binding affinity of approximately 6 µM [DF1]. Accordingly, compounds exhibiting recovery amplitudes comparable to BZD were evaluated over a concentration range of 500 µM to 10 mM. This interval was sufficient to cover the expected displacement behavior of high-affinity competitors, while avoiding unnecessarily high concentrations that could induce aggregation or nonspecific relaxation effects. Owing to the pronounced displacement observed for these ligands, concentrations beyond 10 mM were not required.

Weak and very weak competitors, in contrast, required higher test concentrations to achieve measurable reporter displacement. For such compounds, titrations were performed up to the solubility limit of each ligand, typically between 20 mM and 60 mM (Figure 5.8). In cases where solubility restrictions occurred, DMSO content was kept below 40 % (v/v) to minimize solvent-induced changes in relaxation or protein stability. Concentration points were selected to ensure adequate sampling of both the linear and plateau regions of the dose–response curve, enabling accurate extraction of the apparent displacement constant K_C.

Binding affinity determination

After the careful selection of the primary hit concentration points for the dose-response displacement study, the binding affinities of the competitors K_C were determined first extracting displacement (F)-values (in %) of the reporter ligand TFBA to calculate the IC_{50} from the transverse relaxation rate (R_2) values. R_2-rates of the TFBA were calculated from measured T_2-relaxation times in different binding states: free state ($R_{2,f}$), trypsin-bound state in the absence of a competitor ligand under non-competitive conditions ($R_{2,nc}$), and TFBA displaced in the presence of trypsin and a competitor ligand ($R_{2,c}$) [17].

$$\boxed{F = 100 \times \left(1 - \frac{R_{2,c} - R_{2,f}}{R_{2,nc} - R_{2,f}}\right)} \tag{5.2}$$

Here, F = 0% indicates no displacement (fully bound reporter), and F = 100% represents complete displacement to the free state. The F values were fit with the four-parameter competitor concentration dose-response equation [**?**]:

$$\boxed{F = A - \frac{(A - A_0)}{1 + \left(\frac{[C]}{IC_{50}}\right)^n}} \tag{5.3}$$

F denotes the normalized displacement fraction, defined relative to the baseline signal A_0, which corresponds to the condition without any competitor ligand ($[C] \rightarrow 0$). The upper plateau A was set to 100 % to represent complete displacement of the reporter ligand TFBA. The parameter IC_{50} is obtained from fitting the dose–response relationship of F as a function of the competitor concentration $[C]$ and reflects the concentration of competitor required to displace 50 % of the bound TFBA under the given experimental conditions. The Hill coefficient n, describing the slope of the transition region and indicating potential cooperativity in the displacement process, was fixed to $n = 1$, consistent with a non-cooperative, one-to-one competitive binding mechanism expected for this MR-based assay.

The displacement F slope provides a concentration-dependent visualization for displacement efficiency. Hits clustered into two regimes, strong and weak, where each exhibited an exponential-like displacement response (Figure 5.8C). Meanwhile, the regression curve of hits **2**, **3**, and **9** became more linear, which might be the first indication of possible aggregation between protein and ligands (Figure 5.8D). Another reason could be that ^{19}F-signal intensities of those in competition mode were under the range of the signal detection limit.

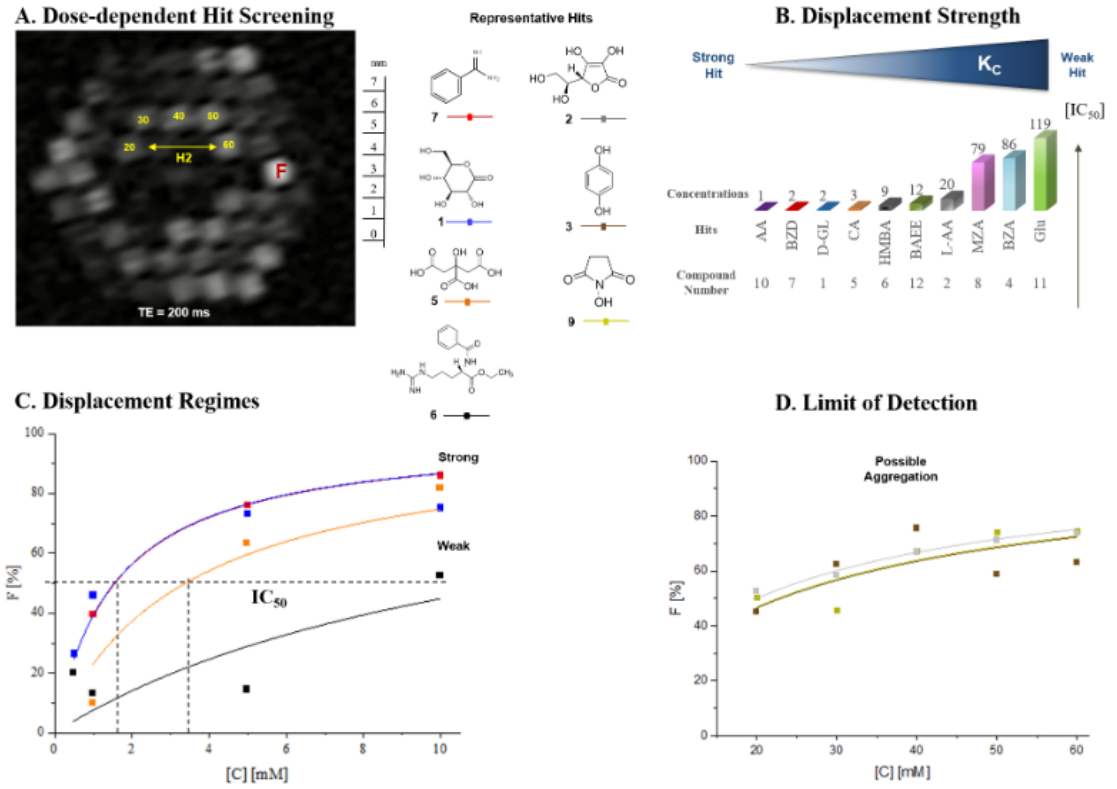

Figure 5.8.: Lead competitor validation for trypsin based on TFBA displacement efficiency. **(A)** Impact of competitor concentration on ^{19}F-signal recovery of free TFBA, shown in a compressed-sensed single T_2-weighted image (TE = 200 ms) of 13 primary hits. Honeycomb cell containing free TFBA is marked in red (F), and dose-dependent displacement of the bound TFBA by hit 2 (H2, yellow). Numbers indicate competitor concentration in the mM range. **(B)** Displacement strength ranking for primary hits, expressed as the competitor concentration ([C], mM) required to achieve 50% TFBA displacement (IC_{50}). Lower IC_{50} values indicate stronger binding competitors. K_C denotes relative competitor strength. **(C)** Two displacement regimes (strong, weak) with representative competitors and their chemical structures (compounds 1-9) plotted as a fraction of free TFBA signal recovery (F, %) versus competitor concentration. Dashed horizontal line marks the IC_{50} threshold. Compound 7 served as a reference strong displacer. **(D)** Outlier displacement profiles (compounds 2, 3, and 8) showing upward curvature at high concentrations, indicating possible protein-ligand aggregation. The imaging parameters were FOV 20 mm × 20 mm, MTX 64 × 64, SL 10 mm, TR/TE = 6 s / 200 ms, NEX 400, TA 2 h. Voxels correspond to a volume of 0.97 mm^3 per sample. Compressed sensing parameters are 43% sampling / 43% center area.

Table 5.1.: K_C of strong competitors of TFBA as determined by a titration in a honeycomb sample holder

Hit	Abbreviation	Chemical Name	K_C [mM]	Literature values [mM] or Explanation
1	D-GL	D-(+)-Glucono-delta-lactone	0.04 ± 0.1	—
5	CA	Citric acid	0.09 ± 0.1	—
6	HMBA	2-Hydroxy-3-methylbutyric acid	0.24 ± 0.1	—
7	BZD	Benzamidine	0.05 ± 0.1	0.013 [78]–0.016 [74]–0.035 [118]
10	AA	Alginic acid	0.04 ± 0.1	—
12	BAEE	N-benzoyl arginine ethyl ester	0.34 ± 0.1	Substrate ($0.25 < K_m < 1$) [128]

By extracting the IC_{50}-parameter (Figure 5.8C), we aimed to achieve rapid and robust estimation of competitive binding affinities, facilitating hit ranking and comparison across compound series without excluding the weak binders, which may never reach the full displacement of the bound TFBA. Utilizing the IC_{50}-values, we classified hits **1**, **5**, **7**, and **10** as strong binders, defined as compounds with $[IC_{50}] < 5\,\text{mM}$, since they require low competitor concentrations to achieve 50% displacement of TFBA. Hits **6**, and **12**, by contrast, exhibited $[IC_{50}] > 5\,\text{mM}$ and were therefore considered weaker displacers (Figure 5.8B).

The determined IC_{50}-values are highly useful to rank individual hits, but they only reflect the potency of a hit in a given assay. Therefore, in order to be able to compare between assays, binding affinities of competitors K_C were determined.Therefore, the following equation was used with the knowledge of the known reporter TFBA ligand's dissociation constant (K_D = 142 µM [76]) [17]:

$$K_C = \frac{(100 - F)[C]K_D}{F([L_T] + K_D)} \tag{5.4}$$

, where L_T is the concentration of the reporter ligand (here TFBA). Rearrangement resulted in the following equation:

$$\mathrm{K}_C = \frac{[IC_{50}]K_D}{[L_T] + K_D} \tag{5.5}$$

The strong competitors were hit **1**, **5**, **7**,and **10** possessing a K_C value starting with 40 µM to 90 µM, where hit **6** and **12** showed a weaker displacement with a K_C values of 240 µM and 340 µM, respectively. Using the honeycomb setup, we could detect a broad spectrum of binding affinities, as listed in Table 5.1.

However, since the IC_{50}-values of hit **2, 3, 4, 9** and **11** were near or outside the range covered by the selected concentration series (Figure 5.8B). Quantification of low-level

Table 5.2.: K_C of weak competitor candidates as determined in the capillary system

Hit	Abbreviation	Chemical Name	K_C [mM]	Literature values [mM]
2	L-AA	L-Ascorbic acid	1.15 ± 0.1	-
3	HQ	Hydroquinone	18.3 ± 4.1	Nonbinder
4	BZA	Benzylamine	0.43 ± 0.2	0.3 [118, 119]
8	MZA	Methylbenzylamine	1.75 ± 0.1	1.5 [118]
9	NHS	N-Hydroxysuccinimide	1.19 ± 0.1	-
11	Glu	Glutamate	9.07 ± 1.2	Nonbinder

displacement (20 to 40% F-values) required a minimum signal contrast index (C_{SI}) of 5 according to the analysis of reference compounds. The binding affinity determination of these hits (listed in Table 5.2) was done at a competitor concentration of 30 mM using the capillary setup comparing to the known trypsin competitor dose-response behavior (described earlier Figure 5.5A)). Hits **4** showed a weak displacement with a K_C value of 430 µM, where the rest of the hits **2**, and **9** displaced the bound TFBA the weakest with a mM range of affinity in a similar range as **8**. Ultimately, we categorized hits **3** and **11** as non-binders since the ^{19}F- signal recovery was less than 10% with a binding affinity of 10 mM – 20 mM.

We confirmed that competitors can be systematically ranked in terms of binding strength by combining two complementary quantitative metrics:

- the dose-dependent displacement of the reporter ligand TFBA using the honeycomb setup for strong and weak binders,
- single-concentration point affinity determination relative to a reference competitors measured under identical experimental conditions for very-weak binders.

Together, these two parameters enabled the extraction of the apparent competitor binding constant K_C directly from a dose–response series, without requiring any additional spectroscopic measurements. Each compartment of the multi-cell holder represented an independent concentration point, allowing K_C values to be determined in parallel for multiple ligands within a single imaging experiment. When benchmarked against literature values, the ^{19}F-MRI–based ligand screening workflow, implemented as a miniaturized T_2-relaxation assay, yielded quantitatively accurate binding affinities. Collectively, these results demonstrate that a relaxation-weighted ^{19}F-MRI approach (using only two echo times) can reliably distinguish strong, weak, and non-binding competitors in a single experiment. This highlights its potential as a high-throughput, spatially resolved screening platform for early-stage drug discovery.

5.7. Antimicrobial investigation: PPAT/CoaD Inhibition

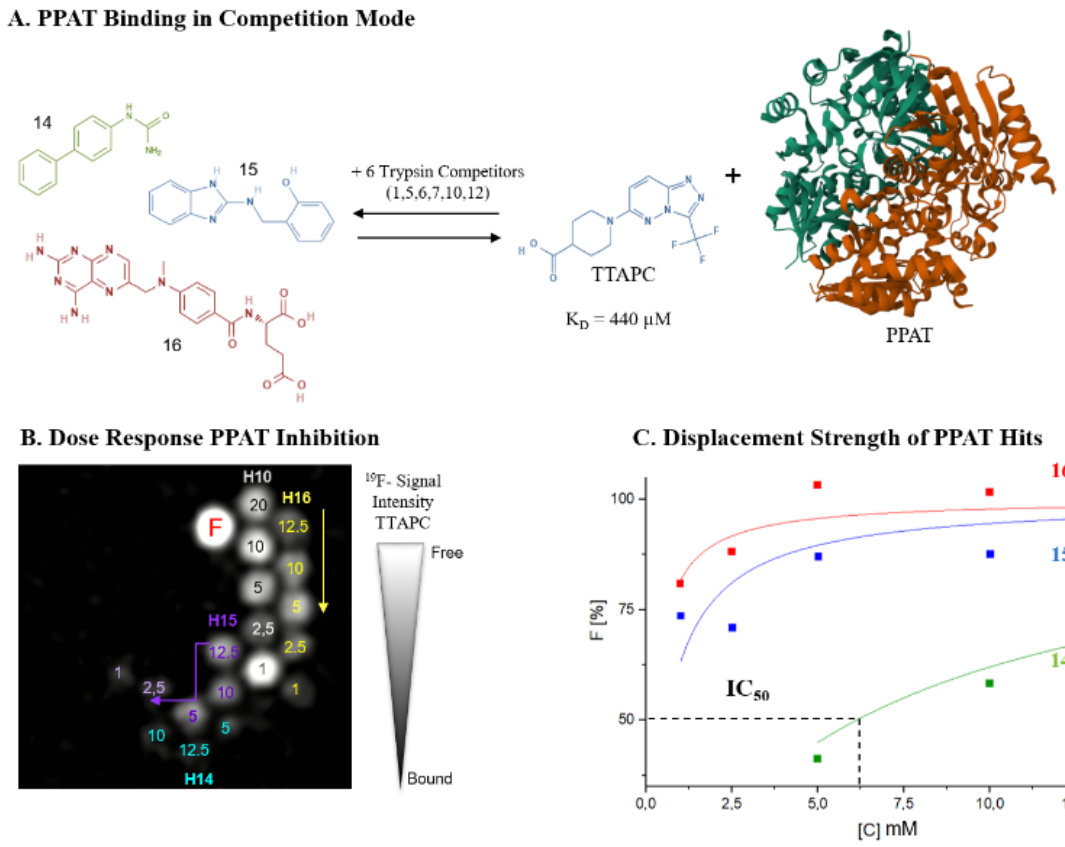

Figure 5.9.: Dose-dependent displacement monitoring for PPAT/CoaD reporter ligand TTAPC via T_2W-^{19}F-mapping.**A)**Lead hits for trypsin, three known CoaD competitors (shown with the chemical structures; **14**- Biphenyl-phenyl urea, **15**-Benzoaminomethylphenol, and **16**-Methotrexate) were screened for TTAPC displacement contribution. **B)** A fully encoded dose-response T_2-mapping showed the ^{19}F-signal alterations of the bound TTAPC by filtering only the displacers using a ligand-specific TE time at 200 ms (Arrows show the direction of the color-dedicated hit concentration series). **C)** Dose-dependent displacement fraction alterations of hits 14, 15, and 16 with determined IC_{50}-values. Black dots denote experimental data, and red lines the fitted models. **D)** Validation on the binding affinity of the lead hits using F-values measured by T_2-relaxation times. The imaging parameters were FOV 20 mm × 20 mm, MTX 64 × 64, SL 10 mm, TR/TE = 200 ms/ 6 s, NEX 400, TA 1 h. A slice ROI area covers s voxels with a volume of 0.97 mm^3 per sample. Compressed sensing parameters are 43% sampling / 43% center area. The PDB ID for the structural visualization of the PPAT/CoAD is 6CCS.

To test the ^{19}F-MRI ligand screening assay´s transferability and reproducibility, we applied this approach to an actual drug target: the enzyme phosphopantetheine adenylyltransferase (PPAT), which is essential for bacterial synthesis of coenzyme A. Here, the displacement of the fluorinated reporter TTAPC (1-[3-(trifluoromethyl)-[1,2,4]triazolo-[4,3-b]-pyridazin-6-yl]-piperidine-4-carboxylic acid) was monitored upon the addition of three new compounds (14, 15, 16), alongside six previously identified trypsin hits (1, 5, 6, 7, 10, 12), which served as controls to assess potential mutual displacement effects. The inclusion of trypsin-derived hits may help elucidate potential similarities in ligand recognition or binding mode between trypsin and the PPAT.

Dose-dependent T_2-mapping of PPAT-bound TTAPC was performed using the same reporter ligand concentration (5 mM) as TFBA. However, the protein concentration was set 25 µM, lower than in the trypsin study as ^{19}F-NMR contrast experiments demonstrated sufficient contrast between TTAPC and PPAT-CoaD using the protein concentration within the range of 20-25 µM [111].

Utilizing a ligand-specific T_2-filter (TE = 200 ms), we identified hits **14**- Biphenyl-phenyl urea, **15**-Benzoaminomethylphenol, and **16**-Methotrexate and **10** as lead competitors for CoaD from the tested compound mixture (Figure 5.9B). Among these, hit **16** emerged as the strongest competitor with a K_D of 18 µM, displacing 93% of bound TTAPC at a concentration of 12.5 mM, corresponding to a 1:2.5 molar ratio of TTAPC to hit 16. In contrast, hit **15** induced only modest displacement, consistent with its approximately six-fold weaker binding affinity relative to the strongest hit**16**. Remarkably, hit **14** produced the smallest yet still quantifiable displacement of the TTAPC, with a measured K_D of 0.5 mM and a signal corresponding to only 30% of the displacement fraction (Figure 5.9D).

Using the same approach to validate K_C values as in trypsin study with TFBA, IC_{50} values were determined from the TTAPC displacement regression curves as a function of competitor concentration (Table 5.3). K_C values are determined as described above corresponding dose–response displacement behavior. **Hit 16** and **hit 15** reached the displacement plateau already at around 2 mM, since free TTAPC generated a short T_2-relaxation time of 370 ms. **Hit 16** was identified as the strongest competitor, exhibiting a 2.5-fold higher affinity with an apparent K_C = 18 µM, than **hit 15** yielded a weaker binding with K_C = 47 µM. **Hit 14** displaced TTAPC with substantially lower potency, showing a 25-fold weaker binding affinity with a binding affinity of K_C = 498 µM.

Table 5.3.: K_C of PPAT hits determined in the honeycomb setup via dose-dependent T_2-mapping.

Hit	Chemical Name	IC_{50} [mM]	K_C [µM]
16	Methotrexate	0,22	18 ± 5
15	Benzoaminomethylphenol	0,58	47 ± 13
14	Biphenyl-phenyl urea	6,16	498 ± 8
10	Alginic acid	-	Nonbinder

Although hit **10** produced an apparent signal recovery of TTAPC signal in the presence of PPAT (Figure 5.9B, gray hit), the dose-dependent R_2 values showed no systematic trend (Figure 5.10), indicating an absence of true competitive displacement evealuted by two criteria: (i) a systematic and interpretable concentration-dependent trend in R_2 or fractional displacement, and (ii) a sufficiently high goodness of fit (R^2), were classified as true competitive binders. Compounds that failed to meet either requirement were excluded in order to avoid misclassification arising from noise, solubility issues, or non-specific signal fluctuations.

Within the PPAT–TTAPC dataset, hit **10** demonstrated no meaningful correlation between competitor concentration and R_2 changes. Instead, the data showed irregular, non-monotonic scatter and poor regression performance, both of which are inconsistent with authentic competitive displacement. Such behavior indicates that the apparent variations in signal were not driven by ligand–protein interactions but rather by experimental artefacts.

Comparing with hit **15**, this hit exhibited a clear, monotonic dose-dependent increase in the free-ligand population, reflected by a measurable reduction in R_2 and a strong linear or sigmoidal regression fit with a high R^2 value. The consistency of this trend across replicates, combined with the robustness of the fit, supports its classification as a genuine competitor capable of displacing TTAPC from PPAT.

To further investigate the anomalous behavior of hit 10, a control experiment was performed using increased volumes of the compound dissolved in DMSO as in the same final ratio as the final hit solution with TTAPC and PPAT. This experiment revealed pronounced phase separation upon mixing with aqueous buffer (Figure 5.11), providing a direct mechanistic explanation for the inconsistent relaxation profiles. Heterogeneous mixtures can locally alter the DMSO:PBS ratio, microviscosity, and chemical-exchange environment, leading to spurious T_2 or R_2 fluctuations that mimic displacement-like signal changes without reflecting true binding events. Consistent with this interpretation, samples containing hit 10 exhibited prolonged T_2 values of ~500 ms, compared to 370 ms for free TTAPC ($T_{2,b} \sim 70$ ms) under identical conditions. Both $R_{2,f}$ and $R_{2,c}$ remained constant at $\approx 2\,s^{-1}$, supporting the conclusion that hit 10 does not bind PPAT under the assay conditions.

By combining miniaturized 61-cell arrays with compressed sensing, we guaranteed a high-throughput MRI (HiT-MRI) rate, and successfully optimized a streamlined workflow for competitive drug screening using ^{19}F-MRI. This workflow has the potential to transform protein-ligand detection into a rapid, parallel, and scalable platform, enabling high-content molecular screening. This opens new possibilities for early-stage drug discovery, fragment screening, and multiplexed assays.

These results demonstrate the robustness of the ^{19}F-MRI–based detection of competitors spanning a wide range of binding affinities, even for structurally complex and disease-relevant protein of PPAT. Beyond the quantitative assessment of ligand binding, the method also proved sensitive to physicochemical irregularities in the samples such as aggregation or phase separation, thereby providing valuable diagnostic information for troubleshooting assay performance. Collectively, this highlights the versatility of the ^{19}F-MRI workflow as both a binding-affinity screening tool and a qualitative quality-control readout for identifying sample-related artifacts or formulation issues.

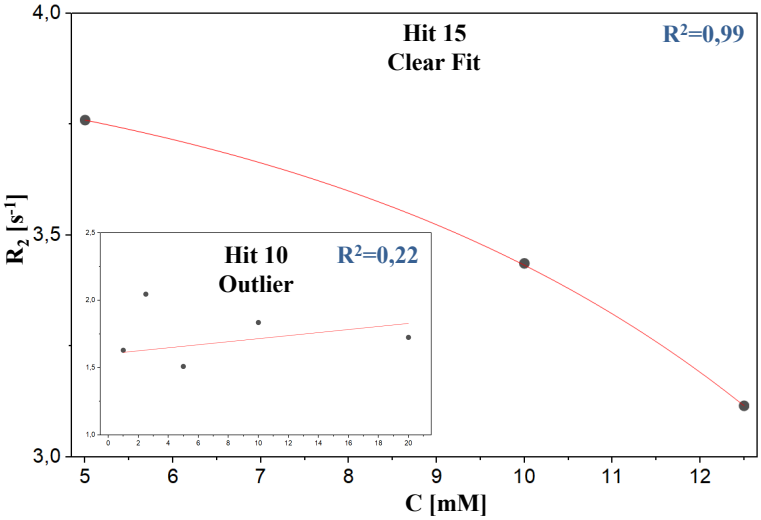

Figure 5.10.: Dose-dependent relaxation rate alterations in comparison of a nonbinder hit 10 and binder hit 15 for the PPAT-TTAPC study. Black dots denote experimental data, and red lines the fitted models. The statistical coefficient of determination R^2 (blue) is given in each panel to indicate the quality of fit.

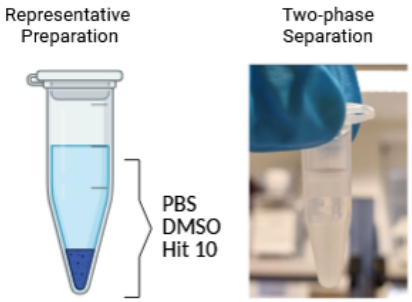

Figure 5.11.: Phase separation of hit 10 upon DMSO addition as a control experiment. The sample separated into two visible phases, demonstrating limited compatibility of hit 10 with DMSO and preventing the formation of a homogeneous competitor solution.

5.8. Conclusion

The speed of drug discovery is inherently constrained by the rate at which compounds can be screened. Equally crucial is the adaptability of the screening workflow, which must support ligands with diverse binding affinities and remain applicable across various protein–ligand systems. To advance our rapid ^{19}F-MRI-based ligand screening approach [DF1] using a capillary sample holder, we introduced an optimization strategy aimed at enhancing throughput, versatility, and MR image undersampling. This was achieved by exploiting the built-in capabilities of the scanner, without the need for complex pulse-sequence programming or additional hardware modifications.

By redesigning the sample holder from a capillary array to a honeycomb geometry, we enabled 61 physically separated compartments to coexist within the same magnetic environment. This configuration allowed successful imaging through multi-array acquisition, making full use of the available physical space within the home-built ^{19}F coil. Each compartment contained an independent ligand-binding reaction, permitting the simultaneous screening of 55 non-fluorinated drug candidates for protein binding within a single measurement.

Using T_2-mapping as the primary readout, binding-induced changes in the ^{19}F signal of the fluorinated reporter ligands TFBA and TTAPC were detected and quantified. Their distinct fluorine moieties enabled direct MR detection and provided a sensitive measure of binding and displacement events. These variations in relaxation behavior provided three key levels of biochemical information:

- Hit/no-hit identification based on single-point measurements of T_2-weighted contrast changes,
- Estimation of the competition fraction ($F\%$) reflecting the displacement efficiency of competing non-fluorinated drug candidates,
- Determination of binding affinities (K_C) from IC_{50} values extracted from the R_2-relaxation analysis in dose–response titrations.

This integrated workflow thus enabled a direct and quantitative connection between MR-observable contrast and underlying molecular binding events.

In the high-throughput screening mode, we successfully identified **13 hit compounds** for trypsin based on the recovered ^{19}F signal intensity of the reporter ligand TFBA, employing a single T_2-filter (TE = 200 ms) in phase 1. These hits were characterized by a significant recovery in reporter signal compared to the unbound state, indicating effective displacement. Subsequently, in phase 2, we determined K_C of **six lead competitors** (**1, 5, 6, 7, 10, 12**) targeting trypsin, and **three lead compounds** (**14–16**) binding to PPAT. This demonstrated that our screening approach can be readily extended from the well-established trypsin model system to the more disease-relevant enzyme PPAT (phosphopantetheine adenylyltransferase), underscoring its general applicability to diverse protein targets.

Strong displacers (**1, 5, 7, 10** for trypsin; **14, 15, 16** for CoaD) were consistently detected within the honeycomb setup, confirming that the assay robustly captures competitive binding interactions even at reduced sample volumes. Optimized experimental conditions enabled detection at sample volumes as low as 50 µL, with reporter ligand concentrations down to 5 mM, without compromising image quality or quantification precision. For weaker binders (**2, 3, 4, 8, 9, 11**), the assay reached the quantitative sensitivity limit of R_2-based analysis within the honeycomb configuration. To overcome this constraint, we integrated a capillary-based system, which substantially improved signal-to-noise ratio (SNR) by increasing the detection volume. This dual-system approach by combining high-throughput screening in honeycomb arrays with high-sensitivity capillary readouts provides a powerful and scalable platform for rapid ^{19}F-MRI-based ligand screening and affinity characterization.

By implementing compressed sensing (CS) within the optimized high-throughput pipeline (Figure 5.12, the total measurement time was substantially reduced by acquiring only 43% of k-space. Despite undersampling beyond the Whittaker–Nyquist–Shannon criterion, robust compound screening was achieved with sufficient SNR > 3 and only minimal deviations in T_2-relaxation times. The complete screening of all samples could thus be performed within approximately 2 h per dataset, corresponding to an average acquisition time of 2 min per sample. This represents a **ninefold reduction** in imaging time compared to conventional multi-point T_2-relaxation mapping (~20 min per measurement [14]), while maintaining high-quality image contrast and reliable quantitative performance.

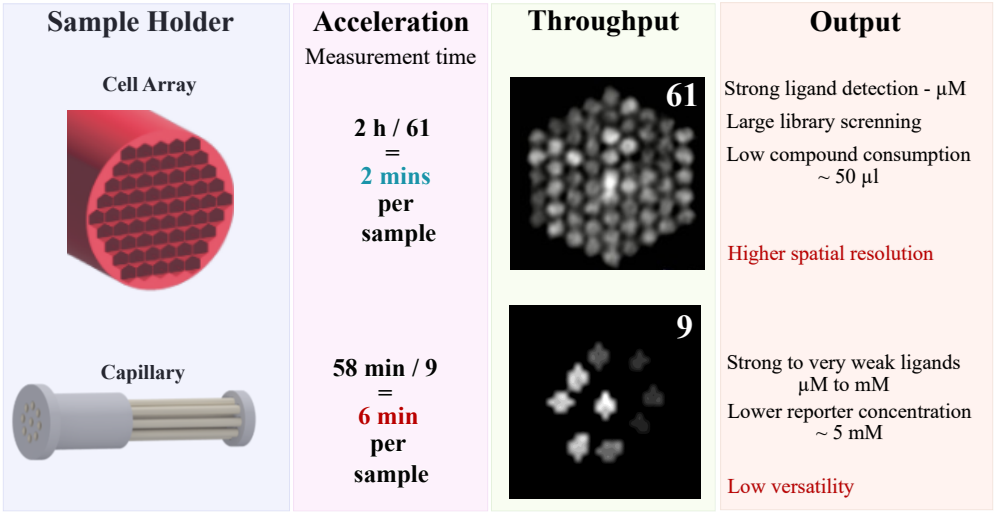

Figure 5.12.: From capillary to honeycomb: Scaling Up ^{19}F-MRI screening throughput. The cell-array (honeycomb) geometry maximizes parallelization (61 samples; ~2 min per sample) and minimizes sample volume (~50 µL), ideal for rapid screening of strong to moderately weak binders. The capillary configuration achieves higher sensitivity for weak/very-weak ligands and supports lower reporter concentrations (5 mM), but with lower throughput (9 samples; ~6 min per sample).

In case of utilizing different sample holder designs, we have shown the necessity of a higher spatial resolution if the voxel size changed from 4 mm^3 to 1 mm^3. More importantly, for the contrast-quantified MRI protocols, it is important to find the trade-off between the amount of the central *k*-space and blurring artifacts on the images, which is followed by the next step of optimization in the total undersampling rate.

The concentrations of the reporter ligand and competing analytes employed in this assay are 2–3 orders of magnitude higher than those typically used in conventional biochemical assays or NMR-based titrations. A reporter concentration of 5 mM was required to achieve sufficient signal-to-noise ratio in ^{19}F-MRI, given the lower intrinsic sensitivity of imaging compared to high-field NMR spectroscopy. Consequently, this high reporter concentration establishes a stringent threshold for competition: only ligands capable of effectively displacing TFBA from the protein binding pocket under these conditions will produce a measurable signal recovery. The strong mass-action bias toward the bound state thus favors the detection of moderate- to high-affinity competitors, while imposing practical challenges for weak binders and poorly soluble compounds.

The screening concentrations for competitor ligands were therefore adjusted up to 30 mM or higher to achieve detectable displacement, which approaches or exceeds the solubility limit of many small organic molecules. Under such conditions, phenomena such as compound aggregation, precipitation, or non-specific adsorption may arise, potentially leading to false-positive effects or deviations from ideal equilibrium behavior. These limitations are inherent to assays relying on high bulk concentrations to compensate for low detection sensitivity [15, 126]. Careful visual inspection of samples, use of highly soluble model compounds, and the absence of non-linear signal behaviour in dose–response curves confirmed that aggregation artefacts were minimal under the conditions tested.

The full potential of the presented MRI-based screening framework is expected to be realized when combined with hyperpolarization of the reporter ligand, which can transiently enhance the ^{19}F signal by several orders of magnitude. Such enhancement would permit operation at reporter and competitor concentrations in the low micromolar range, similar to standard NMR binding assays, while maintaining quantitative imaging contrast [129, 130]. This reduction in concentration would not only alleviate solubility and aggregation issues but also extend the detectable affinity range toward weaker binders.

Despite the current concentration constraints, the assay successfully identified and characterized ligands across a broad affinity range. This robustness stems from the relatively low affinity of the chosen reporter ligand, which allows efficient displacement even by competitors with millimolar K_C values. Moreover, the high aqueous solubility of the tested compounds ensured that experimental concentrations up to 30 mM could be reached without compromising sample integrity. Together, these factors demonstrate that, even in its non-hyperpolarized form, the assay provides a reliable and scalable approach for quantitative affinity screening using ^{19}F-MRI.

6. Gd-based Contrast Tuning for Rapid Ligand Screening

This chapter is based on work that introduces an additional acceleration strategy using paramagnetic relaxation enhancement (PRE) via gadolinium-based contrast agents. The results presented here form the core of a manuscript currently in preparation. The focus of this study is the integration of the Gd-based contrast agents Magnevist and gadolinium chloride into the competitive ligand-screening workflow, with the aim of reducing the overall measurement time and quantifying the achievable acceleration factors within an MRI-based assay.

6.1. Introduction

Magnetic resonance imaging (MRI) provides rich contrast based on nuclear relaxation processes, yet it remains inherently time-consuming because image formation requires the sequential acquisition of k-space lines. Each acquisition is constrained by the relaxation properties of the detected spins. In order to recover sufficient longitudinal magnetization for the next excitation pulse, the system must wait on the order of $3–5 \times T_1$, because longitudinal relaxation (T_1) follows an exponential regrowth toward equilibrium, and only reaches a practically usable fraction of the available magnetization (typically 90–99%) after several multiples of T_1. Without this recovery, the signal becomes saturated, leading to reduced amplitude and unstable image contrast. This requirement, therefore, sets the minimal feasible repetition time (TR) for quantitative relaxation studies. A long T_1 therefore enforces long TR values, directly increasing the acquisition time for a complete dataset.

The transverse relaxation time (T_2) represents one of the most informative parameters in molecular and biomedical imaging, reflecting local molecular motion, spin–spin interactions, and microenvironmental changes. However, the transverse relaxation time T_2 limits the duration of echo sampling (see Figure 2.16): the MR signal decays exponentially during the echo train, restricting the number and spacing of usable echoes, and thereby controlling how densely k-space can be filled within a single TR. As a result, relaxation processes impose fundamental temporal constraints on MRI, where both TR (set by T_1) and TE/echo-train duration (set by T_2) collectively determine the total scan time, especially in experiments relying on fully sampled Cartesian acquisitions.

Several complementary strategies have been developed to address this limitation, including optimized pulse-sequence designs that collect multiple echoes per repetition (e.g., fast spin-echo, RARE, and GRASE sequences) [131–133], echo-planar imaging [134], and,

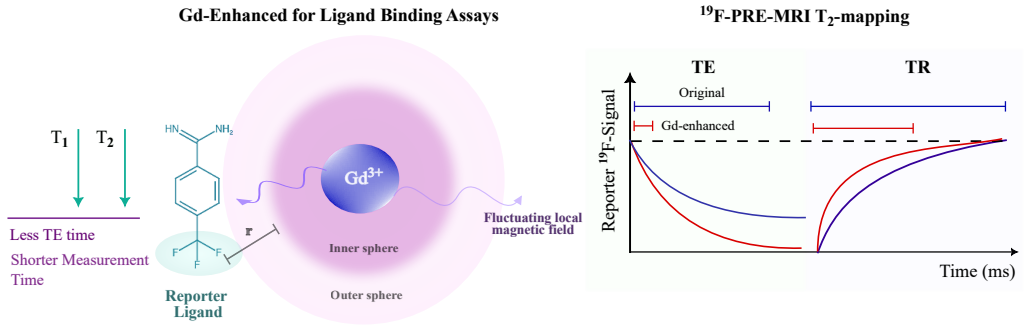

Figure 6.1.: Gd(III)-induced T_2-relaxation enhancement accelerates ^{19}F-MRI ligand-binding measurements. Outer-sphere interactions between the ^{19}F-reporter ligand and Gd_3^+ shorten T_2- (faster signal decay, requiring shorter TE) and T_1-relaxation time (faster recovery, allowing shorter TR). These PRE-driven changes reduce total measurement time without altering binding equilibria, enabling accelerated ligand-binding readout.

more recently, compressed-sensing and deep-learning-based reconstructions that exploit data sparsity to recover images from undersampled acquisitions [135, 136]. Together, these methodological advances have substantially reduced scan times while preserving relaxation-weighted contrast, enabling the way for high-throughput and quantitative MRI applications.

To translate this speed into screening throughput, we adopted three complementary accelerations at the experiment level in this work. First, we parallelize the acquisition scheme in physical space using custom holders that position multiple samples within the field of view (FOV) of an MR scan and exploit a single frequency-encoding (FE) axis for simultaneous acquisition using sample holders imaging cell arrays under one MR scan. Thus, multiple capillaries or the honeycomb cell array formed distinct, resolvable strips along one readout. Second, we utilized nuclei to ^{19}F to remove biological background and simplify readouts to a single resonance per reporter ligand, which enables "hot-spot" imaging and straight intensity/relaxation quantification with no endogenous signal confounds coming from protein or water. Third, we undersampled k-space with compressed sensing (CS), leveraging transform sparsity to recover images from far fewer k-space data points.

Because our readout-based hit screening is fundamentally T_2-relaxation driven, a natural question is whether paramagnetic relaxation agents could further accelerate the experiment. Gadolinium(III) chelates (GCAs) and gadolinium salts are well known to enhance nuclear relaxation via dipolar interactions described by Solomon–Bloembergen–Morgan (SBM) theory [137, 138], where they accelerate the relaxation of nearby nuclei through both inner-sphere (transiently bound water) and outer-sphere (diffusive encounter) mechanisms. The underlying cause is the powerful magnetic moment produced by the unpaired electrons of the paramagnetic Gd^{3+} ion.

In solution, water protons experience strongly fluctuating local magnetic fields as they diffuse in the vicinity of paramagnetic ions; consequently, outer-sphere encounters with freely diffusing Gd^{3+} complexes shorten both T_1 and T_2 not only of water protons but also

of solute heteronuclei such as fluorine, even without the metal ion being covalently bound to the ligand. This effect is termed paramagnetic relaxation enhancement (PRE) because the unpaired electrons of the paramagnetic ion generate strong electron–nucleus dipolar interactions that efficiently accelerate nuclear relaxation.

Because the dipolar interaction responsible for PRE scales with r^{-6}, even small changes in the average distance between the paramagnetic ion and the ^{19}F nucleus of the reporter ligand lead to pronounced differences in transverse relaxation. Outer-sphere PRE does not require binding between the reporter ligand and the paramagnetic ion; instead, transient diffusional encounters generate the effect. Although the distances and correlation times differ fundamentally from the inner-sphere case, the underlying mechanism remains electron–nucleus dipolar coupling, averaged over many stochastic collision trajectories. The observed T_2 shortening therefore reflects the frequency and proximity of diffusional approaches between the ligand and the paramagnetic agent.

When the reporter ligand binds to the protein, it becomes sterically and dynamically shielded, reducing the probability of close encounters with Gd^{3+} and leading to a longer T_2. Strong competitors displace the ligand back into solution, where it again experiences efficient PRE and exhibits shorter T_2 relaxation.

Operationally, the addition of Gd(III)–based contrast agents accelerates nuclear relaxation by steepening the decay of the spin–echo amplitudes. At the micromolar concentrations typically used in biochemical assays, Gd-chelates predominantly enhance T_1 relaxation, whereas pronounced T_2 shortening emerges only at higher Gd concentrations [69]. The combined increase in relaxation rates enables the use of shorter echo trains and/or fewer echoes for quantitative T_2 mapping. When longitudinal relaxation (T_1) is sufficiently shortened, the repetition time (TR) can be reduced proportionally, further decreasing the per-dataset acquisition time.

Here, we present a paramagnetic contrast–enhanced ^{19}F-MRI strategy that exploits T_2-relaxation modulation by gadolinium (Gd^{3+})-based contrast agents to accelerate the ligand-screening workflow by integrating molecular contrast, spatial parallelization, and k-space undersampling. This approach is particularly advantageous when strong competitors induce pronounced T_2 changes in bound reporter ligand, as fewer echoes are required to classify hits with a defined confidence level.

A critical requirement for this strategy is that the binding affinities of the competitors remain unaffected by the presence of the Gd-based contrast agent; in other words, the GCA must not perturb the protein–ligand binding equilibrium. To ensure this, we compared the clinically established chelated agent Magnevist with the widely used inorganic salt $GdCl_3$, evaluating their paramagnetic relaxation enhancement (PRE) behaviour in terms of dual (T_1 and T_2) relaxation shortening.

Our analysis showed that Magnevist induces substantially stronger T_1 and T_2 shortening at micromolar concentrations while leaving the binding-affinity quantification unaffected. In contrast, $GdCl_3$ exhibited significantly weaker PRE effects under the applied experimental conditions and caused protein aggregation. Based on these findings, Magnevist was identified as the optimal contrast agent.

Using 100 µM Magnevist, we successfully screened 61 different compounds in 55 min, scaling the original conventional single-sample-experiment NMR workflow from 18 min per sample to just 54 s. This method thus provides a robust and generalizable platform for T_2-based contrast-enhanced screening, leveraging the unique relaxation properties of Gd to enhance the sensitivity and specificity of ^{19}F-MRI for target-engagement studies in large compound libraries.

6.2. Contrast imaging pipeline

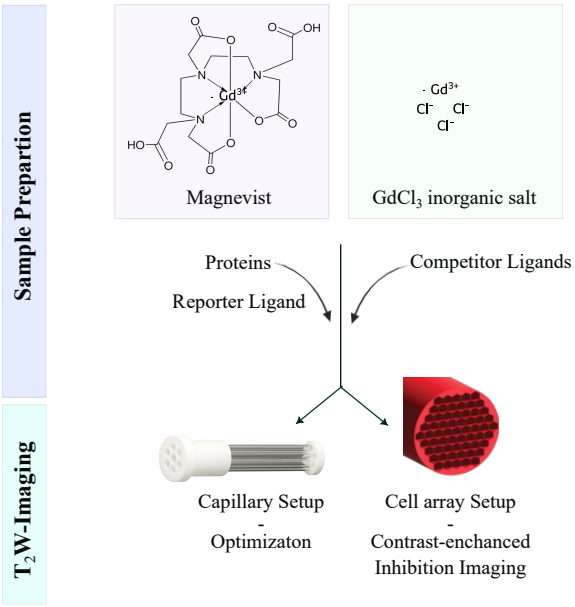

Figure 6.2.: Contrast-enhanced competitive binding pipeline by T_2-weighted ^{19}F-MRI. **(Top)** Paramagnetic relaxation contrast agents used in this work: the chelated gadolinium agent Magnevist (Gd-DTPA) and the inorganic salt $GdCl_3$. **(Middle)** Sample preparation scheme combining protein, ^{19}F reporter ligand, and competitor ligands for displacement assays. **(Bottom-left)** 3D-printed capillary holder (7-capillary configuration) used for method optimization and large-volume tests. **(Bottom-right)** Cell-array (honeycomb) sample holder enabling parallelized measurements and contrast-enhanced inhibition imaging via Gd^{3+} the local transverse relaxation rate R_2 of the reporter alterations.

For the contrast enhancement experiments, contrast agents were Magnevist (Diethylenetriaminepentaacetic acid gadolinium(III) dihydrogen salt hydrate; Sigma-Aldrich, 381667) and gadolinium(III) chloride (anhydrous, ABCR GmbH, AB120501) and dissolved in phosphate-buffered saline solution (PBS, 1×, pH 7.4, ThermoFisher, 10010-015) and subsequently added to protein-ligand mixtures to the desired final concentrations.

4-(trifluoromethyl)benzamidine (TFBA) (Enamine, EN300-73109) was used as a reporter ligand for all contrast imaging experiments. As proteins, trypsin from bovine pancreas (Sigma-Aldrich, T9935), bovine serum albumin (Sigma-Aldrich, A8806) were prepared as described in Chapter 3.2. Benzamidine (BZD) (Sigma-Aldrich, 434760), 4-Methylbenzylamine (MZA, Sigma-Aldrich, 126400250) and benzylamine (BZA, Sigma-Aldrich, 185701) were competitors. As strong competitors, the hits from the inhibition study were used (see Chapter 5-phase 2, hits in Table 5.1).

The solutions were transferred into 2.4 mm OD glass capillaries (CM Scientific) using a microliter syringe (Hamilton Central Europe S.R.L.) or directly into the wells of the holder (Figure 3.5). Both sample holders were then sealed with UV glue (Delo Photobond) to

prevent evaporation and contamination.

The prepared sample holders were positioned inside the radiofrequency (RF) coil prior to data acquisition. All ^{19}F transverse relaxation (T_2) experiments were performed on a Bruker BioSpec 650 MHz (15.2 T) imaging system (Bruker BioSpin, Ettlingen, Germany) interfaced with a custom-built, single-tuned 15 mm ^{19}F RF volume coil. Magnetic resonance imaging was carried out using a RARE (Rapid Acquisition with Relaxation Enhancement) spin-echo sequence and T_1-mapping via saturation-recovery protocol implemented in ParaVision 360 (v3.3, Bruker BioSpin).

Sequence-specific parameters, including repetition time (TR), echo time (TE), RARE factor, field of view (FOV), matrix size, and slice thickness (SL) differed for the capillary and honeycomb setups. For fully sampled 7 capillary MR images, the imaging parameters were FOV 20 mm × 20 mm, MTX 32 × 32, SL 10 mm. For honeycomb setup, the imaging parameters were FOV 20 mm × 20 mm, MTX 64 × 64, SL 10 mm. Compressed sensing parameters are 43% sampling /43% center area.

6.3. Assessment of Gadolinium Sources for PRE ^{19}F-MRI

In our studies, protein–ligand interactions were monitored in a competitive format using a fluorinated reporter ligand TFBA. Binding to the protein trypsin decreased the reporter's molecular mobility, whereas displacement by a competitor restored a more mobile, free state. These two states produced distinct T_2 values, which we quantified using a Carr–Purcell–Meiboom–Gill (CPMG) readout. When combined with the spatial encoding of MRI, this contrast enabled simultaneous monitoring of multiple competitive binding experiments within a single acquisition. However, despite this spatial parallelization, the scan time remained limited by the sequence parameters imposed by relaxation constraints.

To address this, we introduced a paramagnetic contrast agent to induce additional T_1 and T_2 shortening via paramagnetic relaxation enhancement (PRE), with the aim of further accelerating the acquisition. The unpaired electrons of a paramagnetic center create fluctuating magnetic fields that couple to nearby nuclear spins, shortening both longitudinal (T_1) and transverse (T_2) relaxation times through inner- and outer-sphere dipolar interactions [139, 140] (theoretical explanation in Chapter 2.5). In practice, shortened T_1, allows a reduction of TR, providing stronger T_2-weighted contrast within shorter echo times. As a motivation based on the theory, paramagnetic doping should substantially reduce total measurement time while maintaining quantitative sensitivity in practice.

However, since the contrast agent can constitute an additional chemical component in a biochemical assay designed to report protein–ligand binding, its inclusion necessitates careful optimization. The following parameters were considered critical for assay reliability and translational value in early-stage drug discovery:

- **Minimal interaction with proteins or ligands** to prevent perturbation of the native binding equilibrium,
- **Chemical stability and predictable relaxivity** ensuring reproducible T_1/T_2 reduce over time and between batches,
- **Contrast efficiency** sufficient to measurably reduce acquisition time without excessive signal quenching,
- **Unaltered binding affinities** (K_D or K_C) in the presence of the agent, confirming biochemical neutrality,
- **Batch reproducibility and handling safety**, important for high-throughput screening and disposal.

Two different gadolinium-based contrast agents (CA) were chosen in this study: **Magnevist (Gd–DTPA)** as a polyaminocarboxylate chelate and **$GdCl_3$** in inorganic salt form. Both $GdCl_3$ and Magnevist exhibit such dual relaxation behavior, simultaneously shortening the T_1 and T_2 relaxation times of nearby water protons. However, under the magnetic field strengths used in this study, the T_2 shortening dominates, producing predominantly negative (signal-decreasing) contrast that is ideally suited for relaxation-weighted detection [140–142].

Regarding the biodistribution and physicochemical properties, in *in vitro* experiments, $GdCl_3$ is often preferred due to its higher effective relaxivity and the absence of bulky chelating ligands, which allows direct interaction of the free Gd^{3+} ion with surrounding water protons [140, 143]. Magnevist is the most widely used CA and was the first to be approved for clinical use in 1988 [144]. The distinguishing feature is that it provides a well-defined and reproducible relaxivity profile, high complex stability, and minimal nonspecific binding, making it ideally suited for quantitative relaxation studies [141, 142].

Optimal contrast agent concentration

In order to implement and quantify the dual relaxation effect, a concentration series of Magnevist ranging from 50 µM to 2 mM and of $GdCl_3$ from 0.5 mM – 5 mM was investigated. The T_1 relaxation was measured using a saturation–recovery sequence, and T_2 relaxation was mapped with a RARE protocol, employing the well-characterized TFBA–BZD reporter–competitor ligand system bound to trypsin (as described in previous chapters).

The selected concentration ranges were designed to cover the sub-millimolar to low-millimolar regime, in which the relaxivity of small Gd^{3+} ions and their chelates remains approximately linear with concentration under aqueous conditions, while avoiding excessive signal loss or susceptibility artifacts at higher doses [140, 141]. Previous studies in tissue and phantom systems reported a practical upper limit of ≤4 mM for Gd–DTPA [141], supporting the use of 2 mM as an adequate ceiling for the present ^{19}F-MRI experiments. For $GdCl_3$, however, a higher concentration range was explored to achieve relaxation enhancement comparable to that of chelated complexes, compensating for partial hydrolysis, precipitation, and nonspecific binding processes that occur in neutral aqueous media [140].

In Figure 6.3, the paramagnetic relaxation enhancement (PRE) factor is defined as the ratio of the T_2 relaxation time of the fluorinated reporter ligand TFBA in the presence of a contrast agent (CA) to that of the free state without any CA:

$$\boxed{PRE_{\text{Factor}} = \frac{T_{2,\text{CA}}}{T_{2,0}}}$$

Here, $T_{2,\text{CA}}$ denotes the measured transverse relaxation time in the presence of a given contrast agent concentration, while $T_{2,0}$ corresponds to the intrinsic T_2 relaxation time of TFBA in the absence of any CA, serving as the reference baseline.

The ^{19}F-signal intensity of TFBA was used to quantify the PRE effect, as the contrast agents modulate transverse relaxation and thus the T_2-weighted contrast. In the ^{19}F-MR images of seven parallel samples (Figure 6.3A–F), the TFBA signal intensity decreased progressively with increasing concentrations of both Magnevist and $GdCl_3$, demonstrating clear concentration dependence.

Analysis of the PRE factor revealed distinct concentration-dependent behaviors for the two agents. For Magnevist, the PRE increased approximately linearly within the investigated range up to 2 mM, consistent with the expected linear relaxivity regime of chelated Gd^{3+} complexes in dilute aqueous media, where relaxation rates follow an approximately linear relationship with concentration, $R_{1,2} = R^0_{1,2} + r_{1,2}[\text{Gd}]$ [139].

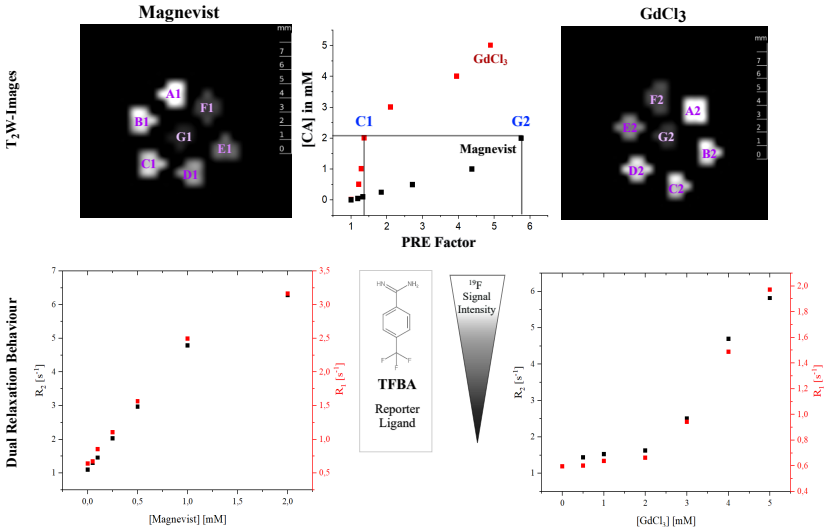

Figure 6.3.: Paramagnetic relaxation enhancement (PRE) and dual relaxation behavior of Magnevist and $GdCl_3$ (**Top**) Representative ^{19}F-T_2-weighted MR images of 7 TFBA samples acquired in the presence of increasing concentrations of Magnevist (left) and $GdCl_3$ (right) contrast agents. Letters (A–C) in the images correspond to samples with different concentrations. "A" is the TFBA in contrast to the agent-free form. "B-F" the concentrations increase, and the "F" sample has the highest concentration. The central plot quantifies the PRE factor as a function of contrast agent concentration of Magnevist up to 2 mM, and for $GdCl_3$ above this range, and the blue letters indicate the concentrations points with the highest and lowest PRE effect.(**Bottom**) Dual relaxation behavior of both contrast agents: longitudinal (R_1, red) and transverse (R_2, black) relaxation rates of the reporter ligand TFBA as a function of [CA]. The chemical structure of TFBA is shown in the center for reference. Imaging parameters are given in the material and methods sections

In contrast, $GdCl_3$ displayed a more complex dependence: the data suggest two linear regimes, one below and a steeper regime above 2 mM. This behavior is consistent with partial hydrolysis of $GdCl_3$ in phosphate buffer and the possible formation of $Gd(OH)_x$ species or transient protein–Gd adducts at higher concentrations, both of which increase local magnetic susceptibility and disproportionately enhance transverse relaxation.

Both contrast agents exhibited dual relaxation behavior, simultaneously increasing the longitudinal (R_1) and transverse (R_2) relaxation rates by approximately $2\,s^{-1} - 3\,s^{-1}$ across the tested range. Although Magnevist exhibits a stronger PRE effect than $GdCl_3$ at low micromolar concentrations, this enhancement arises exclusively from outer-sphere relaxation. Inner-sphere PRE requires direct coordination of the solute to the paramagnetic ion, placing the nucleus within the first coordination sphere. This mechanism is dominant only when the solute contains strongly coordinating donor groups (TFBA has weak donors of amidine, fluorinated aryl groups) capable of replacing a ligand in the metal

complex [140]. Because Gd–DTPA is an octadentate, kinetically inert chelate with no accessible coordination sites, inner-sphere binding of TFBA is chemically implausible. The observed concentration dependence shall therefore attributed solely to outer-sphere diffusional encounters.

Notably, Magnevist achieved a higher PRE factor (≈ 6, (Figure 6.3, blue, C) already at 2 mM, whereas even 5 mM $GdCl_3$ did not reach comparable enhancement. For example, a PRE factor of 1.5 was observed for Magnevist at only 100 µM (blue, B), while $GdCl_3$ required 2 mM (blue, A) to achieve a similar effect. These characteristic concentrations were therefore selected for subsequent comparison of chemical stability and reproducibility of both CAs, also in the presence of trypsin and the competitor ligand BZD, to identify the most suitable agent for this rapid molecular sensing application.

Chemical stability and binding affinity control

One of the central aims of our work is to evaluate protein–contrast-agent interaction: the possibility of any interactions of the gadolinium complexes with the targeted proteins (trypsin and bovine serum albumin) in a screening library. It is important to show in this part of the experimental work that Magnevist and Gd^{3+} do not interact chemically with the proteins, which may cause their aggregation, leading no binding site availability for the reporter ligand.

Therefore, the r_2 alterations of the reporter ligand TFBA were confirmed in two concepts: (i)**Trypsin binding** to ensure the TFBA could bind to the trypsin, excluding the protein aggregation possibility, (ii)**TFBA displacement** by known competitors of BZD, BZA, and MZA for the reproducibility of the binding studies. The chemical stability of contrast agents, 100 µM Magnevist and 2 mM $GdCl_3$, with the same PRE effect upon 300 µM trypsin addition, and the dose-dependent behavior of the TFBA displacement by the strong competitor BZD were investigated using the RARE protocol.

To verify the first criterion regarding the chemical stability of trypsin, the T_2-based signal contrast (C_{T_2}) of the TFBA in free (T_{2_f}) and protein-bound states (T_{2_b}) was compared before ($C_{T_{2_0}}$)and after the addition of the contrast agents ($C_{T_{2_{CA}}}$):

$$\boxed{C_{T_{2_{0,CA}}} = \frac{T_{2,f} - T_{2,b}}{T_{2,f}} \times 100} \tag{6.1}$$

Next, the apparent binding affinities (K_C) of BZD were extracted from the dose-dependent T_2-mapping experiments to assess how the addition of contrast agents influences the displacement behavior. The resulting K_C values obtained before and after supplementation with Magnevist or $GdCl_3$ are summarized in Table 6.1.

For a screening assay intended for early drug discovery, robustness across chemically diverse and unknown candidates is critical. When introducing Magnevist or $GdCl_3$, the binding affinity of the competitor BZD should remain unaffected, confirming that the contrast agent does not perturb protein–ligand interactions and that the observed PRE effect is magnetic rather than chemical. Comparing the apparent K_C values of BZD obtained with and without contrast agents, both Magnevist and $GdCl_3$ produced mean deviations

Table 6.1.: Influence of Gd-based contrast agents on K_C of BZD (µM)

mM BZD	Magnevist	Without CA	$GdCl_3$
25	15.1 ±1.5	15.8 ±2.6	15.2 ±1.5
20	13.3 ±2.2	16.6 ±2.1	18.3 ±2.3
15	11.4 ±1.7	16.1 ±3.5	15.0 ±2.1
10	11.3 ±1.2	12.0 ±1.5	14.0 ±2.2
5	11.5 ±1.2	9.0 ±1.1	13.0 ±2.4

of approximately 2-15% from the reference condition, indicating that neither agent substantially perturbed the binding equilibrium largely. However, the two agents differed markedly in the precision of the extracted values. Magnevist yielded more consistent results chaning the competitor concentration of BZD, with smaller standard deviations across replicate measurements and minimal scatter around the reference K_C, consistent with the chemical inertness and solution stability of its chelated Gd^{3+} complex. In contrast, $GdCl_3$ produced larger variability in the fitted K_C values, reflected in broader error bars and greater between-sample scatter, likely arising from its sensitivity to hydrolysis and buffer composition.

In contrast, $GdCl_3$ tended to produce slightly higher K_C values, reflecting weaker apparent binding and greater variability. Its free ionic form is prone to hydrolysis and exhibits strong sensitivity to pH, buffer composition (e.g., phosphate or carbonate), and the presence of chelating or carboxylate-rich molecules. These factors can lead to precipitation or unspecific interactions with proteins and ligands, thereby altering r_2 independently of target binding and compromising quantitative analysis. Accordingly, Magnevist, with its DTPA-chelated and chemically stable formulation, proved more suitable for reliable affinity measurements.

Experimentally, the addition of protein to $GdCl_3$ frequently resulted in visible particulates in the capillaries, confirming its higher interaction. Moreover, achieving a comparable PRE effect required about 2 mM $GdCl_3$, whereas Magnevist reached the same contrast already at 100 µM—a roughly 20-fold lower concentration. The combination of higher stability, reproducibility, and assay compatibility led us to standardize on Magnevist for all subsequent experiments, as further optimization of $GdCl_3$ conditions (buffer, pH, mixing order) would contradict the goal of a simple, high-throughput screening workflow.

Magnevist for weaker binders: TE-TR parameter optimization

To extend the applicability of the Magnevist-enhanced ligand assay, we evaluated its performance for weakly binding competitors, which naturally show lower displacement efficiency than high-affinity ligands. As established in Chapter 5, low-affinity ligands require higher concentrations to reach near-complete TFBA displacement.

We therefore quantified the apparent binding constants of two weak trypsin competitors benzylamine (BZA) and methylbenzylamine (MZA), under the same conditions used for benzamidine (BZD). Dose–response curves were recorded with 25 mM TFBA and 300 µM trypsin, both with and without 100 µM Magnevist, allowing us to assess whether

accelerated relaxation affects K_C determination across different affinity ranges. The PRE-induced shortening of T_2 and T_1 was additionally used to test whether reduced TE and TR could be implemented for faster T_2-mapping.

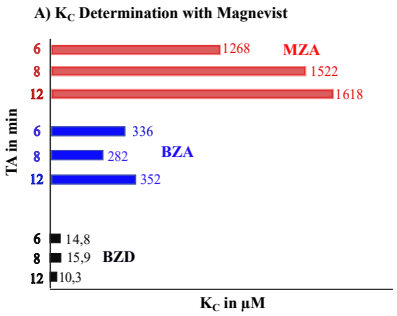

B) Acqusition (AQ) Parameters

TA [min] - AQ Parameters	TE [ms]	TR [s]
6	12 - 372	2,5
8	12 - 492	5
12	20 - 820	5

C) K_C - values without Magnevist

Competitors	K_C Measured TA = 12 min	K_C Literature
MZA	1.7 mM	1.5 mM
BZA	360 µM	300 -350 µM
BZD	13 µM	13-35 µM

Figure 6.4.: Influence of accelerated TE/TR acquisition parameters on the accuracy of K_C determination in the presence of Magnevist for competitors of varying binding strength. (A) Apparent binding constants obtained at three acquisition durations (TA = 12, 8, and 6 min), corresponding to progressively shortened TE and TR values for competitors MZA, BZA, and BZD. (B) Acquisition parameters associated with each temporal acceleration protocol. (C) Reference K_C values obtained without Magnevist under standard acquisition conditions.

Magnevist produced only small changes in the extracted K_C values (TA = 12 min: 10 µM for BZD (baseline 13 µM), 352 µM for BZA (baseline 300 µM), and a larger but still acceptable deviation of 1.6 mM for MZA (baseline 1.7 mM) (Figure 6.4). All deviations remained within the range of reported literature values (Table in Figure 6.4), confirming that Magnevist supports chemically reliable binding validation across strong, weak, and very weak competitors.

To further accelerate the workflow, shorter TE and TR values were used, reducing the acquisition time from 12 min to 6 min. The resulting T_2-maps were then used to re-evaluate the apparent binding affinities in order to quantify how the shortened acquisition window affects the extracted K_C values. The strong competitor BZD showed only minor changes, with K_C values of 10.3 µM, 14.8 µM, and 15.9 µM at TA = 12, 8, and 6 min, respectively (Figure 6.4A). In contrast, the weak competitors exhibited larger shifts, reflecting their smaller PRE-induced T_2 differences. For BZA, the apparent K_C changed from 352 µM (12 min) to 336 µM (8 min) and 282 µM (6 min), while MZA shifted from 1.62 mM (12 min) to 1.52 mM (8 min) and 1.27 mM (6 min). These results confirm that TE/TR acceleration is highly robust for strong binders, where large T_2 differences dominate the displacement contrast, but becomes increasingly sensitive for weak binders whose classification relies on resolving small T_2 changes.

These findings indicate that TE/TR acceleration is highly robust for strong binders but becomes increasingly error-prone for weak and very weak competitors whose determination depends on resolving subtle T_2 differences. Weak competitors are particularly

susceptible to deviations because they generated only small PRE-induced differences in T_2. They produce only very small changes in T_2 because they displace less bound reporter ligand than strong competitors. When TE and TR are shortened, these subtle T_2 differences may become difficult to resolve, and even small fitting errors translate into large shifts in the calculated K_C.

A reduced echo train compresses the dynamic range of the decay, may lower SNR due to incomplete longitudinal recovery, and could increase the relative influence of fitting noise. These may disproportionately affect weak binders, for which the T_2 contrast between bound and free reporter ligand was already small; consequently, small systematic errors in T_2 may propagate into larger deviations in the fitted dose–response curve and the resulting K_C.

Although the acquisition parameters could, in principle, be further optimized for weak competitors, the PRE-based acceleration was benchmarked primarily with the trypsin strong competitors, for which the contrast was most robust under shortened acquisition conditions.

6.4. ^{19}F-PRE: Final acceleration factor in drug discovery

After identifying Magnevist as the most stable and assay-compatible contrast agent, we implemented it in the honeycomb setup as shown in Chapter 5 to quantify the achievable acceleration in sample-parallel binding measurements. In that chapter, under optimized RARE imaging conditions, a 9-fold reduction in total acquisition time was realized compared to fully sampled reference scans (18 min using conventional single-emasurement-setup [DF1]), while maintaining quantitative accuracy in the extracted T_2 values. In this part of the chapter, the maximal reduction factor of the overall measurement time screening 61 compounds in a honeycomb cell array was investigated using Magnevist as a contrast agent with PRE-effect combined with compressed sensing to discover the final acceleration factor.

The selection of 61 samples served not only to exploit the full parallelization capacity of the honeycomb array, but also to broaden its functional use by enabling multiple types of readouts:

- **Acceleration factor:** Comparison of measurement times for binding-affinity validation of strong trypsin competitors (Chapter 5).
- **Protein applicability:** Extension of the assay to an additional protein system, bovine serum albumin (BSA), to benchmark the binding strengths of the known trypsin competitors in an orthogonal environment.
- **Signal-contrast optimization:** Evaluation of displacement behavior in the BSA system using different protein concentrations to optimize ^{19}F signal contrast.

Since the TFBA concentration used during the PRE-effect of Magnevist optimization was 25 mM, in this section it is reduced to 5 mM to achieve the greatest acceleration factor compared to the previous honeycomb setup as described in Chapter 5. Therefore, we first

examined whether the Magnevist concentration of 100 µM should be scaled proportionally to maintain comparable relaxation conditions. This consideration is important because the extent of paramagnetic T_2 shortening depends on the relative ratio of contrast agent to reporter ligand; using an unadjusted Magnevist concentration at lower TFBA levels could otherwise lead to disproportionate PRE effects and overly rapid signal decay.

To validate this assumption, we performed a dedicated control experiment using the capillary setup. Three capillaries containing different concentrations of Magnevist (100 µM and 20 µM for 5 mM TFBA) were measured using the same T_2-mapping RARE protocol applied in the previous optimization experiments (see in Appendix Figure A.2). This assessment enabled us to verify whether the PRE-induced relaxation effects scale appropriately with the reduced TFBA concentration and to determine whether a proportional reduction of Magnevist is required. Contrary to our initial assumption, scaling down the contrast agent to 20 µM was not necessary. The measurements showed that 100 µM Magnevist produced a PRE effect (1.5) of similar magnitude to that observed during the optimization experiments with 25 mM TFBA, whereas it was reduced to 1,2 using 20 µM Magnevist with 5 mM TFBA. Therefore, 100 µM Magnevist was selected for the final application in the honeycomb setup.

The ligand design of the honeycomb setup including two aspects are shown in Figure 6.5 and T_2W-^{19}F-MR images of this setup using 5 mM TFBA with 300 µM trypsin and BSA using 100 µM Magnevist (described detailed in section 6.2) in a competition with 6 trypsin strong competitor ligands (listed in Table 5.1) at a concentration of 30 mM using optimized compressed sensing parameters (shown in Figure A.1).

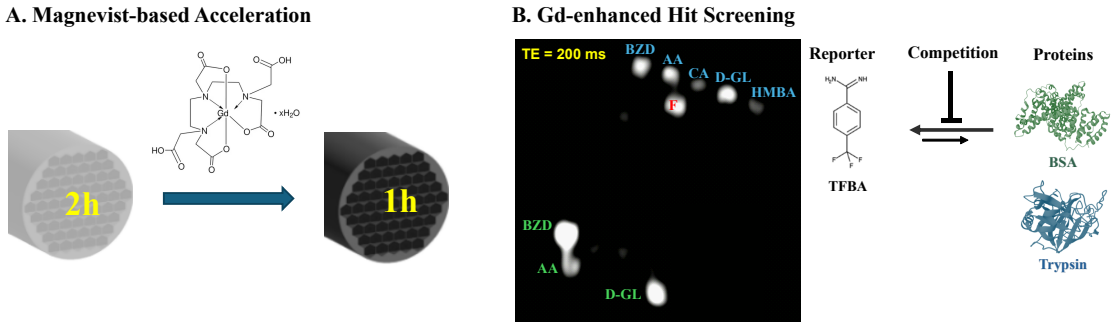

Figure 6.5.: Gd-enhanced ^{19}F-MRI displacement assay for accelerated hit identification across protein targets trypsin and BSA. **(A)** Paramagnetic relaxation enhancement (PRE) induced by Magnevist substantially reduced the acquisition time required for T_2-mapping, decreasing a full honeycomb scan from 2 h to 1 h while preserving the TFBA–protein binding equilibrium. **(B)** Gd-enhanced ^{19}F-MRI displacement images illustrating differential TFBA signal recovery upon competition with non-fluorinated strong hits for proteins trypsin (blue) and BSA (green). Ligands that displaced TFBA were marked in the same color as the corresponding protein target, while free TFBA was marked in red. Imaging parameters were the same as in the Materials and Methods section except for the accelerated acquisition: TR = 2.75 s, TE = 20 ms – 380 ms, compressed-sensing sampling 43 %, and center area 43 %. The PDB ID for the structural visualization of the BSA protein is 3V03.

In total, 61 samples were screened within a measurement time of 55 min, corresponding to a per-sample acquisition time of only 54 s. The competition constants K_C of the strong trypsin ligands were re-evaluated under Magnevist-enhanced conditions, and the resulting values (Table 6.2) deviated only marginally (within ± 20 µM – 30 µM) from those obtained without Magnevist. Since the data for K_C determination without Magnevist was only done on the TFBA-Trypsin system, only these results were compared. Thereby, these results confirmed that the addition of Magnevist does not substantially perturb the TFBA–trypsin or BSA binding equilibrium and can therefore be reliably used to reduce acquisition time. Only hit **12** deviated from this trend for trypsin; this ligand had previously been validated as a weak competitor for trypsin, and the aberrant value observed here is likely caused by bubble formation during sample loading, which partially obstructed the sensitive detection volume and attenuated the TFBA signal.

Building on the robustness of the trypsin–TFBA reference system, we next examined whether the same set of strong hits displayed measurable interactions with BSA. Since the dissociation constant K_D of TFBA for BSA was not determined within the scope of this work, the apparent competition constants K_C could not be calculated for the BSA experiments. Therefore, we quantified binding solely based on the displacement strength F, which reports the relative fraction of TFBA displaced by a competitor, normalized between the fully bound and fully free R_2-relaxation rates of TFBA.

Among the compounds evaluated, only hits **1**, **7**, and **10** produced quantifiable TFBA displacement from BSA, observed as bright contrast in Figure 6.5. Their displacement

Table 6.2.: Comparison of competitor binding affinities for trypsin under Magnevist-enhanced acquisition.

Hit	Compound	K_C [mM] w/o Magnevist	K_C [mM] with Magnevist
1	D-GL	0.04 ± 0.1	0.06 ± 0.1
5	CA	0.09 ± 0.1	0.09 ± 0.1
6	HMBA	0.24 ± 0.1	0.27 ± 0.2
7	BZD	0.05 ± 0.1	0.05 ± 0.1
10	AA	0.04 ± 0.1	0.06 ± 0.1
12	BAEE	0.34 ± 0.1	-

fractions were as follows: hit **7**, 73%; hit **1**, 55%; and hit **10**, 49%. These values indicate that hit **7** is the strongest competitor for BSA, followed by hit **1**, whereas hit **10** exhibited the weakest displacement among the three. Overall, the lower displacement levels compared with the trypsin system suggest weaker interactions with BSA, consistent with the broad and less specific binding characteristics typically associated with serum albumins.

Overall, these results demonstrate that (i) Magnevist effectively accelerates the screening workflow by approximately twofold without compromising the fidelity of the displacement readout, and (ii) the honeycomb cell-array platform is broadly applicable to diverse biochemical questions without requiring any modification of the underlying sample-holder geometry.

6.5. Conclusion

In this work, we established that the gadolinium-based contrast agent Magnevist can be incorporated into the ^{19}F-MRI–driven ligand-screening workflow to substantially reduce the measurement time from 18 min per sample (see the ^{19}F-NMR experiment described in Chapter 4) to just 55 s, without compromising the biochemical integrity of the protein–ligand interactions. This corresponds to an acceleration factor of approximately **20-fold**.

A systematic comparison of chelated versus non-chelated Gd compounds demonstrated that chemically stable formulations provide reliable paramagnetic relaxation enhancement (PRE) while maintaining the native binding equilibrium in competition mode. In particular, Magnevist exhibited no protein-ligand interaction, high chemical robustness, and predictable relaxivity required for quantitative displacement assays based on the T_2-relaxation MR mapping output, whereas the ionic salt $GdCl_3^+$ showed greater sensitivity to the chosen experimental condition, causing a propensity for unspecific interactions. These observations underline the importance of selecting contrast agents.

Dose-response re-evaluation of strong trypsin competitor affinities as a reference system (see Chapter 5) confirmed that the Magnevist usage for PRE-effect did not substantially alter apparent K_C values, validating its robustness for accelerated assays. The honeycomb cell array platform was not only used for trypsin study, but also successfully applied to an additional protein target, BSA, within the same array to find the common competitors, and additionally, the displacement contrast for this protein. This demonstrates that the measurement using honeycomb cell array architecture supports multiple biological hypotheses without the need to redesign or reconfigure the sample holder.

The incorporation of optimized Magnevist into the parallelized honeycomb array enabled T_2-displacement curves to be acquired within seconds per sample, while simultaneously broadening the scientific domain of the workflow, addressing multiple questions. Strong trypsin binders were evaluated for BSA binding as well. Thereby enhancing the conceptual throughput of the assay beyond purely temporal gains. This versatility is essential for early-stage hit validation, where biochemical diversity and the behavior of unknown compounds require a robust and generalizable workflow.

Overall, this Gd-enhanced contrast tuning study for ligand screening establishes a paramagnetically enhanced ^{19}F-MRI assay that meets the core requirements for high-throughput ligand screening: (i) no chemical interference with protein or ligand, (ii) stable and predictable relaxivity alterations, (iii) sufficient contrast efficiency to shorten echo times, (iv) preservation of binding affinities in the presence of the contrast agent, and (v) reproducible handling for multi-sample operation.

By demonstrating that measurement time can be reduced while maintaining quantitative accuracy, the approach offers a promising platform for accelerating early drug-discovery assays and expands the practical utility of ^{19}F-MRI as a parallelized screening modality capable of handling biochemically diverse and unknown compounds.

7. Conclusion & Outlook

This thesis presents a comprehensive strategy for transforming ^{19}F magnetic resonance imaging (MRI) into a practical, rapid, and high-throughput screening platform for the quantitative analysis of ligand libraries. Beginning with bundled NMR tubes and progressing through capillary-based microarrays to a final miniaturized 61-cell honeycomb array, we demonstrated how systematic sample-holder engineering can dramatically enhance spatial parallelization. Each design iteration increased the number of simultaneously analyzable samples by confining individual protein–ligand reactions to discrete voxels, effectively converting the imaging field into a multiplexed biochemical assay while maintaining spectroscopic specificity and biochemical fidelity.

By selectively detecting the ^{19}F signal of fluorinated reporter ligands, a chemically agnostic assay was established that does not require fluorescent, isotopic, or radioactive labeling of proteins or ligands. The transverse-relaxation (T_2) contrast arising from the binding states of the reporter ligand proved robust against protein and water background signals, enabling clean displacement profiles even for weakly binding, non-fluorinated competitors. Voxel-wise T_2-mapping allowed the simultaneous quantification of apparent binding constants (K_C) across dozens of competitors for both trypsin and PPAT, underscoring the biochemical versatility of the platform.

Two complementary sample formats—a capillary array and a high-density honeycomb array—formed the basis for true multi-sample parallelization. In particular, the honeycomb architecture maximized filling factor, ensured reproducible T_2 mapping, and enabled complete displacement curves to be recorded within a single MRI experiment. This eliminated the time-consuming sequential workflow characteristic of conventional NMR assays, which typically require hours to days of measurement time.

Because miniaturized sample geometries require increased spatial resolution, which in turn prolongs acquisition times, a compressed sensing (CS) reconstruction scheme was implemented. By focusing sampling on the contrast-bearing central region of k-space, measurement times were significantly reduced while preserving quantitative accuracy in R_2 and K_C.

Further acceleration was achieved through paramagnetic relaxation enhancement (PRE) using the clinically established contrast agent Magnevist. By substantially shortening both T_1 and T_2, Magnevist enabled reduced echo and repetition times, resulting in more than an order-of-magnitude reduction in acquisition time while maintaining the protein–ligand binding equilibrium. PRE-based acceleration, combined with spatial parallelization, thus unlocked dual-axis speed-up across both sample number and measurement time.

The ^{19}F-MRI platform using integrated methodology of sample parallelization, PRE- and CS-based temporal acceleration enabled the simultaneous analysis of 61 non-fluorinated ligand samples within a single experiment in 54 s per sample. This corresponded to at least a twentyfold acceleration compared with sequential ^{19}F-NMR assays (20 min per sample).

Moreover, the samples could be classified into distinct binding categories, demonstrating the assay's relevance and applicability for early drug discovery workflows.

Taken together, ^{19}F-selective detection—positions MRI as an emerging analytical tool for high-content biochemical screening. The platform is well-suited for functional assays, fragment-based discovery, structure–activity relationship (SAR) investigations, and mechanistic enzymology, expanding the role of MRI beyond anatomical imaging into the domain of early-stage drug discovery.

Several directions offer potential to further increase throughput and expand the platform's capabilities. Sample density may be increased through higher-resolution or multilayer honeycomb arrays, or by integrating automated loading systems and flow-through architectures [32,145], enabling hundreds of distinct protein–ligand mixtures to be screened in a single experiment. Additional gains in acquisition speed could be achieved through rapid *k*-space traversal schemes (e.g., spiral imaging, EPI) [146–148] or more advanced sparse-sampling and model-driven reconstruction methods, potentially pushing per-sample measurement times into the sub-second regime.

Hyperpolarization techniques such as Signal amplification by reversible exchange (SABRE) or dissolution dynamic nuclear polarization (DNP) [75] provide a further route for dramatically boosting signal-to-noise ratio and could enable single-shot displacement measurements. Beyond throughput, the biological scope could be expanded to multienzyme panels, fragment libraries, membrane proteins, and intrinsically disordered proteins. Finally, combining parallelized ^{19}F-MRI with machine-learning-based hit classification, digital-twin experiment optimization, and automated sample handling may ultimately yield a fully integrated, high-throughput screening pipeline for early-stage drug discovery.

A. Appendix

A.1. Chemical preparation of drug candidates with different solubility

Table A.1.: Hydrophobic compounds for drug screening

Solvent	Compound
9*DMSO	Aspartate
	Cystine
	Tyrosine
	Biphely-phenyl urea
	Benzoaminomethylphenol
	Methotrexate
	Aniline
	Salicylic acid
	Ibuprofen
2*Chloroform	Ergosterol
	Adamantane

Table A.2.: Hydrophilic compounds for drug screening

L-Alanine	Sodium acetate	Trizma acetate
R-2-Aminobutanol	S-2-Aminobutanol	Arginine
Asparagine	Cysteine	Methylbenzylamine
Glutamine	Aspartic acid	Glutamic acid
Glycine	Histidine	Isoleucine
Leucine	Lysine	Methionine
Phenylalanine	Proline	Serine
Threonine	Tryptophan	Valine
Glucose	Lactose	Sucrose
Benzamidine	Benzylamine	Starch
Benzoylarginineethylester	Imidazole	Hydroquinone
Glucosamine	L-Ascorbic acid	Glucono-delta-lactone
N-Hydroxysuccinimide	D-Maltose	Nicotinamide
Pyruvic acid	Alginic acid	Polyethylenglycol
D-Alanine	Hydroxy-Methylbutyric acid	Citric acid
Dimethylaminopropyl-Ethylcarboimide	Poly(vinyl alcohol)	Urea
Acetyl-L-phenylalanine	Mannitol	

A.2. *k*-space representation for CS

To visualize the *k*-space distribution of CS sampling, we simulated *k*-space with different CS parameters using a Shepp-Logan phantom [149], which consists of multiple elliptical structures with varying intensities, thereby simulating brain-like tissue contrasts (Figure A.1). To mimic real MRI acquisition, Cartesian undersampling masks were simulated with a fully sampled central *k*-space area (CA) and uniform random sampling across the remaining *k*-space. Three CA values (100%, 43% and 22%) were compared at a fixed overall sampling fraction of 43%.

Overall, our simulated CS undersampling patterns demonstrated that preserving image quality is closely tied to the chosen sampling strategy, with particular emphasis on the importance of the central *k*-space for diagnostic accuracy.

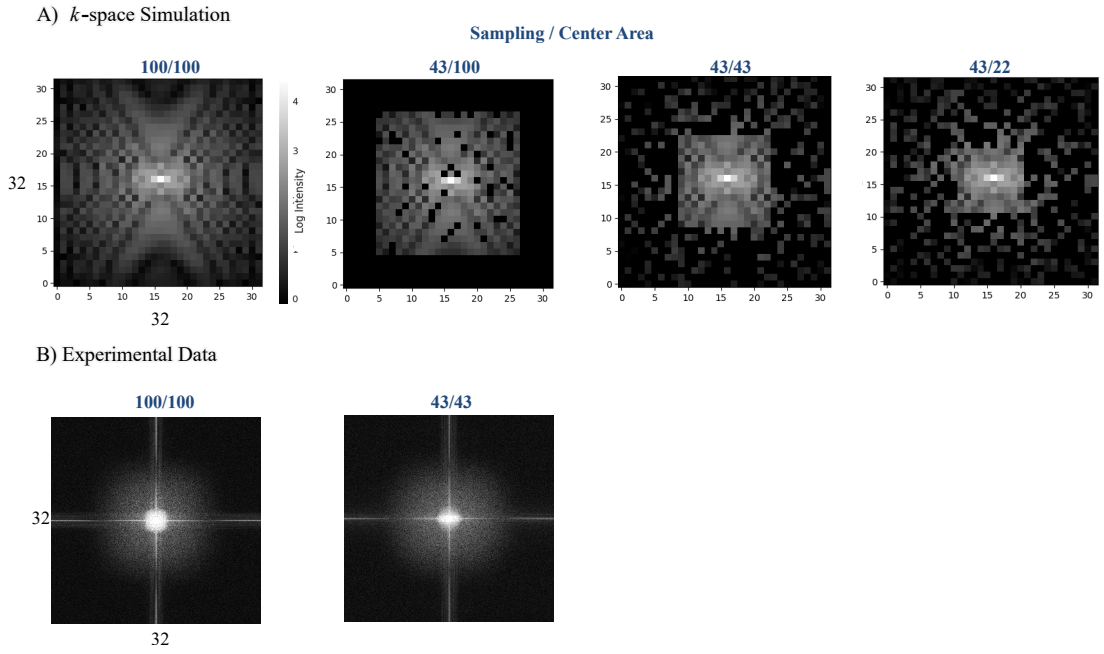

Figure A.1.: Simulated MRI *k*-space representation of Shepp-Logan phantom with varying degrees of compressed sensing undersampling and center *k*-space retention and experimental *k*-space data of the honeycomb image from Figure 3 in fully sampled and undersampled versions. Signal intensity is shown as the logarithmically scaled magnitude of the Fourier transform after applying the undersampling mask. The size of the images was MTX 32×32. The simulated image is for illustrative purposes and not derived from experimental data. The imaging parameters for the experimental data are given in the referred figure.

A.3. Generate a 2D Cartesian undersampling mask

The following Python script reads *k*-space rawdata from a Bruker dataset.

```
import sys, numpy as np
from pathlib import Path
from PIL import Image
from brukerapi.dataset import Dataset

def open_dataset(exp: Path):
    # Try opening the **folder** first
    try:
        return Dataset(str(exp))
    except Exception as e1:
        # Fallback: try opening the **file** directly
        rd = exp / "rawdata.job0"
        if not rd.exists():
```

```
            raise FileNotFoundError(f"rawdata.job0 not found in {exp}")
        try:
            return Dataset(str(rd))
        except Exception as e2:
            print("Tried folder and file; both failed.")
            print("Folder error:", repr(e1))
            print("File error  :", repr(e2))
            raise

if __name__ == "__main__":
    if len(sys.argv) < 2:
        print('Usage: py read_rawdata_job0.py "F:/path/to/EXPno/"')
        sys.exit(1)

    exp = Path(sys.argv[1])
    if not exp.exists():
        raise FileNotFoundError(f"Experiment folder not found: {exp}")

    with open_dataset(exp) as d:
        raw = d.data
        print("dataset type:", d.type, "shape:", raw.shape, "dtype:", raw.dtype)

        # If last axis is [Re,Im], convert to complex
        if raw.dtype.kind != 'c' and raw.shape[-1] == 2:
            raw = raw[..., 0] + 1j * raw[..., 1]

        np.save(exp / "kspace_rawdata_job0.npy", raw)

        # Readout length (nx)
        try:
            nx = int(d["ACQ_size"].value[0])
        except Exception:
            nx = raw.shape[-1]

        flat = raw.reshape(-1, nx)

        # Guess coils (adjust if you know it)
        for ncoils in (32, 16, 8, 4, 2, 1):
            if flat.shape[0] % ncoils == 0:
                break

        ks = flat.reshape(ncoils, flat.shape[0] // ncoils, nx)
        np.save(exp / "kspace_coils.npy", ks)

        # Quick 2D preview: IFFT2 per coil -> RSS
```

```
k2 = ks[:, :ks.shape[1], :]
img = np.fft.ifftshift(np.fft.ifft2(np.fft.fftshift
(k2, axes=(-2, -1))), axes=(-2, -1))
rss = np.sqrt((np.abs(img) ** 2).sum(axis=0))
rss = (rss - rss.min()) / (rss.max() - rss.min() + 1e-12)
Image.fromarray((rss * 255).astype("uint8")).save(exp
/ "img_rss_from_rawdata_job0.png")
```

A.4. Magnevist concentration optimization for TFBA

The T_2-relaxation mapping was recorded using two different Magnevist concentrations (100 µM and 50 µM) to investigate the PRE effect on the reporter ligand TFBA at the concentration of 5 mM using RARE protocol. The ROI is driven over the samples concentration three different samples shown in Figure A.2.

Figure A.2.: T_2-mapping analysis in Bruker ParaVision using freehand ROIs. The left panel shows the multi-echo ^{19}F-MRI image of free TFBA (5 mM with three selected freehand regions of interest (ROIs), each corresponding to distinct sample compartments (1 - 100 µM, 2 - no magnevist, 3 - 50 µM) within the capillary array. The right panel displays the ParaVision fitting interface, showing the mono-exponential signal decay fit for each ROI across all echo times. Extracted fitting parameters include the amplitude (A), offset (C), and T_2 relaxation time, together with associated standard deviations and degrees of freedom. This interface allows direct comparison of T_2values between different sample regions under identical acquisition conditions.

Bibliography

[1] T. R. Carver and C. P. Slichter. Polarization of nuclear spins in metals. *Physical Review*, 92(1):212–213, 1953.

[2] Albert W. Overhauser. Polarization of nuclei in metals. *Physical Review*, 92(2):411–415, 1953.

[3] R. Lekshmi, Manoj Gupta, Sweety Gupta, Deepa Joseph, Ajay S. Krishnan, Pankaj Sharma, Swati Verma, Shreyosi Mandal, and R. S. Namitha. Comparison of magnetic resonance imaging and CT scan–based delineation of target volumes and organs at risk in the radiation treatment planning of head and neck malignancies. *Journal of Medical Imaging and Radiation Sciences*, 54(3):503–510, September 2023.

[4] Nisha Rai, Rajeev K. Ranjan, Anima R. Xalxo, and Suresh K. Toppo. Comparative study of MRI and ultrasound in diagnosing musculoskeletal soft tissue tumours. *Journal of Pharmacy and Bioallied Sciences*, 16:S3806–S3808, December 2024.

[5] Usman Bashir, Andrew Mallia, James Stirling, John Joemon, Jane MacKewn, Geoff Charles-Edwards, Vicky Goh, and Gary J. Cook. PET/MRI in Oncological Imaging: State of the Art. *Diagnostics*, 5(3):333–357, 2015.

[6] J. Perlo, F. Casanova, and B. Blümich. Profiles with microscopic resolution by single-sided NMR. *Journal of Magnetic Resonance*, 176(1):64–70, 2005.

[7] Francesca Iacobellis, Marco Di Serafino, Camilla Russo, Roberto Ronza, Martina Caruso, Giuseppina Dell'Aversano Orabona, Costanza Camillo, Vittorio Sabatino, Dario Grimaldi, Chiara Rinaldo, Luigi Barbuto, Francesco Verde, Giuliana Giacobbe, Maria Laura Schillirò, Enrico Scarano, and Luigia Romano. Safe and informed use of gadolinium-based contrast agent in body magnetic resonance imaging: Where we were and where we are. *Journal of Clinical Medicine*, 13(8), 2024.

[8] Martin Bendszus, Andrea Laghi, Josep Munuera, Lawrence N. Tanenbaum, Bachir Taouli, and Harriet C. Thoeny. MRI Gadolinium-Based Contrast Media: Meeting Radiological, Clinical, and Environmental Needs. *Journal of Magnetic Resonance Imaging*, 60(5):1774–1785, 2024.

[9] Mustafa R. Bashir and Kerry L. Thomas. A New Generation of Gadolinium-based MRI Contrast Agents: Higher Relaxivity, Lower Dose. *Radiology*, 308(1):e231454, 2023. PMID: 37462492.

[10] S. Lawson and J. Zhu. Image compression using wavelets and JPEG2000: A tutorial. *Proceedings of [venue unspecified]*, 2002. Tutorial on DWT and its application to the JPEG2000 image compression standard.

[11] Roberto F. Delgadillo, Timothy C. Mueser, Kathia Zaleta-Rivera, Katie A. Carnes, José González-Valdez, and Lawrence J. Parkhurst. Detailed characterization of the solution kinetics and thermodynamics of biotin, biocytin and haba binding to avidin and streptavidin. *PLOS ONE*, 14(2):e0204194, 2019.

[12] Saghir Ali and Jia Zhou. Highlights on U.S. FDA-approved fluorinated drugs over the past five years (2018–2022). *European Journal of Medicinal Chemistry*, 256:115476, 2023.

[13] Emily Henary, Stefanie Casa, Tyler L. Dost, Joseph C. Sloop, and Maged Henary. The role of small molecules containing fluorine atoms in medicine and imaging applications. *Pharmaceuticals*, 17(3), 2024.

[14] Claudio Dalvit and Anna Vulpetti. Ligand-Based Fluorine NMR Screening: Principles and Applications in Drug Discovery Projects. *Journal of Medicinal Chemistry*, 62(5):2218–2244, 2019.

[15] Alvar D. Gossert and Wolfgang Jahnke. NMR in drug discovery: A practical guide to identification and validation of ligands interacting with biological macromolecules. *Progress in Nuclear Magnetic Resonance Spectroscopy*, 97:82–125, 2016.

[16] Claudio Dalvit, Isabel Gmür, Philip Rößler, and Alvar D. Gossert. Affinity measurement of strong ligands with NMR spectroscopy: Limitations and ways to overcome them. *Progress in Nuclear Magnetic Resonance Spectroscopy*, 138-139:52–69, 2023.

[17] Claudio Dalvit, Maria Flocco, Marina Veronesi, and Brian J Stockman. Fluorine-NMR competition binding experiments for high-throughput screening of large compound mixtures. *Combinatorial chemistry & high throughput screening*, 5(8):605—611, December 2002.

[18] Claudio Dalvit, Paul E. Fagerness, Daneen T. A. Hadden, Ronald W. Sarver, and Brian J. Stockman. Fluorine-NMR Experiments for High-Throughput Screening: Theoretical Aspects, Practical Considerations, and Range of Applicability. *Journal of the American Chemical Society*, 125(25):7696–7703, 2003. PMID: 12812511.

[19] Claudio Dalvit, Annick Parent, Francois Vallée, Magali Mathieu, and Alexey Rak. Fast NMR Methods for Measuring in the Direct and/or Competition Mode the Dissociation Constants of Chemical Fragments Interacting with a Receptor. *ChemMedChem*, 14(11):1115–1127, 2019.

[20] Simon Rüdisser, Nils Goldberg, Marc-Olivier Ebert, Helena Kovacs, and Alvar Gossert. Efficient affinity ranking of fluorinated ligands by ^{19}F NMR: CSAR and FastCSAR. *Journal of Biomolecular NMR*, 74, 11 2020.

[21] Claudio Dalvit, Gianluca Fogliatto, Alan Stewart, Marco Veronesi, and Brian Stockman. WaterLOGSY as a method for primary NMR screening: practical aspects and range of applicability. *Journal of Biomolecular NMR*, 21(4):349–359, 2001.

[22] Julien M. Orts, Alvar D. Gossert, Beat Vögeli, and et al. ^{19}F NMR in Fragment-Based Drug Discovery: Simple, Sensitive, and Efficient. *J. Med. Chem.*, 59(11):5078–5089, 2016.

[23] Anna Vulpetti, Ulrich Hommel, Gregory Landrum, Richard Lewis, and Claudio Dalvit. Design and NMR-Based Screening of LEF, a Library of Chemical Fragments with Different Local Environment of Fluorine. *Journal of the American Chemical Society*, 131(36):12949–12959, 2009. PMID: 19702332.

[24] Guilherme V. de Castro and Alessio Ciulli. Spy vs. spy: selecting the best reporter for ^{19}F NMR competition experiments. *Chemical Communications*, 55:1482–1485, 2019.

[25] Jerrold T. Bushberg, J. Anthony Seibert, Edwin M. Leidholdt, and John M. Boone. *The Essential Physics of Medical Imaging*. Wolters Kluwer Health / Lippincott Williams & Wilkins, Philadelphia, 3 edition, 2012.

[26] W. R. Nitz and P. Reimer. Contrast mechanisms in MR imaging. *European Radiology*, 9(6):1032–1046, 1999.

[27] Denis Le Bihan and Masashi Iima. Diffusion magnetic resonance imaging: What water tells us about biological tissues. *PLoS Biology*, 13(7), 2015.

[28] Susan J. Holdsworth, Stefan Skare, Richard Newbould, and Roland Bammer. Magnetic Resonance Imaging Techniques: fMRI, DWI, and Perfusion MRI. *Clinical Radiology*, 63(12):1375–1387, 2008.

[29] Pedro A. Gómez, Miguel Molina-Romero, Guido Buonincontri, Marion I. Menzel, and Bjoern H. Menze. Designing contrasts for rapid, simultaneous parameter quantification and flow visualization with quantitative transient-state imaging. *Scientific Reports*, 9(1):8468, 2019.

[30] M. Victoria Gomez and Antonio de la Hoz. NMR reaction monitoring in flow synthesis. *Beilstein Journal of Organic Chemistry*, 13:285–300, 2017.

[31] David A. Foley, Eckhard Bez, Anna Codina, Kimberly L. Colson, Michael Fey, Robert Krull, Don Piroli, Mark T. Zell, and Brian L. Marquez. NMR Flow Tube for Online NMR Reaction Monitoring. *Analytical Chemistry*, 86(24):12008–12013, 2014.

[32] Omar Nassar, Mazin Jouda, Michael Rapp, Dario Mager, Jan G. Korvink, and Neil MacKinnon. Integrated impedance sensing of liquid sample plug flow enables automated high throughput NMR spectroscopy. *Microsystems & Nanoengineering*, 7(1):30, 2021.

[33] J. Bart, J. W. G. Janssen, P. J. M. van Bentum, A. P. M. Kentgens, and J. G. E. Gardeniers. Optimization of stripline-based microfluidic chips for high-resolution NMR. *Journal of Magnetic Resonance*, 201(2):175–185, 2009.

[34] William Hale, Gabriel Rossetto, Rachael Greenhalgh, Graeme Finch, and Marcel Utz. High-resolution nuclear magnetic resonance spectroscopy in microfluidic droplets. *Lab on a Chip*, 18:3018–3024, 2018.

[35] T. Hou, J. Smith, E. MacNamara, M. Macnaughtan, and D. Raftery. Analysis of multiple samples using multiplex sample NMR: Selective excitation and chemical shift imaging approaches. *Analytical Chemistry*, 73(11):2541–2546, 2001.

[36] Ēriks Kupče, Ray Freeman, and Robert B. K. John. Parallel acquisition of two-dimensional NMR spectra of several nuclear species. *Journal of the American Chemical Society*, 128(30):9606–9607, 2006.

[37] Ēriks Kupče. NMR with Multiple Receivers. In *Topics in Current Chemistry*, volume 335, pages 71–96. Springer, Berlin, Heidelberg, 2013.

[38] Helga Kovács and Ēriks Kupče. Parallel NMR spectroscopy with simultaneous detection of ^{1}H and ^{19}F nuclei. *Magnetic Resonance in Chemistry*, 54(7):544–560, 2016.

[39] Ēriks Kupče, Timothy D. W. Claridge, and J. Reuben J. Yong. Parallel Nuclear Magnetic Resonance Spectroscopy (PANSY) and NOAH Supersequences: A Primer. *Nature Reviews Methods Primers*, 1(27), 2021.

[40] Ēriks Kupče and Timothy D. W. Claridge. NOAH: NMR Supersequences for Small Molecule Analysis and Structure Elucidation. *Angewandte Chemie International Edition*, 56(39):11779–11783, 2017.

[41] J. Reuben J. Yong, Ēriks Kupče, and Timothy D. W. Claridge. Modular Pulse Program Generation for NMR Supersequences. *Analytical Chemistry*, 94(4):2271–2278, 2022.

[42] Nirbhay N Yadav, Xing Yang, Yuguo Li, Wenbo Li, Guanshu Liu, and Peter C M van Zijl. Detection of dynamic substrate binding using MRI. *Scientific Reports*, 7(1):10138, 2017.

[43] Luis M. De Leon-Rodriguez, A. Valdez Ortiz, Allison L Weiner, Shanrong Zhang, Zoltán Kovács, Thomas Kodadek, and A. Dean Sherry. Magnetic resonance imaging detects a specific peptide-protein binding event. *Journal of the American Chemical Society*, 124 14:3514–5, 2002.

[44] Paul T. Callaghan. *Principles of Nuclear Magnetic Resonance Microscopy*. Oxford University Press, Oxford, UK, 1991.

[45] Jinguo Wang, Mikko I. Kettunen, De-en Hu, Timothy H. Witney, and Kevin M. Brindle. Accelerated Chemical Shift Imaging of Hyperpolarized ^{13}C Using Compressed Sensing. *Magnetic Resonance in Medicine*, 76(6):1720–1732, 2016.

[46] Jian Zhou and Peter C. M. van Zijl. Chemical exchange saturation transfer imaging and spectroscopy. *Progress in Nuclear Magnetic Resonance Spectroscopy*, 48(2–3):109–136, 2006.

[47] Jan Henrik Ardenkjaer-Larsen, Bengt Fridlund, Andreas Gram, Goran Hansson, L. Hansson, Mathilde H. Lerche, Rolf Servin, Marcus Thaning, and Klaus Golman. Increase in signal-to-noise ratio of >10,000 times in liquid-state NMR. *Proceedings of the National Academy of Sciences*, 100(18):10158–10163, 2003.

[48] Axel Haase, Jens Frahm, Dieter Matthaei, Wolfgang Hänicke, and Klaus-Dietmar Merboldt. Selective excitation in magnetic resonance imaging. *Journal of Magnetic Resonance*, 63(3):533–540, 1985.

[49] Jing Yuan Yu, Rami R. Hallac, Jenny Choi, Dong-Hoon Lee, and Mark D. Pagel. Fluorine-19 magnetic resonance imaging in drug discovery and development. *Current Medicinal Chemistry*, 20(3):376–404, 2013.

[50] 3D-Druck-Service. 3d printing service. `https://www.3d-druck-service.ch`. Zurich, Switzerland. Accessed December 10, 2025.

[51] National Electrical Manufacturers Association. *Characterization of Phased Array Coils for Diagnostic Magnetic Resonance Images*, volume MS 9-2008 (R2014, R2020). National Electrical Manufacturers Association, 2008. https://www.nema.org/Standards/view/Determination-of-Image-Uniformity-in-Diagnostic-Magnetic-Resonance-Images (accessed on 18.03.2024).

[52] Andreas K. P. Lundgren and Ray Freeman. *NMR Probeheads for Biophysical and Biomedical Experiments: Theoretical Principles & Practical Guidelines*. Imperial College Press, London, 2000.

[53] Costas D. Constantinides, Ergin Atalar, and Elliot R. McVeigh. Signal-to-noise measurements in magnitude images from NMR phased arrays. *Magnetic Resonance in Medicine*, 38(5):852–857, 1997.

[54] Peter Kellman and Elliot R. McVeigh. Image reconstruction in SNR units: a general method for SNR measurement. *Magnetic Resonance in Medicine*, 54(6):1439–1447, 2005.

[55] David I. Hoult and Collins D. Phil. The B_1 field distribution, RF penetration, and signal inhomogeneity in human head at high field. *Journal of Magnetic Resonance Imaging*, 12(1):46–67, 2000.

[56] F. David Doty, Gary Entzminger, and Aimin Yang. Magnetism and the design of NMR RF coils. *Progress in Nuclear Magnetic Resonance Spectroscopy*, 50(3-4):207–282, 2007.

[57] D. I. Hoult and R. E. Richards. The signal-to-noise ratio of the nuclear magnetic resonance experiment. *J. Magn. Reson.*, 24(1):71–85, 1976.

[58] Arun Kumar, D. Welti, and Richard R. Ernst. NMR Fourier zeugmatography. *Journal of Magnetic Resonance*, 18(1):69–83, 1975.

[59] Daniel A. Erlanson, R. Scott McDowell, and Timothy O'Brien. Fragment-based drug discovery. *Journal of Medicinal Chemistry*, 47:3463–3482, 2004.

[60] Daniel A. Erlanson, Stephen W. Fesik, Ryan E. Hubbard, Walter Jahnke, and H. Jhoti. Twenty years on: the impact of fragments on drug discovery. *Nature Reviews Drug Discovery*, 15:605–619, 2016.

[61] Tim Kirkman et al. How to find a fragment: Methods for screening and validation in fragment-based drug discovery. *ChemMedChem*, 19(24):e202400342, 2024.

[62] Sandeep S Vansal and Dennis R Feller. Direct effects of ephedrine isomers on human -adrenergic receptor subtypes. *Biochemical Pharmacology*, 58(5):807–810, 1999.

[63] Jillian G. Baker, Sheila M. Gardiner, Jeanette Woolard, Christophe Fromont, Gopal P. Jadhav, Shailesh N. Mistry, Kevin S. J. Thompson, Barrie Kellam, Stephen J. Hill, and Peter M. Fischer. Novel selective 1-adrenoceptor antagonists for concomitant cardiovascular and respiratory disease. *The FASEB Journal*, 31(7):3150–3166.

[64] Suzanne B. Shuker, Philip J. Hajduk, Robert P. Meadows, and Stephen W. Fesik. Discovering High-Affinity Ligands for Proteins: SAR by NMR. *Science*, 274(5292):1531–1534, 1996.

[65] Philip J. Hajduk and Stephen W. Fesik. NMR-based screening in drug discovery. *Journal of Medicinal Chemistry*, 40(19):3147–3159, 1997.

[66] Paul A. Bottomley. Mr spectroscopy of the human heart: The status and the challenges. *Radiology*, 220(3):580–591, 2002.

[67] Yong Zhou, Peter C. M. van Zijl, Keith S. St. Lawrence, and et al. Oxygen-17 magnetic resonance imaging of metabolic pathways in brain. *Proc. Natl. Acad. Sci. U.S.A.*, 98(20):11085–11090, 2001.

[68] Xiang Zhu, Nai Zhang, Nigel R. Sibson, and et al. ^{17}O MRI of Cerebral Oxygen Metabolism in Humans at 7 Tesla, journal = Proc. Natl. Acad. Sci. U.S.A. 102(43):15758–15763, 2005.

[69] Klaes Golman, Rianne in't Zandt, and Mathilde Lerche. Metabolic imaging by hyperpolarized ^{13}c magnetic resonance imaging for in vivo tumor diagnosis. *Cancer Res.*, 66(22):10855–10860, 2006.

[70] Hyejin Park and Qiu Wang. State-of-the-art accounts of hyperpolarized ^{15}N-labeled molecular imaging probes for magnetic resonance spectroscopy and imaging. *Chemical Science*, 13:7378–7391, 2022.

[71] Eric T. Ahrens, Rodrigo Flores, Haiwei Xu, and Pierre A. Morel. In Vivo Imaging Platform for Tracking Immunotherapeutic Cells. *Nature Biotechnology*, 23(8):983–987, 2005.

[72] William E Hull and Brian D Sykes. Fluorotyrosine alkaline phosphatase: Internal mobility of individual tyrosines and the role of chemical shift anisotropy as a ^{19}F nuclear spin relaxation mechanism in proteins. *Journal of Molecular Biology*, 98(1):121–153, 1975.

[73] Mohammad Rasool Vaezi K., Jan G. Korvink, and Mazin Jouda. Simultaneous multinuclear MRI via a single RF channel. *Journal of Magnetic Resonance*, 368:107782, 2024.

[74] Yaewon Kim and Christian Hilty. Affinity Screening Using Competitive Binding with Fluorine-19 Hyperpolarized Ligands. *Angewandte Chemie International Edition*, 54(16):4941–4944, 2015.

[75] Yaewon Kim, Mengxiao Liu, and Christian Hilty. Determination of binding affinities using hyperpolarized NMR with simultaneous 4-channel detection. *Journal of Magnetic Resonance*, 295:80–86, 2018.

[76] Youngbok Lee, Haifeng Zeng, Simon Ruedisser, Alvar D. Gossert, and Christian Hilty. Nuclear magnetic resonance of hyperpolarized fluorine for characterization of protein–ligand interactions. *Journal of the American Chemical Society*, 134(42):17448–17451, 2012.

[77] W. Bode and P. Schwager. The refined 1.8 Å crystal structure of bovine -trypsin at 1.8 Å resolution: Interaction of the active site with benzamidine. *Journal of Molecular Biology*, 98(4):693–717, 1976.

[78] Ken Kasai and Shin Ishii. Studies on the interaction of immobilized trypsin and specific ligands by quantitative affinity chromatography. *The Journal of Biochemistry*, 84(5):1061–1069, 11 1978.

[79] Alexandre Blanco, Alfonso Cabezón, Alejandro Seco-González, Daniel Conde-Torres, Paula Antelo-Riveiro, Ángel Piñeiro, and Rebeca Garcia-Fandino. The Role of AI in Drug Discovery: Challenges, Opportunities, and Strategies. *Pharmaceuticals*, 16:891, 06 2023.

[80] Dhamodharan Ganesan and C Gopi Mohan. Machine learning models for predicting the activity of ache and bace1 dual inhibitors for the treatment of alzheimer's disease. *Molecular Diversity*, 26:1–17, 06 2022.

[81] William Peters, Verna Frasca, and Richard Brown. Recent Developments in Isothermal Titration Calorimetry Label Free Screening. *Combinatorial chemistry & high throughput screening*, 12:772–90, 10 2009.

[82] Francisco E Torres, Michael I Recht, Joseph E Coyle, Richard H Bruce, and Glyn Williams. Higher throughput calorimetry: opportunities, approaches and challenges. *Current Opinion in Structural Biology*, 20(5):598–605, 2010.

[83] Xiao Xu, Qidi Ran, Pradip Dey, Rohit Nikam, Rainer Haag, Matthias Ballauff, and Joachim Dzubiella. Counterion-release entropy governs the inhibition of serum proteins by polyelectrolyte drugs. *Biomacromolecules*, 19(2):409–416, 2018. PMID: 29268015.

[84] Jiří Homola, Petr Malík, Kateřina Hegnerová, Marek Piliarik, Ivan Tichý, Petr Štěpánek, Jakub Dostálek, Jaroslav Turánek, Petr Skládal, and Jakub Dostalek. Analysis of biomolecular interactions using a miniaturized surface plasmon resonance sensor. *Sensors and Actuators B: Chemical*, 87(2):276–281, 2002.

[85] Craig S Schneider, Adip G Bhargav, Jimena G Perez, Aniket S Wadajkar, Jeffrey A Winkles, Graeme F Woodworth, and Anthony J Kim. Surface plasmon resonance as a high throughput method to evaluate specific and non-specific binding of nanotherapeutics. *Journal of Controlled Release*, 219:331–344, 2015.

[86] Alexander N Grigorenko, Petr I Nikitin, Alexander A Beloglazov, Anatoly V Zayats, and Andrey K Sarychev. Miniaturized quantum semiconductor surface plasmon resonance platform for detection of biological molecules. *Biosensors*, 3(2):201–209, 2013.

[87] Fangrong Zhang, Gesa Richter, Benjamin Bourgeois, Emil Spreitzer, Armin Moser, Andreas Keilbach, Petra Kotnik, and Tobias Madl. Small-Angle X-ray Scattering for PEGylated Liposomal Doxorubicin Drugs: An Analytical Model Comparison Study. *Molecular Pharmaceutics*, 20(9):4654–4663, 2023.

[88] A.R. von Gundlach, V.M. Garamus, T. Gorniak, H.A. Davies, M. Reischl, R. Mikut, K. Hilpert, and A. Rosenhahn. Small angle X-ray scattering as a high-throughput method to classify antimicrobial modes of action. *Biochimica et Biophysica Acta (BBA) - Biomembranes*, 1858(5):918–925, 2016.

[89] Fangrong Zhang, Gesa Richter, Benjamin Bourgeois, Emil Spreitzer, Armin Moser, Andreas Keilbach, Petra Kotnik, and Tobias Madl. A General Small-Angle X-ray Scattering-Based Screening Protocol for Studying Physical Stability of Protein Formulations. *Pharmaceutics*, 14(1):69, 2022.

[90] Markus Mayer and Bernd Meyer. Characterization of Ligand Binding by Saturation Transfer Difference NMR Spectroscopy. *Angewandte Chemie International Edition*, 38(12):1784–1788, 1999.

[91] Bernd Meyer and Thomas Peters. NMR Spectroscopy Techniques for Screening and Identifying Ligand Binding to Protein Receptors. *Angewandte Chemie International Edition*, 42(8):864–890, 2003.

[92] Claudio Dalvit, Maria Flocco, Stefan Knapp, Marina Mostardini, Rita Perego, Brian J. Stockman, Marina Veronesi, and Mario Varasi. High-Throughput NMR-Based Screening with Competition Binding Experiments. *Journal of the American Chemical Society*, 124(26):7702–7709, 2002. PMID: 12083923.

[93] Claudio Dalvit, Paolo Pevarello, Marco Tatò, Marina Veronesi, Anna Vulpetti, and Michael Sundström. Identification of compounds with binding affinity to proteins via magnetization transfer from bulk water. *Journal of biomolecular NMR*, 18:65–8, 10 2000.

[94] Ales Medek, Philip J. Hajduk, Jamey Mack, and Stephen W. Fesik. The use of differential chemical shifts for determining the binding site location and orientation of protein-bound ligands. *Journal of the American Chemical Society*, 122(6):1241–1242, 2000.

[95] Jasna Fejzo, Christopher A Lepre, Jeffrey W Peng, Guy W Bemis, Ajay, Mark A Murcko, and Jonathan M Moore. The SHAPES strategy: an NMR-based approach for lead generation in drug discovery. *Chemistry Biology*, 6(10):755–769, 1999.

[96] Mike P. Williamson. Using chemical shift perturbation to characterise ligand binding. *Progress in Nuclear Magnetic Resonance Spectroscopy*, 73:1–16, 2013.

[97] Yang Zhou, Chongxue Bie, Peter C. M. van Zijl, Jiadi Xu, Chao Zou, and Nirbhay N. Yadav. Detection of electrostatic molecular binding using the water proton signal. *Magnetic Resonance in Medicine*, 88(2):901–915, 2022.

[98] Luis M. De León-Rodríguez, Alfonso Ortiz, Allison L. Weiner, Shanrong Zhang, Zoltan Kovacs, Thomas Kodadek, and A. Dean Sherry. Magnetic resonance imaging detects a specific peptideprotein binding event. *Journal of the American Chemical Society*, 124(14):3514–3515, 2002. PMID: 11929234.

[99] Hemant Parmar, Tchoyoson C.C. Lim, Hong Yin, Violet Chua, Lay-Wai Khin, Tom Raidy, and Francis Hui. Multi-voxel mr spectroscopic imaging of the brain: utility in clinical setting-initial results. *European Journal of Radiology*, 55(3):401–408, 2005. Non Vascular Intervention Procedures II.

[100] Dmitriy M. Volochnyuk, Sergey V. Ryabukhin, Yurii S. Moroz, Olena Savych, Alexander Chuprina, Dragos Horvath, Yuliana Zabolotna, Alexandre Varnek, and Duncan B. Judd. Evolution of commercially available compounds for HTS. *Drug Discovery Today*, 24(2):390–402, 2019.

[101] Gregory A. Bakken, Andrew S. Bell, Markus Boehm, Jeremy R. Everett, Rosalia Gonzales, David Hepworth, Jacquelyn L. Klug-McLeod, Jeremy Lanfear, Jens Loesel, John Mathias, and Terence P. Wood. Shaping a screening file for maximal lead discovery efficiency and effectiveness: Elimination of molecular redundancy. *Journal of Chemical Information and Modeling*, 52(11):2937–2949, 2012. PMID: 23062111.

[102] Thierry Kogej, Niklas Blomberg, Peter J. Greasley, Stefan Mundt, Mikko J. Vainio, Jens Schamberger, Georg Schmidt, and Jörg Hüser. Big pharma screening collections: more of the same or unique libraries? The AstraZeneca–Bayer Pharma AG case. *Drug Discovery Today*, 18(19):1014–1024, 2013.

[103] Mathew Njoroge, Nicholas M. Njuguna, Peggoty Mutai, Dennis S. B. Ongarora, Paul W. Smith, and Kelly Chibale. Recent Approaches to Chemical Discovery and Development Against Malaria and the Neglected Tropical Diseases Human African Trypanosomiasis and Schistosomiasis. *Chemical Reviews*, 114(22):11138–11163, 2014.

[104] Michael Burdumy, Louisa Traser, Bernhard Richter, Matthias Echternach, Jan G. Korvink, Jürgen Hennig, and Maxim Zaitsev. Acceleration of MRI of the vocal tract provides additional insight into articulator modifications. *Journal of Magnetic Resonance Imaging*, 42(4):925–935, 2015.

[105] H. Nyquist. Certain topics in telegraph transmission theory. *Transactions of the American Institute of Electrical Engineers*, pages 617–644, 1928.

[106] Kieren Hollingsworth. Reducing acquisition time in clinical MRI by data undersampling and compressed sensing reconstruction. *Physics in medicine and biology*, 60:R297–R322, 10 2015.

[107] Jeffrey A. Fessler. Optimization Methods for Magnetic Resonance Image Reconstruction: Key Models and Optimization Algorithms. *IEEE Signal Processing Magazine*, 37(1):33–40, 2020.

[108] Li Feng, Thomas Benkert, Kai Tobias Block, Daniel K. Sodickson, Ricardo Otazo, and Hersh Chandarana. Compressed sensing for body MRI. *Journal of Magnetic Resonance Imaging*, 45(4):966–987, 2017.

[109] Christopher M. Rath, Bret M. Benton, Javier de Vicente, Joseph E. Drumm, Mei Geng, Cindy Li, Robert J. Moreau, Xiaoyu Shen, Colin K. Skepper, Micah Steffek, Kenneth Takeoka, Lisha Wang, Jun-Rong Wei, Wenjian Xu, Qiong Zhang, and Brian Y. Feng. Optimization of CoaD Inhibitors against Gram-Negative Organisms through Targeted Metabolomics. *ACS Infectious Diseases*, 4(3):391–402, 2018. PMID: 29243909.

[110] Robert J. Moreau, Colin K. Skepper, Brent A. Appleton, Anke Blechschmidt, Carl J. Balibar, Bret M. Benton, Joseph E. III Drumm, Brian Y. Feng, Mei Geng, Cindy Li, Mika K. Lindvall, Andreas Lingel, Yipin Lu, Mulugeta Mamo, Wosenu Mergo, Valery Polyakov, Thomas M. Smith, Kenneth Takeoka, Kyoko Uehara, Lisha Wang, Jun-Rong Wei, Andrew H. Weiss, Lili Xie, Wenjian Xu, Qiong Zhang, and Javier de Vicente. Fragment-Based Drug Discovery of Inhibitors of Phosphopantetheine Adenylyltransferase from Gram-Negative Bacteria. *Journal of Medicinal Chemistry*, 61(8):3309–3324, 2018. PMID: 29498517.

[111] Nils Lorz, Barbara Czarniecki, Sandra Loss, Benno Meier, and Alvar D. Gossert. Higher Contrast in ^{1}H-Observed NMR Ligand Screening with the PEARLScreen Experiment. *Angewandte Chemie International Edition*, n/a(n/a):e202423879, 2025.

[112] R. Mark Henkelman. Measurement of signal intensities in the presence of noise in MR images. *Medical Physics*, 12(2):232–233, 1985.

[113] Paul A. Bottomley. Spatial localization in NMR spectroscopy in vivo. *Annals of the New York Academy of Sciences*, 508:333–348, 1987.

[114] Matt A. Bernstein, Kevin F. King, and Xiaohong Joe Zhou. *Handbook of MRI Pulse Sequences*. Elsevier Academic Press, Amsterdam, 2004.

[115] Thomas D. Pollard. A guide to simple and informative binding assays. *Molecular Biology of the Cell*, 21(23):4061–4067, 2010. PMID: 21115850.

[116] William Pomerantz and Caroline Buchholz. ^{19}F NMR Viewed Through Two Different Lenses: Ligand-Observed and Protein-Observed ^{19}F NMR Applications for Fragment-Based Drug Discovery. *RSC Chemical Biology*, 2:1312–1330, 07 2021.

[117] Nobuyuki Ota, Christopher Stroupe, J.M.S. Ferreira-da Silva, Sapan Shah, Marcos Mares-Guia, and Axel Brunger. Non-Boltzmann Thermodynamic Integration (NBTI) for macromolecular systems: relative free energy of binding of trypsin to benzamidine and benzylamine. *Proteins*, 37:641–53, 01 2000.

[118] F. Markwardt, H. Landmann, and P. Walsmann. Comparative studies on the inhibition of trypsin, plasmin, and thrombin by derivatives of benzylamine and benzamidine. *European Journal of Biochemistry*, 6(4):502–506, 1968.

[119] Michaela Antonín Malaníková and Jaroslava Turková. Determination of dissociation constants of complexes of trypsin and its low molecular weight inhibitors by affinity chromatography in zonal and frontal analysis arrangement. *Journal of Solid-Phase Biochemistry*, 2:237–249, 1977.

[120] Jeffrey P Hughes, Stephen Rees, Sonya B Kalindjian, and Karen L Philpott. Principles of early drug discovery. *British Journal of Pharmacology*, 162(6):1239–1249, 2011.

[121] Ricardo Macarron, Michael N Banks, Dario Bojanic, and et al. Impact of high-throughput screening in biomedical research. *Nature Reviews Drug Discovery*, 10:188–195, 2011.

[122] Gregory Sliwoski, Sandeep Kothiwale, Jens Meiler, and Jeremy A Lowe. Computational methods in drug discovery. *Pharmacological Reviews*, 66(1):334–395, 2014.

[123] M. Marquart, J. Walter, J. Deisenhofer, W. Bode, and R. Huber. The geometry of the reactive site and of the peptide group in trypsin, trypsinogen and its complexes with inhibitors. *Journal of Molecular Biology*, 170(4):923–947, 1983.

[124] Lizbeth Hedstrom. Serine protease mechanism and specificity. *Chemical Reviews*, 102(12):4501–4524, 2002.

[125] J. J. Perona and C. S. Craik. Evolutionary divergence of substrate specificity within the chymotrypsin-like serine protease fold. *Protein Science*, 6(3):557–568, 1997.

[126] S. L. McGovern, B. T. Helfand, B. Feng, and B. K. Shoichet. A specific mechanism for non-specific inhibition. *Journal of Medicinal Chemistry*, 45(8):1712–1722, 2002.

[127] J. Seidler, S. L. McGovern, T. N. Doman, and B. K. Shoichet. Identification and prediction of promiscuous aggregating inhibitors among known drugs. *Journal of Medicinal Chemistry*, 46(21):4477–4486, 2003.

[128] Pamela S. Sears and Douglas S. Clark. Comparison of soluble and immobilized trypsin kinetics: Implications for peptide synthesis. *Biotechnology and Bioengineering*, 42(1):118–124, 1993.

[129] Matthias Bütikofer, Gabriela Stadler, and Felix Torres. Rescaling NMR for a Larger Deployment in Drug Discovery: Hyperpolarization and Benchtop NMR as Potential Game-Changers. *Chemistry - Methods*, 4, 09 2024.

[130] Gabriela R. Stadler, Takuya F. Segawa, Matthias Bütikofer, Venita Decker, Sandra Loss, Barbara Czarniecki, Felix Torres, and Roland Riek. Fragment Screening and Fast Micromolar Detection on a Benchtop NMR Spectrometer Boosted by Photoinduced Hyperpolarization. *Angewandte Chemie International Edition*, 62(40):e202308692, 2023.

[131] Herman Y. Carr and Edward M. Purcell. Effects of diffusion on free precession in nuclear magnetic resonance experiments. *Physical Review*, 94(3):630–638, 1954.

[132] Jürgen Hennig, A. Nauerth, and H. Friedburg. RARE Imaging: A Fast Imaging Method for Clinical MR. *Magnetic Resonance in Medicine*, 3(6):823–833, 1986.

[133] Kuni Oshio and David A. Feinberg. GRASE (Gradient-and-Spin-Echo) Imaging: A Novel Fast MRI Technique. *Magnetic Resonance in Medicine*, 20(2):344–349, 1991.

[134] Michael K. Stehling, Robert Turner, and Peter Mansfield. Echo-Planar Imaging: Magnetic Resonance Imaging in a Fraction of a Second. *Science*, 254(5028):43–50, 1991.

[135] Michael Lustig, David Donoho, and John M. Pauly. Sparse MRI: The Application of Compressed Sensing for Rapid MR Imaging. *Magnetic Resonance in Medicine*, 58(6):1182–1195, 2007.

[136] Florian Knoll, Timothy Murrell, Anuroop Sriram, Nazim Yakubova, Jure Zbontar, Michael Rabbat, Aaron Defazio, Matthew J. Muckley, Daniel K. Sodickson, Thomas Köhler, and Kerstin Hammernik. Advancing Machine Learning for MR Image Reconstruction: A Framework for Evaluation of MRI Reconstruction Algorithms. *Magnetic Resonance in Medicine*, 84(6):3054–3070, 2020.

[137] I. Solomon. Relaxation Processes in a System of Two Spins. *Phys. Rev.*, 99:559–565, Jul 1955.

[138] Nicolaas Bloembergen and Louis Morgan. Proton relaxation times in paramagnetic solutions. effects of electron spin relaxation. *The Journal of Chemical Physics*, 27(3):622–630, 1957.

[139] I. Solomon. Relaxation processes in a system of two spins. *Physical Review*, 99(2):559–565, 1955.

[140] Peter Caravan, James J. Ellison, Thomas J. McMurry, and Randall B. Lauffer. Gadolinium(III) Chelates as MRI Contrast Agents: Structure, Dynamics, and Applications. *Chemical Reviews*, 99:2293–2352, 1999.

[141] Kevin M. Donahue, Robert M. Weisskoff, and David Burstein. Water diffusion and exchange as they influence contrast enhancement. *Magnetic Resonance in Medicine*, 32(1):66–76, 1994.

[142] Gregory J. Stanisz and R. Mark Henkelman. Gd-DTPA relaxivity depends on macromolecular content. *Magnetic Resonance in Medicine*, 44(4):665–667, 2000.

[143] A. D. Sherry, P. Caravan, and R. E. Lenkinski. Primer on Gadolinium Chemistry. *Journal of Magnetic Resonance Imaging*, 30:1240–1248, 2009.

[144] Miles A Kirchin and Val M Runge. Contrast agents for magnetic resonance imaging: safety update. *Topics in magnetic resonance imaging : TMRI*, 14(5):426—435, October 2003.

[145] Bert Wouters, Paul Miggiels, Roland Bezemer, Elwin A.W. van der Cruijsen, Erik van Leeuwen, John Gauvin, Klaartje Houben, Karthick Babu Sai Sankar Gupta, Paul Zuijdwijk, Amy Harms, Adriana Carvalho de Souza, and Thomas Hankemeier. Automated Segmented-Flow Analysis - NMR with a Novel Fluoropolymer Flow Cell for High-Throughput Screening. *Analytical Chemistry*, 94(44):15350–15358, 2022.

[146] Carole Lazarus, Pierre Weiss, Nicolas Chauffert, Franck Mauconduit, Loubna El Gueddari, Christophe Destrieux, Ilyess Zemmoura, Alexandre Vignaud, and Philippe Ciuciu. SPARKLING: variable-density k-space filling curves for accelerated T_2-weighted MRI. *Magnetic Resonance in Medicine*, 81(6):3643–3661, 2019.

[147] Yoseo Han, Leonard Sunwoo, and Jong Chul Ye. *k*-Space Deep Learning for Accelerated MRI. *IEEE Transactions on Medical Imaging*, 39(2):377–386, 2020.

[148] Burhaneddin Yaman, Seyed Amir Hossein Hosseini, Steen Moeller, Jutta Ellermann, Kâmil Uğurbil, and Mehmet Akçakaya. Self-supervised learning of physics-guided reconstruction neural networks without fully sampled reference data. *Magnetic Resonance in Medicine*, 84(6):3172–3191, 2020.

[149] L. A. Shepp and B. F. Logan. The Fourier reconstruction of a head section. *IEEE Transactions on Nuclear Science*, 21(3):21–43, 1974.

Publications

Journal articles

- [DF1] Dilara Faderl, Ajmal Chenakkara, Mazin Jouda, Neil MacKinnon, Alvar D. Gossert, and Jan G. Korvink. Accelerated Screening of Protein–Ligand Interactions via Parallel T_2-Weighted ^{19}F-MRI. *Analytical Chemistry*, 96(24):9859–9865, 2024. DOI:10.1021/acs.analchem.4c00333

- [DF2] Mengjia He, Dilara Faderl, Neil MacKinnon, Yen-Tse Cheng, Dominique Buyens, Mazin Jouda, Burkhard Luy, and Jan G. Korvink. A digital twin for parallel liquid-state nuclear magnetic resonance spectroscopy.*Communications Engineering*, 3(1):90, 2024. DOI:10.1038/s44172-024-00233-0

List of Figures

List of Tables

Acknowledgements

I would like to express my deepest gratitude to all the people who supported me throughout this remarkable journey. This thesis would not have been possible without the guidance, encouragement, and kindness I received from so many individuals.

1. **Prof. Dr. Jan Korvink.**

I would like to express my sincere gratitude for your continuous support throughout the course of my Ph.D. Your insightful advice, scientific guidance, and steady leadership enabled me to navigate the challenges of this work and progress with confidence. I am particularly appreciative of your understanding and encouragement during the most demanding phases of my studies. Your support in enabling conference participation provided me with the opportunity to present our work internationally and engage with researchers from diverse disciplines. The recognition and interest expressed by the scientific community made this doctoral journey especially meaningful. For your guidance, the opportunities you facilitated, and your continuous support, I extend my sincere Thanks.

2. **Prof. Dr. Pavel Levkin.**

Thank you for kindly agreeing to be the co-examiner of my Ph.D. defense. I highly appreciate your time and commitment. I look forward to your suggestions, which will undoubtedly guide me as I continue my scientific career.

3. **Dr. Neil MacKinnon.**

You have been an unwavering source of support throughout my entire Ph.D. journey. Your scientific insight, patience, and countless helpful suggestions shaped many of the ideas and solutions in this thesis. Thank you for being both a scientific mentor and a compassionate listener during difficult moments, whether they were personal or work-related. Your understanding of my responsibilities as a mother made it possible for me to stay strong through all the storms. I am deeply grateful.

4. **Dr. Alvar D. Gossert.**

When everything felt dark, you illuminated my path and helped me see the way through my Ph.D. Thank you for running experiments together with me and for helping me understand the underlying practical aspects of our work. Your clarity and support were invaluable.

5. **Dr. Mazin Jouda.**

Thank you for teaching me the technical foundations of MRI and for patiently explaining hardware-related concepts. I also appreciate your understanding of my responsibilities as a parent and for listening to me whenever life—from science to kindergarten to school—became overwhelming. Your support meant more than words can express.

6. SAP support
I would also like to express my sincere appreciation to Nina Giraud. Your support with administrative matters—from SAP to ordering to countless bureaucratic steps—was indispensable. Without your help, this Ph.D. would have taken much longer. Thank you for explaining everything with such patience and for the delicious Pizzaschnecken!

7. My colleagues at IMT.
To my former colleagues Julia Schulte-Hermann, Andrea Cristina Hurtado Rivera, and Francisco Ayuso: Thank you for welcoming me so warmly and supporting me during the early days of my Ph.D.

To my current colleagues Dr. Sören Lehmkuhl, Dr. Jing Yang, Dr. Dario Mager, Shraddha Singhal, Sebastian Corredor, and Hossein Esmaeilizadshali: Thank you for your support, encouragement, and friendship.

To Voxalytic Team, Dr. Ronald Kampmann, and Dr. Sagar Wadhwa: Thank you for your readiness to assist whenever I had questions and for providing outstanding engineering solutions throughout this project. Your expertise and support were essential for overcoming several technical challenges.

To my good friend Dr. Mehrdad Alinaghian Jouzdani: I will never forget your advice, our weekend work sessions, and your constant encouragement. Without your smile and support, I would have felt lost.

To my dearest colleague Ajmal Jamal: Thank you for being such an exceptional colleague and friend throughout this work. During countless measurements, you were always by my side, especially whenever something went wrong, and your calm support helped me continue. Beyond the scientific help, your willingness to listen, even in the most silent and difficult moments, meant more to me than words can express. I am deeply grateful for your presence, your kindness, and your unwavering support.

To my IMT colleague Fernando Arteaga Cardona: Thank you for your friendship and for sharing both the good and difficult days. Your support has always meant a great deal.

A very special Thanks to Dr. Dominique Buyens and Nourhan Abouellel: my forever listeners. Thank you for your patience, your advice, and your constant readiness to help—both professionally and personally.

8. My colleagues in HiScore Project:

Thank you for all the wonderful memories we gathered during the HiSCORE meetings in Paris, Nijmegen, and Switzerland. Although our projects differed scientifically, we met in the midst of our Ph.D. journeys and grew together through countless discussions, shared challenges, and moments of joy. Those experiences connected us beyond research and made this journey truly meaningful.

My dearest friend Sebastiaan Van Dyck: We shared countless voice messages when we could not see each other, and whenever we finally met in person, the energy of the group shifted instantly in a positive direction. You made me laugh deeply and reminded me how joyful life can be when you are surrounded by cherished people like you. Thank you for bringing lightness, humor, and genuine friendship into this journey.

9. My family.

To my beloved son: Thank you for your endless patience when I had to meet deadlines, for waiting quietly while I worked, and for hugging me at the very moments when I needed it most. You tried to understand the world I was working in, and your pride in telling others about the science your mother is doing meant more to me than anything. You gave me strength every single day.

To my mother: Thank you for always waiting for my calls, for your unconditional love, and for being proud of me no matter what I achieved. Your support has been a source of stability throughout every difficult moment, and I am forever grateful for your strength and encouragement.

To my dear friend Marcus: Thank you for being by my side when I needed it most.

To my second mothers, Heidi Faderl and Susanne Reber: With you, I found the warmth and love that make a place feel like home.Thank you for your endless hugs and your unwavering emotional support.

I am deeply grateful to all of you.